Analytical and Numerical Studies of Several Fluid Mechanical Problems

Volume 1 of 1

Submitted by Dali Kong to the University of Exeter
as a thesis for the degree of
Doctor of Philosophy in Mathematics
in May 2012

I certify that all material in this thesis which is not my own work has been identified and that no material has previously been submitted and approved for the award of a degree by this or any other University.

Signature: 孔大力 .....

This page is intentionally left blank.

Abstract

In this thesis, three parts, each with several chapters, are respectively devoted to hydrostatic, viscous and inertial fluids theories and applications. In the hydrostatics part, the classical Maclaurin spheroids theory is generalized, for the first time, to a more realistic multi-layer model, which enables the studies of some gravity problems and direct numerical simulations of flows in fast rotating spheroidal cavities. As an application of the figure theory, the zonal flow in the deep atmosphere of Jupiter is investigated for a better understanding of the Jovian gravity field. High viscosity flows, for example Stokes flows, occur in a lot of processes involving low-speed motions in fluids. Microorganism swimming is such typical a case. A fully three dimensional analytic solution of incompressible Stokes equation is derived in the exterior domain of an arbitrarily translating and rotating prolate spheroid, which models a large family of microorganisms such as cocci bacteria. The solution is then applied to the magnetotactic bacteria swimming problem and good consistency has been found between theoretical predictions and laboratory observations of the moving patterns of such bacteria under magnetic fields. In the analysis of dynamics of planetary fluid systems, which are featured by fast rotation and very small viscosity effects, three dimensional fully nonlinear numerical simulations of Navier-Stokes equations play important roles. A precession driven flow in a rotating channel is studied by the combination of asymptotic analyses and fully numerical simulations. Various results of laminar and turbulent flows are thereby presented. Computational fluid dynamics requires massive computing capability. To make full use of the power of modern high performance computing facilities, a C++ finite-element analysis code is under development based on PETSc platform. The code and data structures will be elaborated, along with the presentations of some preliminary results.

Contents

List of Figures

List of Tables

Acknowledgements

I want to thank the College of Engineering, Mathematics and Physical Sciences, University of Exeter, for the studentship supporting me completing the degree training and research work.

During the three academic years, my primary research projects have been done under the supervision of Professor Keke Zhang. It was his effective supervision and financial support that guaranteed my highly efficient research progress. I have learnt a lot of ideas, methodologies and even wisdom from Prof. Zhang, which certainly will benefit my future career.

Nearly all of my work required intensive numerical computations, especially like a lot of large scale 3-D simulations presented, for example, in the Chapter 5 and Chapter 6. Via team collaborations with Professor Xinhao Liao and Professor Ligang li in Shanghai Astronomical Observatory, Chinese Academy of Sciences, I fortunately gained access to several world-class powerful supercomputing facilities, which are respectively an observatory owned IBM blades server, the 'Downing 4000A' machine in Shanghai Supercomputing Center (http://www.ssc.net.cn/en/index.aspx) and the 'Sunway' machine in Wuxi Supercomputing Center (http://www.wxsc.net.cn/default2.html). I appreciate the assistances I have ever received from Prof. Liao and Prof. Li.

Professor Jun Zou from Department of Mathematics, the Chinese University of Hong Kong, has been giving me great help and guides on both theoretical and practical aspects of finite-element methods and domain-decomposition methods. I want to thank him also for his efforts in arranging my visit to Shenzhen Institutes of Advanced Technology, Chinese Academy of Sciences, where I started getting familiarized with the PETSc platform and CPU-GPU hybrid programming.

I want to thank Dr. Kit Hung Chan from Department of Mathematics, the University of Hong Kong. It was his patient help that led me into the palace of finite-element methods. I first learnt the implementation of a finite-element scheme from his 3D EBE finite-element code.

The research related to the magnetotactic bacteria swimming problem, in Chapter 4, was mainly inspired by the discussion with Professor Yongxin Pan from Institute of Geology and Geophysics, Chinese Academy of

Sciences. I want to thank him not only for his introduction into the background of relevant areas, but also for his visit offer to his laboratory in 2011 summer time.

Finally, this thesis is dedicated to my mother. She has raised me up to more than I can be.

Nomenclature

Roman Symbols

$\mathcal{E}$	Eccentricity
I	Identity matrix/tensor
c	Focal length of a oblate/prolate spheroid
G	Gravitational constant
i	Unit imaginary number $\sqrt{-1}$
s	The distance from the axis in the cylindrical coordinate system
V	Scalar potentials

Greek Symbols

δ_{ij}	The Kronecker delta
η	The angular coordinate of oblate/prolate spheroidal coordinate systems
Ω	Angular speed of rotation
ϕ	The azimuthal coordinate of spherical and oblate/prolate spheroidal coordinate systems
ρ	Mass density
θ	The angular coordinate of spherical coordinate systems
ξ	The radial coordinate of oblate/prolate spheroidal coordinate systems

Other Symbols

$P_l^m(ix)$,$Q_l^m(ix)$	Associate Legendre functions of first and second kind of imaginary arguments
$P_l^m(x)$,$Q_l^m(x)$	Associate Legendre functions of first and second kind

Chapter 1

Introduction

As a branch of continuum mechanics, which models matter from a macroscopic point of view instead of considering matter made out of discrete atoms or molecules, fluid mechanics has been studied since ancient times. Fluids, including liquids, gases and plasmas, are matter which must deform and flow under an applied shear stress. The flowability distinguishes fluids from matter in the solid state. One of the most important underlying assumption in fluid mechanics, also in general continuum mechanics, is the continuum hypothesis that matter filling a domain is distributed continuously. That is to say that physical quantities such as density, temperature, pressure and velocity must be definite and spatially continuous functions within the domain occupied by fluids. This assumption is valid if the typical geometric length scale of the fluid is much larger than the typical distance between two adjacent atoms or molecules. As elaborated in [Wu, 1982], under this condition, macroscopically speaking, an infinitesimal material point still contains a sufficiently large number of microscopic particles such that statistical fluctuations are negligible. The mean values of statistical quantities, which represent the macroscopically localized physical quantities, will be then sufficiently continuous among neighboring material points. In this sense, except for such extreme occasions as spacecrafts flying in very thin outer atmosphere and shock wave region, a lot of geophysical and astrophysical fluid systems satisfy the continuum hypothesis and, hence, can be investigated in the regime of fluid mechanics.

The dynamics of any fluid mechanical problem, under a velocity field $\mathbf{u}(t, \mathrm{x}) \in \mathbb{R}^n$ ($n = 3$ throughout this thesis), can be described by the flow map, a time-dependent orientation-preserving family of diffeomorphisms $\mathrm{x}(t, \alpha) \in \mathbb{R}^n$, $0 \leq t \leq T$ (See [Lei, 2009]). The material point $\alpha \in \mathbb{R}^n$ is deformed to the spatial position $\mathrm{x}(t, \alpha)$ at time t

$$\frac{d\mathrm{x}(t, \alpha)}{dt} = \mathbf{u}(t, \mathrm{x}(t, \alpha)), \quad \mathrm{x}(0, \alpha) = \alpha, \tag{1.1}$$

in which α is usually called Lagrangian coordinates while x is referred to as Eulerian coordinates. In the Lagrangian specification of a flow, one describes the kinematics of the fluid by tracking the motion of each material point labeled by α, as in (1.1),

and hence records the new configuration of the fluid at time t. This leads to the Lagrangian fluid mechanics (see [Bennett, 2006]). However, in many aspects, the Eulerian representation of flow fields is more convenient. By focusing on spatial points rather than fluid material points, the Eulerian representation treats all the physical quantities as scalar or vectorial fields, such as the velocity field $u(t, \mathrm{x})$, the density field $\rho(t, \mathrm{x})$, the pressure field $p(t, \mathrm{x})$ and the temperature field $T(t, \mathrm{x})$. Through looking into the temporal and spatial variations of the physical fields, one then gains an overall picture of the fluid motions. In this thesis, we always work in the Eulerian representation.

Generally, within the area of classical mechanics, flows are governed by conservation laws of mass, momentum and energy. The three fundamental principles result in the governing equations of fluid mechanics as

$$\begin{cases} \dfrac{\partial \rho}{\partial t} + \nabla \cdot (\rho \mathbf{u}) = 0, & \text{The mass conservation law} \\ \rho \left(\dfrac{\partial \mathbf{u}}{\partial t} + \mathbf{u} \cdot \nabla \mathbf{u} \right) = -\nabla p + \nabla \cdot \tau + \rho \mathrm{f}, & \text{The momentum conservation law} \\ \rho \left(\dfrac{\partial E}{\partial t} + \mathbf{u} \cdot \nabla E \right) = (-p\mathrm{I} + \tau) :: \sigma + \nabla \cdot (k \nabla T) + \rho q, & \\ & \text{The energy conservation law} \\ \tau = \tau(\sigma), \sigma = \dfrac{\nabla \mathbf{u} + \nabla \mathbf{u}^T}{2}, & \text{The constitutive equation,} \\ p = p(\rho, T), & \text{The equation of state.} \end{cases} \tag{1.2}$$

In the equations, τ is the shear stress tensor which is a function of the strain tensor σ; f is the external body force acting on the fluid; E is the internal energy; k is the thermal conductivity and q is the heat generation rate. Details of derivations and physical implications of the governing equations can be found in various classical fluid mechanics books, e.g. [Chandrasekhar, 1981; Lamb, 1932].

In the above constitutive equation, if the shear stress τ is only linearly dependent on components of the strain σ and the dependency curves all pass through the origin, it is called a newtonian fluid. Non-newtonian fluids, such as raw rubber and toothpaste, are most often seen that the shear stress can also depend on shear rate or shear rate history (see an Oldroyd-B model formulated in [Oldroyd, 1950]). In this thesis, all the problems we work around only involve newtonian fluids.

We introduce the deformation tensor based on (1.1)

$$F_{ij}(t, \mathrm{x}(t, \alpha)) = \frac{\partial x_i(t, \alpha)}{\partial \alpha_j}. \tag{1.3}$$

If $\det F = 1$ holds, the flow map $\mathrm{x}(t, \alpha)$ is said to be volume-preserving (see [Lei et al., 2008]), which implies that the fluid is incompressible. Its counterpart in the Eulerian representation is $\nabla \cdot \mathbf{u} = 0$. For incompressible Newtonian fluids, the

constitutive equation is

$$\tau_{ij} = \mu \left(\frac{\partial u_j}{\partial x_i} + \frac{\partial u_i}{\partial x_j} \right)$$

and the momentum equation takes the appearance of the famous incompressible Navier-Stokes equation

$$\frac{\partial \mathbf{u}}{\partial t} + \mathbf{u} \cdot \nabla \mathbf{u} = -\frac{\nabla p}{\rho} + \mu \nabla^2 \mathbf{u} + \mathrm{f},$$

where μ is a well defined kinematic viscosity. Incompressible fluids are good approximations of liquids whose compressibility is usually very low; also, if in some gas problems, the compressibility can be neglected for some reasons, we still can apply the model of incompressible fluids to them, usually achieving great simplicity without loss of important physics. In this thesis, Chapter 2 and Chapter 3 deal with the shape theories of rotating planets. Although giant gaseous planets enter the analyses, we still consider the incompressible fluid settings. Relevant discussions and validations can be found in respective chapters. Since Chapter 4 mainly consists of analysis of microorganism's motion in water, the incompressible condition is naturally satisfied. In Chapter 5, we still explore into the incompressible flows inside a precessing channel, which simulate outer core or mantle flows within planets with precession. In the last chapter, however, we touch the regime of compressible fluids. A finite-element code developed for compressible convection problems is elaborated. However, only the first stage of the code development has been done and reported in this thesis. We have already made a preliminary application of the code to a polytropic model of Gaseous planets.

The research areas of fluid mechanics can be divided into hydrostatics, the study of fluids at rest; fluid kinematics, the study of fluids in motion; and fluid dynamics, the study of the interactions between fluids and force acting on them. In this thesis, chapters are basically arranged according to the sequence from hydrostatics to fluid dynamics. Chapter 2 and Chapter 3 are on hydrostatic planetary configuration problems; Chapter 4 discusses a fluid kinematical problem emerging from bacteria swimming processes; Chapter 5 is fully engaged by the dynamics of precession driven flows in a channel geometry; Finally, Chapter 6, though not directly linked to any dynamical problems for the time being, is devoted to future relevant work on compressible thermal convection.

Fluid mechanics equations can often be mathematically complicated and difficult to solve, even approximately. Sometimes, numerical methods are the best candidates to solve such equations. With the help of modern high performance computing facilities, providing massive parallel computing capacities, various well developed and tested numerical schemes can be applied to fluids systems in the proper manner according to the particular nature of each problem. In the sense of accuracy, geometrical flexibility, parallelization etc., methods such as finite-difference, finite-

volume and finite-element all have advantages and drawbacks. The comparison of different numerical methods applied to Navier-Stokes equations can be found, for example, in [Hesthaven and Warburton, 2008]. In this thesis, problems are solved analytically or semi-analytically in Chapter 2–4; While the remaining two chapters are contributed by fully numerical work. In Chapter 5, the reason why we choose a finite-difference method to simulate precession driven flows in a rotating channel is largely because of the regular rectangular geometry; however, in Chapter 6, the newly developed code will be extended to thermal convection problems mainly in spherical and spheroidal domains, in which the finite-element method we adopt can avoid cumbersome schemes and annoying coordinates singularity problems facing finite-difference methods.

This thesis consists of chapters that are relatively independent from one another. Chapter 2 and Chapter 3, can be regarded as two different applications and progresses of the classical Maclaurin spheroids theory (see [Chandrasekhar, 1969; Lamb, 1932]). The Papkovich-Neuber type solutions of the incompressible Stokes equation derived in Chapter 4 are the ensuing work of interesting discussions with Prof. Yongxin Pan on magnetotactic bacteria swimming problems. Even though this individual project has not much to do with the main theme of my PhD research, namely, astrophysical fluid systems, the inter-discipline joint work with biological people proves to be beneficial and promising. The analytical solutions have helped precisely model the swimming behaviors of magnetotactic bacteria under externally imposed magnetic fields. The results have a lot of potential applications in the researches of bio-magnetotaxis and bio-mineralization. The work in Chapter 5 is the first project I did in my PhD programme. Starting from this project, I got myself familiarized with and impressed by modern parallel computing. After the completion of all the numerical work in this Chapter, I became skilled and experienced in this area and could then independently work on parallel computations. In the last chapter, an extensible finite-element code built on PETSc platform (see [Balay et al., 2011]) is presented as a phased work. In the current stage, this code is ready for solving 3-D time-independent general elliptic equations by a Galerkin finite element method. Both the object-oriented-programming (OOP) methodology and the PETSc toolkits make it much easier to extend this code to general convection-diffusion equations and finally, the Navier-Stokes equations.

It is also worth mentioning that most of the contents of this thesis has been published in or accepted by proper peer reviewed journals. Chapter 2 was published in "J. Geophys. Res.,(2010),115,E12003"; Chapter 3 has been published in "ApJ, (2012), 748, 143" after revisions; Chapter 4 has been published in "International Journal of Pure and Applied Mathematics, (2012), 75, 455". Chapter 5 is my contribution to the paper published in "J. Fluid Mech., (2010), 656, 116-146". The last chapter currently does not contain anything published. Within each chapter,

there are more background introductions and literature reviews. And, this thesis only includes my independent work in the publications mentioned above, as declared seriously in the title page.

Chapter 2

Shapes of Two-layer Models of Rotating Planets

2.1 Introduction

As a consequence of the interactions among the Sun, planets and satellites, many planetary bodies are rotating non-uniformly, resulting in precession or libration of those planets ([Tilgner, 2007a; Williams et al., 2001]). [Bullard, 1949] (see also [Malkus, 1968]) proposed that precessionally driven flows in the spheroidal cavity of the Earth's core may generate and maintain the geomagnetic field. It is estimated that there is abundant energy in rotation to sustain the generation of planetary magnetic fields ([Kerswell, 1993]). It has been shown experimentally that the spatially complex flows required for dynamo action can occur in non-uniformly rotating spheroidal systems ([Malkus, 1968; Noir and Cardin, 2001; Noir et al., 2003b; Vanyo et al., 2007]). Recently, it has been convincingly demonstrated that precession-driven flows can indeed generate and sustain magnetic fields ([Tilgner, 2005a; Wu and Roberts, 2008]). A vitally important parameter for the dynamo problem is the geometrical shape of the fluid core, which, due to the effect of rotation, is usually in the form of an oblate spheroid with semi-major axis a_0 and semi-minor axis $a_0\sqrt{1-\mathcal{E}_0^2}$

$$\frac{x^2+y^2}{a_0^2}+\frac{z^2}{a_0^2(1-\mathcal{E}_0^2)}=1, \tag{2.1}$$

where $0 \leq \mathcal{E}_0 < 1$ denotes the eccentricity of the spheroidal core and z is in the direction of rotation. It is the eccentricity of the core $\mathcal{E}_0$ that determines and controls both the style and strength of fluid motion driven by the non-uniform rotation of the planet ([Busse, 1968; Lorenzani and Tilgner, 2001; Roberts and Stewartson, 1965; Zhang et al., 2004]).

More than two centuries ago, Colin Maclaurin solved the problem of the attraction of a homogeneous spheroid when departure from sphericity is so large that it cannot be treated as a small perturbation, determining the relationship between

the eccentricity of a rotating homogeneous spheroid with density ρ_0 and its angular speed Ω. As discussed in detail in many monographs ([Chandrasekhar, 1969; Lamb, 1932]), a rotating homogeneous fluid planet is in the shape of an axisymmetric spheroid with its eccentricity $\mathcal{E}_0$ given by the explicit equation:

$$\epsilon_0 = \frac{\sqrt{1-\mathcal{E}_0^2}}{\mathcal{E}_0^3}(3-2\mathcal{E}_0^2)\sin^{-1}(\mathcal{E}_0) - \frac{3(1-\mathcal{E}_0^2)}{\mathcal{E}_0^2}, \tag{2.2}$$

where $\epsilon_0 = \Omega^2/(2\pi G\rho_0)$ and G is the universal gravitational constant. The shape of the body is usually referred to as the Maclaurin spheroid. In Figure 2.1, ϵ_0 is plotted against the eccentricity $\mathcal{E}_0$ in the interval between 0 and 1. Simply on

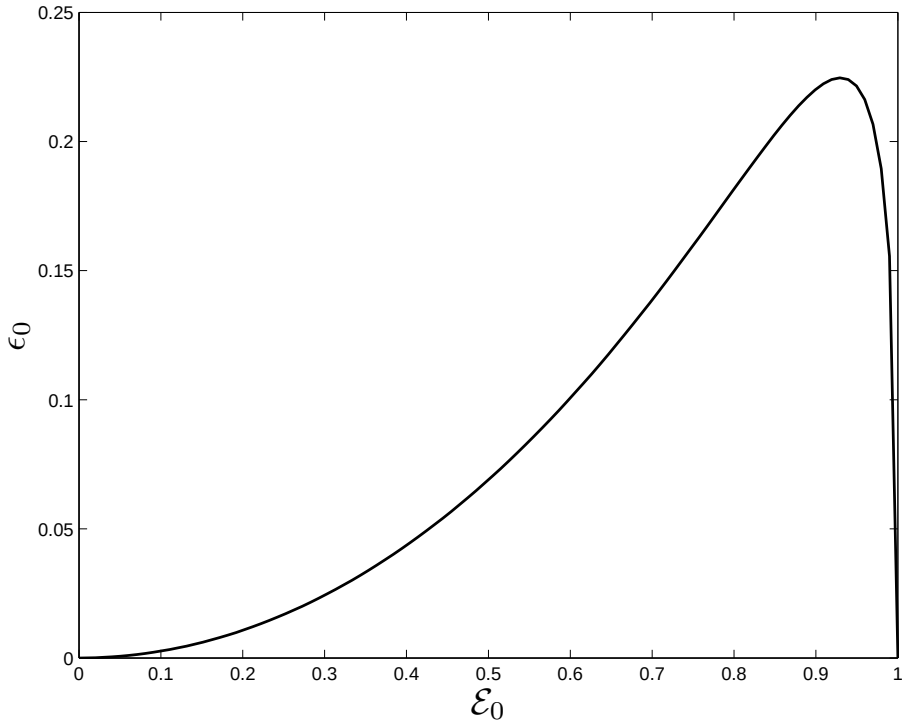

Figure 2.1: The rotation-eccentricity relation of a classical Maclaurin spheroid

observation of the curve, we can realize that for a particular of ϵ_0, there seems to be two values that eccentricity can take. Both eccentricities satisfy the free surface condition. However, only the smaller eccentricity, which minimizes the total energy, is physically possible. The free surface condition and energy minimum principle will be discussed in §2.3. In other words, the descending branch of the curve in Figure 2.1 is only mathematically reasonable. A stable Maclaurin spheroid cannot be more oblate than the shape of a critical eccentricity, about 0.93. After that, there are several bifurcations from the Maclaurin sequence into non-axisymmetric configuration sequences (see [Bardeen, 1971; Chandrasekhar, 1969; Chandrasekhar and Lebovitz, 1964]).

To a first approximation, however, the interiors of many planetary bodies, such as Mercury, the Earth and Ganymede, consist of a core and a mantle with substantially

different densities. Even for such a simple density distribution, the equilibrium figure is never an exact spheroid. Mathematical explanations are presented later in the following chapters. However, such departure from a spheroid is extremely minor, as also verified carefully in later discussions. Therefore, the spheroidal shape is still well applied. Evidently, the eccentricity of the interface between the core and the mantle, which is not observable, would be different from that of the outer surface. However, there is no exact theory of two-layer rotating planets that can determine the shape of a spheroidal fluid core. [Zharkov et al., 1985] have developed an approximate theory for the shape of two-layer rotating models in which departure from sphericity is treated as a small perturbation, though the shapes of non-spherical cores were not explicitly presented.

The primary objective of the present study is to develop a theory for the distortion of a rotating, two-layer Maclaurin spheroid that determines the shapes of both the interface and the outer free surface and does not treat departure from sphericity as a small perturbation. The numerical approach based on direct simulation using a spheroidal code is both difficult and computationally expensive. This is because a spheroidal mesh for direct numerical simulation, which is unknown in the present problem, is required prior to running the simulation. At first glance, one might expect that an analytical formula like (2.2) for the classical Maclaurin spheroid could be derived for a two-layer Maclaurin spheroid. As we demonstrate, however, an extension of the Maclaurin theory from a one-layer to a two-layer model is far from straightforward. It involves the transformation between two different spheroidal coordinates and multiple integrals that must be evaluated numerically in an intricate way with the upper/lower limits of the integrals being complicated functions of the solution of the problem. A great deal of our effort is spent evaluating the quadruple integrals. This mathematical complexity probably explains why the classical Maclaurin theory has never been extended to that of a two-layer spheroid.

In what follows, we begin by presenting the two-layer model and two different systems of spheroidal coordinates in §2.2. The mathematical analysis and the results are presented in §2.3, while a summary and some remarks are given in §2.4.

2.2 Spheroidal Coordinates and Model

2.2.1 Oblate Spheroidal Coordinate System

A general oblate spheroidal coordinate system can be formed by rotating a two-dimensional elliptic coordinate system about its minor axis, which naturally introduces the azimuthal coordinate $\phi \in [0, 2\pi]$. Let the z axis be the one of rotation

and $s = \sqrt{x^2 + y^2}$. The relation

$$\begin{cases} x = s\cos\phi \\ y = s\sin\phi \end{cases} \tag{2.3}$$

is to be found immediately. The other two coordinates grid in an arbitrary meridional $z - s$ cross-section is shown in Figure 2.2. The three coordinates are therefore

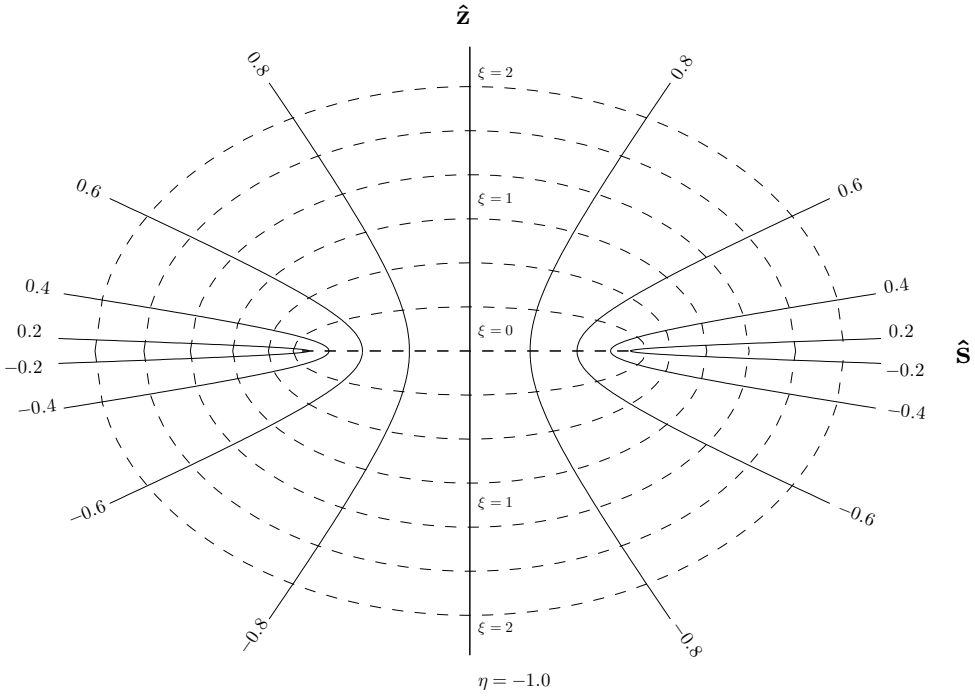

Figure 2.2: Illustration of oblate spheroidal coordinates within a meridional cross section

$\xi \in [0, \infty)$,which is a radial variable, $\eta \in [-1, 1]$, which is an angular variable measuring the angle from the z-axis, and the third azimuthal variable ϕ. The equation of ξ represents confocal spheroids

$$\frac{s^2}{c^2(1+\xi^2)} + \frac{z^2}{c^2\xi^2} = 1, \tag{2.4}$$

while that of η gives confocal hyperboloids

$$\frac{s^2}{c^2(1-\eta^2)} - \frac{z^2}{c^2\eta^2} = 1. \tag{2.5}$$

Eliminating s from above equations yields

$$z = c\xi\eta \tag{2.6}$$

and similarly, eliminating z gives

$$s = c\sqrt{(1+\xi^2)(1-\eta^2)}, \tag{2.7}$$

which further make x and y ready to be found by virtue of Eq.(2.3). In the representation of an oblate spheroidal coordinate system, c, the common focal length of all the spheroidal and hyperboloidal level surfaces, is a key physical parameter. The degenerate surface $\xi = 0$ is a circular disk of radius c which lies in the $x, y-$plane. However, in the limit $\xi \to +\infty$, the spheroids become spheres, as shown mathematically, $\lim_{\xi\to+\infty} \mathcal{E} = \lim_{\xi\to+\infty} 1/\sqrt{1+\xi^2} = 0$; thus, in the spherical limit, $c\xi \to r$, $\eta \to \cos\theta$.

By virtue of three Lamé scaling factors

$$\begin{cases} h_1 = c\sqrt{\dfrac{\xi^2+\eta^2}{1+\xi^2}}, \\ h_2 = c\sqrt{\dfrac{\xi^2+\eta^2}{1-\eta^2}}, \\ h_3 = c\sqrt{(1+\xi^2)(1-\eta^2)}, \end{cases}$$

the Laplace equation of a scalar potential V therefore can be written as

$$\frac{\partial}{\partial\xi}\Big[(1+\xi^2)\frac{\partial V}{\partial\xi}\Big] + \frac{\partial}{\partial\eta}\Big[(1-\eta^2)\frac{\partial V}{\partial\eta}\Big] + \frac{\xi^2+\eta^2}{(1+\xi^2)(1-\eta^2)}\frac{\partial^2 V}{\partial\phi^2} = 0. \tag{2.8}$$

Substituting of the solution of the separable form $V = \Xi(\xi)H(\eta)\Phi(\phi)$ into (2.8) gives rise to three equations

$$\begin{cases} \dfrac{d}{d\xi}\Big[(1+\xi^2)\dfrac{d\Xi}{d\xi}\Big] + \dfrac{m^2\Xi}{1+\xi^2} - l(l+1)\Xi = 0, \quad \xi \in [0,+\infty), \\ \dfrac{d}{d\eta}\Big[(1-\eta^2)\dfrac{dH}{d\eta}\Big] - \dfrac{m^2 H}{1-\eta^2} + l(l+1)H = 0, \quad \eta \in [-1,1], \\ \dfrac{d^2\Phi}{d\phi^2} + m^2\Phi = 0, \quad \phi \in [0,2\pi). \end{cases}$$

To make the appearance of the first equation similar to that of the second, ξ is replaced by $\xi' = i\xi$. Then the new set of equations becomes

$$\begin{cases} \dfrac{d}{d\xi'}\Big[(1-\xi'^2)\dfrac{d\Xi}{d\xi'}\Big] - \dfrac{m^2\Xi}{1-\xi'^2} + l(l+1)\Xi = 0, \quad \mathrm{Im}(\xi') \in [0,+\infty), \\ \dfrac{d}{d\eta}\Big[(1-\eta^2)\dfrac{dH}{d\eta}\Big] - \dfrac{m^2 H}{1-\eta^2} + l(l+1)H = 0, \quad \eta \in [-1,1], \\ \dfrac{d^2\Phi}{d\phi^2} + m^2\Phi = 0, \quad \phi \in [0,2\pi), \end{cases} \tag{2.9}$$

in which l takes values of $0, 1, \cdots$ and m takes values of $0, \cdots, l$. The solution of the third equation of (2.9) is simply

$$\Phi_m = C_m \cos m\phi + D_m \sin m\phi, \quad \phi \in [0, 2\pi)$$

subject to a periodic boundary condition. The first two equations, on an observation, are both associated Legendre equations and hence have analogous solutions as

$$\begin{cases} \Xi_{lm} = A'_{lm} P_l^m(i\xi) + B'_{lm} Q_l^m(i\xi), & \xi \in [0, +\infty], \\ H_{lm} = A_{lm} P_l^m(\eta) \ + B_{lm} Q_l^m(\eta), & \eta \in [-1, 1]. \end{cases}$$

The general solution of the Laplace equation is then

$$V = \sum_{l=0}^{\infty} \sum_{m=0}^{l} \Xi_{lm} H_{lm} \Phi_m. \tag{2.10}$$

Ξ and H are so called oblate spheroidal harmonics (see [Morse and Feshbach, 1953] and [Smythe, 1950]).

2.2.2 Physical Model Settings

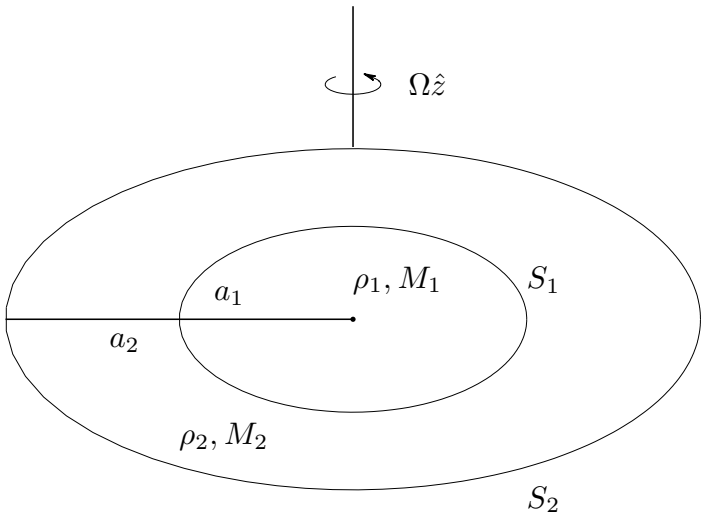

Figure 2.3: A schematic of a meridional cross-section of a rotating two-layer ellipsoid. Subscript 1 denotes variables of the core with mass M_1 and density ρ_1 while 2 stands for the outer layer with mass M_2 and density ρ_2. The whole system rotates with a uniform angular velocity Ω around the axis of symmetry. The semi major axis of the interface is denoted by a_1 while its semi minor axis is $a_1\sqrt{1-\mathcal{E}_1^2}$; the semi major axis of the outer free surface is a_2 with its semi minor axis is $a_2\sqrt{1-\mathcal{E}_2^2}$: $\mathcal{E}_1 \neq \mathcal{E}_2$.

Consider the hydrostatic equilibrium of a rotating, two-layer planet. A schematic of the meridional cross-section of the two-layer model is displayed in Figure 2.3. We assume that the planet is isolated in space and rotates about a fixed axis with angular velocity Ω and that there are no magnetic forces acting on the planet. We also assume that the interface $\mathcal{S}_1$ between the core and the outer layer as well as the outer bounding surface $\mathcal{S}_2$ are axisymmetric and in the shape of oblate spheroids with different eccentricities $\mathcal{E}_1$ and $\mathcal{E}_2$. This is a reasonable assumption because the instability of a Maclaurin spheroid takes place at the critical eccentricity $\mathcal{E}_c \sim 0.93$

which corresponds to an extremely fast rotation that is unusual for planets. In our two-layer model, a homogeneous fluid with mass M_1 and density ρ_1 is confined within the interface surface $\mathcal{S}_1$ characterized by a semi-major axis a_1 and a semi-minor axis $a_1\sqrt{1-\mathcal{E}_1^2}$. Another homogeneous fluid with different mass M_2 and different density ρ_2 is confined within the outer layer confined by the interface $\mathcal{S}_1$ and the outer free surface $\mathcal{S}_2$ characterized by a semi-major axis a_2 and a semi-minor axis $a_2\sqrt{1-\mathcal{E}_2^2}$. The whole system rotates uniformly with angular velocity $\hat{\mathbf{z}}\Omega$, resulting in substantial flattening of both the interface $\mathcal{S}_1$ and the outer surface $\mathcal{S}_2$, which are marked by finite values of $\mathcal{E}_1$ and $\mathcal{E}_2$ with $0 < \mathcal{E}_1 < 1$ and $0 < \mathcal{E}_2 < 1$. The objective of our analysis is to find the values of $\mathcal{E}_1$ and $\mathcal{E}_2$ for a given set of the planetary parameters M_1, ρ_1, M_2, ρ_2 and Ω.

Since the interface $\mathcal{S}_1$ and the outer free surface $\mathcal{S}_2$, in general, have different focal lengths, i.e., $c_1 \neq c_2$, two different oblate spheroidal coordinates are required in the mathematical analysis of the two-layer problem. The first spheroidal coordinates, (ξ_1, η_1, ϕ_1), are defined within the core by

$$x = c_1\sqrt{(1+\xi_1^2)(1-\eta_1^2)}\cos\phi_1, \tag{2.11}$$

$$y = c_1\sqrt{(1+\xi_1^2)(1-\eta_1^2)}\sin\phi_1, \tag{2.12}$$

$$z = c_1\xi_1\eta_1, \tag{2.13}$$

where z is along the axis of rotation and c_1 is the focal length of $\mathcal{S}_1$ defined as the distance from the foci of the ellipse to the center point on the major axis. In the first spheroidal coordinates, $\xi_1 \in [0 \leq \xi_1 \leq \sqrt{1/\mathcal{E}_1^2 - 1}]$. The interface $\mathcal{S}_1$, in terms of the first spheroidal coordinates, is simply given by

$$\xi_1 = \xi_i = \sqrt{1/\mathcal{E}_1^2 - 1},$$

with its semi-major axis being $a_1 = c_1/\mathcal{E}_1$.

The second spheroidal coordinates, (ξ, η, ϕ), are defined based on the focal length of the outer bounding surface $\mathcal{S}_2$ of the two-layer planet

$$x = c_2\sqrt{(1+\xi^2)(1-\eta^2)}\cos\phi, \tag{2.14}$$

$$y = c_2\sqrt{(1+\xi^2)(1-\eta^2)}\sin\phi, \tag{2.15}$$

$$z = c_2\xi\eta, \tag{2.16}$$

where $\xi \in [0 \leq \xi \leq \sqrt{1/\mathcal{E}_2^2 - 1}]$, $\eta \in [-1, 1]$ and $\phi = \phi_1 \in [0, 2\pi]$. Because $c_1 \neq c_2$, there are no level surfaces of ξ that are coincident with the interface $\mathcal{S}_1$, representing the root of the mathematical difficulties in the the two-layer problem. With the second spheroidal coordinates (ξ, η, ϕ), the outer free surface $\mathcal{S}_2$ is simply

given by

$$\xi_o = \sqrt{1/\mathcal{E}_2^2 - 1}$$

with its semi-major axis being $a_2 = c_2/\mathcal{E}_2$. The two different spheroidal coordinates, (ξ_1, η_1) (blue) and (ξ, η) (black), with different focal lengths, c_1 and c_2, are illustrated in Figure 2.4. For application to planetary problems, we assume that $\rho_1 > \rho_2$ and, hence, $c_1 < c_2$.

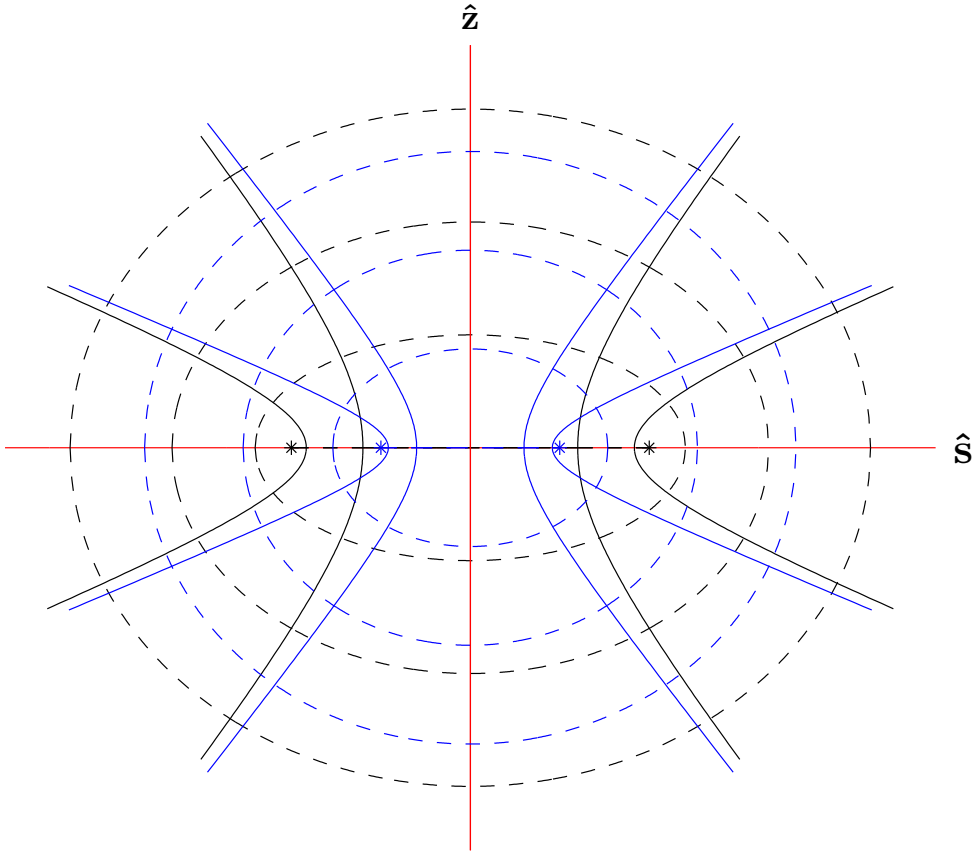

Figure 2.4: Sketch of two different spheroidal coordinates: the first coordinates (ξ_1, η_1) with the focal length c_1 (blue) for the core while the second coordinates (ξ, η) (black) serve as the working coordinates for the whole planet. Note that the interface $\mathcal{S}_1$ must be one of the surfaces with a constant ξ_1.

It is straightforward, from (2.11)-(2.13) and (2.14-2.16) to derive a transformation between the two coordinates (ξ_1, η_1) and (ξ, η)

$$\xi^4 + \left[1 + \frac{c_1^2}{c_2^2}(\eta_1^2 - \xi_1^2 - 1)\right]\xi^2 - \frac{c_1^2}{c_2^2}\xi_1^2\eta_1^2 = 0, \tag{2.17}$$

$$\eta^4 - \left[1 + \frac{c_1^2}{c_2^2}(\eta_1^2 - \xi_1^2 - 1)\right]\eta^2 - \frac{c_1^2}{c_2^2}\xi_1^2\eta_1^2 = 0. \tag{2.18}$$

In particular, our analysis requires that we express the interface $\mathcal{S}_1$ in terms of the second spheroidal coordinates (ξ, η). This is achieved by eliminating η_1 from

(2.17-2.18) and using $\xi_1 = \xi_i$, which gives rise to the interface $\mathcal{S}_1$ in terms of (ξ, η)

$$\xi_{\mathcal{I}}(\eta) = \xi_i \left[\frac{c_1^2(1+\xi_i^2) - c_2^2(1-\eta^2)}{c_2^2(\xi_i^2+\eta^2)} \right]^{1/2}, \tag{2.19}$$

where $\xi_i = \sqrt{1/\mathcal{E}_1^2 - 1}$. That $\xi_{\mathcal{I}}$ is a function of η reflects the central feature of the problem: the level surfaces of ξ cannot be coincident with the interface $\mathcal{S}_1$. With the transformation (2.19), the second spheroidal coordinates (ξ, η) will be adopted as the active coordinates for our analysis and, consequently, the first spheroidal coordinates (ξ_1, η_1) will no longer be needed explicitly. However, apparently, the transformation (2.19) is only conditionally valid when

$$c_1^2(1+\xi_i^2) - c_2^2(1-\eta^2) \geq 0,$$

which categorizes two-layer rotating spheroids problems into two mathematically different types. Depending on the locations of the interface $\mathcal{S}_1$ relative to the two sets of foci, they are discussed in §2.3.3. It is the complicated transformation (2.19) that is responsible for the conclusion that an explicit analytical expression for the shape of a rotating two-layer planet cannot be derived.

2.3 Two-layer Maclaurin spheroids

2.3.1 Governing Equations

In the co-rotating reference frame (also called the mantle frame), the hydrostatic equation for the core with density ρ_1 is

$$-\nabla p - \rho_1 \nabla (V_g + V_c) = 0, \tag{2.20}$$

while for the outer layer with density ρ_2 it is

$$-\nabla p - \rho_2 \nabla (V_g + V_c) = 0, \tag{2.21}$$

where p is the pressure, V_g denotes the gravitational potential which satisfies

$$\frac{\partial}{\partial \xi}\left[(1+\xi^2)\frac{\partial V_g}{\partial \xi}\right] + \frac{\partial}{\partial \eta}\left[(1-\eta^2)\frac{\partial V_g}{\partial \eta}\right] = 4\pi\rho_1 \tag{2.22}$$

for the core and

$$\frac{\partial}{\partial \xi}\left[(1+\xi^2)\frac{\partial V_g}{\partial \xi}\right] + \frac{\partial}{\partial \eta}\left[(1-\eta^2)\frac{\partial V_g}{\partial \eta}\right] = 4\pi\rho_2 \tag{2.23}$$

for the outer layer. The centrifugal potential V_c is given by

$$V_c(\eta,\xi) = -\frac{\Omega^2}{2}\left[c_2^2(1+\xi^2)(1-\eta^2)\right] \tag{2.24}$$

in terms of the second spheroidal coordinates. The centrifugal potential is independent of the density distribution.

For an isolated planetary body, we assume that the pressure p vanishes on the outer free surface $\mathcal{S}_2$

$$p(\xi,\eta) = 0 \ \text{ on } \ \mathcal{S}_2, \tag{2.25}$$

implying that the total potential, gravitational and rotational, must be constant on $\mathcal{S}_2$. At the interface $\mathcal{S}_1$, the pressure must be continuous across $\mathcal{S}_1$ where the density is discontinuous. Upon solving (2.22)–(2.23) by the method of the Green's function, we can derive the gravitational potential V_g for the two-layer problem which can then be used to compute the gravitational energy of the system. The shape of the two-layer hydrostatic equilibrium, marked by the values of $\mathcal{E}_1$ and $\mathcal{E}_2$, is then determined by minimizing the total (gravitational and rotational) potential energy together with the requirement of the free-surface condition on $\mathcal{S}_2$.

It is well known that solutions to (2.22)-(2.23) for the gravitational potential V_g can be expressed in terms of the Green's function

$$V_g(\mathbf{r}) = -\left[\int_{V_1}\frac{\rho_1 G}{|\mathbf{r}-\mathbf{r}'|}\,\mathrm{d}V' + \int_{V_2}\frac{\rho_2 G}{|\mathbf{r}-\mathbf{r}'|}\,\mathrm{d}V'\right], \tag{2.26}$$

where $\int_{V_1}$ denotes the volume integration over the core and $\int_{V_2}$ the volume integration over the outer layer. By expanding $1/|\mathbf{r}-\mathbf{r}'|$ in terms of oblate spheroidal harmonics (see [Smythe, 1950])

$$\frac{1}{|\mathbf{r}-\mathbf{r}'|} = \frac{1}{c_2}\begin{cases}\displaystyle\sum_{l=0}^{\infty}\sum_{m=0}^{l} M_{lm}P_l^m(i\xi)P_l^m(\eta)\cos m(\phi-\phi'), \ \xi<\xi', \\ \displaystyle\sum_{l=0}^{\infty}\sum_{m=0}^{l} N_{lm}Q_l^m(i\xi)P_l^m(\eta)\cos m(\phi-\phi'), \ \xi>\xi',\end{cases} \tag{2.27}$$

where

$$\begin{cases} M_{lm} = i(2-\delta_{0m})(-1)^m(2l+1)\left[\dfrac{(n-m)!}{(n+m)!}\right]^2 Q_l^m(i\xi')P_l^m(\eta'), \\ N_{lm} = i(2-\delta_{0m})(-1)^m(2l+1)\left[\dfrac{(n-m)!}{(n+m)!}\right]^2 P_l^m(i\xi')P_l^m(\eta'), \end{cases}$$

and taking into account the underlying symmetries which lead to $m=0$ and l can only take even values, we can write the solution (2.26) as an expression in terms of

(ξ, η) (for example, [Ansong et al., 2003]),

$$V_g(\xi,\eta) = -2\pi G c_2^2 \sum_{l=0}^{\infty} i(2l+1) P_l(\eta)$$
$$\times \left[Q_l(i\xi) \int_0^{\xi} \int_{-1}^{1} [(\xi')^2 + (\eta')^2] P_l(\eta') P_l(i\xi') \rho' \mathrm{d}\eta' \mathrm{d}\xi' \right.$$
$$\left. + P_l(i\xi) \int_{\xi}^{\xi_o} \int_{-1}^{1} [(\xi')^2 + (\eta')^2] P_l(\eta') Q_l(i\xi') \rho' \mathrm{d}\eta' \mathrm{d}\xi' \right], \tag{2.28}$$

where l is even, $P_l(\eta)$ is the usual Legendre polynomial, $P_l(i\xi)$ is also the Legendre polynomial but with an imaginary argument, while $Q_l(i\xi)$, the Legendre function of the second kind of imaginary argument, is not a polynomial and satisfies

$$\frac{d}{d\xi}\left[(1+\xi^2)\frac{dQ_l}{d\xi}\right] + \frac{m^2 Q_l}{1+\xi^2} - l(l+1)Q_l = 0.$$

For example, we have

$$\begin{aligned} Q_0(i\xi) &= -i \cot^{-1}(\xi), \\ Q_2(i\xi) &= \frac{i}{2}\left(3\xi^2+1\right)\cot^{-1}(\xi) - \frac{3i}{2}\xi. \end{aligned}$$

At the heart of the two-layer problem is the fact that $\rho' = \rho(\eta', \xi')$ in the integrand of (2.28) is a discontinuous function of both η' and ξ'. In the expression (2.28), the first term represents the gravitational potential resulting from the attraction of the mass located within the level surface of the second spheroidal coordinate ξ while the second term gives the gravitational potential due to the attraction of the mass located between the level surface ξ and the outer free surface $\mathcal{S}_2$. Since some level surfaces of the second spheroidal coordinate ξ and η must intercept the interface $\mathcal{S}_1$, the double integral in (2.28) has to be broken into several integrals with some upper/lower limits that are the solution of the problem determining the shape of $\mathcal{S}_1$ and $\mathcal{S}_2$. Making use of (2.24) and (2.28), the condition on the outer free surface at $\xi = \xi_o$ becomes

$$C = -\frac{\Omega^2}{2}(1+\xi_o^2)(1-\eta^2)c_2^2 - 2\pi G c_2^2 \sum_{l=0}^{\infty} i(2l+1) P_l(\eta)$$
$$\times Q_l(i\xi_o) \int_{-1}^{1} \int_{0}^{\xi_o} [(\xi')^2 + (\eta')^2] P_l(\eta') P_l(i\xi') \rho' \mathrm{d}\xi' \mathrm{d}\eta', \tag{2.29}$$

where C is a constant.

With the gravitational potential $V_g(\xi, \eta)$ given by (2.28), we can, for given values

of M_1, ρ_1 and M_2, ρ_2, compute the total self-gravitational energy E_g (see [Lu, 2004]):

$$\begin{aligned} E_g(\mathcal{E}_1, \mathcal{E}_2) &= \frac{1}{2}\int_V \rho(\xi,\eta)V_g(\xi,\eta)\mathrm{d}V \\ &= -2\pi^2 G c_2^5 i \sum_{l=0}^{\infty}(2l+1)\int_{-1}^{+1}\int_0^{\xi_o}\rho(\xi,\eta)(\xi^2+\eta^2) \\ &\times P_l(\eta)\big[A_l(\xi)Q_l(i\xi)+B_l(\xi)P_l(i\xi)\big]\mathrm{d}\xi\mathrm{d}\eta, \end{aligned} \tag{2.30}$$

where c_2 is a function of M_1, ρ_1 and M_2, ρ_2 and coefficients $A_l(\xi)$ and $B_l(\xi)$ are

$$\begin{aligned} A_l(\xi) &= \int_{-1}^{1}\int_0^{\xi}[(\xi')^2+(\eta')^2]P_l(\eta')P_l(i\xi')\rho'\mathrm{d}\xi'\mathrm{d}\eta', \\ B_l(\xi) &= \int_{-1}^{1}\int_{\xi}^{\xi_o}[(\xi')^2+(\eta')^2]P_l(\eta')Q_l(i\xi')\rho'\mathrm{d}\xi'\mathrm{d}\eta'. \end{aligned}$$

Similarly, with the centrifugal energy $V_c(\xi,\eta)$ given by (2.24), we can compute the total centrifugal energy E_c:

$$\begin{aligned} E_c(\mathcal{E}_1, \mathcal{E}_2) &= -\int_V \rho(\xi,\eta)V_c(\xi,\eta)\mathrm{d}V = -\pi\Omega^2 c_2^5 \\ &\times \int_{-1}^{+1}\int_0^{\xi_o}\rho(\xi,\eta)(\xi^2+\eta^2)(1+\xi^2)(1-\eta^2)\mathrm{d}\xi\mathrm{d}\eta, \end{aligned} \tag{2.31}$$

which is also a function of $\mathcal{E}_1$ and $\mathcal{E}_2$. Note that the centrifugal energy E_c also involves a discontinuous function $\rho(\xi,\eta)$ in the integrand. In hydrostatic equilibrium, as a result of the d'Alembert's principle in mechanics, the total potential energy of the system, $E_t = E_g + E_c$, should reach its minimum state which determines the shape of the planet.

2.3.2 An illustration: Classical Maclaurin spheroids

It is the discontinuity of the density $\rho(\xi,\eta)$ in the integrands of (2.30) and (2.31) that causes the difficulties in determining the shape of a rotating two-layer planet. To illustrate this point, let's first remove the discontinuity by assuming a rotating homogeneous fluid, $\rho(\xi,\eta) = \rho_0$, which has the total mass M_0 with the focal length $c_2 = c_0$ and the eccentricity $\mathcal{E}_2 = \mathcal{E}_0$. In this case, it can be readily shown that $A_l(\xi) = B_l(\eta) = 0$ when $l \geq 4$ because of the orthogonality of Legendre polynomials in the interval $[-1, 1]$; and that all the integrals (2.29), (2.30) and (2.31) can be evaluated explicitly and analytically.

By performing a straightforward integration, we can show that equation (2.29)

with constant ρ_0 becomes

$$\begin{aligned} C &= C_0(\rho_0, \mathcal{E}_0) + \big[\frac{\Omega^2 c_0^2(1+\xi_o^2)}{2}\big]\eta^2 \\ &- \pi G\rho_0 c_0^2 \xi_o(1+\xi_o^2)\big[\,(3\xi_o^2+1)\cot^{-1}(\xi_o) - 3\xi_o\big]\eta^2, \end{aligned} \tag{2.32}$$

where C_0 is constant, only dependent upon ρ_0 and $\mathcal{E}_0$. We can also show, from (2.30) with $\rho(\xi,\eta) = \rho_0$, that the total self-gravitational energy E_g is

$$E_g(\mathcal{E}_0) = \frac{16{c_0}^5\,(-1+\mathcal{E}_0^2)\;G\,\pi^2\,{\rho_0}^2\,\sin^{-1}(\mathcal{E}_0)}{15\,\mathcal{E}_0^6}. \tag{2.33}$$

Moveover, from (2.31), the centrifugal energy E_c is given by

$$E_c(\mathcal{E}_0) = \frac{-4\,c_0^5\,\sqrt{\mathcal{E}_0^{-2}-1}\,\pi\,\rho_0\,\Omega^2}{15\,\mathcal{E}_0^4}. \tag{2.34}$$

It follows, by making use of the relation

$$c_0 = \mathcal{E}_0\left[(3M_0/4\pi\rho_0)^{1/3}(1-\mathcal{E}_0^2)^{-1/6}\right], \tag{2.35}$$

that the total potential energy $E_t = E_g + E_c$ takes the form

$$\begin{aligned} E_t(\mathcal{E}_0) &= -\frac{4\pi\rho_0(3M_0/4\pi\rho_0)^{5/3}}{15\mathcal{E}_0(1-\mathcal{E}_0^2)^{5/6}} \\ &\times \big[4G\pi\rho_0(1-\mathcal{E}_0^2)\sin^{-1}(\mathcal{E}_0) + \mathcal{E}_0\sqrt{1-\mathcal{E}_0^2}\Omega^2\big]. \end{aligned} \tag{2.36}$$

(2.35) is derived from the mass-volume formulation

$$M_0 = \rho_0 \cdot \frac{4\pi}{3}\left(\frac{c}{\mathcal{E}}\right)^3\sqrt{1-\mathcal{E}_0^2}.$$

For given ρ_0, the state of minimum energy in the equilibrium, given by $\mathrm{d}E_t(\mathcal{E}_0)/\,\mathrm{d}\mathcal{E}_0 = 0$, gives rise to an equation for $\mathcal{E}_0$

$$\begin{aligned} 0 &= \frac{8\pi\rho_0(3M_0/4\pi\rho_0)^{5/3}}{45\mathcal{E}_0^2(1-\mathcal{E}_0^2)^{3/2}}\big[6G\pi\rho_0\mathcal{E}_0(1-\mathcal{E}_0^2) \\ &+ \mathcal{E}_0^3\Omega^2 + 2G\pi\rho_0(2\mathcal{E}_0^2-3)\sqrt{1-\mathcal{E}_0^2}\sin^{-1}(\mathcal{E}_0)\big], \end{aligned} \tag{2.37}$$

which leads to the classical Maclaurin solution given by (2.2). It can be verified that, with $\mathcal{E}_0$ given by (2.2), the free surface condition (2.32) is also satisfied. In other words, the coefficient of η^2 in (2.32) vanishes for the value of $\mathcal{E}_0$ given by (2.2) with $\xi_o = \sqrt{1/\mathcal{E}_0^2 - 1}$.

2.3.3 Two-layer case

Superficially, it appears that the approach for the classical Maclaurin solution (2.2) might be easily extended to the more realistic two-layer problem. As we shall show, however, determining the shape of a two-layer rotating planet is mathematically much more complicated.

For planetary applications, it is appropriate to assume that $\rho_1 > \rho_2$ in the hydrostatic equilibrium. In contrast to the single layer problem, the coefficients $A_l(\xi)$ and $B_l(\xi)$ for $l \geq 4$ in the expansion (2.30) are generally non-zero. The physical significance of this fact is that the shape of a uniformly rotating two-layered fluid like body cannot be exactly a perfect oblate spheroid. However, because rotating layered celestial bodies such as Jupiter are not observed to be noticeably different from spheroids, it is reasonable to assume that the coefficients $A_l(\xi)$ and $B_l(\xi)$ for $l \geq 4$ in the expansion are much smaller than those of $A_0(\xi)/B_0(\xi)$ and $A_2(\xi)/B_2(\xi)$. This assumption will be validated later and discussed in Section 2.4, showing that the terms neglected are indeed sufficiently small. In addition to the mathematical difficulties involving the discontinuous density, a further complication arises from the fact that we must distinguish between two different cases in the analysis: (i) when either M_1/M_2 is sufficiently large or $\epsilon_2 = \Omega^2/(2\pi G\rho_2)$ is sufficiently small that the foci of the free surface $\mathcal{S}_2$ are located within the core (which will be referred to as the "large-core" case); (ii) when either M_1/M_2 is sufficiently small or $\epsilon_2 = \Omega^2/(2\pi G\rho_2)$ is moderate so that the foci of the free surface $\mathcal{S}_2$ are located within the outer layer (which will be referred to as the "small-core" case). The two different cases are illustrated in Figure 2.5. In the first case, which is shown in Figure 2.5(a), the mathematical analysis is simpler because only the integration over the radial direction ξ needs to be broken up across the interface $\mathcal{S}_1$. The transformation (2.19) is valid for any $\eta \in [-1, 1]$. In the second case, where the focal length c_2 is outside of the interface $\mathcal{S}_1$ as shown in Figure 2.5(b), the integration over both ξ and η must be broken up across the interface $\mathcal{S}_1$. This illustrates the situation that (2.19) cannot be defined for all η but only for $|\eta| > |\eta_{\min}|$. As a consequence, the mathematical analysis for the "small-core" case is much more complicated and cumbersome;it is presented in Appendix A.

Consider the "large-core" case that is marked by $\xi_i \geq \sqrt{c_2^2/c_1^2 - 1}$. For the purpose of simplifying relevant mathematical expressions, we define

$$\begin{aligned} f_1(\xi,\eta) &= \xi^2 + \eta^2, \\ f_2(\xi,\eta) &= (\xi^2+\eta^2)(3\eta^2-1)(3\xi^2+1), \\ f_3(\xi,\eta) &= (\xi^2+\eta^2)\cot^{-1}(\xi), \\ f_4(\xi,\eta) &= (\xi^2+\eta^2)(3\eta^2-1)[(3\xi^2-1)\cot^{-1}(\xi) - 3\xi]. \end{aligned}$$

After some manipulation using equation (2.29), the condition on the outer free

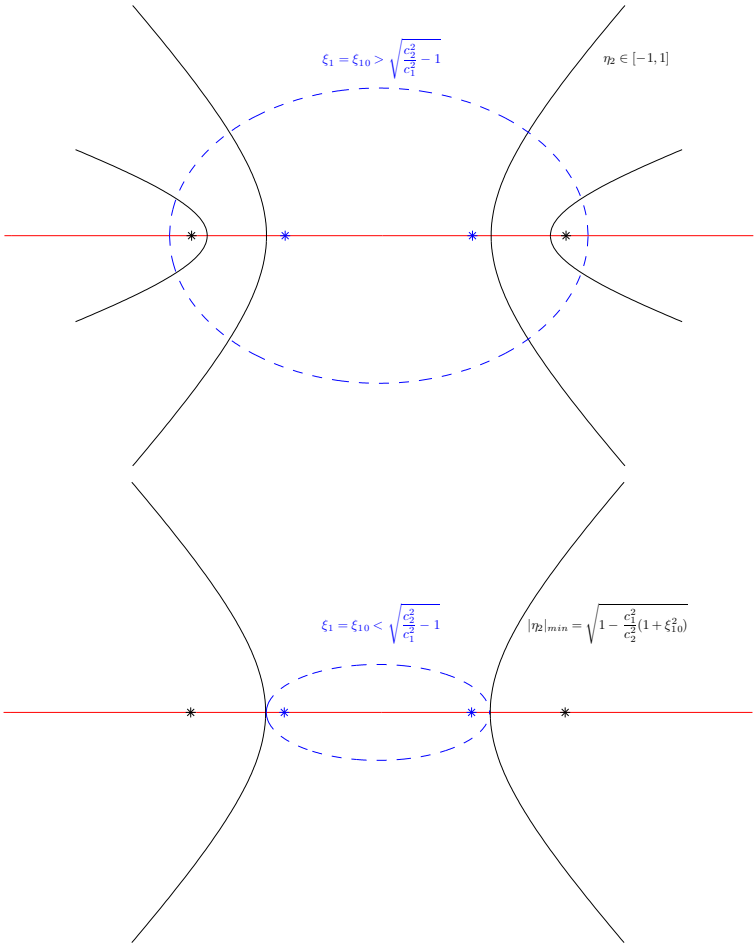

Figure 2.5: Two different cases: (a) when the core is large with the foci c_2 being located within the interface $\mathcal{S}_1$; (b) when the core is small with the foci c_2 being located outside of the interface $\mathcal{S}_1$. The dashed line indicates the location of the interface $\mathcal{S}_1$ at $\xi = \xi_\jmath$. For the large core case, the interface $\mathcal{S}_1$ intersects all the η surfaces while, for the small core case, the interface $\mathcal{S}_1$ only intersects some of the η surfaces.

surface at $\xi = \xi_o$ can be written

$$
\begin{aligned}
C &= 2\pi G c_2^2 \Big\{ \Big[\rho_1 \int_{-1}^{1} \int_{0}^{\xi_\jmath} f_1(\xi', \eta') \mathrm{d}\xi' \mathrm{d}\eta' \\
&+ \rho_2 \int_{-1}^{1} \int_{\xi_\jmath}^{\xi_o} f_1(\xi', \eta') \mathrm{d}\xi' \mathrm{d}\eta' \Big] \sin^{-1}(\mathcal{E}_2) \\
&+ \Big[\rho_1 \int_{-1}^{1} \int_{0}^{\xi_\jmath} f_2(\xi', \eta') \mathrm{d}\xi' \mathrm{d}\eta' \\
&+ \rho_2 \int_{-1}^{1} \int_{\xi_\jmath}^{\xi_o} f_2(\xi', \eta') \mathrm{d}\xi' \mathrm{d}\eta' \Big] \\
&\times \frac{5(3\eta^2 - 1)}{16\mathcal{E}_2^2} \Big[(3 - 2\mathcal{E}_2^2) \sin^{-1}(\mathcal{E}_2) - 3\mathcal{E}_2 \sqrt{1 - \mathcal{E}_2^2} \Big] \Big\} \\
&- \frac{\Omega^2}{2\mathcal{E}_2^2} (1 - \eta^2) c_2^2. \qquad (2.38)
\end{aligned}
$$

It is vitally important to notice that the interface $\xi_\jmath$, given by (2.19), is expressed in terms of the second spheroidal coordinates and, hence, the upper/lower limit of the above integrals is not only a function of η but also $\mathcal{E}_1$ and $\mathcal{E}_2$– the unknown solution of the two-layer problem. Even though the integrands f_1 and f_2 are simple enough, the integrals still have to be evaluated numerically because of their upper/lower limits.

The evaluation of the total gravitational energy E_g is involved in the quadruple integrals with the intriguing upper/lower limits, a result of the existence of the discontinuous interface and the coordinate transformation. Making use of (2.30) and taking account of the discontinuous density distribution, we can derive an integral expression for the total gravitational energy $E_g(\mathcal{E}_1, \mathcal{E}_2)$:

$$
\begin{aligned}
E_g(\mathcal{E}_1, \mathcal{E}_2) = -2\pi G c_2^5 \Big\{ & \\
& \rho_1 \int_{-1}^{1}\int_{0}^{\xi_\jmath} f_3(\xi,\eta)\Big[\int_{-1}^{1} g_1(\xi,\eta')\mathrm{d}\eta'\Big]\mathrm{d}\xi\mathrm{d}\eta \\
+ \quad & \rho_2 \int_{-1}^{1}\int_{\xi_\jmath}^{\xi_o} f_3(\xi,\eta)\Big[\int_{-1}^{1} g_1(\xi,\eta')\mathrm{d}\eta'\Big]\mathrm{d}\xi\mathrm{d}\eta \\
+ \quad & \rho_1 \int_{-1}^{1}\int_{0}^{\xi_\jmath} f_1(\xi,\eta)\Big[\int_{-1}^{1} g_2(\xi,\eta')\mathrm{d}\eta'\Big]\mathrm{d}\xi\mathrm{d}\eta \\
+ \quad & \rho_2 \int_{-1}^{1}\int_{\xi_\jmath}^{\xi_o} f_1(\xi,\eta)\Big[\int_{-1}^{1} g_2(\xi,\eta')\mathrm{d}\eta'\Big]\mathrm{d}\xi\mathrm{d}\eta \\
+ \quad & \frac{5\rho_1}{16} \int_{-1}^{1}\int_{0}^{\xi_\jmath} f_4(\xi,\eta)\Big[\int_{-1}^{1} g_3(\xi,\eta')\mathrm{d}\eta'\Big]\mathrm{d}\xi\mathrm{d}\eta \\
+ \quad & \frac{5\rho_2}{16} \int_{-1}^{1}\int_{\xi_\jmath}^{\xi_o} f_4(\xi,\eta)\Big[\int_{-1}^{1} g_3(\xi,\eta')\mathrm{d}\eta'\Big]\mathrm{d}\xi\mathrm{d}\eta \\
+ \quad & \frac{5\rho_1}{16} \int_{-1}^{1}\int_{0}^{\xi_\jmath} f_2(\xi,\eta)\Big[\int_{-1}^{1} g_4(\xi,\eta')\mathrm{d}\eta'\Big]\mathrm{d}\xi\mathrm{d}\eta \\
+ \quad & \frac{5\rho_2}{16} \int_{-1}^{1}\int_{\xi_\jmath}^{\xi_o} f_2(\xi,\eta)\Big[\int_{-1}^{1} g_4(\xi,\eta')\mathrm{d}\eta'\Big]\mathrm{d}\xi\mathrm{d}\eta\Big\},
\end{aligned}
\tag{2.39}
$$

where g_1 is defined as

$$
\begin{aligned}
g_1 &= \rho_1 \int_0^{\xi} f_1(\xi',\eta')\mathrm{d}\xi', \quad \xi \le \xi'_\jmath; \\
g_1 &= \rho_1 \int_0^{\xi'_\jmath} f_1(\xi',\eta')\mathrm{d}\xi' + \rho_2 \int_{\xi'_\jmath}^{\xi} f_1(\xi',\eta')\mathrm{d}\xi', \quad \xi > \xi'_\jmath
\end{aligned}
$$

with

$$
\xi'_\jmath(\eta') = \xi_i \left[\frac{c_1^2(1+\xi_i^2) - c_2^2[1-(\eta')^2]}{c_2^2[\xi_i^2 + (\eta')^2]}\right]^{1/2};
$$

g_2 is

$$\begin{aligned} g_2 &= \rho_1 \int_{\xi}^{\xi'_\jmath} f_3(\xi', \eta') \mathrm{d}\xi' + \rho_2 \int_{\xi'_\jmath}^{\xi_o} f_3(\xi', \eta') \mathrm{d}\xi', \quad \xi \leq \xi'_\jmath, \\ g_2 &= \rho_2 \int_{\xi}^{\xi_o} f_3(\xi', \eta') \mathrm{d}\xi', \quad \xi > \xi'_\jmath; \end{aligned}$$

g_3 is given by

$$\begin{aligned} g_3 &= \rho_1 \int_{0}^{\xi} f_2(\xi', \eta') \mathrm{d}\xi', \quad \xi \leq \xi'_\jmath, \\ g_3 &= \rho_1 \int_{0}^{\xi'_\jmath} f_2(\xi', \eta') \mathrm{d}\xi' + \rho_2 \int_{\xi'_\jmath}^{\xi} f_2(\xi', \eta') \mathrm{d}\xi', \quad \xi > \xi'_\jmath; \end{aligned}$$

and, finally, g_4 is defined as

$$\begin{aligned} g_4 &= \rho_1 \int_{\xi}^{\xi'_\jmath} f_4(\xi', \eta') \mathrm{d}\xi' + \rho_2 \int_{\xi'_\jmath}^{\xi_o} f_4(\xi', \eta') \mathrm{d}\xi', \quad \xi \leq \xi'_\jmath, \\ g_4 &= \rho_2 \int_{\xi}^{\xi_o} f_4(\xi', \eta') \mathrm{d}\xi', \quad \xi > \xi'_\jmath. \end{aligned}$$

The special feature that the upper/lower limit of the above multiple integrals is the unknown solution of the problem implies that the usual integration scheme with a fixed mesh cannot be adopted in this problem. Meanwhile, because of the discontinuous integrand at $\xi = \xi_\jmath$, a global uniform integration grid is not applicable. Cells in the grid intersected by the discontinuous interface will severely deteriorate the global accuracy of the quadrature approximation, especially for scheme of high algebraic order. A careful choice of the method for numerical integration is therefore essential. We have chosen a moving mesh, as suggested in [Tornbergt, 2002], which always captures the location of the interface $\xi = \xi_\jmath$ of the two different domains. In order to achieve enough numerical accuracy within an acceptable running time, a fourth-order extended Simpson method is employed in the multiple integration and it is replaced by repeated integrations carried out dimension by dimension. The quadrature rule (see [Press et al., 2007]) is

$$\begin{aligned} \int_{x_0}^{x_{N-1}} f(x) \mathrm{d}x = h \Big[\frac{1}{3} f_0 + \frac{4}{3} f_1 + \frac{2}{3} f_2 + \frac{4}{3} f_3 + \\ \cdots + \frac{2}{3} f_{N-3} + \frac{4}{3} f_{N-2} + \frac{1}{3} f_{N-1} \Big] \; + \; O(\frac{1}{N^4}). \end{aligned}$$

Similarly, we can derive the total centrifugal energy E_c from (2.31),

$$\begin{aligned} E_c(\mathcal{E}_1, \mathcal{E}_2) &= -2\pi c_2^5 \Big\{ \\ &\quad \rho_1 \int_{-1}^{1} \int_{0}^{\xi_\jmath} f_1(\xi,\eta)(1+\xi^2)(1-\eta^2)\mathrm{d}\xi\mathrm{d}\eta \\ &+ \rho_2 \int_{-1}^{1} \int_{\xi_\jmath}^{\xi_o} f_1(\xi,\eta)(1+\xi^2)(1-\eta^2)\mathrm{d}\xi\mathrm{d}\eta \Big\}. \end{aligned} \tag{2.40}$$

The total potential energy E_t is given by

$$E_t(\mathcal{E}_1, \mathcal{E}_2) = E_g(\mathcal{E}_1, \mathcal{E}_2) + E_c(\mathcal{E}_1, \mathcal{E}_2)$$

and the minimum of E_t at the hydrostatic equilibrium is marked by the two equations

$$\begin{aligned} 0 &= \frac{\partial}{\partial \mathcal{E}_1} \left[E_t(\mathcal{E}_1, \mathcal{E}_2) + \lambda G(\mathcal{E}_1, \mathcal{E}_2) \right], \\ 0 &= \frac{\partial}{\partial \mathcal{E}_2} \left[E_t(\mathcal{E}_1, \mathcal{E}_2) + \lambda G(\mathcal{E}_1, \mathcal{E}_2) \right], \end{aligned} \tag{2.41}$$

where λ is the Lagrange multiplier and $G(\mathcal{E}_1, \mathcal{E}_2)$ is a constraint derived from the free-surface condition (2.38):

$$\begin{aligned} 0 &= G(\mathcal{E}_1, \mathcal{E}_2) \\ &= -\Omega^2 + \frac{15\pi G}{4} \Big[\rho_1 \int_{-1}^{1} \int_{0}^{\xi_\jmath} f_2(\xi',\eta')\mathrm{d}\xi'\mathrm{d}\eta' \\ &+ \rho_2 \int_{-1}^{1} \int_{\xi_\jmath}^{\xi_o} f_2(\xi',\eta')\mathrm{d}\xi'\mathrm{d}\eta' \Big] \\ &\times \Big[(3 - 2\mathcal{E}_2^2) \sin^{-1}(\mathcal{E}_2) - 3\mathcal{E}_2 \sqrt{1-\mathcal{E}_2^2} \Big]. \end{aligned} \tag{2.42}$$

Equations (2.41), subject to the constraint (2.42), can be solved to determine the eccentricities $\mathcal{E}_1$ and $\mathcal{E}_2$ of a two-layer rotating planet. In the numerical optimization, we choose $\mathcal{E}_2$ as the working variable because therefore the initial guess of iterations towards the minimum can directly utilize the value obtained from a effective classical Maclaurin solution; also, $\mathcal{E}_1$ is no longer a freedom because of the constraint (2.42), which reduces the optimization to a 1-D problem. Because the initial guesses are always close enough to the real energy minimum, there is no concern over convergence issues. A simple 1-D search algorithm is carried out to locate the minimum. The application procedures are then summarized as below:

- Obtain the parameters Q_v, ρ_1, ρ_2, Ω, either from observations or from some model predictions.
- Compute the mean density $\bar{\rho} = \rho_1 Q_v + \rho_2(1 - Q_v)$ and the corresponding effective $\bar{\epsilon} = \Omega^2/(2\pi G\bar{\rho})$.

- Evaluate the effective eccentricity $\bar{\mathcal{E}}$ from the classical Maclaurin formulation (2.2).
- Do the minimum searching iteration of $\mathcal{E}_2$ with the initial guess $\bar{\mathcal{E}}$. In each iteration step, compute $\mathcal{E}_1$ from (2.42) and evaluate the total energy by virtue of (2.39) and (2.40).

In evaluations of (2.38) and (2.41), we note that $\xi_{\mathcal{I}}$, given by (2.19), is related to c_1^2/c_2^2, which represents an essential geometrical parameter of the shape. For a given value of M_1, M_2, ρ_1 and ρ_2, we have

$$\begin{aligned} M_1 &= \frac{4}{3}\pi\rho_1 \frac{c_1^3}{\mathcal{E}_1^3}\sqrt{1-\mathcal{E}_1^2}, \\ M_2 &= \frac{4}{3}\pi\rho_2 \frac{c_2^3}{\mathcal{E}_2^3}\sqrt{1-\mathcal{E}_2^2} - \frac{\rho_2 M_1}{\rho_1}, \end{aligned}$$

which yields

$$\begin{aligned} c_1(\mathcal{E}_1) &= \left[\frac{3M_1}{4\pi\rho_1}(1-\mathcal{E}_1^2)^{-1/2}\right]^{1/3}\mathcal{E}_1 \\ c_2(\mathcal{E}_2) &= \left[\frac{3(\rho_1 M_2 + \rho_2 M_1)}{4\pi\rho_1\rho_2}(1-\mathcal{E}_2^2)^{-1/2}\right]^{1/3}\mathcal{E}_2. \end{aligned}$$

It follows that

$$\frac{c_1}{c_2} = \left[Q_v \frac{\sqrt{1-\mathcal{E}_2^2}}{\sqrt{1-\mathcal{E}_1^2}}\right]^{1/3}\frac{\mathcal{E}_1}{\mathcal{E}_2},$$

with

$$Q_v = \frac{\rho_2 M_1}{\rho_1 M_2 + \rho_2 M_1} = \frac{V_1}{V_1 + V_2}.$$

Consequently, the mathematical problem for determining the shape of a rotating two-layer planet is characterized by the three dimensionless parameters $\rho_1/\rho_2, Q_v$ and $\epsilon_2 = \Omega^2/(2\pi G\rho_2)$: for a given set of the three parameters, we can solve (2.41) subject to the constraint (2.38) to determine the values of $\mathcal{E}_1$ and $\mathcal{E}_2$.

Table 2.1: Four typical solutions of the two-layer problem. The first three solutions correspond to the "large core" case while the fourth solution with $\epsilon_2 = 0.1$ is for the "small core" case. The value of $\mathcal{E}_0$, obtained from the classical solution (2.2) using the mean density $\rho_0 = \rho_1 Q_v + \rho_2(1-Q_v)$, is also shown for comparison.

ϵ_2	ρ_2/ρ_1	M_2/M_1	$\mathcal{E}_1$	$\mathcal{E}_2$	$\mathcal{E}_0$
0.02	0.5	5	0.2242	0.2484	0.2609
0.04	0.5	5	0.3259	0.3500	0.3673
0.05	0.5	0.55	0.3762	0.3870	0.3533
0.10	0.5	5	0.1864	0.5425	0.5735

Table 2.1 shows four typical solutions from our computation of the two-layer model. For the purpose of comparison, the single layer solution given by (2.2) with

the mean density $\rho_0 = (M_1+M_2)/(V_1+V_2)$ is also included. The first three solutions correspond to the "large-core" case while the fourth solution with a larger $\epsilon_2 = 0.1$ is for a "small-core" case, details of which are discussed in the Appendix A. In the fourth solution, it is the faster rotation that causes substantial flattening of the outer layer such that the foci of the outer bounding surface moves out of the core. In this case, the value of $\mathcal{E}_2$ is substantially different from that of $\mathcal{E}_1$. We have also performed a systematic exploration of the parameter space of the problem. In Figure 2.6, eccentricities, $\mathcal{E}_1$ and $\mathcal{E}_2$, are shown as a function of Q_v for the fixed value of $\rho_2/\rho_1 = 0.5$ and $\epsilon_2 = 0.05$. The two asymptotic limits of the two-layer problem are also indicated in the figure. When $Q_v \ll 1$, the two layer solution asymptotically approaches the single layer solution given by (2.2), with $\rho_o = \rho_2$ giving rise to $\mathcal{E}_2 \to \mathcal{E}_0 = 0.4275$ at $\epsilon_0 = 0.05$; when $(1 - Q_v) \ll 1$, the two layer solution asymptotically approaches the single layer solution with $\rho_o = \rho_1$ giving rise to $\mathcal{E}_2 \to \mathcal{E}_0 = 0.3042$ at $\epsilon_0 = 0.05$. Figure 2.7 shows the dependence of the two eccentricities, $\mathcal{E}_1$ and $\mathcal{E}_2$, on the rotation parameter $\epsilon_2 = \Omega^2/(2\pi G\rho_2)$ for the fixed value of $\rho_2/\rho_1 = 0.5$ and $Q_v = 0.5$. As expected, the flattening of the outer free surface, which is observable, is always slightly larger than that of the interface. Eccentricities of the two-layer models, $\mathcal{E}_1$ and $\mathcal{E}_2$, are also shown as a function of ρ_2/ρ_1 for $\epsilon_2 = 0.05$ and $Q_v = 0.5$ in Figure 2.8. In the limit $\rho_2 \to \rho_1$, the two-layer solutions approach the classical solution (2.2) which is indicated by the dashed line in the figure: $\mathcal{E}_2 \to \mathcal{E}_0(\rho_2) = 0.4275$ as $\rho_2/\rho_1 \to 1$.

2.4 Summary and remarks

We have developed a hydrostatic equilibrium theory describing the shape of a two-layer model of a rotating planet (the two-layer Maclaurin spheroid) in which departure from sphericity is not treated as a small perturbation. The theory gives two different values of eccentricities, $\mathcal{E}_1$ and $\mathcal{E}_2$, for the interface and the outer free surface of a two-layer planet. While the value of $\mathcal{E}_2$ represents an observable property of a planet, the eccentricity of the interface between the core and the mantle $\mathcal{E}_1$ is not observable but is an important parameter for understanding the dynamics of planetary fluid cores. We show that the shape of a rotating two-layer planet is determined by the three dimensionless parameters $\rho_1/\rho_2, Q_v$ and $\epsilon_2 = \Omega^2/(2G\rho_2)$. Because the interface and the outer free surface have different values of eccentricity, two different spheroidal coordinates and the transformation between them are required in the analysis. The mathematical problem is further complicated by having to distinguish two different cases: the large "core" with the foci of the outer bounding surface located within the inner core and the small "core" with the foci of the outer surface within the outer layer.

A key assumption in our analysis is that the coefficients $A_l(\xi)$ and $B_l(\xi)$ for $l \geq 4$

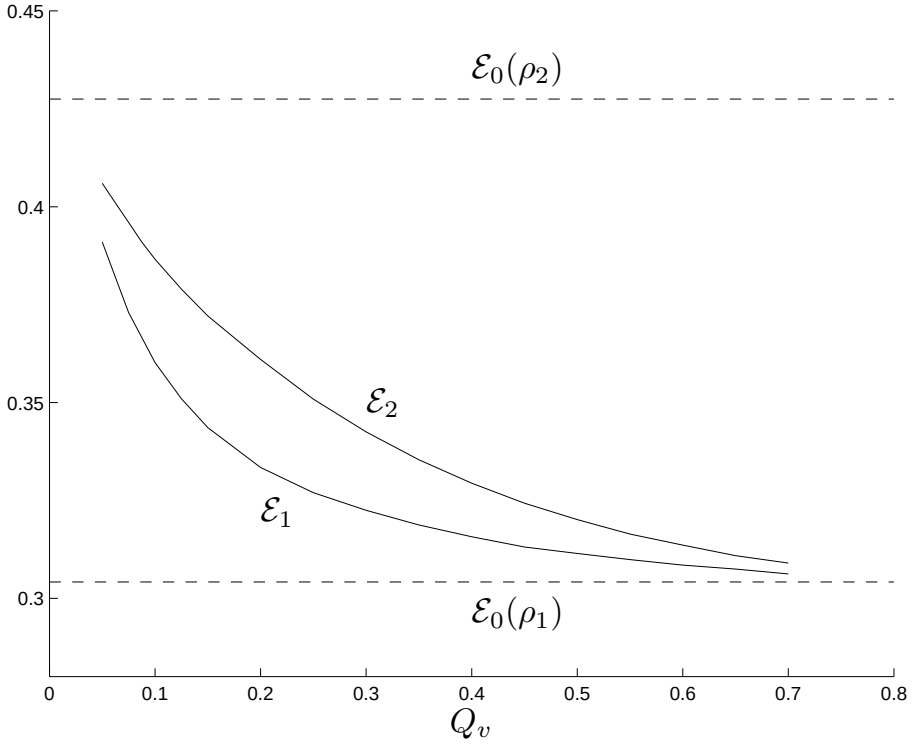

Figure 2.6: Eccentricities of the two-layer models, $\mathcal{E}_1$ and $\mathcal{E}_2$, as a function of Q_v for $\rho_2/\rho_1 = 0.5$ and $\epsilon_2 = 0.05$. The dashed lines indicate the two asymptotic limits of the problem when either $Q_v \to 0$ or $Q_v \to 1$: $\mathcal{E}_0(\rho_1)$ corresponds to the result of (2.2) with $\rho_o = \rho_1$ while $\mathcal{E}_0(\rho_2)$ for the result of (2.2) with $\rho_o = \rho_2$.

in the expansion (2.30), where l is even, are sufficiently small that contributions from the higher-order terms with $l \geq 4$ are negligible. Recall that, while $A_l(\xi)$ and $B_l(\xi)$ for $l \geq 4$ are exactly zero in the single-layer problem, they are not generally zero for the two-layer problem. However, we have performed a careful check revealing that the higher-order terms with $l \geq 4$ are indeed negligibly small. For simple illustration, the gravitational potential V_g given by (2.28) can be evaluated at the outer free surface ξ_o,

$$V_g(\xi_o, \eta) \;=\; \sum_{l=0}^{\infty} \mathcal{C}_l(\xi_o) P_l(\eta), \tag{2.43}$$

where l is even and the coefficients $\mathcal{C}_l(\xi_o)$ can be computed for any two-layer model. For example, when $\rho_1/\rho_2 = 0.5, M_2/M_1 = 5$, $\epsilon_2 = \Omega^2/(2\pi G\rho_2) = 0.04$ with $\mathcal{E}_1 = 0.326$ and $\mathcal{E}_2 = 0.350$, we found that

$$\left|\frac{\mathcal{C}_4(\xi_o)}{\mathcal{C}_2(\xi_o)}\right| = 1.68 \times 10^{-5}, \quad \left|\frac{\mathcal{C}_6(\xi_o)}{\mathcal{C}_2(\xi_o)}\right| = 3.41 \times 10^{-7}.$$

In all the solutions presented in this study, the higher-order terms with $l \geq 4$ can be safely neglected in the expansion.

We apply our two-layer model to planet Earth by neglecting the effect of the

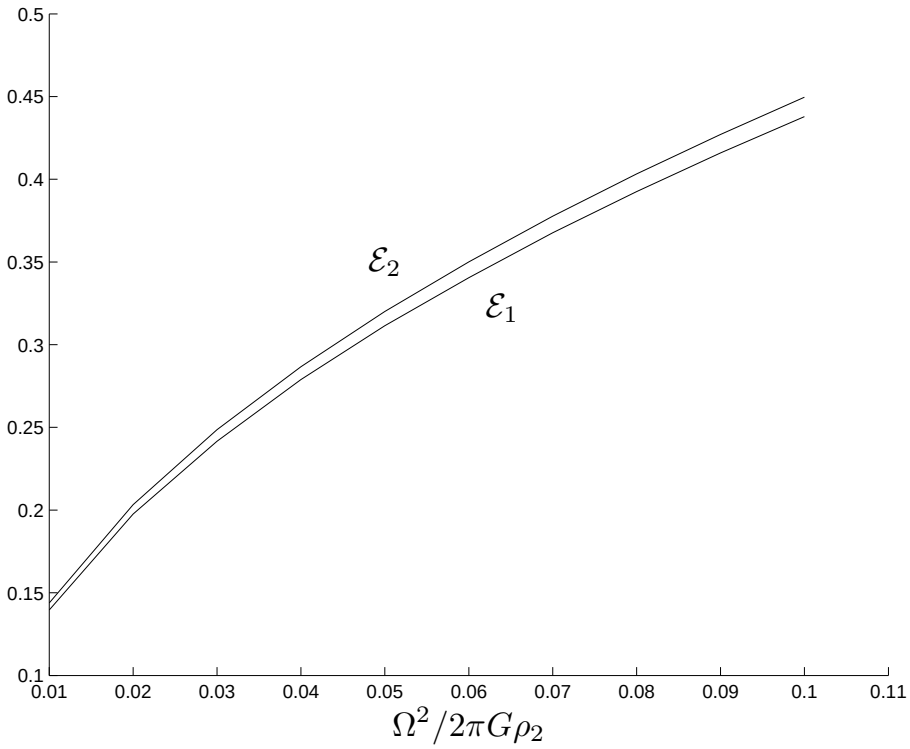

Figure 2.7: Eccentricities of a two-layer planet, $\mathcal{E}_1$ and $\mathcal{E}_2$, as a function of ϵ_2 for $\rho_2/\rho_1 = 0.5$ and $Q_v = 0.5$.

inner solid core. Taking $\rho_1 = 11670\,\mathrm{kg\,m^{-3}}$, $\rho_2 = 4680\,\mathrm{kg\,m^{-3}}$ $\rho_1/\rho_2 = 2.49$ and $M_1/M_2 = 0.5015$, implying $Q_v = 0.1674$, $\Omega = 7.27 \times 10^{-5}\,\mathrm{s^{-1}}$ and giving $\epsilon_2 = \Omega^2/(2\pi G\rho_2) = 0.0027$, our two-layer model yields $\mathcal{E}_1 = 0.071$ and $\mathcal{E}_2 = 0.081$, showing good agreement with the observed value $\mathcal{E}_2 = 0.082$ for the Earth. However, if we use the classical formula (2.2) for the single-layer model with the average density $\rho_0 = 5850\,\mathrm{kg\,m^{-3}}$ we obtain $\mathcal{E}_0 = 0.091$ which is substantially larger than the observed value. The eccentricity of the core-mantle interface in the two-layer model is significantly smaller than that of the surface, and it is in good agreement with the value $\mathcal{E}_1 = 7.13 \times 10^{-2}$ inferred from seismology and geodesy ([Gwinn et al., 1986; Morelli and Dziewonski, 1987]). This agreement is surprising in view of the simplicity of the two-layer model. However, the observed shape of the core-mantle boundary includes a non-hydrostatic component of about 500 m excess equatorial radius. Also, the observed ellipticity of the core is a dynamical ellipticity, ([Mathews et al., 1991]) not an actual geometric or shape ellipticity. The two ellipticities are approximately equivalent, at least for a constant density core.

Application of the two-layer model to other planets in our solar system can only be carried out in an approximate way because of both the simplicity of the model and the uncertainties in the interior structures of the planets. We present an illustrative calculation for Jupiter and Saturn, which rotate much faster than Earth. The density within these gas giants increases monotonically and continuously with depth. There is the possibility of density discontinuities in Jupiter and Saturn if

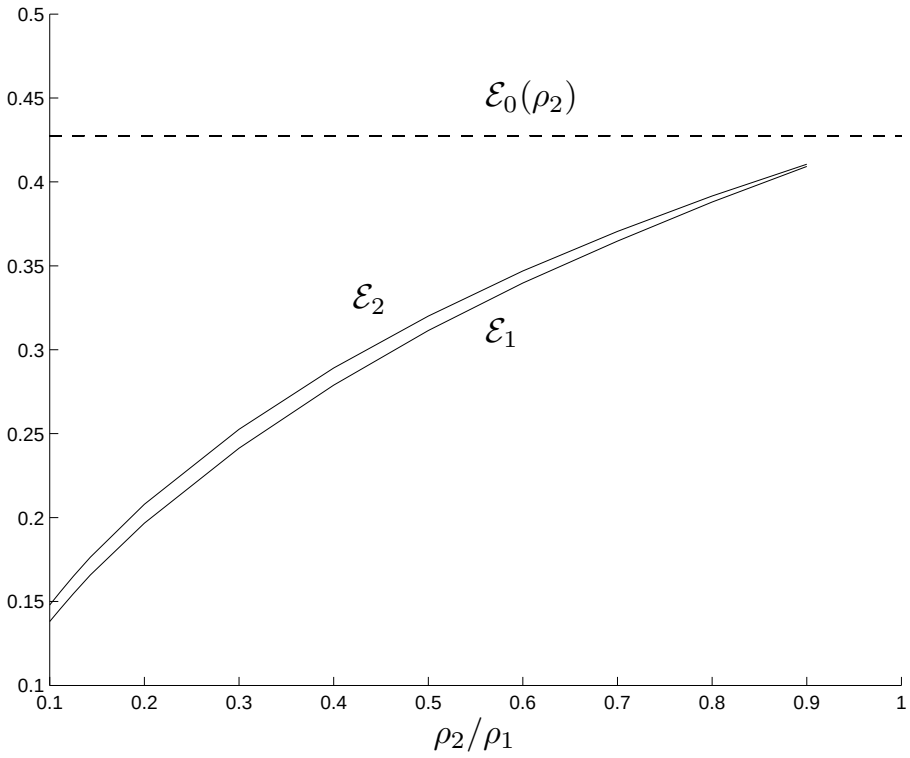

Figure 2.8: Eccentricities of a two-layer planet, $\mathcal{E}_1$ and $\mathcal{E}_2$, as a function of ρ_2/ρ_1 for $\epsilon_2 = 0.05$ and $Q_v = 0.5$. The dashed lines represent the asymptotic solution of the two layer problem in the limit $\rho_2/\rho_1 \to 1$: $\mathcal{E}_0(\rho_2) = 0.4275$ for the single layer solution.

they contain heavy element cores, but that is uncertain. Accordingly, there is no unique way to represent the interiors of these planets with a two-layer model. The parameter values listed in Table 2.2 are simply arbitrary values consistent with the known properties of Jupiter and Saturn intended as illustrative two-layer models. The interface eccentricities $\mathcal{E}_1$ reported in Table 2.2 have no real physical significance. The surface eccentricities $\mathcal{E}_2$ listed in Table 2.2 can be compared with the observed $\mathcal{E}_{\rm obs}$ of the 1 bar pressure level. The model eccentricities are in reasonable agreement with the observed values, although no attempt has been made to fine tune the model parameters to match the observations better. The exact solution for the rotational

Table 2.2: Illustrative two-layer models of Jupiter and Saturn. The eccentricity $\mathcal{E}_0$ from the single-layer formula (2.2) is also given for the purpose of comparison. $\mathcal{E}_{\rm obs}$ is the observed eccentricity of the 1 bar pressure level. Data from R.A. Jacobson (unpublished data, 2003, available from the Jet Propulsion Laboratory (http://ssd.jpl.nasa.gov/)), [Jacobson et al., 2006], and [Lindal et al., 1981, 1985] are summarized in Table 4 of [Helled et al., 2009].

	Q_v	$\bar{\rho}_2/\bar{\rho}_1$	ϵ_2	$\mathcal{E}_1$	$\mathcal{E}_2$	$\mathcal{E}_{\rm obs}$	$\mathcal{E}_0$
Jupiter	0.5120	0.2382	0.0556	0.3659	0.3832	0.3543	0.4502
Saturn	0.1664	0.1918	0.0946	0.4046	0.4804	0.4317	0.5823

distortion of the two-layer Maclaurin spheroid is important for its application to terrestrial-like planets with approximate two-layer internal structures and for its utility as a benchmark solution against which to calibrate the approximate theory of figures and validate more complex numerical models of planetary interiors.

Making use of the available two-layer Maclaurin spheroid solutions, we can review the existing approximation methods. As discussed in the introduction, [Zharkov et al., 1985] established a theory on the shape of a two-layered planetary body. In Figures (2.9)–(2.11), we compare the $\mathcal{E}_2$ computed by the two-layer model with the eccentricity determined by the approximation model. Note because the approximation methods cannot determine the shape of the interface, the $\mathcal{E}_1$ has no counterpart and hence is not plotted. Judged from the figure, for most planets whose rotation is

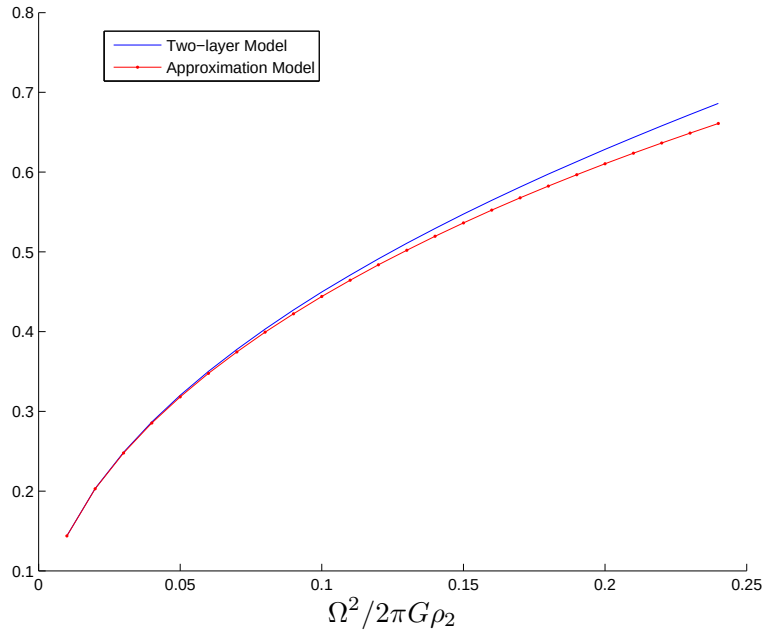

Figure 2.9: A systematic comparison of our two-layer Maclaurin spheroid solutions with the approximation solutions as functions of the rotation rate ϵ_2. The common parameters are $Q_v = 0.5$ and $\rho_2/\rho_1 = 0.5$; the approximation method gives fairly accurate shape eccentricity but underestimate it when the rotation becomes sufficiently fast.

not extremely fast, the approximation method indeed produces excellent eccentricity number. However, in the planetary MHD simulation, usually, it is the eccentricity of the interface in the two-layer model, which corresponds to the location of the core-mantle boundary (CMB) in a realistic planet, that topographically controls the dynamics of the flows inside the core. The approximation method has no means to help, in this sense. Recently, following on this work, [Schubert et al., 2011] have developed a novel approximation theory on the two-layer problem with slow rotation. The new theory has derived solutions of both the interface and the outer surface. The validation of the approximation model is based on the exact theory presented here. I am a coauthor of [Schubert et al., 2011].

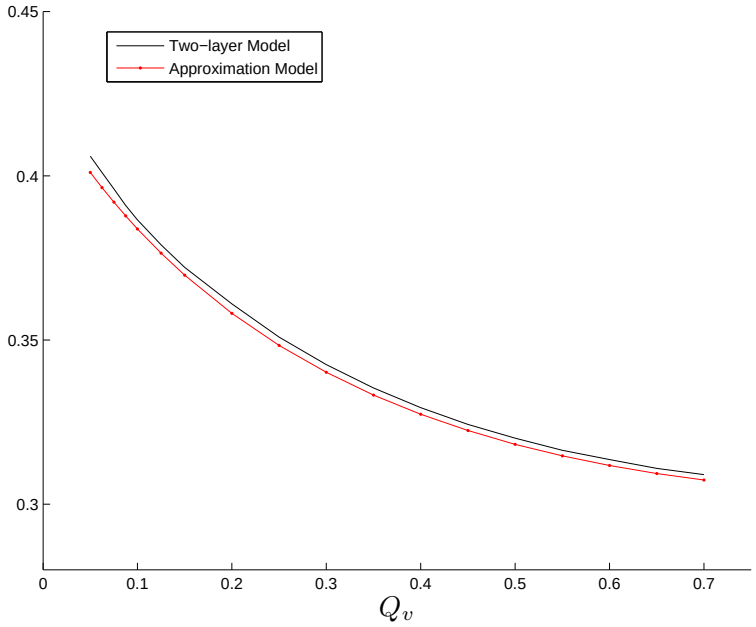

Figure 2.10: A systematic comparison of our two-layer Maclaurin spheroid solutions with the approximation solutions as functions of the volume percentage Q_v. The common parameters are $\epsilon_2 = 0.05$, $\rho_2/\rho_1 = 0.5$; the approximation method constantly underestimates the eccentricity of the body.

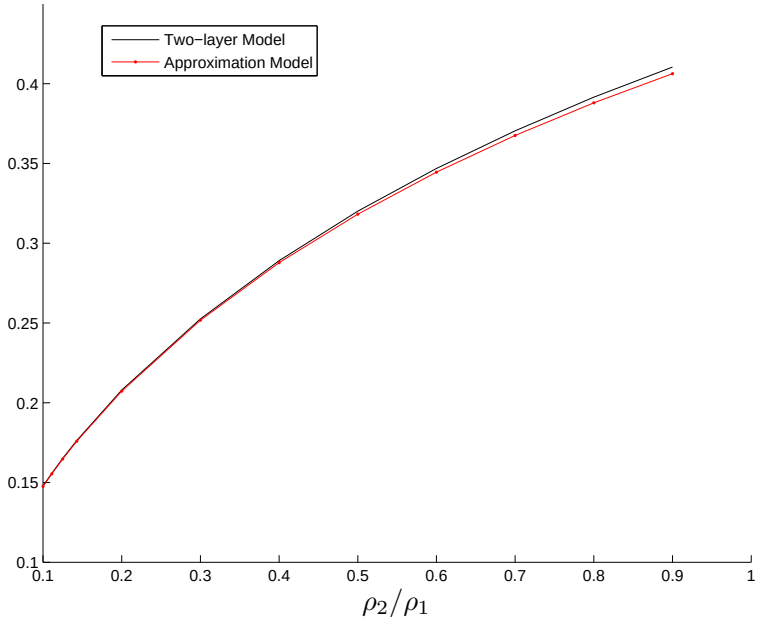

Figure 2.11: A systematic comparison of our two-layer Maclaurin spheroid solutions with the approximation solutions as functions of the density ration ρ_2/ρ_1. The common parameters are $\epsilon_2 = 0.05$,$Q_v = 0.5$; when the density difference of the two layers is small, the approximation method is subject to an accuracy deterioration.

Chapter 3

Variation of Zonal Gravity Coefficients of a Giant Planet Caused by its Deep Zonal Flows

3.1 Introduction

A striking and fascinating feature of giant planets like Jupiter and Saturn is their fast, alternating, cloud level zonal flows (e.g.,[Porco et. al., 2003]). The zonal winds could provide valuable information about dynamical processes in the deep interiors of Jupiter and Saturn depending on the depth to which these winds penetrate. Despite the fact that zonal flows have been accurately measured and extensively studied for a number of decades, their generation and maintenance still remains highly controversial. There exist two profoundly different views of the origin of the zonal flows. One opinion is that they are generated by thermal convection, partly powered by internal heat, which takes place within the deep interiors of the planets (e.g.,[Busse, 1976; Heimpel et al., 2005]). According to this view, giant planets like Jupiter and Saturn share the same essential dynamical features: their deep interiors are thermally unstable and fluid motion driven by thermal instabilities is highly constrained by both rotation and spherical geometry and, consequently, possesses close correlations that can transport momentum and effectively generate strong zonal flows. The observed alternating jets on the surface of a giant planet simply represent the zonal flows that are nearly independent of distance parallel to the rotation axis and extend through the whole interior ([Busse, 1976]). The other view is that the alternating zonal flow is largely confined to a very thin layer of stably stratified atmosphere (e.g., [Scott and Polvani, 2008; Williams, 1976]). The latter view is computationally much easier to model, and it is largely based on the well-known dynamics of the Earth's atmosphere.

If the zonal flows are primarily confined within a thin layer of the atmosphere, we anticipate that they would have a negligible influence on the external gravity field

of the giant planet. On the other hand, if the zonal flows represent deep thermal convection that extends through the whole interior of the planet, we expect that its external gravity field would be slightly modified by the strong zonal flow and that zonal gravity coefficients, such as J_2 and J_4, would also be slightly altered. The zonal gravity coefficients measured by a spacecraft circling a planet from pole to pole might therefore reveal information about the planet's internal dynamics. One of the scientific objectives of the Juno spacecraft (See [NASA, 2012]), now on its way to Jupiter, is to determine how deep the zonal flow persists by measuring the parameters of Jupiter's gravity field.

Deep zonal flows generate an external gravitational signature in two different ways. One way is via dynamics-related gravitational anomalies, i.e., deep zonal flows alter the planetary mass distribution by inducing density anomalies. This was first studied by Hubbard in a series of the papers ([Hubbard, 1974, 1982, 1999]). By assuming that a rotating planet is in hydrostatic equilibrium with a polytropic index of unity in which the pressure p and the density ρ are related by

$$p = K\rho^2,$$

where K is constant, and that the dimensionless rotational parameter

$$q = \frac{\Omega R^2}{GM} \ll 1,$$

where Ω is the angular speed of the planet, R is the radius of the planet, M is the mass and G is the gravitational constant, [Hubbard, 1974] obtained analytically the gravitational coefficients J_2, J_4 and J_6 in powers of q. The analysis was then extended to including the effect of differential rotation on the gravity harmonics and external shape under the assumptions that the differential rotation corresponds to a state of permanent rotation ([Hubbard, 1982]). In an important numerical study for a planet rotating differentially on cylinders parallel to the rotation axis, [Hubbard, 1999] derived an inhomogeneous wave equation for the density,

$$\nabla^2\rho + \frac{2\pi G}{K}\rho = -\frac{1}{2K}\nabla^2(V_c + V_d), \tag{3.1}$$

where V_c is the centrifugal potential as discussed in Chapter 2 while V_d is the rotational potential related to the zonal flow. The wave equation (3.1), subject to the boundary condition $\rho = 0$ at the external surface, was then solved numerically in spherical geometry by expanding ρ in terms of spherical Bessel functions and Legendre polynomials. It was shown that if the zonal flows persist sufficiently deep, they would produce a detectable signature in high-degree zonal components of the Jupiter's gravity field. [Kaspi et al., 1999] recently extended the calculation of [Hubbard, 1999] by using dynamical models based on either simple thermal-wind balance

or a full three-dimensional anelastic, non-hydrostatic, general circulation model. In the thermal-wind model

$$(2\mathbf{\Omega}\cdot\nabla)(\tilde{\rho}\mathbf{u}) = \nabla\rho' \times \mathbf{g}_0, \tag{3.2}$$

where $\tilde{\rho}(r)$ is the hydrostatic radial density profile ([Guillot and Morel, 1995]) , $\mathbf{u}$ is the wind velocity, $\mathbf{g}_0(r)$ is the mean gravity vector, and ρ' denotes the dynamic density anomaly. For given $\tilde{\rho}(r)$, $\mathbf{u}$ and $\mathbf{g}_0(r)$ in spherical geometry, (3.2) could be solved with an additional constraint to determine the density anomaly ρ' and, hence, the dynamical-related gravitational anomaly. It is shown that, to first order, both the thermal-wind analysis and the circulation model agree with the predictions of [Hubbard, 1999]. The second way deep zonal flows modify a planet's gravitational field is by redistributing mass as a result of flow-induced distortions in the shape of the planet (e.g., [Efimov et al., 1977; Trubitsyn et al., 1976; Vasilev et al., 1978]). The relevant results are summarized in the classical book by [Zharkov and Trubitsyn, 1978]. In this case, gravitational anomalies exist even if the density ρ within a planet is uniform. An essential element in the theories (e.g., [Trubitsyn et al., 1976]) is to assume that there exist two small parameters ϵ (measuring the speed of basic rotation) and α (measuring the amplitude of differential rotation),

$$\epsilon = \frac{\Omega_0^2}{2\pi G\rho} \ll 1 \quad \text{and} \quad \alpha = \frac{(\Omega^2 - \Omega_0^2)}{\Omega_0^2} \ll 1,$$

where Ω denotes the differential rotation. On the basis of the two small parameters m and α, the shape of a planet can be expanded as

$$r(t) = r_0\left[1 + \sum_{n=0}^{\infty} r_{2n}(r_0)P_{2n}(t)\right],$$

where $r_{2n} \sim \epsilon^n$ with $\alpha < \epsilon$. It implies, since $\epsilon \ll 1$, that the shape of a differential rotating planet is only slightly different from the perfect sphere given by $r = r_0$. In the spherical perturbation theory, the contribution to coefficients r_{2n} in the expansion is from both the basic rotation Ω_0 and the differential rotation Ω. It follows that the effect of planetary oblateness is neglected in the leading-order approximation and, hence, spherical coordinates, which dramatically simplify the relevant mathematical analysis, can be employed in the perturbation analysis.

All existing studies on the problem have assumed that the effect of rotational distortion is a small perturbation on a spherically symmetric state. Since the changes in low-degree zonal gravitational harmonics in a *rapidly* rotating body are largely dominated by its oblate shape, it is desirable to have a theory that relaxes the restriction of small rotational parameter $\epsilon \ll 1$. The present study attempts to extend the previous theories by permitting an arbitrary size of the rotational parameter ϵ.

We assume that the shape of a rapidly rotating planet can be expanded as

$$\xi(\eta) = \xi_o \left[1 + \sum_{n=0}^{\infty} h_{2n}(\xi_o) P_{2k}(\eta) \right],$$

where its arbitrary oblateness (ξ_o) is taken as the leading-order solution by making use of spheroidal oblate coordinates (ξ, η) (See what is discussed in Chapter 2) and the contribution to coefficients h_{2n} is only from the effect of the differential rotation Ω. At the expense of more complicated mathematical analysis involving in spheroidal oblate coordinates, the spheroidal perturbation theory is capable of dealing with large distortions of a rapidly rotating body away from a spherical shape and offering a way of estimating the values of differential-rotation-induced changes in low-degree zonal gravitational harmonics for arbitrarily rapidly rotating bodies. In order to develop the spheroidal perturbation theory, a new spheroidal polynomial – which is a function of two variables, restricted within the spheroidal cavity and orthogonal over the spheroid – is used to describe the differential rotation in spheroidal geometry of arbitrary eccentricity.

For the purpose of gaining insight into the key physics of the problem, we adopt an analytical approach by assuming that a planet rotates arbitrarily rapidly and has an effective uniform density that is defined on the basis of the observed value of its oblateness. By using the effective density to represent the planet we correctly account for planetary shape contributions to an observable such as the gravitational field. Similar to the model of [Hubbard, 1982], we also assume the differential rotation is a state of permanent rotation arising from deep thermal convection and extending throughout the whole interior along cylinders parallel to the rotation axis ([Busse, 1976]). Two rotation configurations are considered in this study. When a planet is in a state of rigid-body rotation (i.e., no zonal flows), its external gravity field can be derived using the classic Maclaurin theory, which has an exact solution (see, for example, [Lamb, 1932]), allowing us to compute its zonal gravity coefficients $\bar{J}_{2n}, n = 1, 2, 4, \ldots$. When the deep zonal flow is sufficiently strong, we can then, based on the exact solution, develop a perturbation theory for estimating the change in the planet's zonal gravity coefficients, $\Delta J_{2n}, n = 1, 2, 3, \ldots$, caused by the effect of the deep zonal flow. In comparison with the previous theories, the shape of a planet caused by its basic rotation is fully taken into account, enabling us to accurately estimate not only the rotation-induced changes in high-degree zonal gravitational harmonics but also the changes in low-degree harmonics for an arbitrarily rapidly rotating planet.

In what follows we present the model, the mathematical analysis, and its application to Jupiter in §3.2, while a summary and some remarks are given in §3.3.

3.2 Model, Analysis and Application

3.2.1 Model

The controlling effect of rotation on the fluid dynamics of giant planets like Jupiter is succinctly described by the Taylor-Proudman theorem which states that infinitesimal steady motions in an inviscid incompressible fluid must be two dimensional with respect to the direction of the rotation axis. The effect of viscosity can break the rotational constraint and the resulting convective motion, as a consequence of the combined effects of spherical geometry and rotation, is in the form of highly coherent small-scale, spiraling columnar flow $\widetilde{\mathbf{u}}$ which maintains a strong mean zonal flow $\mathbf{U}(s) = U(s)\hat{\boldsymbol{\phi}}$ with $|\widetilde{\mathbf{u}}| \ll |\mathbf{U}|$ (see, for example, [Zhang, 1992]), where s is the distance from the axis of rotation and $\hat{\boldsymbol{\phi}}$ denotes a unit vector in the azimuthal direction. Because of the strong effect of rotation, the convective motion may even penetrate into a stably stratified layer (see, for example, [Zhang and Schubert, 2002]). Following the model of [Busse, 1976], we assume that the observed zonal flows at cloud level represent the axisymmetric azimuthal component of its deep convection that passes through the whole interior of Jupiter and is independent of the distance parallel to the rotation axis.

We consider the hydrostatic equilibrium of a giant planet over a long timescale. We assume that the planet is isolated in space, rotates about a fixed axis with a uniform angular velocity $\boldsymbol{\Omega}$, and consists of a homogeneous fluid with constant density ρ without magnetic force acting on the zonal flows. In the interior of the planet, we also assume that (i) $|\widetilde{\mathbf{u}}| \ll |\mathbf{U}|$, (ii) the zonal flow $\mathbf{U}$ is steady, *i.e.*, $\partial\mathbf{U}/\partial t = 0$, and $\mathbf{U}(s) = U(s)\hat{\boldsymbol{\phi}}$ ([Busse, 1976]), which can be readily derived from its observed profile by assuming that $\mathbf{U}$ extends into the deep interior along cylinders parallel to the rotation axis, and (iii) viscous effects on the mean flow $\mathbf{U}$, to a first approximation, can be neglected. Under the above assumptions, a steady hydrostatic equilibrium of the planet is governed by the following partial differential equations in the co-rotating frame of reference:

$$2\boldsymbol{\Omega} \times \mathbf{U} = -\nabla P - \nabla V_c - \nabla V_g, \tag{3.3}$$

$$\nabla \cdot \mathbf{U} = 0, \tag{3.4}$$

where V_c is the centrifugal potential, V_g is the gravitational potential, and P is the pressure. Here the pressure P and the zonal flow $\mathbf{U}$ satisfy the boundary conditions

$$P = 0, \quad \hat{\mathbf{n}} \cdot \mathbf{U} = 0 \tag{3.5}$$

at the bounding surface, $\mathcal{S}$, of the planet with $\hat{\mathbf{n}}$ denoting its unit normal. Note that $\mathbf{U} = U(s)\hat{\boldsymbol{\phi}}$ automatically satisfies equation (3.4) and the required boundary

condition (3.5). We may introduce a potential, V_z, of the zonal flow, defined as,

$$2\boldsymbol{\Omega} \times \mathbf{U} = -\nabla V_z \tag{3.6}$$

such that (3.3) can be rewritten as

$$\nabla(P + V_c + V_g + V_z) = 0. \tag{3.7}$$

As indicated by (3.3) or (3.7), both the shape of the bounding surface $\mathcal{S}$ and the gravitational potential V_g in the hydrostatic equilibrium state would be affected by the presence of the zonal flow $\mathbf{U}$, indicating that the zonal flow potential V_z can modify the gravity field of a giant planet if it is sufficiently deep and strong. For any fluid planet in the solar system, moreover, it is reasonable to assume that the equilibrium shape of the planet is axisymmetric because the first bifurcation from a Maclaurin spheroid takes place at the critical eccentricity $\mathcal{E}_c \sim 0.93$ (see Chapter 2), corresponding to extremely fast-rotating planets.

Since the zonal flow $\mathbf{U}$ is both axisymmetric with respect to the rotation axis and symmetric with respect to the equatorial plane, the exterior gravitational potential, V_g, can be expanded in terms of spherical harmonics P_{2n},

$$V_g(r,\theta) = -\frac{GM}{r}\left[1 - \sum_{n=1}^{\infty} J_{2n}\left(\frac{R_e}{r}\right)^{2n} P_{2n}(\cos\theta)\right], \quad r \geq R_e, \tag{3.8}$$

where (r, θ, ϕ) are spherical polar coordinates with $\theta = 0$ being at the axis of rotation, R_e denotes the equatorial radius of the giant planet and $J_2, J_4, J_6, \cdots$ are called zonal gravitational field coefficients.

If there exists no deep zonal flow (the state of rigid-body rotation) within a giant planet, its outer surface would be in the shape of a Maclaurin spheroid ([Lamb, 1932]). The effect of the deep strong zonal flow, however, introduces a small modification to (i) the shape of the Maclaurin spheroid, (ii) the gravity field of the Maclaurin spheroid and, hence, (iii) the zonal gravity coefficients of the planet. This physical picture suggests that the mathematical problem may be tackled by a perturbation analysis via the following expansion:

$$\begin{aligned} P &= P_0 + P_1 + \ldots, \\ V_c &= V_{c0} + V_{c1} + \ldots, \\ V_g &= V_{g0} + V_{g1} + \ldots, \\ V_z &= V_{z1} + \ldots, \end{aligned} \tag{3.9}$$

where P_0, V_{c0} and V_{g0} denote the leading-order solution associated with $\mathbf{U} = 0$ while P_1, V_{c1}, V_{g1} represent small variations caused by the zonal flow potential V_{z1}.

Similarly, we also expand the zonal gravity coefficients J_{2n} in the form

$$J_{2n} = \bar{J}_{2n} + \Delta J_{2n} + \ldots, \quad n = 1, 2, 3, \ldots.$$

It follows that we can solve (3.7) together with the relevant boundary conditions analytically in three stages: (i) Find the leading-order solution P_0, V_{c0} and V_{g0} to determine the corresponding gravity coefficients $\bar{J}_2, \bar{J}_4, \bar{J}_6 \cdots$; (ii) Derive the zonal flow potential V_z in oblate spheroidal coordinates; and (iii) Carry out the perturbation analysis to obtain the variations $\Delta J_2, \Delta J_4, \Delta J_6, \cdots$. In this study, we restrict our analysis up to J_{12}.

3.2.2 $\bar{J}_{2n}$ without the effect of the zonal flows

It is insightful and helpful to discuss briefly the Maclaurin problem, even though one can find detailed discussion in Chapter 2, representing the leading-order solution in our perturbation analysis. When the effect of zonal flow is neglected, *i.e.*, $\mathbf{U} = 0$, the leading-order equation (3.7) for the hydrostatic equilibrium becomes

$$\nabla(P_0 + V_{c0} + V_{g0}) = 0. \tag{3.10}$$

For an isolated planetary body, the pressure vanishes on the outer free surface, *i.e.*, $P_0 = 0$ on $\mathcal{S}$, implying that the total potential, gravitational and rotational, must be constant,

$$V_{c0} + V_{g0} = C_0, \tag{3.11}$$

where C_0 is a constant. It should be noted that the eccentricity $\mathcal{E}$ of the giant planet in the hydrostatic equilibrium is assumed to be in the range $0 < \mathcal{E} < \mathcal{E}_c \sim 0.93$.

The Maclaurin spheroids solution is established by using the free surface condition,

$$\epsilon = \frac{\sqrt{1-\mathcal{E}^2}}{\mathcal{E}^3}[(3-2\mathcal{E}^2)\sin^{-1}\mathcal{E}] - \frac{3(1-\mathcal{E}^2)}{\mathcal{E}^2}, \tag{3.12}$$

where $\epsilon = \Omega^2/(2\pi G\rho)$. For planets in the solar system, $\mathcal{E}^2$ is usually small and, thus, ϵ can be expanded as

$$\epsilon = \frac{4}{15}\mathcal{E}^2 + O(\mathcal{E}^4),$$

which can be determined from direct observations. Substitution of the values of c^2, ξ_0 and $2\pi G\rho$ for a planet into (2.28) yields the leading-order gravitational potential, V_{g0}, in oblate spheroidal coordinates. By further projecting V_{g0} onto the potential in spherical coordinates given by (3.8), we can derive the leading-order coefficients $\bar{J}_{2n}, n = 1, 2, 3, \ldots$ for rapidly rotating planets with arbitrary eccentricity $\mathcal{E}$. It should be noted, however, that our primary concern in this study is not the size of $\bar{J}_k$ but the variations in the gravitational coefficients caused by the effect of the zonal flow $\mathbf{U}$.

3.2.3 Potential of the zonal flow

A crucial ingredient in the perturbation analysis involves the derivation of the zonal flow potential V_z defined by (3.6). If the zonal flow $\mathbf{U}$ extends all the way from the southern to northern hemispheres along the direction of rotation ([Busse, 1976]), V_z can be, for a given zonal flow $\mathbf{U}$, derived in a spheroid of arbitrary eccentricity.

A source of mathematical difficulty in solving the potential problem defined by (3.6) is the conflict between the spheroidal and cylindrical polar coordinates. While the $z-$independence of the zonal flows is strongly indicative of adopting cylindrical polar coordinates, the geometry of the planet's shape clearly suggests the use of oblate spheroidal coordinates. This conflict points to the necessity of a special orthogonal polynomial, denoted as $G_n(s)$, which should possess the following three properties. First, the polynomial must be a function of two variables η and ξ, restricted within the spheroidal cavity, but taking only a single argument s. Second, since the zonal flow vanishes at the axis of rotation, the polynomial must be odd, *i.e.*, $G_{2k-1}(s)$ with $k = 1, 2, 3, \ldots$ and $(2k-1)$ denoting its order. Third, the zonal flow is defined within a spheroid and the polynomial G_{2k-1} should be thus orthogonal over the spheroid, *i.e.*,

$$\int_V G_{2k-1}(\xi,\eta)G_{2n-1}(\xi,\eta)\,\mathrm{d}V = 0, \quad \text{if} \quad k \neq n,$$

where $\int_V$ denotes the volume integration over the spheroid. If such a polynomial meeting the three requirements exists and can be found, it resolves the conflict between the spheroidal and cylindrical coordinates, and can be then employed in the representation of a zonal flow within a spheroid. A new Legendre-type polynomial recently discovered for describing the zonal flow in *spherical geometry* ([Liao and Zhang, 2010]) can be extended to *spheroidal geometry of arbitrary eccentricity*. It can be shown that

$$G_{2k-1}(\xi,\eta) = \frac{1}{(1-\mathcal{E}^2)^{\frac{1}{4}}}\sum_{j=1}^{k}\frac{(-1)^{k-j}[2(k+j)-1]!!}{2^{k-1}(k-j)!(j-1)!(2j)!!}(s/R_e)^{2j-1}, \tag{3.13}$$

where $s = c\sqrt{(1+\xi^2)(1-\eta^2)}$, does satisfy the three requirements. Equation (3.6) suggests that $\mathbf{U}$ and V_z can be expanded as

$$\mathbf{U}(\xi,\eta) = \Omega R_e\sum_{k=1}^{\infty}c_k G_{2k-1}(\xi,\eta)\hat{\boldsymbol{\phi}}, \tag{3.14}$$

$$V_z(\xi,\eta) = \Omega^2 R_e^2\sum_{k=1}^{\infty}c_k V_{2k}(\xi,\eta), \tag{3.15}$$

with

$$V_{2k}(\xi,\eta) = \frac{1}{(1-\mathcal{E}^2)^{\frac{1}{4}}} \sum_{j=1}^{k} \frac{(-1)^{k-j+1}[2(k+j)-1]!!}{2^{k-1}(k-j)!(j-1)!(2j)!!j} (s/R_e)^{2j}.$$

Upon using the property

$$\int_V [G_{2k-1}(\xi,\eta)]^2 \, \mathrm{d}V = \frac{4\pi(2k+1)!!(2k-1)!!}{(4k+1)(2k)!!(2k-2)!!} R_e^3,$$

we obtain an expression for the zonal flow potential V_z:

$$V_z(\xi,\eta) = \Omega R_e \sum_{k=1} \left[\frac{1}{\int_V G_{2k-1}^2 \mathrm{d}V} \int_V U(s) G_{2k-1}(s/R_e) \mathrm{d}V \right] V_{2k}(s/R_e), \tag{3.16}$$

where $U(s)$ can be derived from the observed profile of the zonal wind on a giant planet. For example, Figure 3.1 depicts the observed zonal flow speed at Jovian top atmosphere. It should be stressed that the above analysis is only possible in

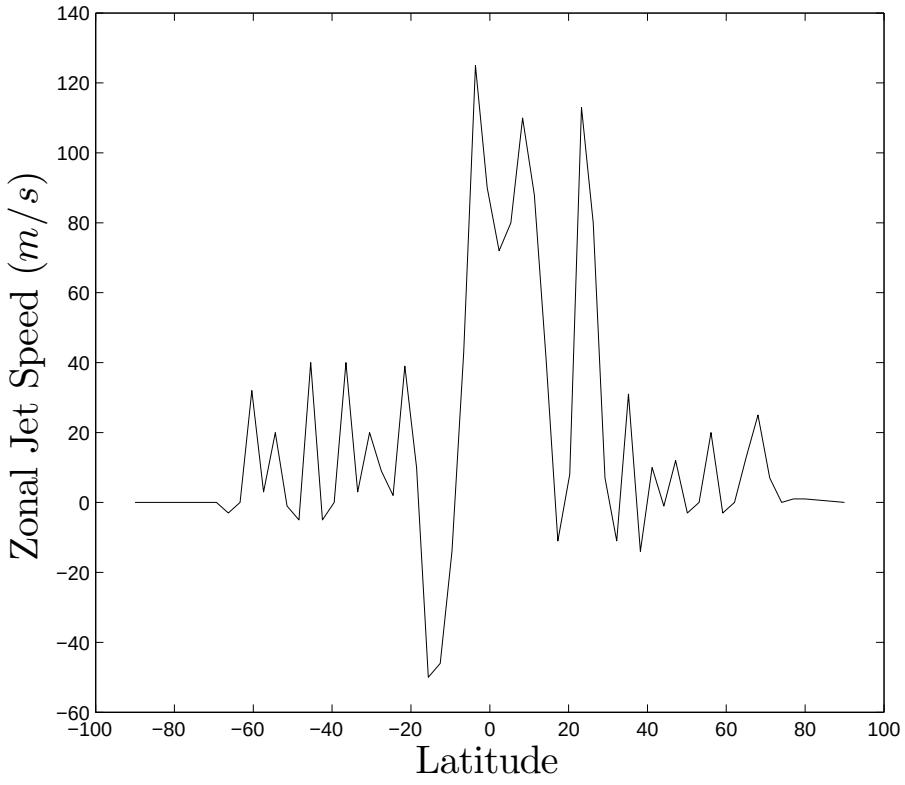

Figure 3.1: The Jovian atmospheric zonal jet speed profile, data are from [Porco et. al., 2003]

spheroidal geometry with uniform density with the zonal flow extending all the way along the cylinders parallel to the axis of rotation. For the analysis discussed later, we can further expand V_z at the outer surface $\xi = \xi_o$ as a series of spheroidal Legendre polynomials

$$V_z(\xi_o,\eta) = \sum_{k=0}^{\infty} \mathcal{D}_{2k} P_{2k}(\eta). \tag{3.17}$$

Table 3.1: Coefficients $\beta_{(2k)(2n)}$ for the expansion of $P_2(\eta)P_{2k}(\eta)$ in equation (3.21).

(2k)/(2n)	0	2	4	6	8
0	0	1	0	0	0
2	1/5	2/7	18/35	0	0
4	0	2/7	20/77	5/11	0
6	0	0	45/143	14/55	28/65

Table 3.2: In this table, $\bar{J}_n$ is the value of zonal gravity coefficients in the state of rigid-body rotation, ΔJ_n represent the variation induced by the zonal flows and J_n is the value of the zonal gravity coefficients in the presence of the zonal flows.

n	$\bar{J}_n$	J_n	ΔJ_n	$\Delta J_n/\bar{J}_n$
2	$+2.510802 \times 10^{-2}$	$+2.517941 \times 10^{-2}$	$+7.139042 \times 10^{-5}$	0.284333%
4	-1.350884×10^{-3}	-1.360343×10^{-3}	-9.458775×10^{-6}	0.700191%
6	$+9.421630 \times 10^{-5}$	$+9.644272 \times 10^{-5}$	$+2.226413 \times 10^{-6}$	2.363086%
8	-7.527873×10^{-6}	-7.351529×10^{-6}	$+1.763433 \times 10^{-7}$	2.342538%
10	$+6.523407 \times 10^{-7}$	-7.495363×10^{-7}	-1.401877×10^{-6}	214.8995%
12	-6.332729×10^{-8}	-6.638417×10^{-7}	-6.005144×10^{-7}	948.2712%

Furthermore, it can be demonstrated that

$$\frac{|V_z|}{|V_{c0}|} = \mathrm{O}\left(\frac{U_{typical}}{\Omega R_e}\right)$$

which is usually small in comparison to unity for giant planets, indicating that we only need to consider the leading-order term in the V_z expansion (3.9) by taking $V_z = V_{z1}$ in the perturbation analysis.

3.2.4 Perturbation analysis

Under the influence of the zonal flow potential V_z, the shape of the outer surface of a giant planet can no longer be a perfect spheroid described by $\xi_o = \sqrt{1/\mathcal{E}^2 - 1}$. Its distorted outer surface, ξ_s, in the equilibrium may be expanded in terms of spheroidal Legendre functions:

$$\xi_s \;=\; \xi_o \left[1 + \sum_{k=0}^{\infty} h_{2k} P_{2k}(\eta)\right], \tag{3.18}$$

where $k = 0, 1, 2, \ldots$, and $|h_{2k}| \ll 1$. The reason why only even Legendre Polynomials contribute is that the zonal flows are assumed to be symmetric with respect to the equatorial plane.

We are now in a position to derive the next-order centrifugal (V_{c1}) and gravitational (V_{g1}) potentials in the expansion (3.9). It is worth pointing out that, for the

purpose of determining ΔJ_n, the evaluation of the potentials, V_{c1} and V_{g1}, is only required at the outer surface ξ_s. It is straightforward to show that the centrifugal potential perturbation V_{c1} at ξ_s is of the form

$$V_{c1}(\xi_s,\eta)=-\frac{\Omega^2 c^2}{2}\left\{1+\xi_o^2\left[1+\sum_{k=0}^{\infty}h_{2k}P_{2k}(\eta)\right]^2\right\}\left(1-\eta^2\right)-V_{c0}(\xi_0,\eta). \tag{3.19}$$

A further expansion in terms of h_{2k} yields a leading-order expression:

$$V_{c1}(\xi_s,\eta) \;=\; -\frac{2}{3}\Omega^2 c^2\xi_o^2\left\{\left[\sum_{k=0}^{\infty}h_{2k}P_{2k}(\eta)\right]-\left[\sum_{k=0}^{\infty}h_{2k}P_{2k}(\eta)\right]P_2(\eta)\right\}, \tag{3.20}$$

where the terms, $P_{2k}(\eta)P_2(\eta)$, can be written, for example, as

$$\begin{aligned}
P_0(\eta)P_2(\eta) &= P_2(\eta),\\
P_2(\eta)P_2(\eta) &= \frac{1}{5}P_0(\eta)+\frac{2}{7}P_2(\eta)+\frac{18}{35}P_4(\eta),\\
P_4(\eta)P_2(\eta) &= \frac{2}{7}P_2(\eta)+\frac{20}{77}P_4(\eta)+\frac{5}{11}P_6(\eta),\\
P_6(\eta)P_2(\eta) &= \frac{45}{143}P_4(\eta)+\frac{14}{55}P_6(\eta)+\frac{28}{65}P_8(\eta),\quad\cdots
\end{aligned}$$

which can be extended to any P_{2k} needed in the analysis. It is then mathematically helpful to introduce the coefficients $\beta_{(2n)(2k)}$ defined by the following relationship

$$P_2(\eta)P_{2k}(\eta)=\sum_{n=0}^{k+1}\beta_{(2n)(2k)}P_{2n}(\eta). \tag{3.21}$$

Several examples of coefficients $\beta_{(2n)(2k)}$ are listed in Table 3.1. Making use of the coefficients $\beta_{(2n)(2k)}$, the expression for $V_{c1}(\xi_s,\eta)$ becomes

$$\begin{aligned}
V_{c1}(\xi_s,\eta) \;=\; & -\frac{2}{3}\Omega^2 c^2\xi_o^2\left[\sum_{k=0}^{\infty}h_{2k}P_{2k}(\eta)\right]\\
&+\frac{2}{3}\Omega^2 c^2\xi_o^2\Big\{\left[h_0\beta_{00}+h_2\beta_{02}+h_4\beta_{04}+\cdots\right]P_0(\eta)\\
&+\left[h_0\beta_{20}+h_2\beta_{22}+h_4\beta_{24}+\cdots\right]P_2(\eta)\\
&+\left[h_2\beta_{42}+h_4\beta_{44}+h_6\beta_{46}+\cdots\right]P_4(\eta)+\cdots\Big\},
\end{aligned} \tag{3.22}$$

where h_{2k} will be determined by the free surface condition. Expression (3.22) may be simply written as

$$V_{c1}\left(\xi_s,\eta\right)=\sum_{k=0}\mathcal{C}_k P_{2k}(\eta), \tag{3.23}$$

where $\mathcal{C}_k$ is a function of h_{2k}.

While the derivation for the centrifugal potential V_{c1} at ξ_s is relatively simple, it is much more complicated to obtain the gravitational potential V_{g1}. Similar to the

procedure discussed for the leading-order problem, we may write the gravitational potential perturbation V_{g1} as

$$V_{g1}(\xi,\eta) = \left[-2\pi G\rho c^2 i \sum_{k=0}^{\infty} (4k+1) A_{2k} Q_{2k}(i\xi) P_{2k}(\eta)\right] - V_{g0}, \tag{3.24}$$

where the coefficients A_{2k} are given by

$$A_{2k} = \int_{-1}^{1}\int_{0}^{\xi_o[1+\sum_{k=0}^{\infty} h_{2k}P_{2k}(\eta')]} (\xi'^2+\eta'^2) P_{2k}(\eta') P_{2k}(i\xi') \mathrm{d}\xi' \mathrm{d}\eta'.$$

A major task is then to derive the analytical expression for A_{2k}. We shall explicitly discuss only the leading coefficients, A_0, A_2, A_4 and A_6. First, consider the special case with $k=0$ for which we have

$$\begin{aligned} A_0 &= \int_{-1}^{1}\int_{0}^{[\xi_o+\xi_o\sum_{k=0}^{\infty} h_{2k}P_{2k}(\eta')]} (\xi'^2+\eta'^2)\mathrm{d}\xi'\mathrm{d}\eta' \\ &= \frac{2}{3}\xi_o(1+\xi_o^2) + \left[(2\xi_o^2+\frac{2}{3})h_0 + \frac{4}{15}h_2\right]\xi_o. \end{aligned}$$

This integral actually is related to the total mass of the planet which must be conserved. Mass conservation implies that

$$\left[(2\xi_o^2+\frac{2}{3})h_0 + \frac{4}{15}h_2\right] = 0, \tag{3.25}$$

providing a relationship between h_0 and h_2. Consider now the $k=1$ term given by

$$\begin{aligned} A_2 &= \int_{-1}^{1}\int_{0}^{[\xi_o+\xi_o\sum_{k=0}^{\infty} h_{2k}P_{2k}(\eta')]} (\xi'^2+\eta'^2) P_2(\eta') P_2(i\xi') \mathrm{d}\xi'\mathrm{d}\eta' \\ &= -\frac{2}{15}\xi_o(1+\xi_o^2) - \frac{1}{105}(1+3\xi_o^2)\left[14h_0 + (11+21\xi_o^2)h_2 + 4h_4\right]\xi_o, \end{aligned}$$

where the first term corresponds to the leading order problem which will be subtracted later. Expressions for higher-order terms, $k=2$ and $k=3$, are

$$\begin{aligned} A_4 &= \int_{-1}^{1}\int_{0}^{\xi_o[1+\sum_{k=0}^{\infty} h_{2k}P_{2k}(\eta')]} (\xi'^2+\eta'^2) P_4(\eta') P_4(i\xi') \mathrm{d}\xi'\mathrm{d}\eta' \\ &= \frac{[1716h_2 + 1050h_6 + (2535+5005\xi_o^2)h_4](3+30\xi_o^2+35\xi_o^4)\xi_o}{180180}, \end{aligned}$$

and

$$\begin{aligned} A_6 &= \int_{-1}^{1}\int_{0}^{\xi_o[1+\sum_{k=0}^{\infty} h_{2k}P_{2k}(\eta')]} (\xi'^2+\eta'^2) P_6(\eta') P_6(i\xi') \mathrm{d}\xi'\mathrm{d}\eta' \\ &= -\frac{[850h_4 + 616h_8 + (1411+2805\xi_o^2)h_6](5+105\xi_o^2+315\xi_o^4+231\xi_o^6)\xi_o}{291720}, \end{aligned}$$

Similar but lengthy and more complicated equations for A_{2k} with large k can be derived. Substitution of A_{2k}, $k = 0, 1, 2, 3, \cdots$, into (3.24) yields an analytical expression for the exterior gravitational potential V_{g1}:

$$\begin{aligned}
& V_{g1}(\xi,\eta) = \pi G\rho c^2\Big\{ \\
& -\frac{4}{3}\xi_o(1+\xi_o^2)\cot^{-1}\xi - \frac{2}{3}\xi_o(1+\xi_o^2)[(3\xi^2+1)\cot^{-1}\xi - 3\xi]P_2(\eta) \\
+\ & \frac{2}{21}\xi_o(3\xi_o^2+1)[14h_0 + (11+21\xi_o^2)h_2 + 4h_4]iQ_2(i\xi)P_2(\eta) \\
-\ & \frac{18\,[1716h_2 + 1050h_6 + (2535+5005\xi_o^2)h_4]\,(3+30\xi_o^2+35\xi_o^4)\xi_o}{180180}\,[iQ_4(i\xi)P_4(\eta)] \\
+\ & \frac{26\,[850h_4 + 616h_8 + (1411+2805\xi_o^2)h_6]\,(5+105\xi_o^2+315\xi_o^4+231\xi_o^6)\xi_o}{291720} \\
\times\ & iQ_6(i\xi)P_6(\eta) + \ldots\Big\} - V_{g0}(\xi,\eta),
\end{aligned} \tag{3.26}$$

which is valid for $\xi \geq \xi_s$. It is important to note that coefficients h_{2k} in (3.26) are unknown and will be determined by the boundary condition on the bounding surface of the planet. This requires one to express the gravitational potential V_{g1} at the outer surface $\xi_s = \xi_o[1 + \sum_{k=0}^{\infty} h_{2k}P_{2k}(\eta)]$. After making some rearrangements, we can rewrite (3.26) at ξ_s in terms of $P_{2k}(\eta)$:

$$\begin{aligned}
& V_{g1}(\xi_s,\eta) = \frac{4}{3}\pi G\rho c^2\Big\{\xi_o^2\,[h_0P_0(\eta) + h_2P_2(\eta) + h_4P_4(\eta) + \cdots] \\
-\ & \frac{1}{2}\xi_o^2\left[6\xi_o(1+\xi_o^2)\cot^{-1}\xi_o - 6\xi_o^2 - 4\right]\Big[(h_0\beta_{00} + h_2\beta_{02} + h_4\beta_{04} + \cdots)\,P_0(\eta) \\
+\ & (h_0\beta_{20} + h_2\beta_{22} + h_4\beta_{24} + \cdots)\,P_2(\eta) \\
+\ & (h_2\beta_{42} + h_4\beta_{44} + h_6\beta_{46} + \cdots)\,P_4(\eta) + \cdots\Big] \\
-\ & \frac{1}{28}\xi_o(3\xi_o^2+1)[14h_0 + (11+21\xi_o^2)h_2 + 4h_4][(3\xi_o^2+1)\cot^{-1}\xi_o - 3\xi_o]P_2(\eta) \\
-\ & \frac{27}{2}\frac{[1716h_2 + 1050h_6 + (2535+5005\xi_o^2)h_4]\,(3+30\xi_o^2+35\xi_o^4)}{180180}\xi_o iQ_4(i\xi_o)P_4(\eta) \\
& +\frac{39}{2}\frac{[850h_4 + 616h_8 + (1411+2805\xi_o^2)h_6]\,(5+105\xi_o^2+315\xi_o^4+231\xi_o^6)}{291720} \\
\times\ & \xi_o iQ_6(i\xi_o)P_6(\eta) + \cdots\Big\},
\end{aligned}$$

which can be written in the form

$$V_{g1}(\xi_s,\eta) = \sum_{k=0} \mathcal{G}_k P_{2k}(\eta). \tag{3.27}$$

By imposing the free surface condition,

$$V_{c1}(\xi_s,\eta) + V_{g1}(\xi_s,\eta) + V_{z1}(\xi_s,\eta) = C_1,$$

where C_1 is constant, we obtain that

$$\mathcal{C}_k + \mathcal{G}_k + \mathcal{D}_k = 0, \quad k = 1, 2, \cdots .$$

This leads to a system of the following linear equations about h_{2k}:

$$\left(2\xi_o^2 + \frac{2}{3}\right) h_0 + \frac{4}{15} h_2 = 0, \tag{3.28}$$

$$\begin{aligned}
&\frac{4}{3}\xi_o^2 h_2 - \frac{1}{21}\xi_o(3\xi_o^2+1)\left[14h_0 + (11+21\xi_o^2)h_2 + 4h_4\right]\left[(3\xi_o^2+1)\cot^{-1}\xi_o - 3\xi_o\right] \\
- &\frac{2}{3}\xi_o^2[6\xi_o(1+\xi_o^2)\cot^{-1}\xi_o - 6\xi_o^2 - 4]\left[h_0\beta_{20} + h_2\beta_{22} + h_4\beta_{24} + \cdots\right] \\
- &\frac{4\epsilon}{3}\xi_o^2 h_2 + \frac{4\epsilon}{3}\xi_o^2\left[h_0\beta_{20} + h_2\beta_{22} + h_4\beta_{24} + \cdots\right] + \frac{\mathcal{D}_2}{\pi G\rho c^2} = 0,
\end{aligned} \tag{3.29}$$

$$\begin{aligned}
- &18iA_4Q_4(i\xi_o) + \frac{4}{3}\xi_o^2 h_4 \\
- &\frac{2}{3}\xi_o^2[6\xi_o(1+\xi_o^2)\cot^{-1}\xi_o - 6\xi_o^2 - 4]\left[h_2\beta_{42} + h_4\beta_{44} + h_6\beta_{46} + \cdots\right] \\
- &\frac{4\epsilon}{3}\xi_o^2 h_4 + \frac{4\epsilon}{3}\xi_o^2\left[h_2\beta_{42} + h_4\beta_{44} + h_6\beta_{46} + \cdots\right] + \frac{\mathcal{D}_4}{\pi G\rho c^2} = 0,
\end{aligned} \tag{3.30}$$

$$\begin{aligned}
- &26iA_6Q_6(i\xi_o) + \frac{4}{3}\xi_o^2 h_6 \\
- &\frac{2}{3}\xi_o^2[6\xi_o(1+\xi_o^2)\cot^{-1}\xi_o - 6\xi_o^2 - 4]\left[h_4\beta_{64} + h_6\beta_{66} + h_8\beta_{68} + \cdots\right] \\
- &\frac{4\epsilon}{3}\xi_o^2 h_6 + \frac{4\epsilon}{3}\xi_o^2\left[h_4\beta_{64} + h_6\beta_{66} + h_8\beta_{68} + \cdots\right] + \frac{\mathcal{D}_6}{\pi G\rho c^2} = 0,
\end{aligned} \tag{3.31}$$

$$\vdots$$

which can be readily solved for determining h_{2k}. Note that the equations for h_{2k} with $k \geq 4$ are not explicitly given because of their length and complexity. In practice, the infinite linear system should be truncated according to the precision of observations of the zonal flow. The highest expansion order of V_z in (3.17) determines the dimension of the linear system to be solved.

In summary, when the zonal flow potential V_z is sufficiently large, the perfect spheroidal shape, described by $\xi = \xi_o$ in oblate spheroidal coordinates, would be slightly distorted. The precise departure from the perfect spheroidal shape is determined by the values of $h_{2k}, k = 1, 2, \cdots$, a solution of the linear system (3.29)–(3.31). After determining the distorted shape of the giant planet, which is described by (3.18), we can then compute the gravitational potential V_{g1} and the variations $\Delta J_2, \Delta J_4, \Delta J_6, \cdots$. It should be noted that the validity of the perturbation analysis requires only the condition $U_{typical}/(\Omega R_e) \ll 1$, where $U_{typical}$ denotes the typical speed of the zonal flows.

3.2.5 Application to Jupiter

We now apply the general perturbation theory to Jupiter. In this case, the linear system (3.29)-(3.31) can be further simplified. Since $\mathcal{E}^2 \ll 1$ and $\epsilon \ll 1$ for Jupiter, we may simplify (3.29)-(3.31) by recognizing, for example, that

$$\frac{[6\xi_o(1+\xi_o^2)\cot^{-1}\xi_o - 6\xi_o^2 - 4][h_0\beta_{20} + h_2\beta_{22} + h_4\beta_{24} + \cdots]}{\frac{4}{3}h_2} \sim O(\mathcal{E}^2),$$
$$\frac{(4k+1)\pi G\rho c^2 i A_{2k} Q_{2k}(i\xi_o)}{\frac{4}{3}\pi G\rho c^2 \xi_o^2 h_2} \sim O(1).$$

It follows that the leading-order linear system (3.29)-(3.31) becomes

$$0 = \left(2\xi_o^2 + \frac{2}{3}\right)h_0 + \frac{4}{15}h_2, \tag{3.32}$$

$$\begin{aligned} -\frac{\mathcal{D}_2}{\pi G\rho c^2} &= -\frac{2}{3}\xi_o(3\xi_o^2+1)[(3\xi_o^2+1)\cot^{-1}\xi_o - 3\xi_o]h_0 \\ &+ \left\{\frac{4}{3}\xi_o^2 - \frac{1}{21}\xi_o(3\xi_o^2+1)(11+21\xi_o^2)[(3\xi_o^2+1)\cot^{-1}\xi_o - 3\xi_o]\right\}h_2 \\ &- \frac{4}{21}\xi_o(3\xi_o^2+1)[(3\xi_o^2+1)\cot^{-1}\xi_o - 3\xi_o]h_4, \end{aligned} \tag{3.33}$$

$$\begin{aligned} -\frac{\mathcal{D}_4}{\pi G\rho c^2} &= -\frac{1716}{10010}iQ_4(i\xi_o)\xi_o(3+30\xi_o^2+35\xi_o^4)h_2 \\ &+ \left\{\frac{4}{3}\xi_o^2 - \frac{1}{10010}iQ_4(i\xi_o)\xi_o(3+30\xi_o^2+35\xi_o^4)(2535+5005\xi_o^2)\right\}h_4 \\ &- \frac{1050}{10010}iQ_4(i\xi_o)\xi_o(3+30\xi_o^2+35\xi_o^4)h_6, \end{aligned} \tag{3.34}$$

$$\begin{aligned} -\frac{\mathcal{D}_6}{\pi G\rho c^2} &= \frac{850}{11220}iQ_6(i\xi_o)\xi_o(5+105\xi_o^2+315\xi_o^4+231\xi_o^6)h_4 + \\ &\left\{\frac{4}{3}\xi_o^2 + \frac{iQ_6(i\xi_o)\xi_o}{11220}(5+105\xi_o^2+315\xi_o^4+231\xi_o^6)(1411+2805\xi_o^2)\right\}h_6, \end{aligned} \tag{3.35}$$

$$\vdots$$

Again explicit equations for h_{2k} with $k \geq 4$ are not presented because of their length and complexity. The above linear system can be readily solved for given ξ_0, c, $\pi G\rho$ and $\mathcal{D}_{2k}$.

Application of the general theory to a giant planet requires the following five steps. First, we need to determine the effective density ρ, or the quantity $\pi G\rho$, on the left side of (3.32)–(3.35). From the observed value of $\mathcal{E}^2$ for Jupiter at the one-bar pressure level, which is $\mathcal{E}^2 = 0.1255$ ([Seidelmann et. al., 2007]), we can compute ϵ according to (3.12), which gives $\epsilon = 0.03407$. Since the angular velocity Ω of Jupiter is well known ($\Omega = 1.7585 \times 10^{-4} s^{-1}$), the relationship $\epsilon = \Omega^2/(2\pi G\rho)$ can be further employed to give

$$\pi G\rho = \frac{\Omega^2}{2\epsilon} = 4.5376 \times 10^{-7} s^{-1}.$$

Table 3.3: In this table, up to $2k = 12$, the values of $\mathcal{D}_{2k}$ and h_{2k} for a Jupiter model are listed. $\mathcal{D}_{2k}$ has the dimension of potential in SI units. h_{2k} is dimensionless.

k	0	1	2	3	4	5
$\mathcal{D}_{2k} \times 10^{-5}$	−1.2436	1.4940	−0.2958	0.1582	0.0960	−0.1942
$h_{2k} \times 10^{3}$	0.0025	−0.1379	0.0131	−0.0075	−0.0035	0.0072

In other words, we use the observed eccentricity $\mathcal{E}$ of Jupiter to determine its effective density ρ. In the second step, we must compute the focal length c of oblate spheroidal Jupiter which is also required in (3.32)–(3.35). Note that the outer surface of Jupiter is given by $\xi_o = \sqrt{1/\mathcal{E}^2 - 1} = 2.6392$ and, hence, the corresponding focal length c is given by $c = R_e\mathcal{E} = 2.5331 \times 10^7$ m, where R_e is the equatorial radius with $R_e = 7.1492 \times 10^7$ m. Thirdly, by fitting the observed profile [Seidelmann et. al., 2007] of the Jovian zonal flow to $U(s)$, which is shown in Figure 3.3(a) as a function of spheroidal latitudes η, we can compute the values of $\mathcal{D}_{2n}$ according to equations (3.16) and (3.17) in connection with the potential of the zonal flow. In the fourth step, we make use of the values of c^2, ξ_0 and $\pi G\rho$, via equation (2.28), to obtain the leading-order gravitational potential, V_{g0}, in oblate spheroidal coordinates. This is then projected onto the potential in spherical coordinates given by (3.8) to obtain the leading-order coefficients $\bar{J}_2$, $\bar{J}_4, \cdots, \bar{J}_{12}$, which are shown in Table 3.2. Finally, for given ξ_0, $\pi G\rho$ and $\mathcal{D}_{2k}$, the linear system of equations (3.32)-(3.35) can be solved for $h_0, h_2, h_4, \cdots$, which, via equation (3.18), give rise to the modified shape of Jupiter in the presence of the strong deep zonal flows. In Table 3.3, the first several $\mathcal{D}_{2k}$ and h_{2k} are presented. Inserting the values of $h_0, h_2, h_4, \cdots$, into (3.26) yields an analytical expression for the perturbation of the exterior gravitational potential V_{g1}. By further projecting $(V_{g0} + V_{g1})$ in oblate spheroidal coordinates onto (3.8) in spherical polar coordinates, we can then derive the variation of zonal gravitational coefficients ΔJ_n caused by the Jovian zonal flows.

The results of our computation, up to ΔJ_{12}, for Jupiter are given in Table 3.2. The departure from the spheroidal shape, caused by the deep zonal flow, is shown in Figure 3.3(b) as a function of spheroidal latitudes η. From Table 3.2 it is seen that the variation of J_2, the most significant coefficient in the planet's gravity field, is about $\Delta J_2/\bar{J}_2 = 0.3\%$. As a result of the latitudinally small scale of the zonal flow, it is also anticipated that $|\Delta J_4/\bar{J}_4|$ would be much greater than $|\Delta J_2/\bar{J}_2|$. In fact, the shape-driven harmonic at the 10th zonal gravity coefficient becomes larger than that of a rigidly-rotating planet, *, i.e.,* $\Delta J_{2n} \geq \bar{J}_{2n}$ when $n \geq 5$. If the zonal flow is deep and strong enough, a giant planet like Jupiter cannot be in the shape of a perfect spheroid $\xi = \xi_o$ in oblate spheroidal coordinates. In addition to the oblateness caused by the effect of rapid rotation, the deep zonal flow may induce about 6 km positive height in the equatorial region and about 8 km negative height

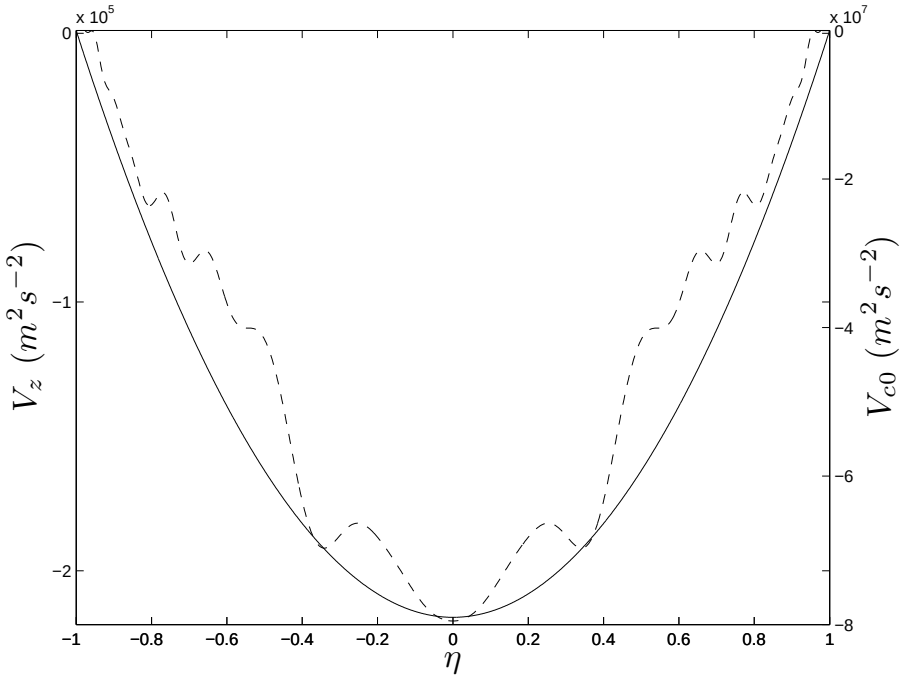

Figure 3.2: The potentials plotted against the angular coordinate η, the dashed line represents the zonal flow potential V_z curve whose vertical ticks are on the left vertical axis; the solid line depicts the centrifugal potential V_{c0} with vertical ticks on the right hand side. It is apparent that the zonal flow causes a potential two magnitudes smaller than the rotational centrifugal potential.

in polar regions, as shown in Figure 3.3(b). For Jupiter, $U_{typical}/(\Omega R_e) = 8 \times 10^{-3}$ when taking the typical speed $U_{typical} \sim 100\text{m s}^{-1}$, consistent with the assumption of the V_z expansion (3.9) in the perturbation analysis. In Figure 3.2, V_{z1} is plotted together with V_{c0}, also verify that the zonal flow only causes a small perturbation to the uniform rotation.

3.3 Summary and some remarks

If the zonal flow of a giant planet is sufficiently deep and strong, it is capable of changing its spheroidal shape and, hence, producing a significant perturbation to its exterior gravitational field. We investigate, via an analytical method using oblate spheroidal coordinates, the variation of zonal gravity coefficients caused by deep zonal flow for an arbitrarily rapidly rotating planet. In order to develop an analytical theory, we have assumed that the planet has an effective uniform density and that the zonal flow passes through the whole interior of the planet along cylinders that are parallel to the axis of rotation, as proposed by [Busse, 1976; Hubbard, 1982]. Under these assumptions, we have developed a perturbation theory that can be used to compute the variation of J_{2n} up to J_{12} for arbitrarily rapidly rotating planets that have arbitrary eccentricity and are marked by $U_{typical}/(\Omega R_e) \ll 1$. In comparison to the dynamic-related gravitational anomalies ([Hubbard, 1999; Kaspi et al., 1999]),

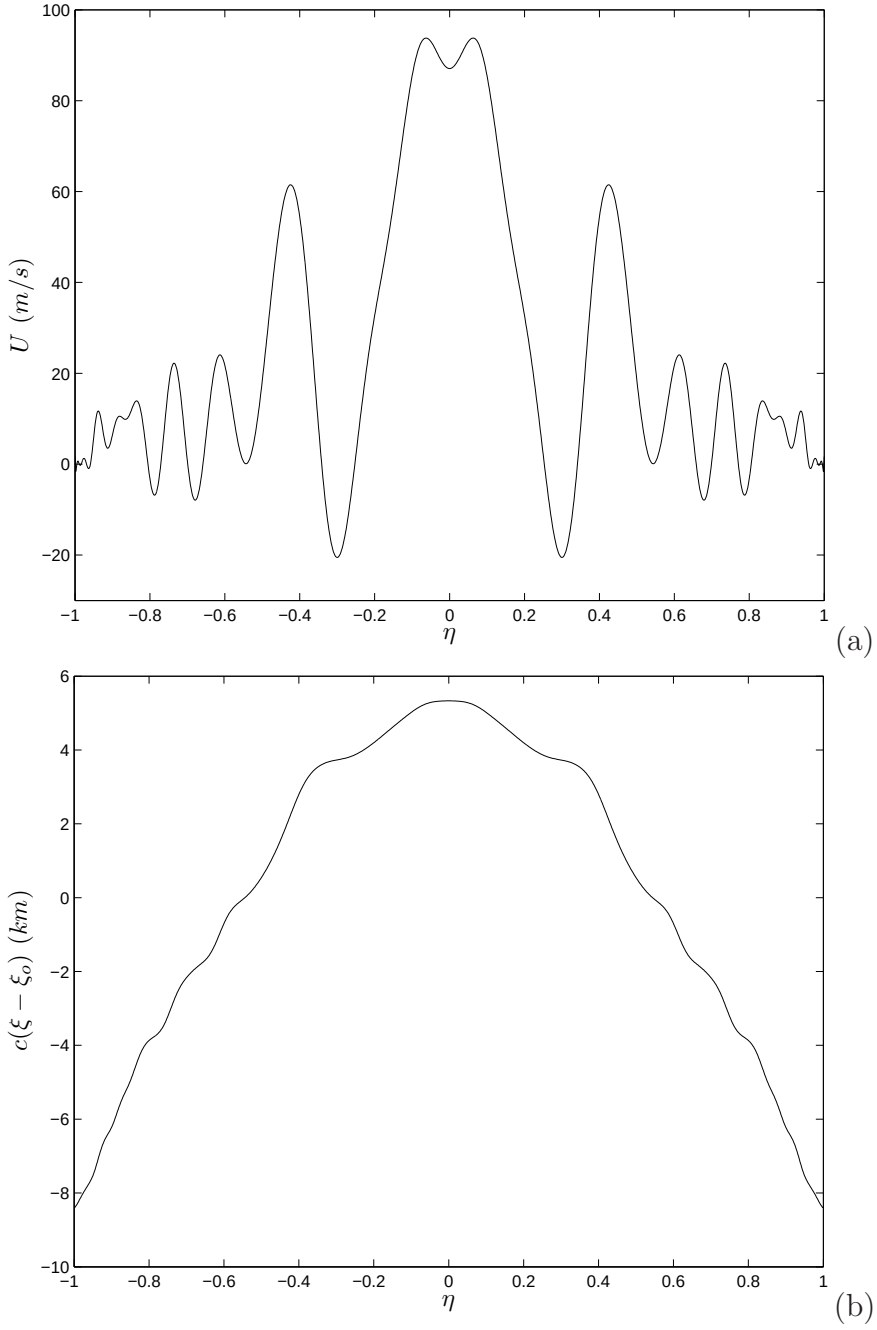

Figure 3.3: (a) The profile of the Jovian zonal flow U, fitted to the observed data, as a function of spheroidal latitudes η; (b) The corresponding dimensional departure, $c(\xi - \xi_o)$, from the shape of rigid-body rotation caused by the effect of the zonal flow.

this study is only concerned with the hydrostatic-related gravitational anomalies. It is important to point out that the changes in low-degree zonal gravitational harmonics in a rapidly rotating planet are largely dominated by the oblate shape of the planet. By taking the arbitrary oblateness, using spheroidal oblate coordinates, into the leading-order solution, we are able to accurately estimate the changes in low-degree zonal gravitational harmonics that are only induced by the effect of a differential rotation for rapidly rotating planets. In this sense, the spheroidal theory in this chapter represents a useful and significant extension comparing to the previous spherical theories.

The primary objective of our analysis is to provide a basic understanding of how the hydrostatic-related gravitational anomalies can be generated, via the distortion of the shape, by the deep zonal flows without assuming a small rotational parameter. In order to make analytical progress we have assumed the uniform density which represents a major weakness of the model, implying that all of the multipole components of the gravity potential arise from the surface shape alone. Since the density profile of Jupiter is certainly non-uniform with the outer zonal-flow region containing low-density material and since the zonal flow may not extend through the whole interior, our analysis would overestimate the variations that can be caused by the Jovian zonal flows. For a realistic Jupiter or Saturn, we must take account of both the radial variation of its density and the possible confinement of the zonal flow to the outer low-density region of the planet. In this case, an analytical approach similar to this study would be unlikely and, instead, a more complicated numerical model will be needed to offer an accurate estimate on the variation of J_{2n} caused by the Jupiter's or Saturn's zonal flow.

Chapter 4

Papkovich-Neuber Type Solution of Stokes Flow in the Exterior Domain of a Prolate Spheroid

4.1 Introduction

Coccobacillus, a bacterium having a nearly elongated spheroidal shape, can swim slowly in liquid, such as water, under the influence of viscous drag forces. The motion of swimming microorganisms is marked by a very small Reynolds number Re (see [Purcell, 1977]), a dimensionless number defined as

$$Re = \frac{U_0 a \rho}{\mu},$$

where U_0 is the typical velocity of the bacterium, ρ is the liquid density, a denotes the semi-major axis of the spheroid and μ is the dynamic viscosity of the liquid. The size of Re provides a measure of the ratio of inertial to viscous forces. Since the swimming speed U_0 is very low and its characteristic dimension a is extremely small, the Stokes' approximation (for example, see [Lamb, 1932], [Batchelor, 1967], [Shankar, 2007]), which neglects the inertial term in the Navier-Stokes equation in the limit $Re \to 0$, is usually adopted for describing the motion of microorganisms ([Koiller et al., 1996]).

Understanding the dynamics of swimming microorganisms having an elongated spheroidal shape requires mathematical solutions of the Stokes' flow in connection with the movement of a spheroid with arbitrary eccentricity in an infinite expanse of viscous and incompressible fluid. The shape of the spheroid, as depicted in Figure 4.1, may be written in the form

$$\frac{x^2}{a^2(1-\mathcal{E}^2)} + \frac{y^2}{a^2(1-\mathcal{E}^2)} + \frac{z^2}{a^2} = 1, \tag{4.1}$$

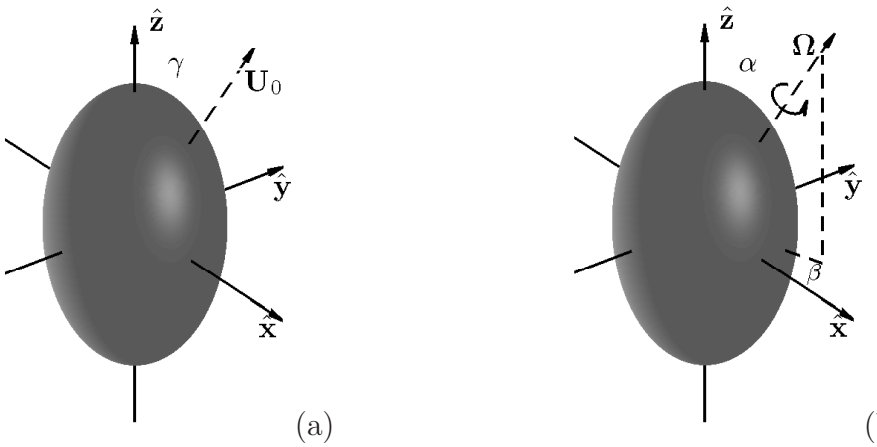

Figure 4.1: Sketch of geometry for the Stokes flow in the exterior of a prolate spheroid: (a) driven by a spheroid moving with a speed $U_0 = |\mathbf{U}_0|$ at an arbitrary angle of attack γ, and (b) driven by a rotating spheroid with an angular velocity $\mathbf{\Omega}$ marked by two rotating angles α and β. The bounding surface of the spheroid is described by (4.1) in Cartesian coordinates or by $\xi = \xi_0 = 1/\mathcal{E}$ in prolate spheroidal coordinates which is discussed in Section 4.2.

where $\mathcal{E}$ is its eccentricity with $0 < \mathcal{E} < 1$. Two different types of movement need to be considered. First, the spheroid makes slow translation in a viscous fluid and, hence, drives a small-Reynolds-number flow in its exterior, which is illustrated in Figure 4.1(a). In general, there exists an angle, γ, between the direction of translation and the symmetry axis z, which is usually referred to as angle of attack. Second, a flow can be also driven by a spheroid that is slowly rotating with an angular velocity $\mathbf{\Omega}$, which is depicted in Figure 4.1(b). Note that the angle between the symmetry axis z and the angular velocity $\mathbf{\Omega}$, denoted by α, is generally non-zero. Mathematically, the problem of the slow flow is governed by the Stokes equation and the equation of continuity,

$$\begin{cases} \mu \nabla^2 \mathbf{u} = \nabla p, \\ \nabla \cdot \mathbf{u} = 0, \end{cases} \tag{4.2}$$

where $\mathbf{u}$ is the velocity of the flow and p is the pressure, subject to the conditions that the velocity $\mathbf{u}$ coincides with the bounding surface of the spheroid at each of its points and $\mathbf{u} \to 0$ far away from the spheroid.

A classical, well-known Stokes flow is concerned with a sphere *i.e.*, $\mathcal{E} = 0$ in (4.1), that is immersed in an infinite expanse of very viscous, incompressible fluid and moving slowly (see, for example, [Batchelor, 1967]). Spherical geometry removes the angle of attack γ as a dependent parameter and allows the introduction of a two-dimensional stream function ψ satisfying

$$\left[\frac{\partial^2}{\partial r^2} + \frac{\sin\theta}{r^2} \frac{\partial}{\partial \theta} \left(\frac{1}{\sin\theta} \frac{\partial}{\partial \theta} \right) \right]^2 \psi = 0, \tag{4.3}$$

where (r, θ, ϕ), with the corresponding unit vectors $(\hat{\mathbf{r}}, \hat{\boldsymbol{\theta}}, \hat{\boldsymbol{\phi}})$, are spherical polar

coordinates with $\theta = 0$ at the direction of its movement and $r = 0$ at the center of the sphere. Upon writing the stream function ψ as

$$\psi(r, \theta) = f(r) \sin^2 \theta,$$

the fourth-order partial differential equation (4.3) for ψ can be reduced a fourth-order ordinary differential equation for $f(r)$ that can be readily solved. The similar idea was also employed to solve the Stokes problem by making use of a prolate spheroid using spheroidal coordinates, but the earlier work focused on the symmetric problem in that the symmetry axis of the spheroid and the uniform flow at distant points (or the rotation axis in the case of rotational flow) is parallel, i.e., $\gamma = 0$ or $\alpha = 0$. Detailed discussion and bibliography on the earlier work about spherical or spheroidal Stokes flows can be found in the Lamb's book ([Lamb, 1932]).

For non-spherical geometries, there are two classes of methods. What is the most commonly seen is called "Coordinates Methods", which are based on the choices of appropriate coordinate systems to facilitate separation of the variables for the body geometry in question. The most remarkable pieces of work include [Oberbeck, 1876], dating back to 1876 and [Edwardes, 1892], published in 1892. Oberbeck found the analytical solution of Stokes flow driven by a triaxial ellipsoid translating in a direction parallel to one of its axes; Edwardes solved the corresponding problem for such an ellipsoid rotating about one of its principal axes (also see [Jeffery, 1922], [Happel and Brenner, 1983] and [Lamb, 1932] for more reviews on related work in early times). All these studies are based on the use of ellipsoidal coordinates and on some complicated analyses of ellipsoidal harmonics. More recently, [Payne and Pell, 1960] considered the Stokes problem in which the configuration of various obstacles has an axis of symmetry and the uniform flow at distant points is parallel to the symmetry axis (see also, for example, [Taseli and Demiralp, 1997]). In other words, the Stokes flows around a prolate spheroid are assumed to be axisymmetric with the attack angle $\gamma = 0$ as illustrated in Figure 4.1(a). By expanding the stream function ψ in terms of the products combining Gegenbauer functions of various degrees, [Dassios and Vafeas, 2008] studied the Stokes flow passing a spheroid under the assumption that it moves parallel to the symmetry axis ($\gamma = 0$) and, hence, the flow is axisymmetric. However, by virtue of "Coordinates Methods", there hasn't been any progress in general Stokes flows, around a prolate spheroid, without good symmetry. For a non-zero angle of attack, $0 < \gamma < 90^0$, or an off-axis angular velocity, Stokes flows become fully three-dimensional and, consequently, the approach of employing a scalar stream function ψ seems to be difficult.

The other class of methods are called "Singularity Methods", which utilize such singularities as "Stokeslet" and so on. [Chwang and Wu, 1975] successfully employed a singularity method to construct exact solutions to the Stokes-flow problem for a spheroid translating or rotating in a viscous fluid, but the form of the solution

with cartesian coordinates is inconvenient for the study of our bacteria swimming problem.

Upon recognizing similarity between the governing equations for an elastic material and a Stokes flow, [Tran-Cong and Blake, 1982] applied the Papkovich-Neuber formulation ([Papkovich, 1932], [Neuber, 1934]) to the problem of Stokes flows. They showed that the general solution of the Papkovich-Neuber type for the Stokes problem (4.2) can be written in the form

$$\begin{cases} \mathbf{u} = \nabla(\mathbf{r} \cdot \mathbf{\Psi} + \chi) - 2\mathbf{\Psi}, \\ p = 2\mu(\nabla \cdot \mathbf{\Psi}), \end{cases} \tag{4.4}$$

where $\mathbf{r}$ is the position vector, $\mathbf{\Psi}$, a vector harmonic function, satisfies $\nabla^2\mathbf{\Psi} = 0$ and χ, a scalar harmonic function, is a solution to $\nabla^2\chi = 0$. They also provided a mathematical proof of the existence and completeness for the general solution (4.4). The powerful Papkovich-Neuber formulation (4.4) has been then successfully applied to the three-dimensional Stokes flow within two infinite cones with coincident apices ([Hall et al., 2009]) and to the three-dimensional Stokes flow between concentric spheres ([Shankar, 2009]). However, the Papkovich-Neuber formulation – which would produce the analytical solution in terms of prolate spheroidal coordinates appropriate for describing the swimming motion of bacteria – has not been applied to deriving a three-dimensional solution for the spheroidal Stokes flow with arbitrary angles of α, β and γ. The mathematical complication and difficulty of deriving such a solution with the Papkovich-Neuber formulation stem from both spheroidal geometry/coordinates and three-dimensionality that make the relevant analysis lengthy and cumbersome.

It is thus desirable to apply the Papkovich-Neuber formulation to deriving the three-dimensional solution that describes the Stokes flow driven by the translation of a prolate spheroid with arbitrary eccentricity $\mathcal{E}$ at an arbitrary angle γ shown in Figure 4.1(a) or driven by a rotating spheroid with arbitrary angles α and β illustrated in Figure 4.1(b). The primary objective of the present study is to obtain, via the Papkovich-Neuber formulation (4.4), an analytical three-dimensional solution for the Stokes flow driven by either a translating prolate spheroid at an arbitrary angle of attack γ or a rotating spheroid with arbitrary angles α and β in an infinite expanse of viscous and incompressible fluid. We shall also derive an expression for the corresponding drag and torque on the spheroid as a function of α, β, γ and $\mathcal{E}$. In what follows we shall begin in §4.2 by presenting briefly prolate spheroidal coordinates used in our analysis. This is followed by deriving three-dimensional solutions for the spheroidal Stokes flow in §4.3 and by obtaining an expression for the drag and torque in §4.4. The chapter closes in §4.5 with a summary and some remarks.

4.2 Prolate spheroidal coordinates

It would be helpful to provide a brief introduction to prolate spheroidal coordinates that are to be used in our analysis. Similar to the oblate spheroidal coordinates

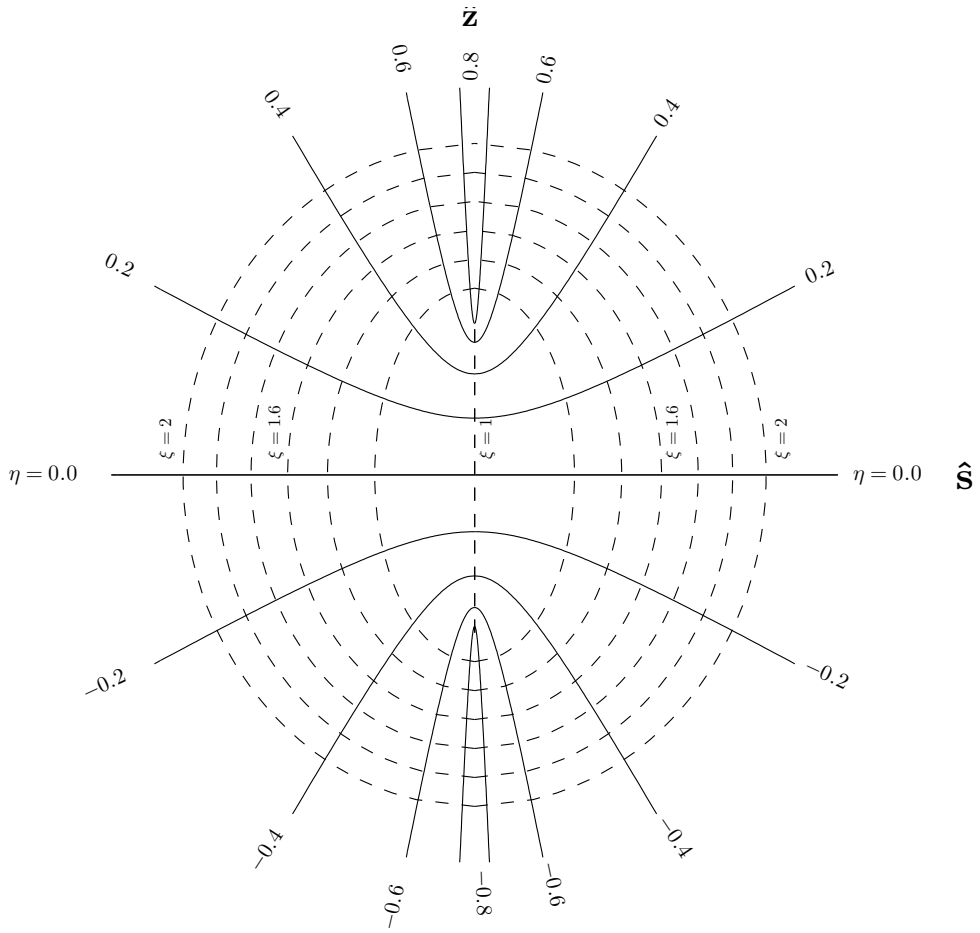

Figure 4.2: The sketch of a prolate spheroidal coordinate system at a meridional cross-section, the prolate spheroidal coordinate system can be compared with the oblate one plotted in Figure 2.2.

defined and intensively used in Chapter 2 and Chapter 3, our prolate spheroidal coordinates are defined by three sets of orthogonal level surfaces: the radial coordinate $\xi \in [1, \infty)$ characterizes spheroidal surfaces

$$\frac{z^2}{c^2\xi^2} + \frac{x^2+y^2}{c^2(\xi^2-1)} = 1,$$

the angular coordinate $\eta \in [-1, 1]$ determines hyperboloids

$$\frac{z^2}{c^2\eta^2} - \frac{x^2+y^2}{c^2(1-\eta^2)} = 1,$$

and, finally, the third coordinate is azimuthal angle ϕ which is the same as that in spherical polar coordinates. Figure 4.2 depicts the meridional cross section of the sketch of a prolate spheroidal coordinate system. Here c is the common focal

length for all the spheroids and hyperboloids, the bounding surface of the spheroid is described by $\xi = \xi_0 = 1/\mathcal{E}$ and the domain of the Stokes flow concerned in this paper is defined in $\{\xi_0 \le \xi < \infty,\ -1 \le \eta \le 1,\ 0 \le \phi \le 2\pi\}$. In the spherical limit, we have $\mathcal{E} \to 0, c \to 0$ but $c\xi_0 \to a$ along with $c\xi \to r,\ \ \eta \to \cos\theta$ and $\phi \to \phi$.

The transformation between prolate spheroid coordinates (ξ, η, ϕ) and the corresponding Cartesian coordinates (x, y, z) is given by

$$\begin{cases} x = c\sqrt{(\xi^2-1)(1-\eta^2)}\cos\phi, \\ y = c\sqrt{(\xi^2-1)(1-\eta^2)}\sin\phi, \\ z = c\xi\eta. \end{cases} \tag{4.5}$$

We shall use $(\hat{\boldsymbol{\xi}}, \hat{\boldsymbol{\eta}}, \hat{\boldsymbol{\phi}})$ to denote the unit vectors of prolate spheroid coordinates (ξ, η, ϕ) while $(\hat{\mathbf{x}}, \hat{\mathbf{y}}, \hat{\mathbf{z}})$ for the Cartesian unit vectors. With the above transformation, we can derive, for example, the following differential operators needed in our analysis:

$$\begin{aligned}
\nabla V &= \hat{\boldsymbol{\xi}}\frac{1}{c}\sqrt{\frac{\xi^2-1}{\xi^2-\eta^2}}\frac{\partial V}{\partial \xi} + \hat{\boldsymbol{\eta}}\frac{1}{c}\sqrt{\frac{1-\eta^2}{\xi^2-\eta^2}}\frac{\partial V}{\partial \eta} + \hat{\boldsymbol{\phi}}\frac{1}{c}\frac{1}{\sqrt{(\xi^2-1)(1-\eta^2)}}\frac{\partial V}{\partial \phi}, \\
\nabla^2 V &= \frac{1}{c^2(\xi^2-\eta^2)}\left\{\frac{\partial}{\partial \xi}\left[(\xi^2-1)\frac{\partial V}{\partial \xi}\right] + \frac{\partial}{\partial \eta}\left[(1-\eta^2)\frac{\partial V}{\partial \eta}\right]\right\} \\
&+ \frac{1}{c^2(\xi^2-1)(1-\eta^2)}\frac{\partial^2 V}{\partial \phi^2}, \\
\nabla\cdot\mathbf{F} &= \frac{1}{c(\xi^2-\eta^2)}\left\{\frac{\partial}{\partial \xi}\left[\hat{\boldsymbol{\xi}}\cdot\mathbf{F}\sqrt{(\xi^2-1)(\xi^2-\eta^2)}\right] + \frac{\partial}{\partial \eta}\left[\hat{\boldsymbol{\eta}}\cdot\mathbf{F}\sqrt{(1-\eta^2)(\xi^2-\eta^2)}\right]\right\} \\
&+ \frac{1}{c\sqrt{(\xi^2-1)(1-\eta^2)}}\frac{\partial}{\partial \phi}\hat{\boldsymbol{\phi}}\cdot\mathbf{F},
\end{aligned}$$

where V is a scalar function while $\mathbf{F}$ denotes a vector function.

4.3 3D spheroidal Stokes flow, drag and torque

4.3.1 Scalar and vector prolate spheroidal harmonics

The Papkovich-Neuber formulation (4.4) requires a solution to the scalar harmonic equation

$$\nabla^2\chi = 0. \tag{4.6}$$

This part of the analysis is relatively straightforward as, by standard separation of variables,

$$\chi(\xi, \eta, \phi) = \Xi(\xi)H(\eta)\Phi(\phi),$$

one can readily show that the harmonic equation (4.6) gives rise to the three equations

$$\begin{aligned}
&\frac{d}{d\xi}\left[(1-\xi^2)\frac{d\Xi}{d\xi}\right]-\frac{m^2}{1-\xi^2}\Xi+l(l+1)\Xi=0, \quad \xi>1;\\
&\frac{d}{d\eta}\left[(1-\eta^2)\frac{dH}{d\eta}\right]-\frac{m^2}{1-\eta^2}H+l(l+1)H=0, \quad -1\le\eta\le 1;\\
&\frac{d^2\Phi}{d\phi^2}+m^2\Phi=0, \quad 0\le\phi\le 2\pi,
\end{aligned}$$

whose solutions are associated with Legendre functions of the first (P_l^m) and second (Q_l^m) kind defined outside the unit circle in the complex plane. Ξ, H are so called prolate spheroidal harmonics. Applying the conditions at $\xi\to\infty$ and $\eta=\pm 1$, it can be shown that the general solution for (4.6) in terms of prolate spheroidal harmonics is

$$\chi(\xi,\eta,\phi)=\sum_{l=0}^{\infty}\sum_{m=0}^{l}(D_{lm}\cos m\phi+D'_{lm}\sin m\phi)Q_l^m(\xi)P_l^m(\eta), \quad \xi>\xi_0, \tag{4.7}$$

where D_{lm} and D'_{lm} are unknown coefficients to be determined by the non-slip condition at the bounding surface $\xi=\xi_0$.

An essential but much more difficult task is to solve the vector harmonic equation

$$\nabla^2\boldsymbol{\Psi}=0 \tag{4.8}$$

in prolate spheroidal coordinates. To derive the component form of (4.8), we have to find the identities

$$\begin{cases}
\hat{\boldsymbol{\xi}}=\xi\sqrt{\dfrac{1-\eta^2}{\xi^2-\eta^2}}\cos\phi\hat{\mathbf{x}}+\xi\sqrt{\dfrac{1-\eta^2}{\xi^2-\eta^2}}\sin\phi\hat{\mathbf{y}}+\eta\sqrt{\dfrac{\xi^2-1}{\xi^2-\eta^2}}\hat{\mathbf{z}},\\
\hat{\boldsymbol{\eta}}=-\eta\sqrt{\dfrac{\xi^2-1}{\xi^2-\eta^2}}\cos\phi\hat{\mathbf{x}}-\eta\sqrt{\dfrac{\xi^2-1}{\xi^2-\eta^2}}\sin\phi\hat{\mathbf{y}}+\xi\sqrt{\dfrac{1-\eta^2}{\xi^2-\eta^2}}\hat{\mathbf{z}},\\
\hat{\boldsymbol{\phi}}=-\sin\phi\hat{\mathbf{x}}+\cos\phi\hat{\mathbf{y}},
\end{cases} \tag{4.9}$$

and

$$\begin{aligned}
&\frac{\partial\hat{\boldsymbol{\xi}}}{\partial\xi}=\frac{\eta\sqrt{1-\eta^2}}{(\xi^2-\eta^2)\sqrt{\xi^2-1}}\hat{\boldsymbol{\eta}},\ \frac{\partial\hat{\boldsymbol{\eta}}}{\partial\xi}=-\frac{\eta\sqrt{1-\eta^2}}{(\xi^2-\eta^2)\sqrt{\xi^2-1}}\hat{\boldsymbol{\xi}},\ \frac{\partial\hat{\boldsymbol{\phi}}}{\partial\xi}=0,\\
&\frac{\partial\hat{\boldsymbol{\xi}}}{\partial\eta}=\frac{\xi\sqrt{\xi^2-1}}{(\xi^2-\eta^2)\sqrt{1-\eta^2}}\hat{\boldsymbol{\eta}},\ \frac{\partial\hat{\boldsymbol{\eta}}}{\partial\eta}=-\frac{\xi\sqrt{\xi^2-1}}{(\xi^2-\eta^2)\sqrt{1-\eta^2}}\hat{\boldsymbol{\xi}},\ \frac{\partial\hat{\boldsymbol{\phi}}}{\partial\eta}=0,\\
&\frac{\partial\hat{\boldsymbol{\xi}}}{\partial\phi}=\xi\sqrt{\frac{1-\eta^2}{\xi^2-\eta^2}}\hat{\boldsymbol{\phi}},\ \frac{\partial\hat{\boldsymbol{\eta}}}{\partial\phi}=-\eta\sqrt{\frac{\xi^2-1}{\xi^2-\eta^2}}\hat{\boldsymbol{\phi}},\\
&\frac{\partial\hat{\boldsymbol{\phi}}}{\partial\phi}=-\xi\sqrt{\frac{1-\eta^2}{\xi^2-\eta^2}}\hat{\boldsymbol{\xi}}+\eta\sqrt{\frac{\xi^2-1}{\xi^2-\eta^2}}\hat{\boldsymbol{\eta}}.
\end{aligned}\tag{4.10}$$

Then, evidently, the vector equation (4.8) can be cast into the three components in spheroidal coordinates:

$$\begin{aligned}
0 &= \nabla^2(\hat{\boldsymbol{\xi}}\cdot\boldsymbol{\Psi})-\frac{2}{c^2(\xi^2-\eta^2)}\Big[\frac{\xi^2(\xi^2-1)+(1-\eta^2)}{(\xi^2-1)(\xi^2-\eta^2)}\hat{\boldsymbol{\xi}}\cdot\boldsymbol{\Psi}\\
&+ \frac{\eta\sqrt{(\xi^2-1)(1-\eta^2)}}{\xi^2-\eta^2}\frac{\partial\hat{\boldsymbol{\eta}}\cdot\boldsymbol{\Psi}}{\partial\xi}\\
&+ \frac{\xi\sqrt{(\xi^2-1)(1-\eta^2)}}{\xi^2-\eta^2}\frac{\partial\hat{\boldsymbol{\eta}}\cdot\boldsymbol{\Psi}}{\partial\eta}-\frac{\xi\eta}{\xi^2-\eta^2}\sqrt{\frac{\xi^2-1}{1-\eta^2}}\hat{\boldsymbol{\eta}}\cdot\boldsymbol{\Psi}\\
&+ \frac{\xi}{\xi^2-1}\sqrt{\frac{\xi^2-\eta^2}{1-\eta^2}}\frac{\partial\hat{\boldsymbol{\phi}}\cdot\boldsymbol{\Psi}}{\partial\phi}\Big],
\end{aligned}\tag{4.11}$$

$$\begin{aligned}
0 &= \nabla^2(\hat{\boldsymbol{\eta}}\cdot\boldsymbol{\Psi})-\frac{1}{c^2(\xi^2-\eta^2)}\Big[\frac{(\xi^2-1)+2\eta^2(1-\eta^2)}{(1-\eta^2)(\xi^2-\eta^2)}\hat{\boldsymbol{\eta}}\cdot\boldsymbol{\Psi}\\
&- 2\eta\frac{\sqrt{(\xi^2-1)(1-\eta^2)}}{\xi^2-\eta^2}\frac{\partial\hat{\boldsymbol{\xi}}\cdot\boldsymbol{\Psi}}{\partial\xi}\\
&- 2\xi\frac{\sqrt{(\xi^2-1)(1-\eta^2)}}{\xi^2-\eta^2}\frac{\partial\hat{\boldsymbol{\xi}}\cdot\boldsymbol{\Psi}}{\partial\eta}-\frac{2\xi\eta}{\xi^2-\eta^2}\sqrt{\frac{1-\eta^2}{\xi^2-1}}\hat{\boldsymbol{\xi}}\cdot\boldsymbol{\Psi}\\
&- \frac{2\eta}{1-\eta^2}\sqrt{\frac{\xi^2-\eta^2}{\xi^2-1}}\frac{\partial\hat{\boldsymbol{\phi}}\cdot\boldsymbol{\Psi}}{\partial\phi}\Big],
\end{aligned}\tag{4.12}$$

$$\begin{aligned}
0 &= \nabla^2(\hat{\boldsymbol{\phi}}\cdot\boldsymbol{\Psi})-\frac{1}{c^2(\xi^2-\eta^2)}\Big[\frac{\xi^2-\eta^2}{(\xi^2-1)(1-\eta^2)}\hat{\boldsymbol{\phi}}\cdot\boldsymbol{\Psi}\\
&- \frac{2\xi}{\xi^2-1}\sqrt{\frac{\xi^2-\eta^2}{1-\eta^2}}\frac{\partial\hat{\boldsymbol{\xi}}\cdot\boldsymbol{\Psi}}{\partial\phi}+\frac{2\eta}{1-\eta^2}\sqrt{\frac{\xi^2-\eta^2}{\xi^2-1}}\frac{\partial\hat{\boldsymbol{\eta}}\cdot\boldsymbol{\Psi}}{\partial\phi}\Big].
\end{aligned}\tag{4.13}$$

It is clear that finding an analytical solution to (4.11)–(4.13) in prolate spheroidal coordinates is not straightforward. It is significant to note that, however, because of spheroidal geometry and the non-slip condition, all the quantities in the Papkovich-

Neuber formulation (4.4) are required to be expressed in prolate spheroidal coordinates.

After making several different attempts, it is unveiled that a mathematically convenient way of tackling (4.8) is to adopt a Cartesian system first and, then, transform it to the prolate spheroidal system by using the transformation which is the inverse of (4.9),

$$\begin{cases} \hat{\mathbf{x}} = \xi\sqrt{\dfrac{1-\eta^2}{\xi^2-\eta^2}}\cos\phi\hat{\boldsymbol{\xi}} - \eta\sqrt{\dfrac{\xi^2-1}{\xi^2-\eta^2}}\cos\phi\hat{\boldsymbol{\eta}} - \sin\phi\hat{\boldsymbol{\phi}}, \\ \hat{\mathbf{y}} = \xi\sqrt{\dfrac{1-\eta^2}{\xi^2-\eta^2}}\sin\phi\hat{\boldsymbol{\xi}} - \eta\sqrt{\dfrac{\xi^2-1}{\xi^2-\eta^2}}\sin\phi\hat{\boldsymbol{\eta}} + \cos\phi\hat{\boldsymbol{\phi}}, \\ \hat{\mathbf{z}} = \eta\sqrt{\dfrac{\xi^2-1}{\xi^2-\eta^2}}\hat{\boldsymbol{\xi}} + \xi\sqrt{\dfrac{1-\eta^2}{\xi^2-\eta^2}}\hat{\boldsymbol{\eta}}. \end{cases} \tag{4.14}$$

If we consider $\Psi = \Psi_x(\xi,\eta,\phi)\hat{\mathbf{x}} + \Psi_y(\xi,\eta,\phi)\hat{\mathbf{y}} + \Psi_z(\xi,\eta,\phi)\hat{\mathbf{z}}$, then the three components respectively satisfy the scalar harmonic equation

$$\begin{cases} \Psi_x(\xi,\eta,\phi) = \displaystyle\sum_{l=0}^{\infty}\sum_{m=0}^{l}(A_{lm}\cos m\phi + A'_{lm}\sin m\phi)Q_l^m(\xi)P_l^m(\eta), \\ \Psi_y(\xi,\eta,\phi) = \displaystyle\sum_{l=0}^{\infty}\sum_{m=0}^{l}(B_{lm}\cos m\phi + B'_{lm}\sin m\phi)Q_l^m(\xi)P_l^m(\eta), \\ \Psi_z(\xi,\eta,\phi) = \displaystyle\sum_{l=0}^{\infty}\sum_{m=0}^{l}(C_{lm}\cos m\phi + C'_{lm}\sin m\phi)Q_l^m(\xi)P_l^m(\eta). \end{cases} \tag{4.15}$$

We find that the general solution to (4.11)–(4.13) in prolate spheroidal coordinates, satisfying the conditions at $\xi \to \infty$ and $\eta = \pm 1$, is given by

$$\begin{aligned} \hat{\boldsymbol{\xi}}\cdot\boldsymbol{\Psi} &= \Psi_x\xi\sqrt{\frac{1-\eta^2}{\xi^2-\eta^2}}\cos\phi + \Psi_y\xi\sqrt{\frac{1-\eta^2}{\xi^2-\eta^2}}\sin\phi + \Psi_z\eta\sqrt{\frac{\xi^2-1}{\xi^2-\eta^2}} \\ &= \sum_l\sum_m\Big[\xi\sqrt{\frac{1-\eta^2}{\xi^2-\eta^2}}\cos\phi(A_{lm}\cos m\phi + A'_{lm}\sin m\phi) \\ &+ \xi\sqrt{\frac{1-\eta^2}{\xi^2-\eta^2}}\sin\phi(B_{lm}\cos m\phi + B'_{lm}\sin m\phi) \\ &+ \eta\sqrt{\frac{\xi^2-1}{\xi^2-\eta^2}}(C_{lm}\cos m\phi + C'_{lm}\sin m\phi)\Big]Q_l^m(\xi)P_l^m(\eta), \end{aligned} \tag{4.16}$$

$$\begin{aligned}
\hat{\boldsymbol{\eta}}\cdot\boldsymbol{\Psi} &= -\Psi_x\eta\sqrt{\frac{\xi^2-1}{\xi^2-\eta^2}}\cos\phi-\Psi_y\eta\sqrt{\frac{\xi^2-1}{\xi^2-\eta^2}}\sin\phi+\Psi_z\xi\sqrt{\frac{1-\eta^2}{\xi^2-\eta^2}}\\
&= \sum_l\sum_m\Big[-\eta\sqrt{\frac{\xi^2-1}{\xi^2-\eta^2}}\cos\phi(A_{lm}\cos m\phi+A'_{lm}\sin m\phi)\\
&- \eta\sqrt{\frac{\xi^2-1}{\xi^2-\eta^2}}\sin\phi(B_{lm}\cos m\phi+B'_{lm}\sin m\phi)\\
&+ \xi\sqrt{\frac{1-\eta^2}{\xi^2-\eta^2}}(C_{lm}\cos m\phi+C'_{lm}\sin m\phi)\Big]Q_l^m(\xi)P_l^m(\eta), \qquad (4.17)
\end{aligned}$$

$$\begin{aligned}
\hat{\boldsymbol{\phi}}\cdot\boldsymbol{\Psi} &= -\Psi_x\sin\phi+\Psi_y\cos\phi\\
&= \sum_l\sum_m\Big[-\sin\phi(A_{lm}\cos m\phi+A'_{lm}\sin m\phi\\
&+ \cos\phi(B_{lm}\cos m\phi+B'_{lm}\sin m\phi\Big]Q_l^m(\xi)P_l^m(\eta). \qquad (4.18)
\end{aligned}$$

By using the vector harmonic function $\boldsymbol{\Psi}$ given by (4.16)–(4.18), we can now derive $\mathbf{r}\cdot\Psi$ and $\nabla\cdot\boldsymbol{\Psi}$ needed in the Papkovich-Neuber formulation:

$$\begin{aligned}
\mathbf{r}\cdot\boldsymbol{\Psi} &= c\sum_{l=0}^{\infty}\sum_{m=0}^{l}\Big[\sqrt{(\xi^2-1)(1-\eta^2)}\cos\phi(A_{lm}\cos m\phi+A'_{lm}\sin m\phi)\\
&+ \sqrt{(\xi^2-1)(1-\eta^2)}\sin\phi(B_{lm}\cos m\phi+B'_{lm}\sin m\phi)\\
&+ \xi\eta(C_{lm}\cos m\phi+C'_{lm}\sin m\phi)\Big]Q_l^m(\xi)P_l^m(\eta) \qquad (4.19)
\end{aligned}$$

and

$$\begin{aligned}
\nabla\cdot\boldsymbol{\Psi} &= \frac{1}{c}\sum_{l=0}^{\infty}\sum_{m=0}^{l}\Big\{\frac{\sqrt{(\xi^2-1)(1-\eta^2)}}{\xi^2-\eta^2}\left(\xi\frac{dQ_l^m(\xi)}{d\xi}P_l^m(\eta)-\eta\frac{dP_l^m(\eta)}{d\eta}Q_l^m(\xi)\right)\\
&\times [\cos\phi(A_{lm}\cos m\phi+A'_{lm}\sin m\phi)+\sin\phi\,(B_{lm}\cos m\phi+B'_{lm}\sin m\phi)]\\
&+ \frac{1}{\xi^2-\eta^2}\left[\eta(\xi^2-1)\frac{dQ_l^m(\xi)}{d\xi}P_l^m(\eta)+\xi(1-\eta^2)\frac{dP_l^m(\eta)}{d\eta}Q_l^m(\xi)\right]\\
&\times (C_{lm}\cos m\phi+C'_{lm}\sin m\phi)-\frac{m}{\sqrt{(\xi^2-1)(1-\eta^2)}}Q_l^m(\xi)P_l^m(\eta)\\
&\times \Big[\sin\phi(-A_{lm}\sin m\phi+A'_{lm}\cos m\phi)+\cos\phi(-B_{lm}\sin m\phi\\
&+ B'_{lm}\cos m\phi)\Big]\Big\}. \qquad (4.20)
\end{aligned}$$

All coefficients in the above expressions, such as A_{lm} and A'_{lm}, have to be determined as a function of three characteristic angles α, β and γ of the problem. Our remaining task is, according to whether a prolate spheroid is in the movement of translation or rotation, to derive a three-dimensional solution for the Stokes flow by determining all the unknown coefficients.

4.3.2 Flow driven by translation at an arbitrary angle γ

Consider first a solid prolate spheroid of eccentricity $\mathcal{E}$ that moves slowly with the speed of $U_0 = |\mathbf{U}_0|$ at an angle of attack $0 < \gamma \leq 90^o$. Geometry of the problem, together with the coordinate system, is illustrated in Figure 4.1(a). Without loss of generality, we shall assume the translation velocity $\mathbf{U}_0$ has only x and z components, *i.e.*, the spheroid is always moving within xoz plane.

We are considering a spheroid translating in a vast static fluid, which leads to $\mathbf{u}(\eta, \xi \to \infty, \phi) = 0$. The no-slip boundary condition at the bounding surface of the spheroid $\xi = \xi_0$ imposes that

$$\begin{aligned}
\mathbf{u}(\eta, \xi = \xi_0, \phi) &= U_0 \sin\gamma \hat{\mathbf{x}} + U_0 \cos\gamma \hat{\mathbf{z}} \\
&= [\nabla(\mathbf{r} \cdot \boldsymbol{\Psi} + \chi) - 2\boldsymbol{\Psi}](\eta, \xi = \xi_0, \phi) \\
&= U_0 \left(\cos\gamma \sqrt{\frac{\xi_0^2 - 1}{\xi_0^2 - \eta^2}} \eta + \sin\gamma \sqrt{\frac{1 - \eta^2}{\xi_0^2 - \eta^2}} \xi_0 \cos\phi \right) \hat{\boldsymbol{\xi}} \\
&+ U_0 \left(\cos\gamma \sqrt{\frac{1 - \eta^2}{\xi_0^2 - \eta^2}} \xi_0 - \sin\gamma \sqrt{\frac{\xi_0^2 - 1}{\xi_0^2 - \eta^2}} \eta \cos\phi \right) \hat{\boldsymbol{\eta}} \\
&- U_0 (\sin\gamma \sin\phi) \hat{\boldsymbol{\phi}}, \qquad (4.21)
\end{aligned}$$

where $\nabla\chi(\eta, \xi = \xi_0, \phi)$ can be obtained from (4.7) while $\nabla\mathbf{r} \cdot \boldsymbol{\Psi}(\eta, \xi = \xi_0, \phi)$ and $\boldsymbol{\Psi}(\eta, \xi = \xi_0, \phi)$ can be derived from (4.16)–(4.19). By noticing that $P_0(\eta) = 1$,$P_1(\eta) = \eta$ and $P_1^1(\eta) = \sqrt{1 - \eta^2}$, we can deduce from (4.21) that

$$A_{lm} = A'_{lm} = B_{lm} = B'_{lm} = D_{lm} = D'_{lm} = 0, \quad \text{if } m \geq 2 \text{ and } l \geq 2.$$

In consequence, the expressions (4.8) and (4.16)–(4.20) can be simplified as

$$\begin{aligned}
\chi(\xi, \eta, \phi)/c &= D_{00} Q_0(\xi) + D_{10} Q_1(\xi) \eta \\
&\quad + (D_{11} \cos\phi + D'_{11} \sin\phi) Q_1^1(\xi) \sqrt{1 - \eta^2}, \qquad (4.22)
\end{aligned}$$

$$\begin{aligned}
\hat{\boldsymbol{\xi}}\cdot\boldsymbol{\Psi} &= \left(\xi\sqrt{\frac{1-\eta^2}{\xi^2-\eta^2}}\cos\phi A_{00}+\xi\sqrt{\frac{1-\eta^2}{\xi^2-\eta^2}}\sin\phi B_{00}+\eta\sqrt{\frac{\xi^2-1}{\xi^2-\eta^2}}C_{00}\right)Q_0(\xi)\\
&+ \left(\xi\sqrt{\frac{1-\eta^2}{\xi^2-\eta^2}}\cos\phi A_{10}+\xi\sqrt{\frac{1-\eta^2}{\xi^2-\eta^2}}\sin\phi B_{10}+\eta\sqrt{\frac{\xi^2-1}{\xi^2-\eta^2}}C_{10}\right)Q_1(\xi)\eta\\
&+ \left[\xi\sqrt{\frac{1-\eta^2}{\xi^2-\eta^2}}\cos\phi(A_{11}\cos\phi+A'_{11}\sin\phi)\right.\\
&+ \xi\sqrt{\frac{1-\eta^2}{\xi^2-\eta^2}}\sin\phi(B_{11}\cos\phi+B'_{11}\sin\phi)\\
&\left.+\eta\sqrt{\frac{\xi^2-1}{\xi^2-\eta^2}}(C_{11}\cos\phi+C'_{11}\sin\phi)\right]Q_1^1(\xi)\sqrt{1-\eta^2},
\end{aligned}\tag{4.23}$$

$$\begin{aligned}
\hat{\boldsymbol{\eta}}\cdot\boldsymbol{\Psi} &= \left(-\eta\sqrt{\frac{\xi^2-1}{\xi^2-\eta^2}}\cos\phi A_{00}-\eta\sqrt{\frac{\xi^2-1}{\xi^2-\eta^2}}\sin\phi B_{00}+\xi\sqrt{\frac{1-\eta^2}{\xi^2-\eta^2}}C_{00}\right)Q_0(\xi)\\
&+ \left(-\eta\sqrt{\frac{\xi^2-1}{\xi^2-\eta^2}}\cos\phi A_{10}-\eta\sqrt{\frac{\xi^2-1}{\xi^2-\eta^2}}\sin\phi B_{10}+\xi\sqrt{\frac{1-\eta^2}{\xi^2-\eta^2}}C_{10}\right)Q_1(\xi)\eta\\
&+ \left[-\eta\sqrt{\frac{\xi^2-1}{\xi^2-\eta^2}}\cos\phi(A_{11}\cos\phi+A'_{11}\sin\phi)\right.\\
&- \eta\sqrt{\frac{\xi^2-1}{\xi^2-\eta^2}}\sin\phi(B_{11}\cos\phi+B'_{11}\sin\phi)\\
&\left.+\xi\sqrt{\frac{1-\eta^2}{\xi^2-\eta^2}}(C_{11}\cos\phi+C'_{11}\sin\phi)\right]Q_1^1(\xi)\sqrt{1-\eta^2},
\end{aligned}\tag{4.24}$$

$$\begin{aligned}
\hat{\boldsymbol{\phi}}\cdot\boldsymbol{\Psi} &= (-\sin\phi A_{00}+\cos\phi B_{00})Q_0(\xi)+(-\sin\phi A_{10}+\cos\phi B_{10})Q_1(\xi)\eta\\
&+ [-\sin\phi(A_{11}\cos\phi+A'_{11}\sin\phi)+\cos(\phi)(B_{11}\cos\phi\\
&+ B'_{11}\sin\phi)]\,Q_1^1(\xi)\sqrt{1-\eta^2},
\end{aligned}\tag{4.25}$$

$$\begin{aligned}
\mathbf{r}\cdot\Psi/c &= \sqrt{(\xi^2-1)(1-\eta^2)}\,(\cos\phi A_{00}+\sin\phi B_{00}+\xi\eta C_{00})\,Q_0(\xi)\\
&+ \sqrt{(\xi^2-1)(1-\eta^2)}\,(\cos\phi A_{10}+\sin\phi B_{10}+\xi\eta C_{10})\,Q_1(\xi)\eta\\
&+ \left[\sqrt{(\xi^2-1)(1-\eta^2)}\cos\phi(A_{11}\cos\phi+A'_{11}\sin\phi)\right.\\
&+\sqrt{(\xi^2-1)(1-\eta^2)}\sin\phi(B_{11}\cos\phi+B'_{11}\sin\phi)\\
&\left.+\xi\eta(C_{11}\cos\phi+C'_{11}\sin\phi)\right]Q_1^1(\xi)\sqrt{1-\eta^2},
\end{aligned}\tag{4.26}$$

which now contain only 16 unknown coefficients.

To determine the 16 unknown coefficients in (4.22)–(4.25), we first look at the

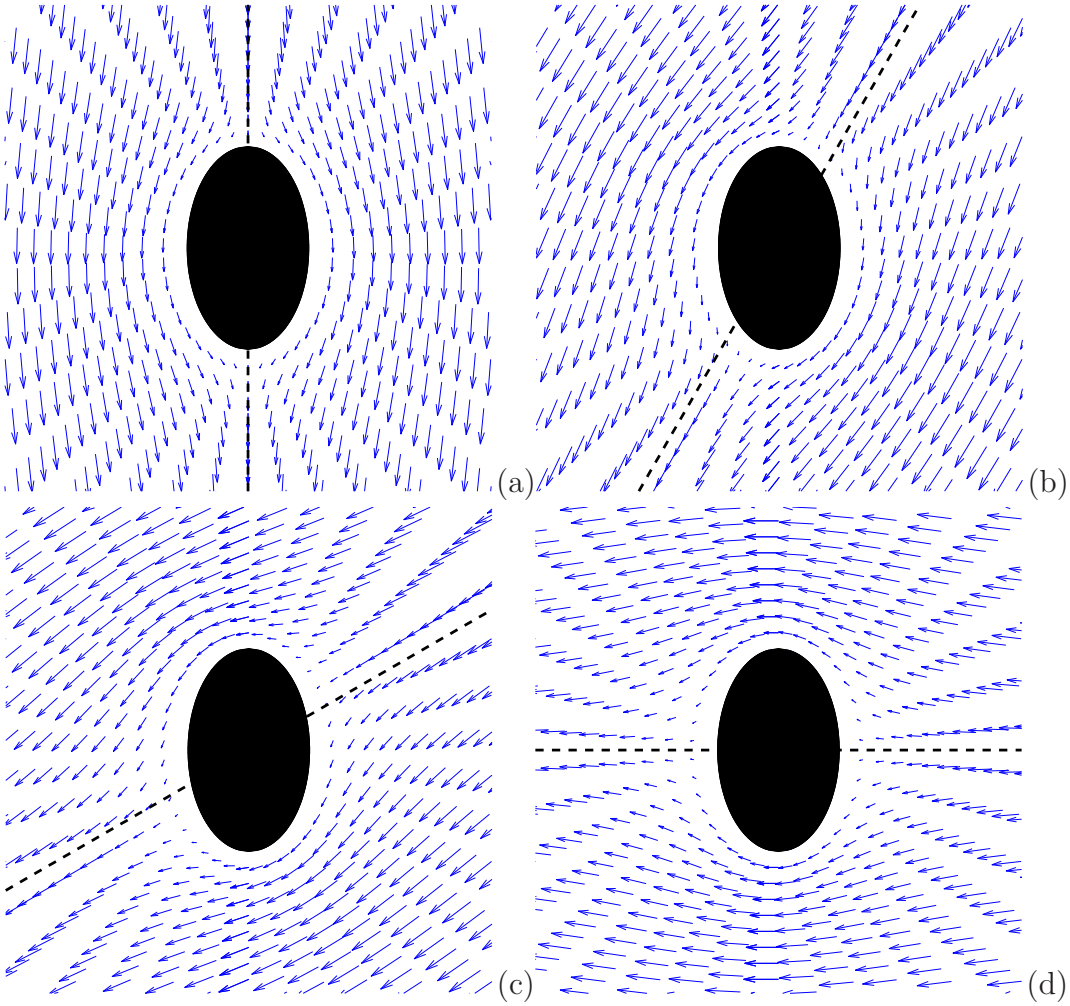

Figure 4.3: Flow structure in the $xz-$plane for a spheroid of eccentricity $\mathcal{E} = 0.8$, computed from (4.34)–(4.36), is plotted for four different angles of attack: (a) $\gamma = 0$; (b) $\gamma = 30^o$; (c) $\gamma = 60^o$; and (d) $\gamma = 90^o$. The symmetry axis of the spheroid is vertical with the dashed line indicating the direction of translation. For the sake of better presentation, we plot the flows as seen in a co-translating reference system.

azimuthal component, the simplest of the three components, of (4.21):

$$\begin{aligned}
\hat{\boldsymbol{\phi}} \cdot \mathbf{u}(\xi = \xi_o) &= \frac{1}{\sqrt{(\xi^2-1)(1-\eta^2)}} \frac{\partial}{\partial \phi} \left(\frac{\mathbf{r} \cdot \Psi + \chi}{c} \right) - 2\hat{\boldsymbol{\phi}} \cdot \boldsymbol{\Psi} \\
&= [-\sin 2\phi A_{11} + \cos(2\phi) A'_{11} + \cos 2\phi B_{11} + \sin 2\phi B'_{11}] Q_1^1(\xi) \sqrt{1-\eta^2} \\
&\quad + \frac{\xi\eta}{\sqrt{\xi^2-1}} (-C_{11} \sin\phi + C'_{11} \cos\phi) Q_1^1(\xi) \\
&\quad + \frac{1}{\sqrt{\xi^2-1}} (-D_{11} \sin\phi + D'_{11} \cos\phi) Q_1^1(\xi) \\
&\quad + (A_{00} \sin\phi - B_{00} \cos(\phi)) Q_0(\xi) + (A_{10} \sin\phi - B_{10} \cos\phi) Q_1(\xi) \eta \\
&\quad + 2[\sin\phi (A_{11} \cos\phi + A'_{11} \sin\phi) \\
&\quad - \cos\phi (B_{11} \cos\phi + B'_{11} \sin\phi)] Q_1^1(\xi) \sqrt{1-\eta^2} \\
&= U_0 \left(\sin\gamma \sin\phi \right),
\end{aligned}$$

which immediately leads to

$$A_{10} = A_{11} = A'_{11} = B_{00} = B_{10} = B_{11} = B'_{11} = C_{11} = C'_{11} = D'_{11} = 0 \tag{4.27}$$

and

$$A_{00}Q_0(\xi_0) - D_{11}\frac{Q_1^1(\xi_0)}{\sqrt{\xi_0^2-1}} = -U_0\sin\gamma. \tag{4.28}$$

In other words, of the 16 unknown coefficients in (4.22)–(4.25) ten of them are zero. Other 6 coefficients are determined by examining the $\hat{\boldsymbol{\xi}}$ and $\hat{\boldsymbol{\eta}}$ components of (4.21), which are

$$\begin{aligned}
\hat{\boldsymbol{\xi}}\cdot\mathbf{u}(\xi=\xi_o) &= \sqrt{\frac{\xi^2-1}{\xi^2-\eta^2}}\frac{\partial}{\partial\xi}\left(\frac{\mathbf{r}\cdot\Psi+\chi}{c}\right) - 2\hat{\boldsymbol{\xi}}\cdot\boldsymbol{\Psi} \\
&= \sqrt{\frac{\xi^2-1}{\xi^2-\eta^2}}\left\{\left(\xi\sqrt{\frac{1-\eta^2}{\xi^2-\eta^2}}\cos\phi A_{00} + \eta C_{00}\right)Q_0(\xi)\right. \\
&\quad + \left(\sqrt{(\xi^2-1)(1-\eta^2)}\cos\phi A_{00} + \xi\eta C_{00} + D_{00}\right)\frac{dQ_0(\xi)}{d\xi} \\
&\quad \left. + C_{10}Q_1(\xi)\eta^2 + (\xi\eta C_{10} + D_{10})\eta\frac{dQ_1(\xi)}{d\xi} + D_{11}\frac{dQ_1^1(\xi)}{d\xi}\sqrt{1-\eta^2}\cos\phi\right\} \\
&\quad -2\left(\xi\sqrt{\frac{1-\eta^2}{\xi^2-\eta^2}}\cos\phi A_{00} + \eta\sqrt{\frac{\xi^2-1}{\xi^2-\eta^2}}C_{00}\right)Q_0(\xi) \\
&- 2\eta\sqrt{\frac{\xi^2-1}{\xi^2-\eta^2}}C_{10}Q_1(\xi)\eta \\
&= U_0\left(\cos\gamma\sqrt{\frac{\xi_0^2-1}{\xi_0^2-\eta^2}}\eta + \sin\gamma\sqrt{\frac{1-\eta^2}{\xi_0^2-\eta^2}}\xi_0\cos\phi\right)
\end{aligned} \tag{4.29}$$

and

$$\begin{aligned}
\hat{\boldsymbol{\eta}}\cdot\mathbf{u}(\xi=\xi_o) &= \sqrt{\frac{1-\eta^2}{\xi^2-\eta^2}}\frac{\partial}{\partial\eta}\left(\frac{\mathbf{r}\cdot\Psi+\chi}{c}\right) - 2\hat{\boldsymbol{\eta}}\cdot\Psi \\
&= \left(-C_{00}\xi Q_0(\xi) + D_{10}Q_1(\xi)\right)\sqrt{\frac{1-\eta^2}{\xi^2-\eta^2}} \\
&+ \left(A_{00}\sqrt{\xi^2-1}Q_0(\xi) - D_{11}Q_1^1(\xi)\right)\frac{\eta\cos\phi}{\sqrt{\xi^2-\eta^2}} \\
&= U_0\left(\cos\gamma\sqrt{\frac{1-\eta^2}{\xi_0^2-\eta^2}}\xi_0 - \sin\gamma\sqrt{\frac{\xi_0^2-1}{\xi_0^2-\eta^2}}\eta\cos\phi\right).
\end{aligned} \tag{4.30}$$

From (4.29)–(4.30) we can deduce that

$$C_{10} = D_{00} = 0$$

and

$$C_{00}\left(\xi_0\frac{dQ_0(\xi_0)}{d\xi}-Q_0(\xi_0)\right)+D_{10}\frac{dQ_1(\xi_0)}{d\xi}=U_0\cos\gamma, \tag{4.31}$$

$$C_{00}\left(\xi_0\frac{dQ_0(\xi_0)}{d\xi}-Q_0(\xi_0)\right)+D_{10}\frac{dQ_1(\xi_0)}{d\xi}=U_0\cos\gamma, \tag{4.32}$$

$$A_{00}\left(\frac{\xi_0^2-1}{\xi_0}\frac{dQ_0(\xi_0)}{d\xi}-Q_0(\xi_0)\right)+D_{11}\frac{\sqrt{\xi_0^2-1}}{\xi_0}\frac{dQ_1^1(\xi_0)}{d\xi}=U_0\sin\gamma. \tag{4.33}$$

Solving the linear system of equations (4.28) and (4.31)–(4.33) gives the 4 non-zero coefficients:

$$\begin{aligned}
A_{00} &= U_0\sin\gamma\left[\frac{\xi_0^2-3}{4}\ln\frac{\xi_0+1}{\xi_0-1}-\frac{\xi_0}{2}\right]^{-1},\\
C_{00} &= U_0\cos\gamma\left[-\frac{\xi_0^2+1}{2}\ln\frac{\xi_0+1}{\xi_0-1}+\xi_0\right]^{-1},\\
D_{10} &= U_0\cos\gamma\left[\frac{\xi_0^2+1}{2\xi_0^2}\ln\frac{\xi_0+1}{\xi_0-1}-\frac{1}{\xi_0}\right]^{-1},\\
D_{11} &= U_0\sin\gamma\left[\frac{\xi_0^2-3}{2(\xi_0^2-1)}\ln\frac{\xi_0+1}{\xi_0-1}-\frac{\xi_0}{\xi_0^2-1}\right]^{-1}.
\end{aligned}$$

It follows that the explicit three-dimensional solution describing a Stokes flow driven by the translation of a prolate spheroid of arbitrary eccentricity $\mathcal{E}$ at an angle of attack γ is

$$\begin{aligned}
\frac{\hat{\boldsymbol{\xi}}\cdot\mathbf{u}}{U_0} &= \sqrt{\frac{\xi^2-1}{\xi^2-\eta^2}}\left[\frac{\frac{1}{2}\ln\frac{\xi+1}{\xi-1}+\frac{\xi}{\xi^2-1}}{\frac{\xi_0^2+1}{2}\ln\frac{\xi_0+1}{\xi_0-1}-\xi_0}+\frac{\frac{1}{2}\ln\frac{\xi+1}{\xi-1}-\frac{\xi}{\xi^2-1}}{\frac{\xi_0^2+1}{2\xi_0^2}\ln\frac{\xi_0+1}{\xi_0-1}-\frac{1}{\xi_0}}\right]\eta\cos\gamma\\
&\quad+\frac{\sqrt{1-\eta^2}}{\sqrt{\xi^2-\eta^2}}\left[\frac{-\frac{\xi}{2}\ln\frac{\xi+1}{\xi-1}-1}{\frac{\xi_0^2-3}{4}\ln\frac{\xi_0+1}{\xi_0-1}-\frac{\xi_0}{2}}+\frac{\frac{\xi}{2}\ln\frac{\xi+1}{\xi-1}-\frac{\xi^2-2}{\xi^2-1}}{\frac{\xi_0^2-3}{2(\xi_0^2-1)}\ln\frac{\xi_0+1}{\xi_0-1}-\frac{\xi_0}{\xi_0^2-1}}\right]\cos\phi\sin\gamma, \qquad (4.34)\\
\frac{\hat{\boldsymbol{\eta}}\cdot\mathbf{u}}{U_0} &= \frac{\sqrt{1-\eta^2}}{\sqrt{\xi^2-\eta^2}}\left[\frac{\frac{\xi}{2}\ln\frac{\xi+1}{\xi-1}}{\frac{\xi_0^2+1}{2}\ln\frac{\xi_0+1}{\xi_0-1}-\xi_0}+\frac{\frac{\xi}{2}\ln\frac{\xi+1}{\xi-1}-1}{\frac{\xi_0^2+1}{2\xi_0^2}\ln\frac{\xi_0+1}{\xi_0-1}-\frac{1}{\xi_0}}\right]\cos\gamma\\
&\quad+\frac{1}{\sqrt{\xi^2-\eta^2}}\left[\frac{\frac{\sqrt{\xi^2-1}}{2}\ln\frac{\xi+1}{\xi-1}}{\frac{\xi_0^2-3}{4}\ln\frac{\xi_0+1}{\xi_0-1}-\frac{\xi_0}{2}}-\frac{\frac{\sqrt{\xi^2-1}}{2}\ln\frac{\xi+1}{\xi-1}-\frac{\xi}{\sqrt{\xi^2-1}}}{\frac{\xi_0^2-3}{2(\xi_0^2-1)}\ln\frac{\xi_0+1}{\xi_0-1}-\frac{\xi_0}{\xi_0^2-1}}\right]\eta\cos\phi\sin\gamma, \qquad (4.35)\\
\frac{\hat{\boldsymbol{\phi}}\cdot\mathbf{u}}{U_0} &= \left[\frac{\frac{1}{2}\ln\frac{\xi+1}{\xi-1}}{\frac{\xi_0^2-3}{4}\ln\frac{\xi_0+1}{\xi_0-1}-\frac{\xi_0}{2}}-\frac{\frac{1}{2}\ln\frac{\xi+1}{\xi-1}-\frac{\xi}{\xi^2-1}}{\frac{\xi_0^2-3}{2(\xi_0^2-1)}\ln\frac{\xi_0+1}{\xi_0-1}-\frac{\xi_0}{\xi_0^2-1}}\right]\sin\phi\sin\gamma, \qquad (4.36)\\
\frac{p}{\mu U_0} &= -\frac{2}{c}\Bigg[\frac{\xi}{\xi^2-\eta^2}\sqrt{\frac{1-\eta^2}{\xi^2-1}}\frac{\sin\gamma}{\frac{\xi_0^2-3}{4}\ln\frac{\xi_0+1}{\xi_0-1}-\frac{\xi_0}{2}}\cos\phi\\
&\quad+\frac{\eta}{\xi^2-\eta^2}\frac{\cos\gamma}{-\frac{\xi_0^2+1}{2}\ln\frac{\xi_0+1}{\xi_0-1}+\xi_0}\Bigg]. \qquad (4.37)
\end{aligned}$$

Computed from the expressions (4.34)–(4.36), Figure 4.3 depicts flow structure in the $xz-$plane for a spheroid of eccentricity $\mathcal{E} = 0.8$ at four different angles of attack, $\gamma = 0, 30^o, 60^o$ and 90^o. It can be seen that, while the spatial axisymmetry of the flow is clearly displayed when $\gamma = 0$, the Stokes flow becomes fully three-dimensional when $\gamma \neq 0$.

It may be worth mentioning that the classical solution for spherical geometry can be recovered by taking the limits in (4.34)–(4.37),

$$\mathcal{E} \to 0, \gamma \to 0,\ c\xi_0 \to a = r_0,\ \eta \to \cos\theta,\ c\xi \to r,$$

which yield

$$\begin{cases} \hat{\mathbf{r}} \cdot \mathbf{u} = \left(\dfrac{3r_0}{2r} - \dfrac{r_0^3}{2r^3}\right) U_0 \cos\theta, \\ \hat{\boldsymbol{\theta}} \cdot \mathbf{u} = \left(\dfrac{3r_0}{4r} + \dfrac{r_0^3}{4r^3}\right) U_0 \sin\theta, \\ \hat{\boldsymbol{\phi}} \cdot \mathbf{u} = 0, \\ p = \dfrac{3}{2r^2} \mu r_0 U_0 \cos\theta, \end{cases} \tag{4.38}$$

in spherical polar coordinates, where $r_0 = a$ denotes the radius of the sphere.

4.3.3 Flow driven by rotation at arbitrary angles

Consider now the three-dimensional Stokes flow driven by a spheroid rotating with the angular velocity $\boldsymbol{\Omega}$ in the form

$$\begin{aligned} \frac{\boldsymbol{\Omega}}{\Omega_0} &= \sin\alpha\cos\beta\hat{\mathbf{x}} + \sin\alpha\sin\beta\hat{\mathbf{y}} + \cos\alpha\hat{\mathbf{z}} \\ &= \left(\sin\alpha\cos\beta\xi\sqrt{\frac{1-\eta^2}{\xi^2-\eta^2}}\cos\phi + \sin\alpha\sin\beta\xi\sqrt{\frac{1-\eta^2}{\xi^2-\eta^2}}\sin\phi + \cos\alpha\eta\sqrt{\frac{\xi^2-1}{\xi^2-\eta^2}}\right)\hat{\boldsymbol{\xi}} \\ &+ \left(-\sin\alpha\cos\beta\eta\sqrt{\frac{\xi^2-1}{\xi^2-\eta^2}}\cos\phi - \sin\alpha\sin\beta\eta\sqrt{\frac{\xi^2-1}{\xi^2-\eta^2}}\sin\phi + \cos\alpha\xi\sqrt{\frac{1-\eta^2}{\xi^2-\eta^2}}\right)\hat{\boldsymbol{\eta}} \\ &+ \left(-\sin\alpha\cos\beta\sin\phi + \sin\alpha\sin\beta\cos\phi\right)\hat{\boldsymbol{\phi}}, \end{aligned} \tag{4.39}$$

where $\alpha \in [0, \pi]$ and $\beta \in [0, 2\pi]$. The geometry of the problem, as well as the definition of α and β, is shown in Figure 4.1(b).

In this case, the no-slip boundary condition imposes the following condition at

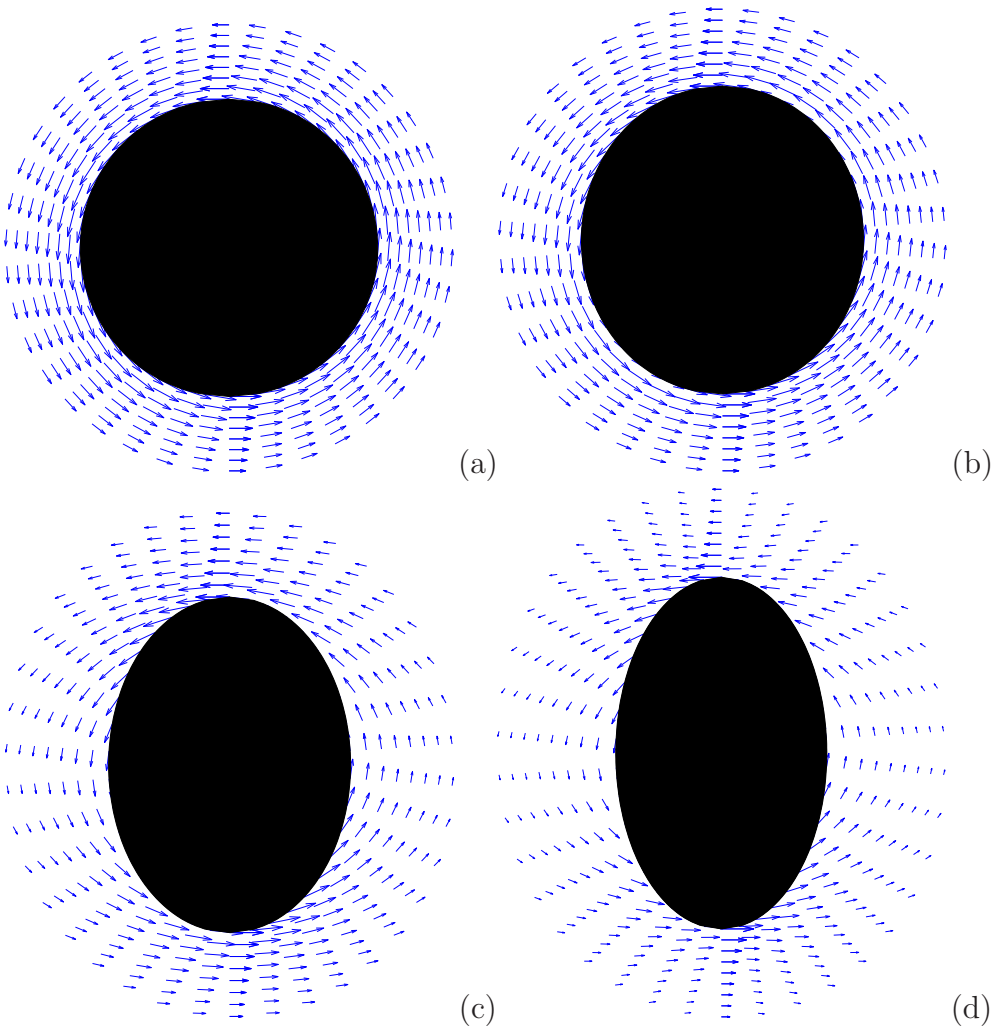

Figure 4.4: Flow structure in the plane perpendicular to, and viewed from, the axis of rotation with a spheroid of eccentricity $\mathcal{E} = 0.8$ is plotted at $\beta = 0$ for four different angles of α: (a)$\alpha = 0$, (b)$\alpha = 30$, (c)$\alpha = 60$ and (d) $\alpha = 90$.

the bounding surface, $\xi = \xi_0$, of the spheroid:

$$\begin{aligned}
\mathbf{u}(\eta, \xi = \xi_0, \phi) &= [\nabla(\mathbf{r}\cdot\boldsymbol{\Psi} + \chi) - 2\boldsymbol{\Psi}](\eta, \xi = \xi_0, \phi) \\
&= (\boldsymbol{\Omega}\times\mathbf{r})\,|_{\xi=\xi_0} \\
&= c\Omega_0\Big\{(-\sin\alpha\cos\beta\sin\phi + \sin\alpha\sin\beta\cos\phi)\eta\sqrt{\frac{1-\eta^2}{\xi_0^2-\eta^2}}\hat{\boldsymbol{\xi}} \\
&+ (\sin\alpha\cos\beta\sin\phi - \sin\alpha\sin\beta\cos\phi)\xi_0\sqrt{\frac{\xi_0^2-1}{\xi_0^2-\eta^2}}\hat{\boldsymbol{\eta}} \\
&+ \big[-(\sin\alpha\cos\beta\cos\phi + \sin\alpha\sin\beta\sin\phi)\xi_0\eta \\
&+ \cos\alpha\sqrt{(\xi_0^2-1)(1-\eta^2)}\big]\hat{\boldsymbol{\phi}}\Big\}. \qquad (4.40)
\end{aligned}$$

Here $\nabla\chi(\eta, \xi = \xi_0, \phi)$ can be obtained from (4.7), while $\nabla\mathbf{r}\cdot\boldsymbol{\Psi}(\eta, \xi = \xi_0, \phi)$ and $\boldsymbol{\Psi}(\eta, \xi = \xi_0, \phi)$ can be derived from (4.16)–(4.19). Similar to the translation problem, we can also deduce from (4.40) that

$$A_{lm} = A'_{lm} = B_{lm} = B'_{lm} = D_{lm} = D'_{lm} = 0, \ \text{ if } \ m \geq 2 \ \text{ and } \ l \geq 2.$$

It follows there exist also 16 unknown coefficients to be determined by the non-slip condition (4.40) at $\xi = \xi_o$. First, the azimuthal component of (4.40) gives rise to the equation

$$\begin{aligned}
&[-\sin 2\phi A_{11} + \cos 2\phi A'_{11} + \cos 2\phi B_{11} + \sin 2\phi B'_{11}]\,Q_1^1\xi\sqrt{1-\eta^2} \\
+\ &\frac{\xi\eta}{\sqrt{\xi^2-1}}(-C_{11}\sin\phi + C'_{11}\cos\phi)Q_1^1(\xi) + \frac{1}{\sqrt{\xi^2-1}}(-D_{11}\sin\phi + D'_{11}\cos\phi)Q_1^1(\xi) \\
+\ &(\sin\phi A_{00} - \cos\phi B_{00})Q_0(\xi) + (\sin\phi A_{10} - \cos\phi B_{10})Q_1(\xi)\eta \\
+\ &\big[\sin 2\phi A_{11} + 2\sin^2\phi A'_{11} - 2\cos^2\phi B_{11} - \sin 2\phi B'_{11}\big]\,Q_1^1\xi\sqrt{1-\eta^2} \\
=\ &c\Omega_0\big[-\sin\alpha\cos\beta\cos\phi\xi_0\eta - \sin\alpha\sin\beta\sin\phi\xi_0\eta \\
+\ &\cos\alpha\sqrt{(\xi_0^2-1)(1-\eta^2)}\big], \qquad (4.41)
\end{aligned}$$

from which we can obtain that

$$A_{00} = B_{00} = D_{11} = D'_{11} = 0$$

and

$$-B_{10}\frac{Q_1(\xi_0)}{\xi_0} + C'_{11}\frac{Q_1^1(\xi_0)}{\sqrt{\xi_0^2-1}} = -\sin\alpha\cos\beta\Omega_0 c, \qquad (4.42)$$

$$A_{10}\frac{Q_1(\xi_0)}{\xi_0} - C_{11}\frac{Q_1^1(\xi_0)}{\sqrt{\xi_0^2-1}} = -\sin\alpha\sin\beta\Omega_0 c, \qquad (4.43)$$

$$A'_{11}\frac{Q_1^1(\xi_0)}{\sqrt{\xi_0^2-1}} - B_{11}\frac{Q_1^1(\xi_0)}{\sqrt{\xi_0^2-1}} = \cos\alpha\Omega_0 c. \qquad (4.44)$$

From the $\xi-$component of (4.40), we obtain the equation

$$\begin{aligned}
&\frac{\sqrt{\xi^2-1}Q_1(\xi)}{\sqrt{\xi^2-\eta^2}}(A_{10}\cos\phi+B_{10}\sin\phi)-\frac{\xi Q_1^1(\xi)}{\sqrt{\xi^2-\eta^2}}(C_{11}\cos\phi+C'_{11}\sin\phi)\\
-\quad&\frac{C_{00}\sqrt{1-\eta^2}\xi Q_0(\xi)}{\sqrt{\xi^2-\eta^2}}+\frac{D_{10}\sqrt{1-\eta^2}Q_1(\xi)}{\sqrt{\xi^2-\eta^2}}\\
=\quad&(\sin\alpha\cos\beta\sin\phi-\sin\alpha\sin\beta\cos\phi)\xi_0\sqrt{\frac{\xi_0^2-1}{\xi_0^2-\eta^2}},
\end{aligned}$$

which, after making use of (4.42) and (4.43), leads to

$$C_{00}=D_{10}=0.$$

Finally, the $\xi-$component of (4.40) yields the equation:

$$\begin{aligned}
&\frac{1}{\sqrt{\xi^2-\eta^2}}\Big\{-\eta Q_1(\xi)\left[C_{10}\eta\sqrt{\xi^2-1}+A_{10}\xi\sqrt{1-\eta^2}\cos\phi+B_{10}\xi\sqrt{1-\eta^2}\sin\phi\right]\\
&-Q_1^1(\xi)\Big[C_{11}\eta\sqrt{\xi^2-1}\sqrt{1-\eta^2}\cos\phi+A_{11}\xi(1-\eta^2)\cos^2\phi+B'_{11}\xi(1-\eta^2)\sin^2\phi\\
&\qquad+(A'_{11}+B_{11})\xi\sin\phi\cos\phi(1-\eta^2)+C'_{11}\eta\sqrt{1-\eta^2}\sqrt{\xi^2-1}\sin\phi\Big]\\
&+D_{00}\sqrt{\xi^2-1}\frac{dQ_0(\xi)}{d\xi}+C_{10}\eta^2\xi\sqrt{\xi^2-1}\frac{dQ_1(\xi)}{d\xi}\\
+\quad&A_{10}\eta\sqrt{1-\eta^2}(\xi^2-1)\cos\phi\frac{dQ_1(\xi)}{d\xi}\\
&+B_{10}\eta\sqrt{1-\eta^2}(\xi^2-1)\sin\phi\frac{dQ_1(\xi)}{d\xi}+C_{11}\eta\sqrt{1-\eta^2}\xi\sqrt{\xi^2-1}\cos\phi\frac{dQ_1^1(\xi)}{d\xi}\\
&+C'_{11}\eta\sqrt{1-\eta^2}\xi\sqrt{\xi^2-1}\sin\phi\frac{dQ_1^1(\xi)}{d\xi}+A_{11}(\xi^2-1)(1-\eta^2)\cos^2\phi\frac{dQ_1^1(\xi)}{d\xi}\\
&+(A'_{11}+B_{11})(\xi^2-1)(1-\eta^2)\sin\phi\cos\phi\frac{dQ_1^1(\xi)}{d\xi}\\
+\quad&B'_{11}(\xi^2-1)(1-\eta^2)\sin^2\phi\frac{dQ_1^1(\xi)}{d\xi}\Big\}\\
=\quad&c\Omega\Big\{(-\sin\alpha\cos\beta\sin\phi+\sin\alpha\sin\beta\cos\phi)\eta\sqrt{\frac{1-\eta^2}{\xi_0^2-\eta^2}},
\end{aligned}$$

which gives

$$\begin{aligned}
A_{11}=B'_{11}=C_{10}=D_{00}=0,\\
A'_{11}+B_{11}=0,
\end{aligned}\tag{4.45}$$

and

$$A_{10}\left[(\xi_0^2-1)\frac{dQ_1(\xi_0)}{d\xi}-\xi_0 Q_1(\xi_0)\right] + C_{11}\sqrt{\xi_0^2-1}\left[\xi_0\frac{dQ_1^1(\xi_0)}{d\xi}-Q_1^1(\xi_0)\right] = \sin\alpha\sin\beta\Omega c, \tag{4.46}$$

$$B_{10}\left[(\xi_0^2-1)\frac{dQ_1(\xi_0)}{d\xi}-\xi_0 Q_1(\xi_0)\right] + C'_{11}\sqrt{\xi_0^2-1}\left[\frac{dQ_1^1(\xi_0)}{d\xi}-Q_1^1(\xi_0)\right] = -\sin\alpha\cos\beta\Omega c. \tag{4.47}$$

The remaining six non-zero coefficients are determined by solving the linear system of equations (4.42)–(4.47):

$$A_{10} = \sin\alpha\sin\beta\Omega c/\left(\frac{1}{2\xi_0}-\frac{\xi_0^2+1}{4\xi_0^2}\ln\frac{\xi_0+1}{\xi_0-1}\right), \tag{4.48}$$

$$A'_{11} = \cos\alpha\Omega c/\left(-\frac{2\xi_0}{\xi_0^2-1}+\ln\frac{\xi_0+1}{\xi_0-1}\right), \tag{4.49}$$

$$B_{10} = \sin\alpha\cos\beta\Omega c/\left(-\frac{1}{2\xi_0}+\frac{\xi_0^2+1}{4\xi_0^2}\ln\frac{\xi_0+1}{\xi_0-1}\right), \tag{4.50}$$

$$B_{11} = \cos\alpha\Omega c/\left(\frac{2\xi_0}{\xi_0^2-1}-\ln\frac{\xi_0+1}{\xi_0-1}\right), \tag{4.51}$$

$$C_{11} = \sin\alpha\sin\beta\Omega c/\left(\frac{\xi_0}{\xi_0^2-1}-\frac{1}{2}\frac{\xi_0^2+1}{\xi_0^2-1}\ln\frac{\xi_0+1}{\xi_0-1}\right), \tag{4.52}$$

$$C'_{11} = \sin\alpha\cos\beta\Omega c/\left(-\frac{\xi_0}{\xi_0^2-1}+\frac{1}{2}\frac{\xi_0^2+1}{\xi_0^2-1}\ln\frac{\xi_0+1}{\xi_0-1}\right). \tag{4.53}$$

Substitution of them into (4.4) yields the explicit three-dimensional solution describing the Stokes flow driven by the rotation of a prolate spheroid of arbitrary eccentricity $\mathcal{E}$ with rotating angles α and β:

$$\frac{\hat{\boldsymbol{\xi}}\cdot\mathbf{u}}{\Omega_0 c} = -\eta\sqrt{\frac{1-\eta^2}{\xi^2-\eta^2}}\left[\frac{\frac{1}{2}\ln\frac{\xi+1}{\xi-1}}{\frac{\xi_0^2+1}{4\xi_0^2}\ln\frac{\xi_0+1}{\xi_0-1}-\frac{1}{2\xi_0}}-\frac{\frac{\xi}{\xi^2-1}+\frac{1}{2}\ln\frac{\xi+1}{\xi-1}}{\frac{1}{2}\frac{\xi_0^2+1}{\xi_0^2-1}\ln\frac{\xi_0+1}{\xi_0-1}-\frac{\xi_0}{\xi_0^2-1}}\right] \times \sin\alpha\sin(\phi-\beta), \tag{4.54}$$

$$\frac{\hat{\boldsymbol{\eta}}\cdot\mathbf{u}}{\Omega_0 c} = \frac{\sqrt{\xi^2-1}}{\sqrt{\xi^2-\eta^2}}\left[\frac{\frac{1}{2}\xi\ln\frac{\xi+1}{\xi-1}-1}{\frac{\xi_0^2+1}{4\xi_0^2}\ln\frac{\xi_0+1}{\xi_0-1}-\frac{1}{2\xi_0}}-\frac{\frac{1}{2}\xi\ln\frac{\xi+1}{\xi-1}-\frac{\xi^2}{\xi^2-1}}{\frac{1}{2}\frac{\xi_0^2+1}{\xi_0^2-1}\ln\frac{\xi_0+1}{\xi_0-1}-\frac{\xi_0}{\xi_0^2-1}}\right] \times \sin\alpha\sin(\phi-\beta), \tag{4.55}$$

$$\frac{\hat{\boldsymbol{\phi}}\cdot\mathbf{u}}{\Omega_0 c} = \eta\left[\frac{\frac{1}{2}\xi\ln\frac{\xi+1}{\xi-1}-\frac{\xi^2}{\xi^2-1}}{\frac{1}{2}\frac{\xi_0^2+1}{\xi_0^2-1}\ln\frac{\xi_0+1}{\xi_0-1}-\frac{\xi_0}{\xi_0^2-1}}-\frac{\frac{1}{2}\xi\ln\frac{\xi+1}{\xi-1}-1}{\frac{\xi_0^2+1}{4\xi_0^2}\ln\frac{\xi_0+1}{\xi_0-1}-\frac{1}{2\xi_0}}\right]\sin\alpha\cos(\phi-\beta) + \frac{\frac{1}{2}\ln\frac{\xi+1}{\xi-1}-\frac{\xi}{\xi^2-1}}{\frac{1}{2}\ln\frac{\xi_0+1}{\xi_0-1}-\frac{\xi_0}{\xi_0^2-1}}\sqrt{(\xi^2-1)(1-\eta^2)}\Omega c\cos\alpha, \tag{4.56}$$

$$\frac{p}{\mu\Omega_0} = -\frac{2\eta}{\xi^2-\eta^2}\sqrt{(\xi^2-1)(1-\eta^2)}\frac{\sin\alpha\sin(\phi-\beta)}{\frac{\xi_0^2+1}{4}\ln\frac{\xi_0+1}{\xi_0-1}-\frac{\xi_0}{2}}. \tag{4.57}$$

Figure 4.4 shows the flow structure computed from (4.54)–(4.56), in the plane passing $z = 0$ and perpendicular to the axis of rotation $\mathbf{\Omega}$, with four different angles of α at $\beta = 0$ for a spheroid of eccentricity $\mathcal{E} = 0.8$. It can be seen in Figure 4.4 that, while the flow at $\alpha = 0$ is axisymmetric, it becomes fully three-dimensional when $\alpha \neq 0$.

As discussed in the previous section, the classical solution for spherical geometry can be also recovered by taking the limits $\mathcal{E} \to 0, \gamma \to 0$ and $c\xi_0 \to a = r_0$ in (4.54)–(4.57), which yield

$$\begin{aligned}
\hat{\mathbf{r}} \cdot \mathbf{u} &= 0, \\
\hat{\boldsymbol{\theta}} \cdot \mathbf{u} &= -\frac{r_0^2}{r^2}\Omega_0 r_0 \sin\alpha \sin(\phi - \beta), \\
\hat{\boldsymbol{\phi}} \cdot \mathbf{u} &= -\frac{r_0^2}{r^2}\Omega_0 r_0 \cos\theta \sin\alpha \cos(\phi - \beta) + \frac{r_0^3}{r^3}\Omega r_0 \sin\theta \cos\alpha, \\
p &= 0.
\end{aligned}$$

Since the Stokes equation (4.2) is linear, the solution of the general flow, driven by both the translation and rotation of a spheroid, can be written as a linear combination of (4.34)–(4.36) and (4.54)–(4.56).

4.4 Drag and torque

On the basis of two three-dimensional solutions given by (4.34)–(4.36)and (4.54)–(4.56), we can compute two important quantities, the drag force $\mathbf{D}$ and the torque $\mathbf{T}$ on a spheroid due to its translation and rotation. For practical applications, such as to the dynamics of swimming microorganism, it is usually useful to express components of $\mathbf{D}$ and $\mathbf{T}$ in the Cartesian coordinate system.

Consider first the drag force $\mathbf{D}$ on a translating spheroid at an angle of attack γ. We may write $\mathbf{D}$ in the form

$$\mathbf{D} = \int_S \mathbf{f}\, \mathrm{d}S = c^2\sqrt{\xi_0^2 - 1}\int_0^{2\pi}\int_{-1}^{1}\sqrt{\xi_0^2 - \eta^2}\left(f_\xi \hat{\boldsymbol{\xi}} + f_\eta \hat{\boldsymbol{\eta}} + f_\phi \hat{\boldsymbol{\phi}}\right)\mathrm{d}\eta\,\mathrm{d}\phi,$$

where $\int_S$ denotes the surface integration over the bounding surface S of a prolate spheroid, $\mathbf{f}$ in tensor notation is

$$f_i = (-p\delta_{ij} + 2\mu\sigma_{ij})n_j,$$

with n_j being unit normal at the bounding surface S and

$$\sigma_{ij} = \frac{1}{2}\left(\frac{\partial u_i}{\partial x_j} + \frac{\partial u_j}{\partial x_i}\right).$$

The below analysis, with the help of (4.10), for the tensor σ_{ij} is lengthy in prolate

spheroidal coordinates:

$$
\begin{aligned}
\nabla\mathbf{u} &= \left(\frac{\hat{\boldsymbol{\xi}}}{c}\sqrt{\frac{\xi^2-1}{\xi^2-\eta^2}}\frac{\partial}{\partial\xi}+\frac{\hat{\boldsymbol{\eta}}}{c}\sqrt{\frac{1-\eta^2}{\xi^2-\eta^2}}\frac{\partial}{\partial\eta}+\frac{\hat{\boldsymbol{\phi}}}{c}\frac{1}{\sqrt{(\xi^2-1)(1-\eta^2)}}\frac{\partial}{\partial\phi}\right)\\
&\quad\otimes\left(u_\xi\hat{\boldsymbol{\xi}}+u_\eta\hat{\boldsymbol{\eta}}+u_\phi\hat{\boldsymbol{\phi}}\right)\\
&= \frac{1}{c}\sqrt{\frac{\xi^2-1}{\xi^2-\eta^2}}\hat{\boldsymbol{\xi}}\otimes\left[\left(\frac{\partial u_\xi}{\partial\xi}-u_\eta\frac{\eta\sqrt{1-\eta^2}}{(\xi^2-\eta^2)\sqrt{\xi^2-1}}\right)\hat{\boldsymbol{\xi}}\right.\\
&\quad\left.+\left(\frac{\partial u_\eta}{\partial\xi}+u_\xi\frac{\eta\sqrt{1-\eta^2}}{(\xi^2-\eta^2)\sqrt{\xi^2-1}}\right)\hat{\boldsymbol{\eta}}+\frac{\partial u_\phi}{\partial\xi}\hat{\boldsymbol{\phi}}\right]\\
&+ \frac{1}{c}\sqrt{\frac{1-\eta^2}{\xi^2-\eta^2}}\hat{\boldsymbol{\eta}}\otimes\left[\left(\frac{\partial u_\xi}{\partial\eta}-u_\eta\frac{\xi\sqrt{\xi^2-1}}{(\xi^2-\eta^2)\sqrt{1-\eta^2}}\right)\hat{\boldsymbol{\xi}}\right.\\
&\quad\left.+\left(\frac{\partial u_\eta}{\partial\eta}+u_\xi\frac{\xi\sqrt{\xi^2-1}}{(\xi^2-\eta^2)\sqrt{1-\eta^2}}\right)\hat{\boldsymbol{\eta}}+\frac{\partial u_\phi}{\partial\eta}\hat{\boldsymbol{\phi}}\right]\\
&+ \frac{1}{c}\frac{1}{\sqrt{(\xi^2-1)(1-\eta^2)}}\hat{\boldsymbol{\phi}}\otimes\left[\left(\frac{\partial u_\xi}{\partial\phi}-u_\phi\xi\sqrt{\frac{1-\eta^2}{\xi^2-\eta^2}}\right)\hat{\boldsymbol{\xi}}\right.\\
&\quad+\left(\frac{\partial u_\eta}{\partial\phi}+u_\phi\sqrt{\frac{\xi^2-1}{\xi^2-\eta^2}}\right)\hat{\boldsymbol{\eta}}\\
&\quad\left.+\left(\frac{\partial u_\phi}{\partial\phi}+u_\xi\xi\sqrt{\frac{1-\eta^2}{\xi^2-\eta^2}}-u_\eta\eta\sqrt{\frac{\xi^2-1}{\xi^2-\eta^2}}\right)\hat{\boldsymbol{\phi}}\right], \qquad (4.58)
\end{aligned}
$$

where $\otimes$ denotes the tensor product of two vectors. On the surface of the spheroid, the normal vector $\mathbf{n}=\hat{\boldsymbol{\xi}}$ and we therefore can compute the shear stress

$$
\begin{aligned}
&\left(\nabla\mathbf{u}+\nabla\mathbf{u}^T\right)\cdot\hat{\boldsymbol{\xi}}\\
=\;&(\nabla\mathbf{u})\cdot\hat{\boldsymbol{\xi}}+\left(\hat{\boldsymbol{\xi}}^T\cdot\nabla\mathbf{u}\right)^T\\
=\;&\hat{\boldsymbol{\xi}}\frac{2}{c}\sqrt{\frac{\xi^2-1}{\xi^2-\eta^2}}\left(\frac{\partial u_\xi}{\partial\xi}-u_\eta\frac{\eta\sqrt{1-\eta^2}}{(\xi^2-\eta^2)\sqrt{\xi^2-1}}\right)\\
+\;&\hat{\boldsymbol{\eta}}\left[\frac{1}{c}\sqrt{\frac{1-\eta^2}{\xi^2-\eta^2}}\left(\frac{\partial u_\xi}{\partial\eta}-u_\eta\frac{\xi\sqrt{\xi^2-1}}{(\xi^2-\eta^2)\sqrt{1-\eta^2}}\right)\right.\\
&\left.+\frac{1}{c}\sqrt{\frac{\xi^2-1}{\xi^2-\eta^2}}\left(\frac{\partial u_\eta}{\partial\xi}+u_\xi\frac{\eta\sqrt{1-\eta^2}}{(\xi^2-\eta^2)\sqrt{\xi^2-1}}\right)\right]\\
+\;&\hat{\boldsymbol{\phi}}\left[\frac{1}{c}\frac{1}{\sqrt{(\xi^2-1)(1-\eta^2)}}\left(\frac{\partial u_\xi}{\partial\phi}-u_\phi\xi\sqrt{\frac{1-\eta^2}{\xi^2-\eta^2}}\right)+\frac{1}{c}\sqrt{\frac{\xi^2-1}{\xi^2-\eta^2}}\frac{\partial u_\phi}{\partial\xi}\right]\\
\triangleq\;&f_\xi\hat{\boldsymbol{\xi}}+f_\eta\hat{\boldsymbol{\eta}}+f_\phi\hat{\boldsymbol{\phi}}. \qquad (4.59)
\end{aligned}
$$

By virtue of the expressions for $\mathbf{u}$ given by (4.34)–(4.36) and the expression for p given by (4.37) and, then, by evaluating them at the bounding surface $\xi=\xi_0$, we

can obtain $\mathbf{f}$ as a function of η and ϕ from (4.59).

$$\begin{aligned}
\mathbf{f} &= \left\{-p+\frac{2\mu}{c}\sqrt{\frac{\xi^2-1}{\xi^2-\eta^2}}\left[\frac{\partial\hat{\boldsymbol{\xi}}\cdot\mathbf{u}}{\partial\xi}-\frac{(\hat{\boldsymbol{\eta}}\cdot\mathbf{u})\eta\sqrt{1-\eta^2}}{(\xi^2-\eta^2)\sqrt{\xi^2-1}}\right]\right\}\hat{\boldsymbol{\xi}} \\
&+ \left\{\frac{\mu}{c}\sqrt{\frac{1-\eta^2}{\xi^2-\eta^2}}\left[\frac{\partial\hat{\boldsymbol{\xi}}\cdot\mathbf{u}}{\partial\eta}-\frac{(\hat{\boldsymbol{\eta}}\cdot\mathbf{u})\xi\sqrt{\xi^2-1}}{(\xi^2-\eta^2)\sqrt{1-\eta^2}}\right]\right. \\
&+ \left.\frac{\mu}{c}\sqrt{\frac{\xi^2-1}{\xi^2-\eta^2}}\left[\frac{\partial\hat{\boldsymbol{\eta}}\cdot\mathbf{u}}{\partial\xi}+u_\xi\frac{(\hat{\boldsymbol{\xi}}\cdot\mathbf{u})\eta\sqrt{1-\eta^2}}{(\xi^2-\eta^2)\sqrt{\xi^2-1}}\right]\right\}\hat{\boldsymbol{\eta}} \\
&+ \left\{\frac{\mu}{c\sqrt{(\xi^2-1)(1-\eta^2)}}\left[\frac{\partial\hat{\boldsymbol{\xi}}\cdot\mathbf{u}}{\partial\phi}-(\hat{\boldsymbol{\phi}}\cdot\mathbf{u})\xi\sqrt{\frac{1-\eta^2}{\xi^2-\eta^2}}\right]\right. \\
&+ \left.\frac{\mu}{c}\sqrt{\frac{\xi^2-1}{\xi^2-\eta^2}}\frac{\partial\hat{\boldsymbol{\phi}}\cdot\mathbf{u}}{\partial\xi}\right\}\hat{\boldsymbol{\phi}},
\end{aligned}$$

which can be then transformed into the corresponding Cartesian coordinate

$$\begin{aligned}
\mathbf{f} &= \left\{\hat{\boldsymbol{\xi}}\cdot\mathbf{f}\sqrt{\frac{1-\eta^2}{\xi^2-\eta^2}}\xi\cos\phi-\hat{\boldsymbol{\eta}}\cdot\mathbf{f}\sqrt{\frac{\xi^2-1}{\xi^2-\eta^2}}\eta\cos\phi-\hat{\boldsymbol{\phi}}\cdot\mathbf{f}\sin\phi\right\}\hat{\mathbf{x}} \\
&+ \left\{\hat{\boldsymbol{\xi}}\cdot\mathbf{f}\sqrt{\frac{1-\eta^2}{\xi^2-\eta^2}}\xi\sin\phi-\hat{\boldsymbol{\eta}}\cdot\mathbf{f}\sqrt{\frac{\xi^2-1}{\xi^2-\eta^2}}\eta\sin\phi+\hat{\boldsymbol{\phi}}\cdot\mathbf{f}\cos\phi\right\}\hat{\mathbf{y}} \\
&+ \left\{\hat{\boldsymbol{\xi}}\cdot\mathbf{f}\eta\sqrt{\frac{\xi^2-1}{\xi^2-\eta^2}}+(\hat{\boldsymbol{\eta}}\cdot\mathbf{f})\xi\sqrt{\frac{1-\eta^2}{\xi^2-\eta^2}}\right\}\hat{\mathbf{z}}. \qquad (4.60)
\end{aligned}$$

After a further integration over the spheroidal surface, we are able to derive an analytical formula for the drag force $\mathbf{D}$ on a moving spheroid:

$$\begin{aligned}
\frac{\mathbf{D}}{2\pi\mu U_0} &= -\left[\frac{8+4(\xi_0^2-1)\left(-2+\xi_0\ln\frac{\xi_0+1}{\xi_0-1}\right)}{2\xi_0-(\xi_0^2-3)\ln\frac{\xi_0+1}{\xi_0-1}}+\frac{2\xi_0^2-\xi_0(\xi_0^2-1)\ln\frac{\xi_0+1}{\xi_0-1}}{\frac{\xi_0}{2}-\frac{\xi_0^2-3}{4}\ln\frac{\xi_0+1}{\xi_0-1}}\right]c\sin\gamma\hat{\mathbf{x}} \\
&- \left[\frac{4\xi_0^2(\xi_0^2-1)\left(2-\frac{\xi_0^2-1}{\xi_0}\ln\frac{\xi_0+1}{\xi_0-1}\right)}{2\xi_0-2\xi_0^3+(\xi_0^4-1)\ln\frac{\xi_0+1}{\xi_0-1}}+\frac{(\xi_0^2-1)\left(2-\xi_0\ln\frac{\xi_0+1}{\xi_0-1}\right)}{\frac{\xi_0}{4}-\frac{\xi_0^2+1}{4}\ln\frac{\xi_0+1}{\xi_0-1}}\right]c\cos\gamma\hat{\mathbf{z}}, \qquad (4.61)
\end{aligned}$$

which is valid for a prolate spheroid of arbitrary eccentricity $\mathcal{E}$ and for an arbitrary angle of attack γ. It can be demonstrated that the general formula (4.61) in the spherical limit $\mathcal{E}\to 0$ becomes

$$\mathbf{D}=-6\pi\mu r_0 U_0(\sin\gamma\hat{\mathbf{x}}+\cos\gamma\hat{\mathbf{z}}),$$

consistent with the classical result for a sphere.

Table 4.1 shows various values of $\mathbf{D}/(U_o\mu)$ with $a=1$, computed from formula

Table 4.1: The values of $\mathbf{D}/(U_o\mu)$ and $|\mathbf{D}|/(U_o\mu)$, computed from (4.61), for $a = 1$ and $\gamma = 30^o$ as a function of eccentricity $\mathcal{E}$.

e	$\hat{\mathbf{x}} \cdot \mathbf{D}/(U_o\mu)$	$\hat{\mathbf{z}} \cdot \mathbf{D}/(U_o\mu)$	$\lvert\mathbf{D}\rvert/(U_o\mu)$
0.9000000	-6.0965387	-8.9913082	10.8633055
0.8526842	-6.6360387	-10.1181591	12.1001716
0.8053684	-7.0631336	-11.0311030	13.0985911
0.7580526	-7.4178095	-11.8015304	13.9391542
0.7107368	-7.7201962	-12.4662984	14.6632202
0.6634211	-7.9820636	-13.0473907	15.2953503
0.6161053	-8.2109703	-13.5591593	15.8515246
0.5687895	-8.4120920	-14.0115690	16.3428075
0.5214737	-8.5891394	-14.4118497	16.7772086
0.4741579	-8.7448645	-14.7654189	17.1607182
0.4268421	-8.8813600	-15.0764333	17.4979255
0.3795263	-9.0002464	-15.3481365	17.7924065
0.3322105	-9.1027937	-15.5830878	18.0469798
0.2848947	-9.1900036	-15.7833174	18.2638789
0.2375789	-9.2626660	-15.9504341	18.4448727
0.1902632	-9.3213992	-16.0857028	18.5913506
0.1429474	-9.3666784	-16.1900982	18.7043830
0.0956316	-9.3988555	-16.2643445	18.7847647
0.0483158	-9.4181734	-16.3089426	18.8330454
0.0010000	-9.4247751	-16.3241877	18.8495488

(4.61) at the attack angle $\gamma = 30^o$, for different values of eccentricity $\mathcal{E}$. Of particular interest is that the drag force $|\mathbf{D}|$ on a spheroid with $\mathcal{E} = 0.9$ is nearly half of that for a sphere with the same polar radius. In the spherical limit $\mathcal{E} \to 0$, (4.61) gives

$$\mathbf{D}/(U_o\mu) = -9.4247780\hat{\mathbf{x}} - 16.3241943\hat{\mathbf{z}}, \quad |\mathbf{D}|/(U_o\mu) = 18.8495559.$$

Our results suggest that the drag force $|\mathbf{D}|$ on prolate spheroids of different $\mathcal{E}$ with the same polar radius attains its maximum in the spherical limit $\mathcal{E} \to 0$ at any angles of γ.

Finally, consider the torque $\mathbf{T}$ on a rotating spheroid

$$\mathbf{T} = \int_S \mathbf{r} \times \mathbf{f} \, \mathrm{d}S,$$

where $\mathbf{f}$ can be derived by using the expression (4.60) but with $\mathbf{u}$ given by (4.54)–(4.56) evaluated at the spheroidal surface $\xi = \xi_0$. After a lengthy analysis analogous

to that for the drag force, the torque $\mathbf{T}$ on a rotating spheroid is found to be

$$\begin{aligned}\mathbf{T} &= \left\{ \frac{-8\xi_0^2}{-2\xi_0+(\xi_0^2+1)\ln\frac{\xi_0+1}{\xi_0-1}} \left[\frac{2\pi(\xi_0^2-1)\tanh^{-1}\frac{1}{\xi_0}}{\xi_0} + \frac{2\pi}{3} \right] \right. \\ &- \left. \frac{2\pi}{3} \frac{(\xi_0^2-1)\left[-4+6\xi_0^2-3\xi_0(\xi_0^2-1)\ln\frac{\xi_0+1}{\xi_0-1}\right]}{-\frac{\xi_0}{2}+\frac{\xi_0^2+1}{4}\ln\frac{\xi_0+1}{\xi_0-1}} \right\} \\ &\times \Omega\mu c^3 \left(\sin\alpha\cos\beta\hat{\mathbf{x}} + \sin\alpha\sin\beta\hat{\mathbf{y}}\right) \\ &+ \frac{1}{3}\left[\frac{32\pi c^3\Omega\mu(\xi_0^2-1)}{-2\xi_0+(\xi_0^2-1)\ln\frac{\xi_0+1}{\xi_0-1}}\cos\alpha \right]\hat{\mathbf{z}}, \end{aligned} \tag{4.62}$$

which is valid for a prolate spheroid of arbitrary eccentricity $\mathcal{E}$ rotating with any angles of α and β. It can be also demonstrated that (4.62) in the spherical limit $\mathcal{E} \to 0$ ($c\xi_0 \to r_0$) gives rise to

$$\mathbf{T} = -8\pi\mu r_0^3\Omega_0(\sin\alpha\cos\beta\hat{\mathbf{x}} + \sin\alpha\sin\beta\hat{\mathbf{y}} + \cos\alpha\hat{\mathbf{z}}),$$

which is consistent with the classical result for spherical geometry.

Table 4.2 shows the various values of $\mathbf{T}/(\Omega_o\mu)$ and $|\mathbf{T}|/(\Omega_o\mu)$ for $a = 1$, computed from formula (4.62), with rotating angles $\alpha = 30^o$ and $\beta = 0$ for different values of eccentricity $\mathcal{E}$. Note that (4.62) in the spherical limit $\mathcal{E} \to 0$ with $\alpha = 30^o$ and $\beta = 0$ yields

$$\mathbf{T}/(\Omega_o\mu) = -12.5663706\hat{\mathbf{x}} - 21.7655924\hat{\mathbf{z}}, \quad |\mathbf{T}|/(\Omega_o\mu) = 25.1327412.$$

It is of interest to notice that the torque $|\mathbf{T}|$ on a spheroid with $\mathcal{E} = 0.9$ and $\alpha = 30^o$ is only about 20% of that on a sphere. Moreover, the torque $|\mathbf{T}|$ on spheroids of different $\mathcal{E}$ at any rotating angles α and β attains its maximum in the spherical limit $\mathcal{E} \to 0$.

What is also worth mentioning is that the net torque has been verified to be zero for a pure translation motion of a prolate spheroid; and the total drag force is also zero for a pure rotational motion. In other words, translation and rotation are two decoupled motions. The drag force will not produce torque to change the rotation and vice versa.

4.5 Summary and some remarks

This work is primarily motivated by the desire to understand the dynamics of slowly swimming microorganism that has the shape of an elongated prolate spheroid. On the basis of the Papkovich-Neuber formulation (4.4) together with prolate spheroidal coordinates, we have obtained, for the first time, the three-dimensional solution for the Stokes flow driven either by translation at an arbitrary angle γ or by rotation

Table 4.2: The various values of $\mathbf{T}/(\Omega_o\mu)$ and $|\mathbf{T}|/(\Omega_o\mu)$, computed from (4.62), for $a = 1$ with rotating angles $\gamma = 30^o$ and $\beta = 0$ as a function of eccentricity $\mathcal{E}$.

e	$\hat{\mathbf{x}} \cdot \mathbf{D}/(\Omega_o\mu)$	$\hat{\mathbf{z}} \cdot \mathbf{D}/(\Omega_o\mu)$	$\|\mathbf{D}\|/(\Omega\mu)$
0.9000000	-3.5254670	-3.2402146	4.7883095
0.8526842	-4.5556942	-4.8409623	6.6475007
0.8053684	-5.4994100	-6.4329125	8.4632071
0.7580526	-6.3674815	-7.9956578	10.2213191
0.7107368	-7.1661988	-9.5137719	11.9107624
0.6634211	-7.8999458	-10.9749500	13.5225246
0.6161053	-8.5721112	-12.3690549	15.0490734
0.5687895	-9.1854721	-13.6875615	16.4839995
0.5214737	-9.7423803	-14.9232064	17.8217862
0.4741579	-10.2448633	-16.0697530	19.0576543
0.4268421	-10.6946841	-17.1218265	20.1874518
0.3795263	-11.0933790	-18.0747942	21.2075751
0.3322105	-11.4422820	-18.9246770	22.1149094
0.2848947	-11.7425432	-19.6680817	22.9067842
0.2375789	-11.9951406	-20.3021503	23.5809394
0.1902632	-12.2008898	-20.8245194	24.1354991
0.1429474	-12.3604505	-21.2332907	24.5689513
0.0956316	-12.4743319	-21.5270076	24.8801329
0.0483158	-12.5428961	-21.7046388	25.0682186
0.0010000	-12.5663605	-21.7655664	25.1327137

with arbitrary angles α and β. We have also derived, using the analytical expression for the flow, two useful formulas for the drag and couple of a spheroid as a function of $\mathcal{E}$, α, β and γ.

With the formulas for the drag vector $\mathbf{D}$ given by (4.61) and the toque vector $\mathbf{T}$ given by (4.62), we are now in a position to write down the governing equations for the motion of spheroidal, magnetotactic swimming microorganism that has the shape of prolate spheroid. Since main geometric and physical parameters of the microorganism are known, we would be capable of comparing the observed trajectories of microorganism in laboratories to those computed from a dynamic model and, hence, offering some helpful insight into the complex dynamics of swimming microorganism. As introduced in Chapter 1, originally, this work was motivated by the studies of magnetotactic bacteria, which can swim along the external magnetic field lines. In the laboratory of Institute of Geophysics and Geology, Chinese Academy of Sciences, we did experiments and observed the trajectories of the motions of spheroidal bacteria under time-varying magnetic fields. The Figure 4.5 contains two typical examples of such trajectories. We also present the orbits predicted by the dynamical model incorporating our drag and torque theories. Quantitatively, the theoretical trajectories are consistent with the observations, which further validate our Stokes flow formulations. The manuscript [Cui et al.] discussing the bacteria swimming, has been submitted to *Fluid Dynamics Research* and is now in the

revision stage.

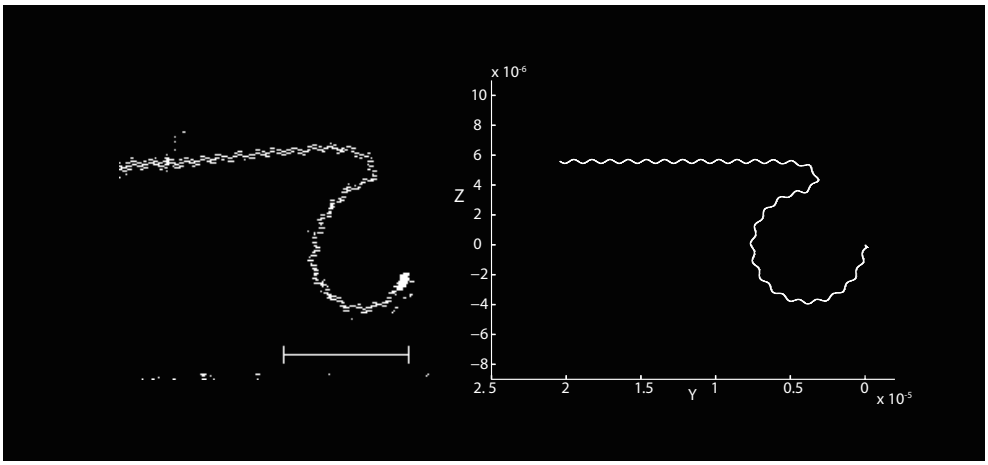

(a)

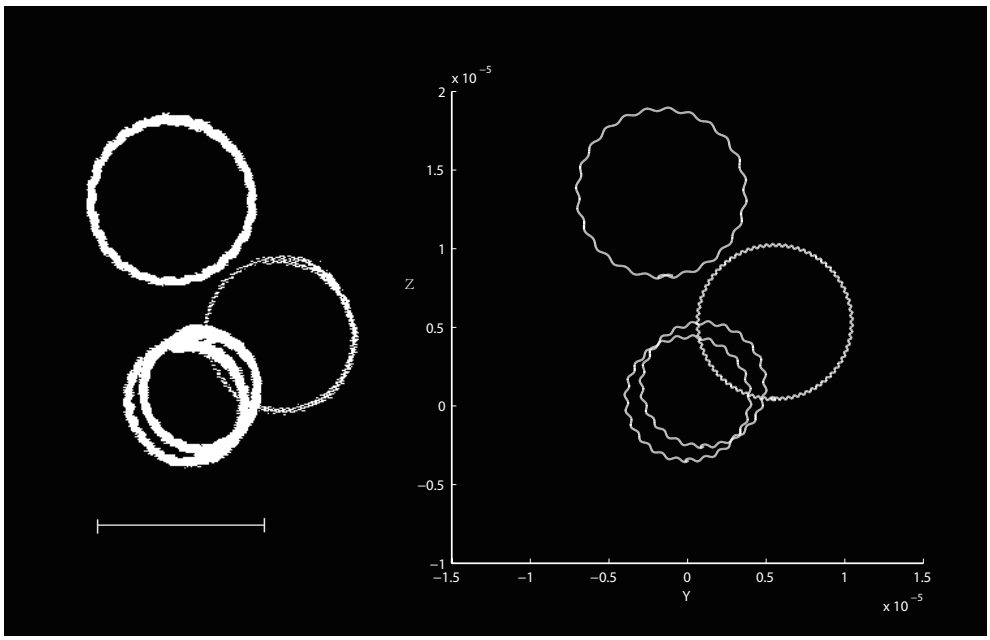

(b)

Figure 4.5: The comparison between observed and theoretical swimming paths of magnetotactic bacteria (courtesy of Z. Cui), in both panels, the left-hand-side is the realistic trajectories captured by a CCD camera while the right-hand-side is the numerical paths obtained by solving solid body dynamical equations. In both cases, the scale markers in the observed photos are $10\mu m$ in length while the units in the numerical plots are meter. The magnetic field in (a) is switched from a constant field to a rotational field. Only one bacterium is captured in the microscope; the magnetic field in (b), however, keeps rotating uniformly, bringing several bacteria into circular swimming.

Chapter 5

Fluid Flows in Precessing Narrow Annular Channels

5.1 Introduction

It has been conjectured that precessionally driven flows in the Earth's fluid core may be sufficiently strong and complex to be responsible for generating and maintaining the geomagnetic field ([Bullard, 1949]). This conjecture has been supported by laboratory and numerical experiments demonstrating that wavelike instabilities and transition to turbulent flows can occur in precessing spherical/spheroidal systems (see, for example, [Hollerbach and Kerswell, 1995; Kerswell, 1993; Malkus, 1968; Noir et al., 2001, 2003a; Tilgner, 1999; Tilgner and Busse, 2001; Vanyo et al., 1995]) and in precessing cylinders (see, for example, [Gans, 1970; Kobine, 1995; Malkus, 1989; Manasseh, 1992; Meunier et al., 2008]), by the theoretical estimate of abundant precessional energy (see, for example, [Kerswell, 1996]) and by convincing numerical experiments showing that precession-driven flows can indeed generate and sustain magnetic fields (see, for example, [Tilgner, 2005b, 2007b; Wu and Roberts, 2008, 2009]). Although the timescale of precessionally driven flows is usually much shorter compared with that of planetary convection, the persistent nature of precession makes it significant in many problems of geophysical and astrophysical fluid dynamics.

Motivated by the desire to understand the fundamental dynamics and physics, [Mason and Kerswell, 2002] carried out an important study of precessionally driven flow in planar geometry, the simplest of all existing models of the precessional problem. They consider a viscous, incompressible fluid confined between two infinitely extended parallel plane boundaries that rotate rapidly about their normal with angular velocity $\mathbf{\Omega}$ that itself precesses slowly about a horizontal axis fixed in space with angular velocity $\mathbf{\Omega}_p$. It should be noted that there is no essential loss of generality in assuming that $\mathbf{\Omega}$ is perpendicular to $\mathbf{\Omega}_p$ because any component of $\mathbf{\Omega}_p$ parallel to $\mathbf{\Omega}$ may be absorbed into a redefined $\mathbf{\Omega}$ ([Wu and Roberts, 2009]). In unbounded

planar geometry, the precessional motion of the two parallel boundaries drives flows against viscous dissipation. When the precessional rate increases, their numerical simulation shows that the precessionally driven flow changes from two-dimensional laminar to three-dimensional chaotic. To avoid the thin viscous boundary layers on the top and bottom of the plane layer, which are numerically expensive to resolve, the stress-free boundary condition is employed in their numerical study. In a further development of the same planar geometry model, [Wu and Roberts, 2008] include the effects of a self-generated magnetic field, demonstrating that, if the fluid is sufficiently electrically conducting, the precessing flow at a sufficiently large precessional rate can support dynamo action.

Motivated by possible geophysical and astrophysical applications, annular geometry has been widely employed to study/mimic fluid motion taking place in the equatorial region or low latitudes of rotating spherical shells (see, for example, [Busse, 1994; Eccles et al., 2009; Gilman, 1973; Jones et al., 2003]). There are several reasons why annular geometry has been used in modelling rotating flows. First, in comparison to either spherical-shell geometry or unbounded planar geometry, rotating annular configuration is readily experimentally realizable (see, for example, [Busse, 1994; Davies-Jones and Gilman, 1971; Eccles et al., 2009]). Second, as a consequence of rapid rotation, the key dynamics in the equatorial region would be different from that in the polar regions in rotating spherical shells. Third, the mathematical degeneracy characterizing unbounded planar geometry is removed by the presence of two lateral sidewalls (see, for example, [Davies-Jones and Gilman, 1971]). At the same time, the mathematical simplicity and clarity of planar geometry–using local cartesian coordinates–remain unchanged in annular geometry when the gap-width of an annulus is sufficiently small in comparison with its radius. This narrow-gap approximation has been usually employed in the theoretical studies of fluid dynamics in a rotating annulus (see, for example, [Busse, 2005; Davies-Jones and Gilman, 1971; Jones et al., 2003]). A major advantage of neglecting the curvature effect in a narrow annulus is that a relatively simple analytical description of fluid motion is permitted, offering a helpful insight into the essential dynamics of rotating flows (see, for example, [Busse, 2005; Liao et al., 2006]). This approximation is supported by both the numerical and experimental studies on convection in a rotating annulus, demonstrating that the primary features of the flows in a narrow-gap annulus with the curvature effect are captured by a narrow-gap annulus that uses the narrow-gap approximation to neglect the curvature effect (see, for example, [Busse, 1994; Li et al., 2008]). Although this study is primarily motivated by possible geophysical and astrophysical applications, the problem of precessionally driven flows in annular/cylindrical geometry may have industrial applications because propellant tanks in a flying spacecraft can be subject to the precessional forcing (see, for example, [Vanyo, 1993]).

The primary objective of the present study is to understand, through both asymptotic and numerical analysis, the fundamental dynamics of the precessionally driven flow of a viscous, incompressible fluid confined in a rotating narrow annulus using the narrow-gap approximation, the same geometry proposed by [Davies-Jones and Gilman, 1971] and [Gilman, 1973] (see also[Busse, 2005]). The narrow annular channel rotates rapidly about its axis of symmetry with angular velocity $\mathbf{\Omega}$ that itself precesses slowly about an axis that is fixed in space and perpendicular to $\mathbf{\Omega}$. A non-slip velocity boundary condition, appropriate for experimental studies of the problem, will be used. A major advantage of the narrow annular configuration is that it is approximately realizable in laboratory experiments ([Davies-Jones and Gilman, 1971; Gilman, 1973]). A major disadvantage of the realistic non-slip condition is that the thin Ekman boundary layers are numerically expensive to resolve. This is, however, rewarded by the benefits that the non-slip precessing solutions are directly comparable with experimental results and, perhaps more significantly, that the Ekman boundary layers associated with the non-slip condition play a central role at resonance ([Roberts and Stewartson, 1965]).

In addition to the Ekman number E and the Poincaré number ϵ in the planar precessional problem ([Mason and Kerswell, 2002; Wu and Roberts, 2008]), the existence of four rigid walls in channel geometry not only introduces a new parameter Γ, the aspect ratio of the depth to the width of a channel, but also introduces new dynamics into the precessional problem. Depending upon the size of the aspect ratio Γ, the precessing flow in a channel can be divided into three different categories: (a) a single principal inertial mode is at exact resonance with the Poincaré forcing; (b) two principal inertial modes are at exact resonance with the Poincaré forcing; and (c) multiple inertial modes are excited at non-resonance. When the precessional forcing is small, we shall derive three asymptotic expressions that describe precessionally driven flows of the three different types in a channel with the non-slip boundary condition. The asymptotic analysis was done by Prof. Keke Zhang in [Zhang et al., 2010]. We shall demonstrate that the viscous boundary layers, in connection with the non-slip boundary condition, are physically and mathematically important in determining the primary properties, such as the amplitude, of a precessing flow at exact resonance. We shall also perform 2D linear numerical analysis, conducted by Prof. Xinhao Liao also in [Zhang et al., 2010], and fully 3D nonlinear simulation, showing a satisfactory quantitative agreement between the asymptotic expressions and the numerical analyses for small and moderate Reynolds numbers. Moreover, we shall study the transition from 2D precessing flow to 3D small-scale turbulence for large Reynolds numbers, revealing a breakdown of the laminar flow to small-scale turbulence at a moderate precessional rate at exact resonance.

In what follows we shall begin by presenting the mathematical equations of the problem in §5.2. The asymptotic analysis for the three types of precessionally

driven flows is discussed briefly in §5.3 while the 2D linear numerical analysis and 3D nonlinear simulation are presented in §5.4. A summary and some remarks are given in §5.5.

5.2 Mathematical Formulation

Consider a viscous, incompressible fluid occupying an annular channel with inner radius $r_i d$, outer radius $r_o d$ and depth d. A parameter Γ is introduced to denote the aspect ratio of the channel $\Gamma = (r_o d - r_i d)/d$. When the gap of the annulus is sufficiently small, *i.e.*, $\Gamma/r_o \ll 1$, which will be referred as a narrow annular channel ([Busse, 2005]), the effect of the curvature can be neglected by using the small-gap approximation with the periodic condition along the channel ([Busse, 2005; Gilman, 1973]). The configuration of the narrow annular channel will be adopted in the present study of precessionally driven flows.

The narrow annular channel rotates rapidly with angular velocity $\hat{\mathbf{z}}\Omega$ about its axis of symmetry and precesses slowly about an axis that is perpendicular to $\hat{\mathbf{z}}$ and fixed in space, which is similar to that in the precessional problem of planar geometry ([Mason and Kerswell, 2002; Wu and Roberts, 2008]). In this article, we shall call the $\hat{\mathbf{z}}-$direction "vertical" while the $x-$ and $y-$directions, perpendicular to $\hat{\mathbf{z}}$, are termed "horizonal" ([Wu and Roberts, 2008]). We shall also adopt a frame of reference that is attached to the precessing channel and in that the boundaries of the channel are at rest (herein referred to as the body or mantle frame). In the body frame of reference, we choose a Cartesian coordinate system in which the fluid cavity of the channel is defined by $0 \le y \le \Gamma d$, $0 \le z \le d$ and $-\infty < x < \infty$. The four walls of the channel are: $y = 0$ located at one vertical wall (called "outer sidewall"), $y = \Gamma d$ at the another vertical wall (called "inner sidewall") while $z = 0$ at one horizonal wall (called "bottom") and $z = d$ at the another horizontal wall (called "top"). Moreover, the $x-$direction, which is parallel to the four walls, will be termed "azimuthal". The above terminology is introduced because of its correspondence with an annular channel under the small-gap approximation ([Busse, 2005; Gilman, 1973]). In the body frame of reference, the precessionally driven flow in an incompressible fluid is governed by the two equations (see, for example, [Greenspan, 1968])

$$\frac{\partial \mathbf{u}}{\partial t} + \mathbf{u}\cdot\nabla\mathbf{u} + 2(\Omega\hat{\mathbf{z}} + \mathbf{\Omega}_p)\times\mathbf{u} = -\frac{1}{\rho}\nabla p + \nu\nabla^2\mathbf{u} + \mathbf{r}\times[\mathbf{\Omega}_p\times(\Omega\hat{\mathbf{z}})]\,, \tag{5.1}$$

$$\nabla\cdot\mathbf{u} = 0, \tag{5.2}$$

where t is time, ρ is the fluid density, $\mathbf{\Omega}_p$ represents the precession vector which is fixed in space, p is a reduced pressure and $\mathbf{r}$ is the position vector, $\mathbf{u}$ is the three-dimensional velocity field $\mathbf{u} = (u_x, u_y, u_z)$ with the corresponding unit vectors

$(\hat{\mathbf{x}}, \hat{\mathbf{y}}, \hat{\mathbf{z}})$. The last term on the right-hand side of (5.1) is known as the Poincaré forcing which drives precessional flows against viscous dissipation. In the Cartesian coordinates attached to the channel, the precession vector $\mathbf{\Omega}_p$ is time-dependent and given by

$$\mathbf{\Omega}_p = (\epsilon\Omega)\,(\hat{\mathbf{x}}\cos\Omega t - \hat{\mathbf{y}}\sin\Omega t)\,, \tag{5.3}$$

whose amplitude is $|\mathbf{\Omega}_p| = \epsilon\Omega$. We shall employ the depth d as the length scale, Ω^{-1} as the unit of time and $\rho d^2\Omega^2$ as the unit of pressure, which lead to the dimensionless governing equations ([Mason and Kerswell, 2002; Wu and Roberts, 2008]):

$$\begin{aligned} \frac{\partial \mathbf{u}}{\partial t} + \mathbf{u}\cdot\nabla\mathbf{u} + 2\hat{\mathbf{z}}\times\mathbf{u} + \nabla p &= E\nabla^2\mathbf{u} + 2\epsilon\mathbf{u}\times(\hat{\mathbf{x}}\cos t - \hat{\mathbf{y}}\sin t) \\ &+ 2\epsilon z\,(\hat{\mathbf{x}}\cos t - \hat{\mathbf{y}}\sin t)\,, \qquad (5.4) \\ \nabla\cdot\mathbf{u} &= 0, \qquad (5.5) \end{aligned}$$

where the Ekman number, $E = \nu/\Omega d^2$, provides the measure of relative importance between the typical viscous force and the Coriolis force, and the Poincaré number $\epsilon = |\mathbf{\Omega}_p|/\Omega$ quantifies the strength of the precessional forcing ([Wu and Roberts, 2008]). In comparison with the pressure in (5.1), the pressure p in (5.4) is modified by including a potential term $\epsilon(xz\cos t - yz\sin t)$ from the Poincaré forcing. We shall also introduce the Reynolds number Re ([Meunier et al., 2008]) defined as

$$Re = \frac{(\epsilon\Omega)d^2}{\nu} = \frac{\epsilon}{E}.$$

In the body frame, the flow on the bounding surface of a precessing channel is at rest, which requires

$$\hat{\mathbf{n}}\cdot\mathbf{u} = \hat{\mathbf{n}}\times\mathbf{u} = 0 \tag{5.6}$$

on the four boundaries of a channel – the bottom at $z = 0$, the top at $z = 1$, the outer sidewall at $y = 0$ and the inner sidewall at $y = \Gamma$ – where $\hat{\mathbf{n}}$ denotes the unit normal of the bounding surface. The problem defined by (5.4)-(5.5) subject to the boundary conditions (5.6) will be solved asymptotically for an arbitrarily small but fixed E with small and moderate Reynolds numbers in §3 and numerically for both weakly and strongly precessing flows in §4.

5.3 Asymptotic analysis

When the Poincaré number ϵ is sufficiently small at a fixed small E, we may assume that the higher-order terms in (5.4), $\mathbf{u}\cdot\nabla\mathbf{u}$ and $\epsilon\mathbf{u}\times(\hat{\mathbf{x}}\cos t - \hat{\mathbf{y}}\sin t)$, can be neglected, leading to

$$\frac{\partial \mathbf{u}}{\partial t} + 2\hat{\mathbf{z}}\times\mathbf{u} + \nabla p = E\nabla^2\mathbf{u} + 2\epsilon z\,(\hat{\mathbf{x}}\cos t - \hat{\mathbf{y}}\sin t)\,, \tag{5.7}$$

$$\nabla \cdot \mathbf{u} = 0, \tag{5.8}$$

solutions of which, as we shall demonstrate later, provide a satisfactory quantitative agreement with the fully nonlinear solutions in the range $0 < Re \leq \mathrm{O}(10^2)$ for the exactly resonant precessing flow and in the range $0 < Re \leq \mathrm{O}(10^3)$ for the non-resonant flow. Because the asymptotic analysis was done by Prof. Keke Zhang (see [Zhang et al., 2010]), in this thesis, we only include selected formulations and expressions for a better presentation of the physical aspect of the dynamics.

In the asymptotic analysis, we postulate the following underlying physics and dynamics for a weakly precessing flow in a channel: the precessing flow can be approximated by either a single inviscid inertial mode or several inviscid inertial modes which is/are selected by a combined influence of the geometric factor (Γ) and the spatial-temporal structure of the Poincaré forcing, modified by viscous effects mainly via the viscous boundary layers on the four bounding surfaces and energetically driven by precession against viscous dissipation. It follows that our asymptotic analysis with the non-slip boundary condition will be based on three hypotheses: (i) the weakly precessing flow is oscillatory and axisymmetric ($\partial/\partial x = 0$) since the Poincaré forcing, the final term in (5.4), is oscillatory and independent of the azimuthal variable x; (ii) the leading-order interior precessing flow can be represented by either a single inertial mode or by a combination of several inertial modes whose explicit analytical expressions in the inviscid limit are available; and (iii) there exist strong viscous boundary layers on the bounding surface of the channel that either control (in the case of resonant excitation) or modify (in the case of non-resonant excitation) the leading-order precessing flow. In connection with hypothesis (ii), an axisymmetric inertial mode in the inviscid limit is governed by the two equations

$$2i\sigma_{jn}\mathbf{u}_{jn} + 2\hat{\mathbf{z}}\times\mathbf{u}_{jn} + \nabla p_{jn} = 0, \tag{5.9}$$

$$\nabla \cdot \mathbf{u}_{jn} = 0, \tag{5.10}$$

where $i = \sqrt{-1}$ and σ_{jn} is the half-frequency of an inertial mode, subject to the condition of vanishing normal flow

$$\hat{\mathbf{n}} \cdot \hat{\mathbf{u}}_{jn} = 0 \tag{5.11}$$

at the bounding surface of the channel. Two integer numbers, j and n, describe the radial and vertical structure of an inertial mode, respectively. The half-frequency of an axisymmetric inertial mode in (5.9), σ_{jn}, is given by

$$\sigma_{jn} = \frac{n}{\sqrt{n^2 + (j/\Gamma)^2}}, \quad \text{for} \quad j = 1, 2, \cdots; n = \pm 1, \pm 2, \cdots, \tag{5.12}$$

satisfying the bound $0 < |\sigma_{jn}| < 1$ (see, for example,[Liao and Zhang, 2009]), while

explicit solutions for the pressure p_{jn} and the velocity $\mathbf{u}_{jn}$ can be written in the complex form

$$p_{jn}(y,z) = \cos\left(\frac{j\pi y}{\Gamma}\right)\cos n\pi z, \tag{5.13}$$

$$\hat{\mathbf{x}}\cdot\mathbf{u}_{jn}(y,z) = \frac{j\pi}{2\Gamma(1-\sigma_{jn}^2)}\left[\sin\left(\frac{j\pi y}{\Gamma}\right)\cos n\pi z\right], \tag{5.14}$$

$$\hat{\mathbf{y}}\cdot\mathbf{u}_{jn}(y,z) = \frac{i\sigma_{jn}j\pi}{2\Gamma(1-\sigma_{jn}^2)}\left[\sin\left(\frac{j\pi y}{\Gamma}\right)\cos n\pi z\right], \tag{5.15}$$

$$\hat{\mathbf{z}}\cdot\mathbf{u}_{jn}(y,z) = -\frac{in\pi}{2\sigma_{jn}}\left[\cos\left(\frac{j\pi y}{\Gamma}\right)\sin n\pi z\right]. \tag{5.16}$$

In (5.13)-(5.16), the aspect ratio Γ represents a key parameter in controlling the primary character of precessionally driven flows. We shall concentrate on the regime of moderate aspect ratio with $E^{1/2} \ll \Gamma \leq \mathrm{O}(1)$.

It follows that, as the aspect ratios Γ varies at a fixed small E, precessionally driven flows may be divided into three different categories: (i) the single-inertial-mode resonance at $\Gamma = \sqrt{3}$ where only a single inertial mode $(j = 3, n = 1)$ is significant at exact resonance, for which the higher modes like $(j = 9, n = 3)$ make a negligible contribution, (ii) the double-inertial-mode resonance at $\Gamma = 1/\sqrt{3}$ where two principal inertial modes, $(j = 1, n = 1)$ and $(j = 3, n = 3)$, are significant at exact resonance with the Poincaré forcing, and (iii) multiple-inertial-mode excitation at non-resonance when $|\Gamma - 1/\sqrt{3}| \gg E^{1/2}$ or $|\Gamma - \sqrt{3}| \gg E^{1/2}$, in which a large number of inertial modes may be excited by the Poincaré forcing. We shall not consider the weak resonance taking place when $\Gamma \gg 1$ with large values of n and j. Evidently, the simplest asymptotic solution is offered by the single-mode resonance at $\Gamma = \sqrt{3}$, which will be discussed first.

5.3.1 Single-inertial-mode resonance

In a precessing channel with aspect ratio $\Gamma = \sqrt{3}$, an asymptotic solution $\mathbf{u}$ for a weakly precessing flow with $\epsilon \ll 1$ at a fixed small E can be, following the three hypotheses, separated into a single-inertial-mode interior flow $\mathbf{u}_{31}$ and the corresponding boundary-layer correction $\widetilde{\mathbf{u}}_{31}$, together with a weak geostrophic flow $\mathbf{u}_G$. An asymptotic expansion for the velocity $\mathbf{u}$ and the reduced pressure p takes the form

$$\mathbf{u}(y,z,t) = [(\mathbf{u}_G + \widetilde{\mathbf{u}}_G) + (\mathcal{C}_{31}\mathbf{u}_{31} + \hat{\mathbf{u}}) + \widetilde{\mathbf{u}}_{31}]\,\mathrm{e}^{it}, \tag{5.17}$$

$$p(y,z,t) = [(p_G + \widetilde{p}_G) + (\mathcal{C}_{31}p_{31} + \hat{p}) + \widetilde{p}_{31}]\,\mathrm{e}^{it}, \tag{5.18}$$

where $\mathcal{C}_{31}$ is an unknown complex number to be determined in the second-order problem, $|\mathbf{u}_G| = \mathrm{O}(\epsilon)$ denotes the interior geostrophic flow while $|\widetilde{\mathbf{u}}_G| = \mathrm{O}(\epsilon)$ corresponds

to its boundary correction, the single inertial mode $(\mathbf{u}_{31}, p_{31})$ for the interior precessing flow, given by (5.13)-(5.16) with $j = 3$ and $n = 1$ and with $|\mathcal{C}_{31}\mathbf{u}_{31}| = \mathrm{O}(\epsilon/E^{1/2})$, is corrected by the viscous boundary layer $(\widetilde{\mathbf{u}}_{31}, \widetilde{p}_{31})$ with $|\widetilde{\mathbf{u}}_{31}| = \mathrm{O}(\epsilon/E^{1/2})$, which generates, through the boundary flux, the secondary interior flow, $(\hat{\mathbf{u}}, \hat{p})$, where $|\hat{\mathbf{u}}| = \mathrm{O}(\epsilon)$. The interior geostrophic flow, $\mathbf{u}_G$, is independent of z [see, for example, Greenspan, 1968].

An analytical expression for the weakly precessing flow at exact resonance satisfying the non-slip boundary condition is then obtained:

$$
\begin{aligned}
\mathbf{u} &= (\mathbf{u}_G + \widetilde{\mathbf{u}}_G) - \frac{96(\epsilon/\sqrt{E})\mathrm{e}^{it}}{\pi^4\left\{9\sqrt{2}[(1+\sqrt{3})+(1-\sqrt{3})i]+32\sqrt{3}\pi^2\sqrt{E}\right\}} \\
&\times \left\{\left(\frac{\pi\sin\sqrt{3}\pi y}{2\sqrt{3}}\right)\left\{\left[4\cos\pi z - \exp\left(-\frac{\sqrt{6}(1+i)z}{2\sqrt{E}}\right) - 3\exp\left(-\frac{\sqrt{2}(1-i)z}{2\sqrt{E}}\right)\right.\right.\right. \\
&+ \left.\left.\left. \exp\left(-\frac{\sqrt{6}(1+i)(1-z)}{2\sqrt{E}}\right) + 3\exp\left(-\frac{\sqrt{2}(1-i)(1-z)}{2\sqrt{E}}\right)\right]\hat{\mathbf{x}}\right.\right. \\
&+ i\left[2\cos\pi z + \exp\left(-\frac{\sqrt{6}(1+i)z}{2\sqrt{E}}\right) - 3\exp\left(-\frac{\sqrt{2}(1-i)z}{2\sqrt{E}}\right)\right. \\
&- \left.\left. \exp\left(-\frac{\sqrt{6}(1+i)(1-z)}{2\sqrt{E}}\right) + 3\exp\left(-\frac{\sqrt{2}(1-i)(1-z)}{2\sqrt{E}}\right)\right]\hat{\mathbf{y}}\right\} - i\pi\sin\pi z \\
&\times \left[\cos\sqrt{3}\pi y - \exp\left(-\frac{\sqrt{2}(1+i)y}{2\sqrt{E}}\right) + \exp\left(-\frac{\sqrt{2}(1+i)(\Gamma-y)}{2\sqrt{E}}\right)\right]\hat{\mathbf{z}}\Bigg\}, \qquad (5.19)
\end{aligned}
$$

which is valid for moderate values of the Reynolds number Re for $\Gamma = \sqrt{3}$. Note that the real part of (5.19) represents the required asymptotic solution for the precessing flow.

In the asymptotic solution (5.19), the oscillatory geostrophic flow satisfying the non-slip boundary condition can be derived by a similar procedure. The leading-order expression takes the form:

$$
\begin{aligned}
\mathbf{u}_G + \widetilde{\mathbf{u}}_G &= \frac{i\epsilon}{2}\left\{\left[-2 + \exp\left(-\frac{\sqrt{6}(1+i)z}{2\sqrt{E}}\right) + \exp\left(-\frac{\sqrt{2}(1-i)z}{2\sqrt{E}}\right)\right.\right. \\
&+ \left.\left. \exp\left(-\frac{\sqrt{6}(1+i)(1-z)}{2\sqrt{E}}\right) + \exp\left(-\frac{\sqrt{2}(1-i)(1-z)}{2\sqrt{E}}\right)\right]\hat{\mathbf{x}}\right. \\
&+ i\left[-\exp\left(-\frac{\sqrt{6}(1+i)z}{2\sqrt{E}}\right) + \exp\left(-\frac{\sqrt{2}(1-i)z}{2\sqrt{E}}\right)\right. \\
&- \left.\left. \exp\left(-\frac{\sqrt{6}(1+i)(1-z)}{2\sqrt{E}}\right) + \exp\left(-\frac{\sqrt{2}(1-i)(1-z)}{2\sqrt{E}}\right)\right]\hat{\mathbf{y}}\right. \\
&+ \left. 2\left[\exp\left(-\frac{\sqrt{2}(1+i)y}{2\sqrt{E}}\right) + \exp\left(-\frac{\sqrt{2}(1-i)(\Gamma-y)}{2\sqrt{E}}\right)\right]\hat{\mathbf{x}}\right\}\mathrm{e}^{it}. \qquad (5.20)
\end{aligned}
$$

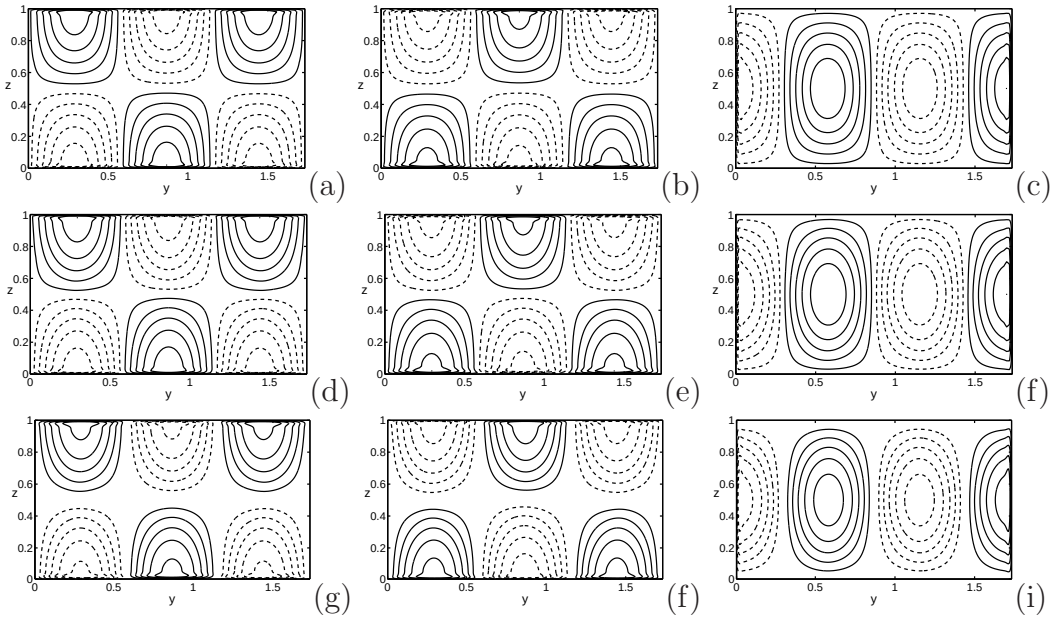

Figure 5.1: Contours of (a) u_x, (b) u_y and (c) u_z (upper panels) in a vertical yz plane for the asymptotic solution computed from the analytical expression (5.19)(courtesy of Prof. Keke Zhang); contours of (d) u_x, (e) u_y and (f) u_z (middle panels) computed from the 2D numerical analysis(courtesy of Prof. Xinhao Liao); contours of (g) u_x, (h) u_y and (i) u_z (lower panels) from direct 3D numerical simulation. The parameters for all three solutions are $\epsilon = 5 \times 10^{-4}$ and $\Gamma = \sqrt{3}$ at $E = 5 \times 10^{-5}$.

which is valid for any value of the aspect ratio Γ. To measure the strength of the resonant precessing flow, we introduce the averaged kinetic energy, $E_{\rm kin}$, defined as

$$E_{\rm kin} = \frac{1}{2\pi}\int_0^{2\pi}\frac{1}{2V}\left[\int_V |{\rm Re}(\mathbf{u})|^2 {\rm d}V\right]{\rm d}t, \tag{5.21}$$

where V denotes the volume of the channel. Using the analytical expressions (5.19) and (5.20), we obtain

$$E_{\rm kin} = \frac{1}{4}\left[\frac{6144(\epsilon/\sqrt{E})^2}{\pi^6\left\{9\sqrt{2}[(1+\sqrt{3})] + 32\sqrt{3}\pi^2\sqrt{E}\right\}^2 + 162(1-\sqrt{3})^2]} + \epsilon^2\right], \tag{5.22}$$

where the small contribution from the viscous boundary layers is not included. The asymptotic solution represented by the analytical expressions (5.19) and (5.22) will be compared directly to the result of 2D and 3D numerical simulations.

The typical structure of the weakly precessing flow satisfying the non-slip boundary condition, computed directly from the analytical expression (5.19), is illustrated in Figure 5.1(a,b,c) for $\epsilon = 5 \times 10^{-4}$, $\Gamma = \sqrt{3}$ and $E = 5 \times 10^{-5}$. Also displayed in Figure 5.1, for the purpose of easy comparison, are the 2D numerical solution (Figure 5.1(d,e,f)) and the fully 3D nonlinear simulation (Figure 5.1(g,h,i)) obtained at exactly the same parameters. Evidently, there are no noticeable differences among the three solutions obtained via three fundamentally different meth-

ods. Furthermore, the kinetic energy $E_{\rm kin}$ computed from the expression (5.22) for $\epsilon = 5.0 \times 10^{-4}$ and $\Gamma = \sqrt{3}$ is $E_{kin} = 5.11 \times 10^{-6}$ while the 2D numerical analysis yields $E_{kin} = 4.95 \times 10^{-6}$ and our direct 3D nonlinear simulation gives $E_{\rm kin} = 4.47 \times 10^{-6}$ (the details of the numerics will be discussed in §5.4). For a larger Poincaré number $\epsilon = 10^{-3}$, the asymptotic expression (5.22) gives rise to $E_{kin} = 2.05 \times 10^{-5}$ for $E = 5 \times 10^{-5}$ while the corresponding 2D numerics yields $E_{kin} = 1.98 \times 10^{-5}$ and the 3D nonlinear simulation gives $E_{\rm kin} = 1.80 \times 10^{-5}$.

A satisfactory quantitative agreement between the asymptotic analysis and the 2D and 3D numerical simulation is achieved for small and moderate Reynolds numbers. This not only validates the asymptotic analysis but also confirms the crucial role played by viscosity at exact resonance. Comparison between the asymptotic and numerical results also indicates that the asymptotic solution (5.19) offers a reasonably good approximation to the fully nonlinear 3D simulation in the range $0 < E^{1/2}Re < \mathrm{O}(1)$, which will be discussed further.

5.3.2 Double-inertial-mode resonance

Consider now a precessing channel with aspect ratio $\Gamma = 1/\sqrt{3}$ which is also at exact resonance with the Poincaré forcing. In this case, while the principal inertial mode $\mathbf{u}_{11}$ is predominant, the secondary resonant mode $\mathbf{u}_{33}$ makes a substantial contribution and, hence, should be included. An asymptotic solution $\mathbf{u}$ describing a weakly precessing flow for $E \ll 1$ and $\Gamma = 1/\sqrt{3}$ can be written in the form

$$\mathbf{u}(y,z,t) = [(\mathbf{u}_G + \widetilde{\mathbf{u}}_G) + (\mathcal{C}_{11}\mathbf{u}_{11} + \mathcal{C}_{33}\mathbf{u}_{33}) + \hat{\mathbf{u}} + \widetilde{\mathbf{u}}]\, \mathrm{e}^{it}, \tag{5.23}$$

$$p(y,z,t) = [(p_G + \widetilde{p}_G) + (\mathcal{C}_{11}p_{11} + \mathcal{C}_{33}p_{33}) + \hat{p} + \widetilde{p}]\, \mathrm{e}^{it}, \tag{5.24}$$

where $\mathcal{C}_{11}$ and $\mathcal{C}_{33}$ are complex coefficients to be determined, the two inviscid resonant inertial modes, $(\mathbf{u}_{11}, p_{11})$ and $(\mathbf{u}_{33}, p_{33})$, whose expressions are given by (5.13)-(5.16), must be corrected by the viscous boundary layer $\widetilde{\mathbf{u}}$ on the four bounding surfaces of the channel, and the secondary interior flow, $[\hat{\mathbf{u}}, \hat{p}]$, where $|\hat{\mathbf{u}}| \ll |\mathcal{C}_{11}\mathbf{u}_{11} + \mathcal{C}_{33}\mathbf{u}_{33}|$, is induced by the viscous effects. The expression for the geostrophic flow, $\mathbf{u}_G$ and $\widetilde{\mathbf{u}}_G$ given by (5.20), remains unchanged.

An analytical expression for the precessing flow at the double-mode resonance at $\Gamma = 1/\sqrt{3}$ is

$$\mathbf{u} = (\mathbf{u}_G + \widetilde{\mathbf{u}}_G) + \mathbf{V}_{11} + \mathbf{V}_{33}, \tag{5.25}$$

where the geostrophic flow $(\mathbf{u}_G + \widetilde{\mathbf{u}}_G)$ is still given by (5.20) while $\mathbf{V}_{11}$, in association

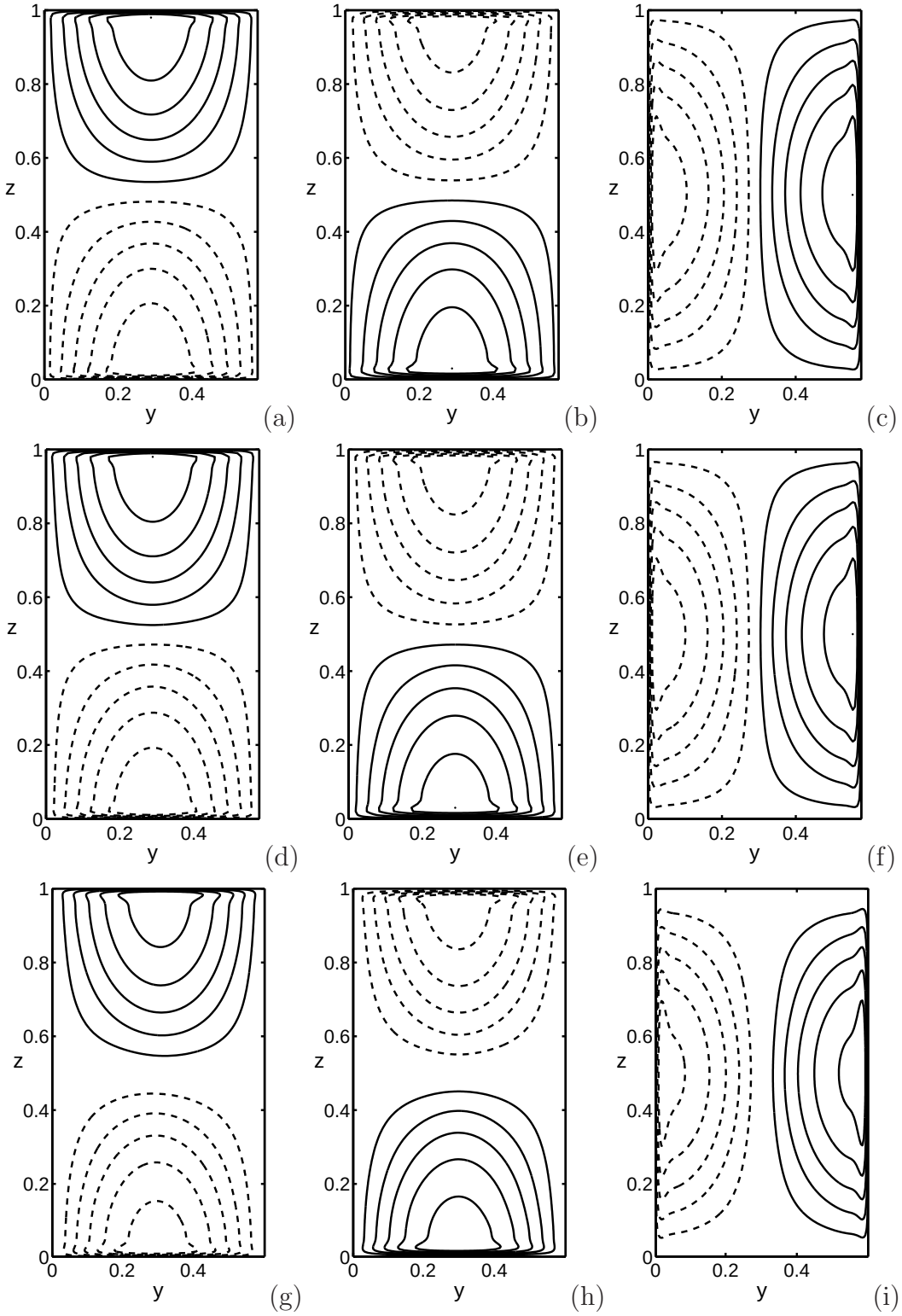

Figure 5.2: Contours of (a) u_x, (b) u_y and (c) u_z in a vertical yz plane computed from the asymptotic solution (5.25)-(5.27) (upper panels); (d) u_x, (e) u_y and (f) u_z for the 2D numerical solution (middle panels); (g) u_x, (h) u_y and (i) u_z for direct 3D nonlinear numerical simulation (lower panels). The parameters for the three solutions are $\epsilon = 5 \times 10^{-4}$, $\Gamma = 1/\sqrt{3}$ and $E = 5 \times 10^{-5}$.

with the primary resonant mode $\mathbf{u}_{11}$, takes the form

$$\begin{aligned}
\mathbf{V}_{11} &= -\frac{288(\epsilon/\sqrt{E})\mathrm{e}^{it}}{\pi^4\left\{3\sqrt{2}[(7+3\sqrt{3})+(7-3\sqrt{3})i]+32\sqrt{3}\pi^2\sqrt{E}\right\}} \\
&\times \left\{\left(\frac{\pi\sin\sqrt{3}\pi y}{2\sqrt{3}}\right)\left\{\left[4\cos\pi z-\exp\left(-\frac{\sqrt{6}(1+i)z}{2\sqrt{E}}\right)-3\exp\left(-\frac{\sqrt{2}(1-i)z}{2\sqrt{E}}\right)\right.\right.\right. \\
&+ \left.\left.\left.\exp\left(-\frac{\sqrt{6}(1+i)(1-z)}{2\sqrt{E}}\right)+3\exp\left(-\frac{\sqrt{2}(1-i)(1-z)}{2\sqrt{E}}\right)\right]\hat{\mathbf{x}}\right.\right. \\
&+ \left. i\left[2\cos\pi z+\exp\left(-\frac{\sqrt{6}(1+i)z}{2\sqrt{E}}\right)-3\exp\left(-\frac{\sqrt{2}(1-i)z}{2\sqrt{E}}\right)\right.\right. \\
&- \left.\left.\exp\left(-\frac{\sqrt{6}(1+i)(1-z)}{2\sqrt{E}}\right)+3\exp\left(-\frac{\sqrt{2}(1-i)(1-z)}{2\sqrt{E}}\right)\right]\hat{\mathbf{y}}\right\}-i\pi\sin\pi z \\
&\times \left[\cos\sqrt{3}\pi y-\exp\left(-\frac{\sqrt{2}(1+i)y}{2\sqrt{E}}\right)+\exp\left(-\frac{\sqrt{2}(1+i)(\Gamma-y)}{2\sqrt{E}}\right)\right]\hat{\mathbf{z}}\Bigg\}, \quad (5.26)
\end{aligned}$$

and $\mathbf{V}_{33}$, in association with the secondary resonant mode $\mathbf{u}_{33}$, is given by

$$\begin{aligned}
\mathbf{V}_{33} &= -\frac{288(\epsilon/\sqrt{E})\mathrm{e}^{it}}{\pi^4\left\{3\sqrt{2}[(7+3\sqrt{3})+(7-3\sqrt{3})i]+288\sqrt{3}\pi^2\sqrt{E}\right\}} \\
&\times \left\{\left(\frac{\pi\sin 3\sqrt{3}\pi y}{54\sqrt{3}}\right)\left\{\left[4\cos 3\pi z-\exp\left(-\frac{\sqrt{6}(1+i)z}{2\sqrt{E}}\right)-3\exp\left(-\frac{\sqrt{2}(1-i)z}{2\sqrt{E}}\right)\right.\right.\right. \\
&+ \left.\left.\left.\exp\left(-\frac{\sqrt{6}(1+i)(1-z)}{2\sqrt{E}}\right)+3\exp\left(-\frac{\sqrt{2}(1-i)(1-z)}{2\sqrt{E}}\right)\right]\hat{\mathbf{x}}\right.\right. \\
&+ \left. i\left[2\cos 3\pi z+\exp\left(-\frac{\sqrt{6}(1+i)z}{2\sqrt{E}}\right)-3\exp\left(-\frac{\sqrt{2}(1-i)z}{2\sqrt{E}}\right)\right.\right. \\
&- \left.\left.\exp\left(-\frac{\sqrt{6}(1+i)(1-z)}{2\sqrt{E}}\right)+3\exp\left(-\frac{\sqrt{2}(1-i)(1-z)}{2\sqrt{E}}\right)\right]\hat{\mathbf{y}}\right\}-i\frac{\pi}{27}\sin 3\pi z \\
&\times \left[\cos 3\sqrt{3}\pi y-\exp\left(-\frac{\sqrt{2}(1+i)y}{2\sqrt{E}}\right)+\exp\left(-\frac{\sqrt{2}(1+i)(\Gamma-y)}{2\sqrt{E}}\right)\right]\hat{\mathbf{z}}\Bigg\}. \quad (5.27)
\end{aligned}$$

Note that the secondary resonant mode, $\mathbf{u}_{33}$, makes about 5% contribution towards the amplitude of the precessing flow. The total kinetic energy of the flow including the geostrophic flow is given by

$$\begin{aligned}
E_{kin} &= \frac{512(\epsilon/\sqrt{E})^2}{\pi^6}\left\{\frac{27}{\left[3\sqrt{2}(7+3\sqrt{3})+32\pi^2\sqrt{3E}\right]^2+18(7-3\sqrt{3})^2}\right. \\
&+ \left.\frac{1}{27\left[3\sqrt{2}(7+3\sqrt{3})+288\pi^2\sqrt{3E}\right]^2+486(7-3\sqrt{3})^2}\right\}+\frac{\epsilon^2}{4}, \quad (5.28)
\end{aligned}$$

where the small contribution from the viscous boundary layers is excluded.

The analytical expressions (5.25) and (5.28) are compared directly to the 2D numerical analysis and fully 3D direct numerical simulations. The spatial structure of the precessing flow for $\Gamma = 1/\sqrt{3}$, computed from the expression (5.25), is displayed in Figure 5.2(a,b,c) for $\epsilon = 5 \times 10^{-4}$ and $E = 5 \times 10^{-5}$. Also displayed in the figure are the 2D numerical solution (Figure 5.2(d,e,f)) and the direct 3D nonlinear simulation (Figure 5.2(g,h,i)) obtained at exactly the same parameters. There are no significant differences among the three solutions obtained in completely different ways. Moreover, the kinetic energy $E_{\rm kin}$ computed from the asymptotic expression (5.28) is $E_{\rm kin} = 2.28 \times 10^{-5}$ for $\epsilon = 5.0 \times 10^{-4}$ and $\Gamma = 1/\sqrt{3}$ at $E = 5 \times 10^{-5}$ while the 2D numerical analysis yields $E_{\rm kin} = 2.13 \times 10^{-5}$ and the direct 3D nonlinear simulation gives $E_{\rm kin} = 2.01 \times 10^{-5}$. For a larger Poincaré number $\epsilon = 10^{-3}$, the expression (5.28) gives $E_{kin} = 9.15 \times 10^{-5}$ for $\Gamma = 1/\sqrt{3}$ at $E = 5 \times 10^{-5}$ while the corresponding 2D numerics yields $E_{kin} = 8.54 \times 10^{-5}$ and the direct 3D nonlinear simulation produces a similar 2D precessing flow with $E_{\rm kin} = 8.16 \times 10^{-5}$.

Our results again support the hypothesis that the viscous effect, which is primarily from the viscous boundary layers, is essential in determining both the structure and amplitude of weakly precessing flows at exact resonance. The asymptotic solution given by (5.25)-(5.27) offers reasonably accurate approximation to the direct fully 3D nonlinear simulation for the range $0 < Re < \mathrm{O}(E^{-1/2})$. When $Re = \mathrm{O}(E^{-1/2})$, i.e., $\epsilon \approx 7 \times 10^{-3}$ for $E = 5 \times 10^{-5}$, however, the nonlinear effect becomes important and leads to a fully three-dimensional precessing flow, which will be discussed later.

5.3.3 Multiple-inertial-mode excitation at non-resonance

Finally, consider a precessing channel with non-resonant aspect ratios, i.e., $|3n\Gamma - \sqrt{3}j| \gg E^{1/2}$ for moderate integers n and j, where n is odd, at an asymptotically small E. In this case, it is anticipated that a large number of inertial modes would be excited by the precessional forcing. An asymptotic solution for a weakly precessing flow, $\mathbf{u}$ and p, can be still separated, at leading order, into the interior flow and the boundary-layer flow in the form

$$\mathbf{u}(y,z,t) = \left[(\mathbf{u}_G + \widetilde{\mathbf{u}}_G) + \left(\sum_{j,n} \mathcal{C}_{jn}\mathbf{u}_{jn}\right) + \hat{\mathbf{u}} + \widetilde{\mathbf{u}}\right] \mathrm{e}^{it}, \tag{5.29}$$

$$p(y,z,t) = \left[(p_G + \widetilde{p}_G) + \left(\sum_{j,n} \mathcal{C}_{jn}p_{jn}\right) + \hat{p} + \widetilde{p}\right] \mathrm{e}^{it}, \tag{5.30}$$

where $\mathcal{C}_{jn}$ are unknown complex coefficients, $\mathbf{u}_G$ and $\widetilde{\mathbf{u}}_G$ are the interior and boundary geostrophic flow, $(\mathbf{u}_{jn}, p_{jn})$ represent inertial modes given by (5.13)-(5.16), $\widetilde{\mathbf{u}}$ is the viscous boundary layer while $[\hat{\mathbf{u}}, \hat{p}]$ represents the secondary interior flow with

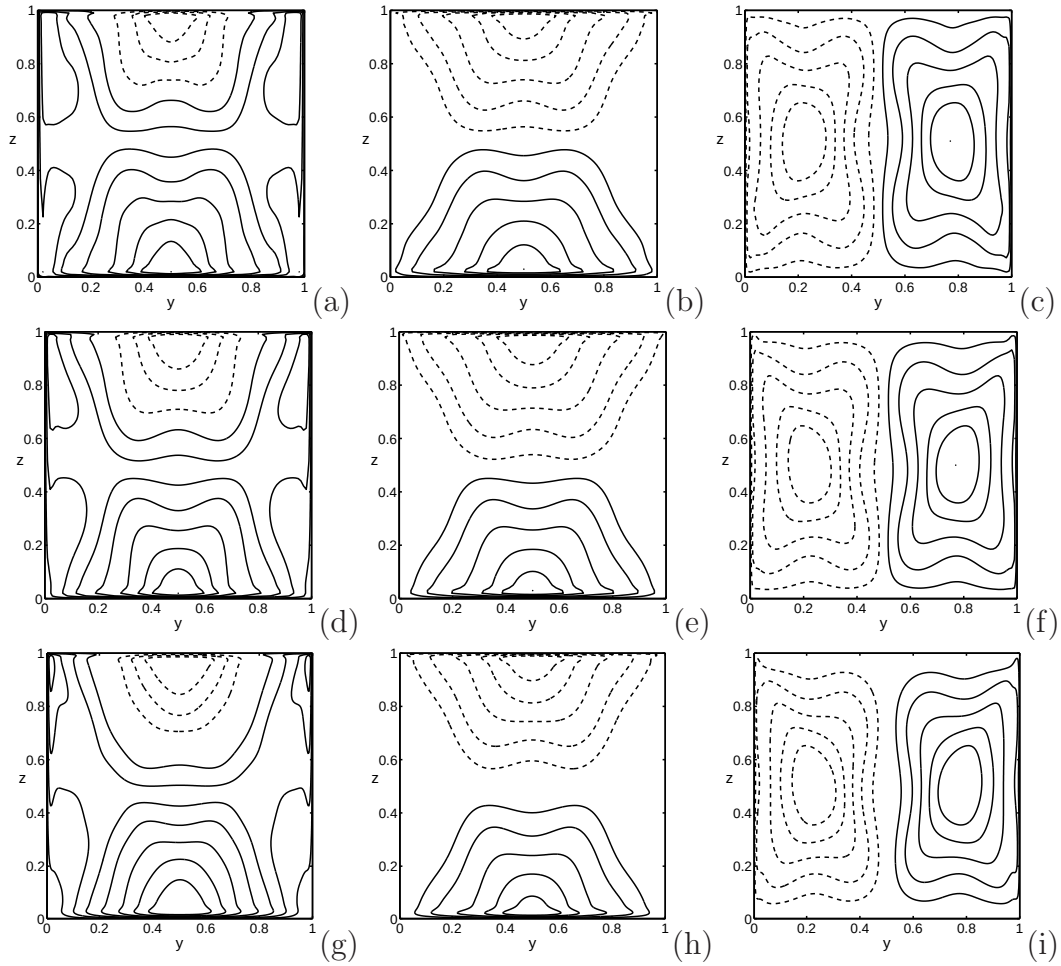

Figure 5.3: Contours of (a) u_x, (b) u_y and (c) u_z in a vertical yz plane from the non-resonant asymptotic solution (5.31) (top panels) ; (d) u_x, (e) u_y and (f) u_z from the 2D numerical analysis (middle panels); (g) u_x, (h) u_y and (i) u_z from the 3D direct simulation (lower panels). The parameters are $\epsilon = 5 \times 10^{-4}$, $\Gamma = 1$ and $E = 5 \times 10^{-5}$.

$|\hat{\mathbf{u}}| \ll |\sum_{j,n} \mathcal{C}_{jn}\mathbf{u}_{jn}|$.

An asymptotic solution with the non-slip boundary condition for a non-resonant channel can be written in the form

$$\begin{aligned}
\mathbf{u} &= \widetilde{\mathbf{u}} + (\mathbf{u}_G + \widetilde{\mathbf{u}}_G) + \sum_{j,n}\left[\frac{4\epsilon j^2}{n^2\pi^3(j^2+n^2\Gamma^2)^{1/2}}\right] \\
&\times \left\{\frac{[1-(-1)^j][1-(-1)^n]}{[(j^2+n^2\Gamma^2)^{1/2}-n\Gamma][(j^2+n^2\Gamma^2)^{1/2}-2n\Gamma]}\right\} \\
&\times \left\{-\frac{(j^2+n^2\Gamma^2)^{1/2}}{j}\sin\frac{j\pi y}{\Gamma}\cos n\pi z\left[\hat{\mathbf{x}}\sin t + \hat{\mathbf{y}}\frac{n\Gamma\cos t}{(j^2+n^2\Gamma^2)^{1/2}}\right]\right. \\
&+ \left.\hat{\mathbf{z}}\left[\cos\frac{j\pi y}{\Gamma}\sin n\pi z\cos t\right]\right\}, \qquad (5.31)
\end{aligned}$$

valid for an asymptotically small E with non-resonant aspect ratios Γ. Note that the analytical expression (5.31) is non-singular because of the non-resonant condition. In the asymptotic solution (5.31), while the geostrophic flow $(\mathbf{u}_G + \widetilde{\mathbf{u}}_G)$ is still given by (5.20), the viscous boundary layer $\widetilde{\mathbf{u}}$ is given by

$$\begin{aligned}
\widetilde{\mathbf{u}} &= -\sum_{j,n}\frac{i2\epsilon j^2[1-(-1)^j][1-(-1)^n]\mathrm{e}^{it}}{n^2\pi^3(j^2+n^2\Gamma^2)[(j^2+n^2\Gamma^2)^{1/2}-n\Gamma][(j^2+n^2\Gamma^2)^{1/2}-2n\Gamma]} \\
&\times \left\{(-\hat{\mathbf{x}}+i\hat{\mathbf{y}})\left[\frac{j(j^2+n^2\Gamma^2)^{1/2}}{(j^2+n^2\Gamma^2)^{1/2}+n\Gamma}\sin\frac{j\pi y}{\Gamma}\right]\exp\left(-\frac{\sqrt{6}(1+i)z}{2\sqrt{E}}\right)\right. \\
&- (\hat{\mathbf{x}}+i\hat{\mathbf{y}})\left[\frac{j(j^2+n^2\Gamma^2)^{1/2}}{(j^2+n^2\Gamma^2)^{1/2}-n\Gamma}\sin\frac{j\pi y}{\Gamma}\right]\exp\left(-\frac{\sqrt{2}(1-i)z}{2\sqrt{E}}\right) \\
&+ (-1)^n(-\hat{\mathbf{x}}+i\hat{\mathbf{y}})\left[\frac{j(j^2+n^2\Gamma^2)^{1/2}}{(j^2+n^2\Gamma^2)^{1/2}+n\Gamma}\sin\frac{j\pi y}{\Gamma}\right]\exp\left(-\frac{\sqrt{6}(1+i)(1-z)}{2\sqrt{E}}\right) \\
&- (-1)^n(\hat{\mathbf{x}}+i\hat{\mathbf{y}})\left[\frac{j(j^2+n^2\Gamma^2)^{1/2}}{(j^2+n^2\Gamma^2)^{1/2}-n\Gamma}\sin\frac{j\pi y}{\Gamma}\right]\exp\left(-\frac{\sqrt{2}(1-i)(1-z)}{2\sqrt{E}}\right) \\
&+ \hat{\mathbf{z}}i\left[2(j^2+n^2\Gamma^2)^{1/2}\right]\sin n\pi z \\
&\times \left.\left[\exp\left(-\frac{\sqrt{2}(1+i)y}{2\sqrt{E}}\right)+(-1)^j\exp\left(-\frac{\sqrt{2}(1+i)(\Gamma-y)}{2\sqrt{E}}\right)\right]\right\}. \qquad (5.32)
\end{aligned}$$

It should be mentioned that we have carefully compared the numerical solution for the equation which contains all the viscous terms, to the explicit analytical solution (5.31) for $E \ll 1$: the difference between them is negligibly small at a non-resonant Γ. On the basis of the explicit asymptotic solution (5.31), we can also derive an analytical expression for the kinetic energy of the precessing flow

$$E_{kin} = \frac{\epsilon^2}{4} + \sum_{j,n}\frac{8\epsilon^2[1-(-1)^j][1-(-1)^n]}{n^4\pi^6[(j^2+n^2\Gamma^2)^{1/2}-n\Gamma]^2[(j^2+n^2\Gamma^2)^{1/2}-2n\Gamma]^2}, \qquad (5.33)$$

where the contribution from the boundary layers is again neglected.

ϵ	Re	E_{kin}(Asymptotic)	E_{kin}(2D numerics)	E_{kin}(3D simulation)
10^{-4}	2×10^{0}	8.666×10^{-9}	8.670×10^{-9}	8.616×10^{-9}(2D flow)
5×10^{-4}	1×10^{1}	2.167×10^{-7}	2.168×10^{-7}	2.152×10^{-9}(2D flow)
10^{-3}	2×10^{1}	8.666×10^{-7}	8.670×10^{-7}	8.603×10^{-7}(2D flow)
5×10^{-3}	1×10^{2}	2.167×10^{-5}	2.168×10^{-5}	2.151×10^{-5} (2D flow)
10^{-2}	2×10^{2}	8.666×10^{-5}	8.670×10^{-5}	8.563×10^{-5}(2D flow)
5×10^{-2}	1×10^{3}	2.167×10^{-3}	2.168×10^{-3}	2.189×10^{-3}(2D flow)
7.5×10^{-2}	1.5×10^{3}			(3D flow)

Table 5.1: Kinetic energies, E_{kin}, computed from the asymptotic expression (5.33) (courtesy of Prof. Keke Zhang), along with the corresponding values calculated from the 2D numerical analysis (courtesy of Prof. Xinhao Liao) and direct 3D nonlinear numerical simulation for $\Gamma = 1$ and $E = 5 \times 10^{-5}$.

For a given ϵ and non-resonant Γ, we can compute the spatial structure of a precessing flow satisfying the non-slip boundary condition from the expressions (5.31), which is shown in Figure 5.3(a,b,c) for $\epsilon = 5\times10^{-4}$ and $\Gamma = 1$ at $E = 5\times10^{-5}$. It can be then directly compared with the 2D numerical solution shown in Figure 5.3(d,e,f) and the 3D nonlinear simulation in Figure 5.3(g,h,i) at exactly the same parameters. There are no significantly noticeable differences in the spatial structure of the three solutions. Furthermore, kinetic energies, $E_{\rm kin}$, computed from the analytical formula (5.33) for several different values of ϵ at $\Gamma = 1$ are given in Table 5.1, along with the corresponding values calculated from the 2D and 3D numerical analysis. Evidently, the asymptotic solution (5.31) offers an accurate approximation to the fully three-dimensional nonlinear simulation up to $Re \leq \mathrm{O}(10^3)$, which corresponds to $\epsilon = 5 \times 10^{-2}$ for $E = 5 \times 10^{-5}$. When Re increases further, the precessing flow becomes fully three dimensional and the asymptotic solution (5.31) becomes physically irrelevant.

5.4 Numerical simulation

5.4.1 2D linear numerical analysis

In [Zhang et al., 2010], we also undertake a linear numerical analysis which is valid for any value of Ekman number E and any size of the aspect ratio Γ. The idea is that because the weak precession driven flows are 2-D, we may expand a velocity in terms of two potentials, Ψ and Φ, in the form

$$\mathbf{u} = \{\nabla \times [\Psi(y,z)\hat{\mathbf{x}}] + \Phi(y,z)\hat{\mathbf{x}}\}\, \mathrm{e}^{it}.$$

Ψ and Φ are then substituted into the linearized equation

$$\frac{\partial \mathbf{u}}{\partial t} + 2\hat{\mathbf{z}} \times \mathbf{u} + \nabla p \;=\; E\nabla^2\mathbf{u} + 2\epsilon z\,(\hat{\mathbf{x}}\cos t - \hat{\mathbf{y}}\sin t)\,.$$

Finally, the governing equations of Ψ and Φ are solved numerically by a spectral method.

How and when a precessionally driven 2D flow becomes fully three-dimensional at a large Reynolds number remains an open question which must be answered by direct 3D nonlinear simulation of the problem.

5.4.2 Fully 3D nonlinear simulation

In comparison to the plane-geometry problem ([Mason and Kerswell, 2002]) which permits periodic boundary conditions in both the $x-$ and $y-$direction, the precessional problem in channel-geometry with the non-slip boundary condition is numerically more challenging. It would be difficult, because of the existence of the two vertical sidewalls, to employ the widely-used pseudo-spectral method with Fourier series. We choose to tackle the fully three-dimensional, nonlinear problem by employing a finite difference code "NaSt3DGP" developed by the research group in the Division of Scientific Computing and Numerical Simulation at the University of Bonn (see [Griebel et al., 1998]). We mainly modified the code by adding to it the Coriolis and the Poincaré force terms. "NaSt3DGP" is parallelized by MPI and implements a first-order temporal discretization along with a second-order finite difference scheme based on the Chorin-type projection scheme ([Chorin, 1968]), which decouples the momentum and continuity equations. The projection scheme leads to the time discretization of equations (5.4)-(5.5) in the form

$$\begin{aligned}\frac{(\mathbf{u}_m - \mathbf{u}^n)}{\Delta t} &= E\nabla^2\mathbf{u}^n - \mathbf{u}^n\cdot\nabla\mathbf{u}^n - 2\hat{\mathbf{z}}\times\mathbf{u}^n + 2\epsilon z\left(\hat{\mathbf{x}}\cos t_n - \hat{\mathbf{y}}\sin t_n\right)\\ &\quad +2\epsilon\mathbf{u}^n\times\left(\hat{\mathbf{x}}\cos t_n - \hat{\mathbf{y}}\sin t_n\right),\end{aligned} \tag{5.34}$$

where $\mathbf{u}^n$ represents the velocity at the $n-$th time step $t = t_n$ while $\mathbf{u}_m$ denotes the velocity at an intermediate time between $t = t_n$ and $t = t_{n+1}$. The solution of (5.34) gives rise to the intermediate velocity $\mathbf{u}_m$ which is then used to solve the Poisson equation for the pressure p^{n+1} at the $(n+1)-$th time step $t = t_{n+1}$,

$$\nabla^2 p^{n+1} = \frac{1}{\Delta t}\nabla\cdot\mathbf{u}_m. \tag{5.35}$$

After solving (5.35), we can readily compute the velocity field $\mathbf{u}^{n+1}$ at $t = t_{n+1}$ by

$$\mathbf{u}^{n+1} = \mathbf{u}_m - \Delta t\nabla p^{n+1}. \tag{5.36}$$

No spatial symmetries are imposed on our direct 3D numerical simulation which usually starts with an arbitrary 3D initial condition, even though the nonlinear solution for moderate values of Re is not only two dimensional (independent of x) but also possesses spatial symmetries in the $y-$ and $z-$ direction. Our numerical method is largely similar to that used by ([Wu and Roberts, 2008]) although their

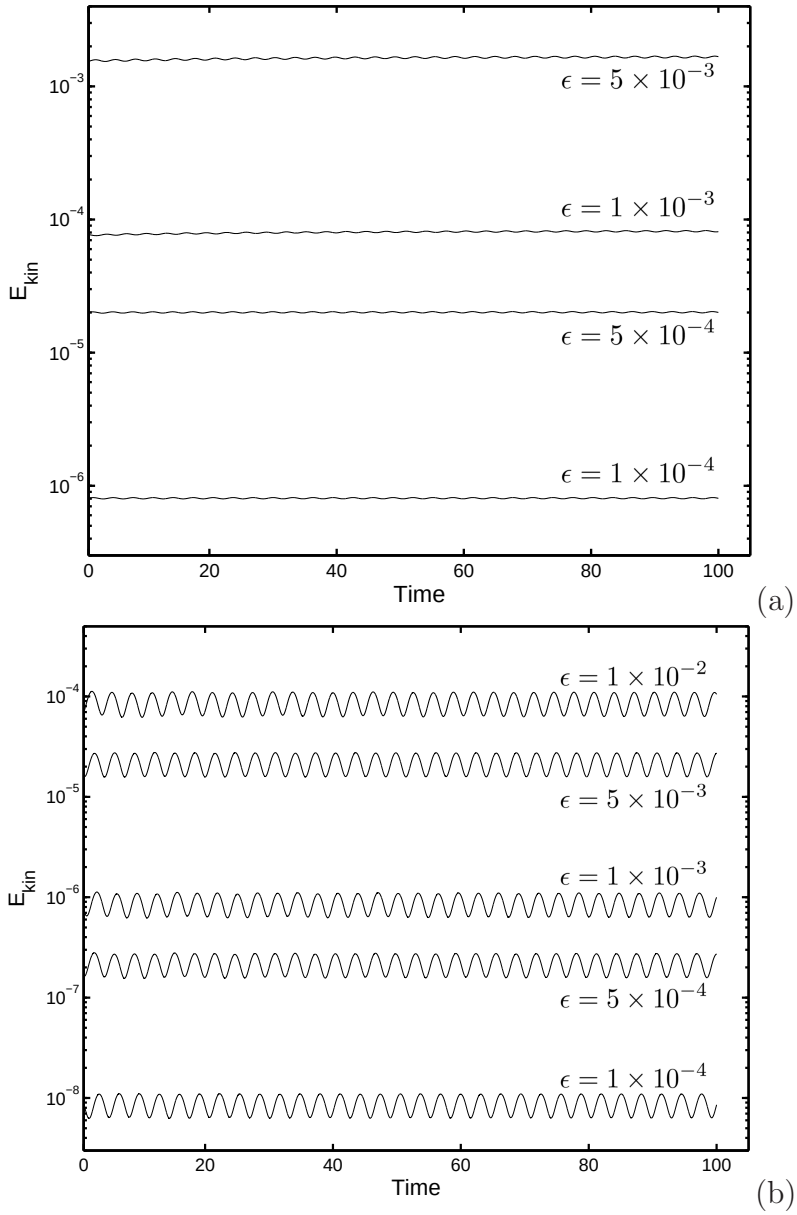

Figure 5.4: Kinetic energies, E_{kin}, of the 2D precessing flow resulting from 3D direct numerical simulation are plotted against time for several different values of ϵ: (a) for the strongly resonant case with $\Gamma = 1/\sqrt{3}$ at $E = 5 \times 10^{-5}$ and (b) for the non-resonant case with $\Gamma = 1$ at $E = 5 \times 10^{-5}$.

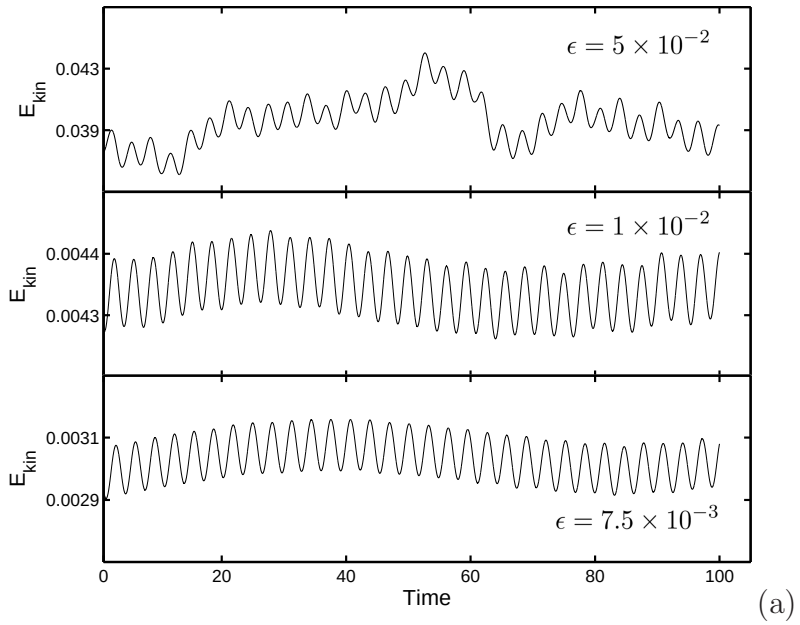

(a)

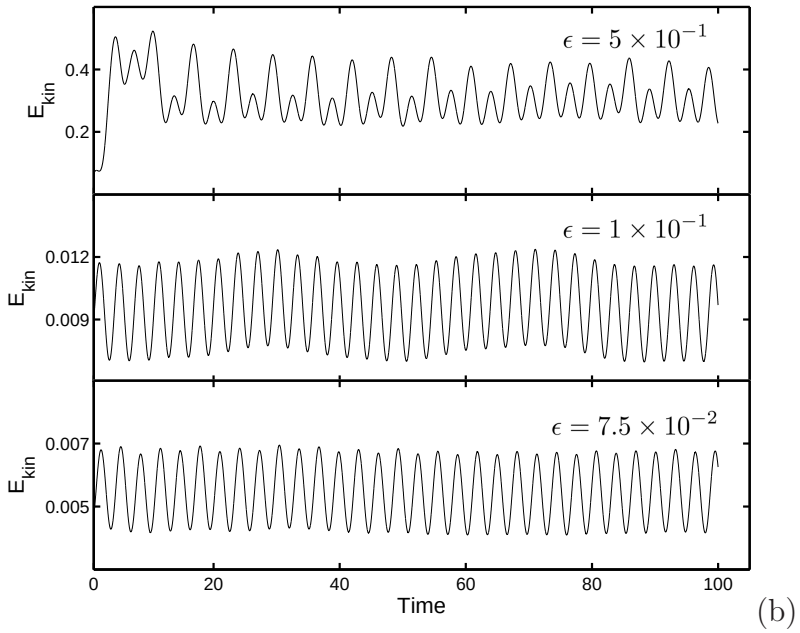

(b)

Figure 5.5: Kinetic energies, E_{kin}, of the 3D precessing flow from the 3D direct numerical simulation are plotted against time (a) for the resonant case with $\Gamma = 1/\sqrt{3}$ at $E = 5 \times 10^{-5}$, (b) for the non-resonant case with $\Gamma = 1$ at $E = 5 \times 10^{-5}$.

time integration is a third order scheme while our scheme is of first order.

In addition to the physical parameters like the Ekman number E and the Poincaré number ϵ, a new parameter enters into the 3D nonlinear simulation: the size of the computational box defined by the upper and lower non-slip surfaces at $z = 0, 1$, by the two vertical non-slip sidewalls at $y = 0, \Gamma$ and by the periodic boundary condition at $x = 0, L$, where L may be regarded as an additional parameter for the 3D simulation. A thin computational box with $L \ll 1$ is computationally inexpensive, but it may be incapable of capturing the crucial spatial scales of 3D instabilities; a very wide box with $L \gg 1$, on the other hand, is computationally too expensive or may be unnecessary in the understanding of key nonlinear dynamics. On a balance between the computational cost and the essential physics, we choose $L = 1$, which equivalently imposes the periodic boundary conditions $\mathbf{u}(x = 0) = \mathbf{u}(x = 1)$ and $p(x = 0) = p(x = 1)$, for all our direct 3D nonlinear simulation.

While our 3D numerical code was carefully validated by comparing with the asymptotic solutions, the accuracy of the 3D simulation was also carefully checked by computing the nonlinear solutions at exactly the same parameters but using different spatial resolutions. The time advancing step is self adaptive and restricted by proper CFL conditions. It should be noted that we do not anticipate, physically and mathematically, boundary-layer type structure in the $x-$direction along the channel, implying that $|\partial/\partial x| \ll |\partial/\partial z|$ and $|\partial/\partial x| \ll |\partial/\partial y|$. Our primary concern is with the viscous boundary layers located on the four bounding surfaces of a channel, in connection with the spatial resolution in the $y-$ and $z-$direction. It is found that there are no significant differences between the nonlinear solutions simulated with either 300 or 200 grids in the $z-$direction for $E \geq 5 \times 10^{-5}$. Consequently, we have typically used, for example at $\Gamma = \sqrt{3}$, the spatial resolution with a grid system $[50 \times 350 \times 200]$ covering $0 \leq x \leq 1$, $0 \leq y \leq \Gamma$ and $0 \leq z \leq 1$ for our direct 3D simulations, providing a reasonable numerical accuracy for the moderately strong nonlinear solutions presented in this chapter.

The finite-difference equations (5.34)-(5.36), treated as an initial-value problem, are integrated forward in time, starting from an arbitrary 3D flow, until the numerical solution attains an oscillatory or a chaotic state, usually taking up to $\mathrm{O}(10^2)$ non-dimensional time units. While a 3D simulation for a 2D weakly nonlinear flow is, because of relatively large Δt, usually less expensive, simulating a strongly nonlinear flow, however, would typically take a three-week runtime to integrate (5.34)-(5.36), with $\Delta t = \mathrm{O}(10^{-4})$, to the $\mathrm{O}(10^2)$ time units using 60 processors (each processor with 3612 MHz) on an IBM parallel computer. Throughout this project, as declared in the acknowledgement page of this thesis, we ran our jobs on various supercomputing facilities and a large amount of data has been accumulated.

Consider first the exact resonance for $\Gamma = 1/\sqrt{3}$ at which the strongest precessing flow occurs for a given ϵ. The primary objectives of our direct 3D nonlinear

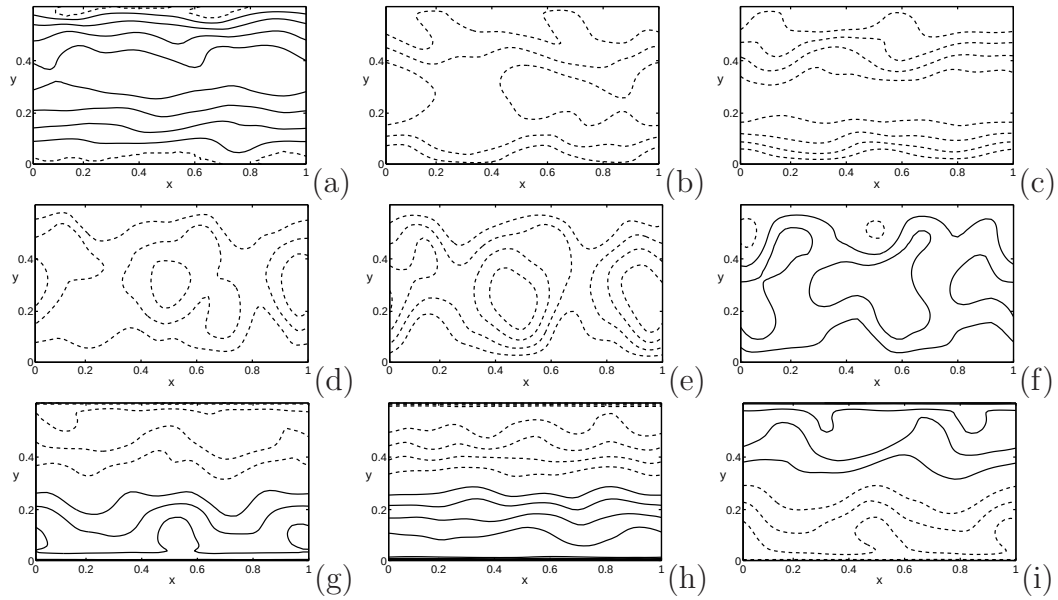

Figure 5.6: Snapshots of a 3D precessing flow at three different instants in a horizontal xy plane: contours of u_x at $z = 1/4$ are displayed in (a)-(c), contours of u_y at $z = 1/4$ are displayed in (d)-(f), and contours of u_z at $z = 1/2$ are displayed in (g)-(i). The parameters for this nonlinear solution are $\epsilon = 7.5 \times 10^{-3}$ and $\Gamma = 1/\sqrt{3}$ at $E = 5 \times 10^{-5}$.

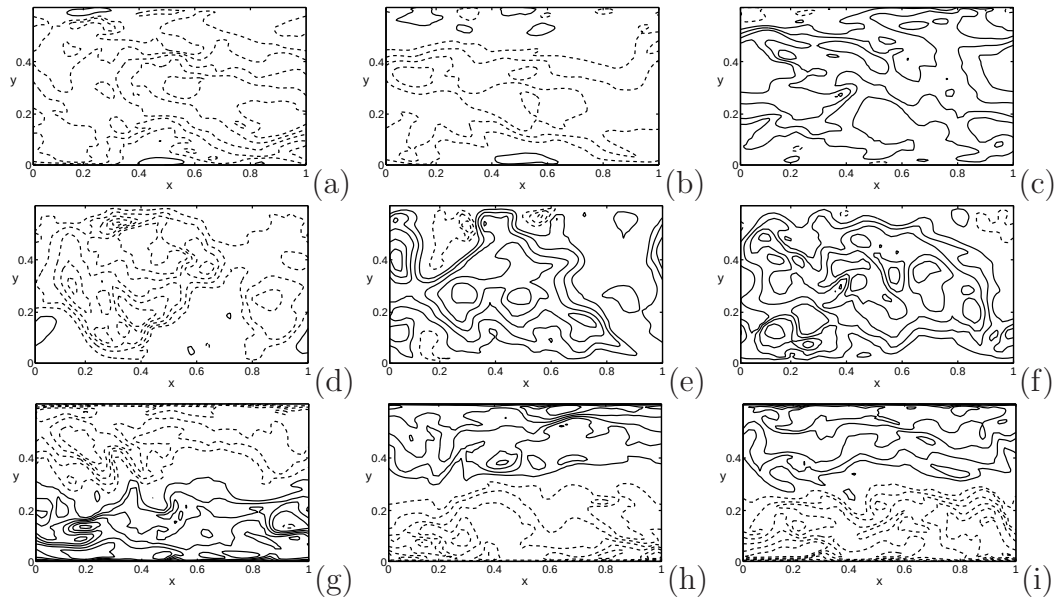

Figure 5.7: Snapshots of 3D solutions in a horizontal xy plane at three different instants: contours of u_x at $z = 1/4$ are displayed in (a)-(c); contours of u_y at $z = 1/4$ are displayed in (d)-(f); contours of u_z at $z = 1/2$ are displayed in (g)-(i). The parameters for this nonlinear solution are $\epsilon = 5 \times 10^{-2}$ and $\Gamma = 1/\sqrt{3}$ at $E = 5 \times 10^{-5}$.

simulation are twofold: to check the validity of the asymptotic expression (5.25) for moderate Reynolds numbers and to identify the transition regimes from 2D laminar flow to 3D turbulence for large Reynolds numbers at fixed small Ekman number $E = 5 \times 10^{-5}$. For a small or moderate value of Re, although a numerical simulation starts with an arbitrary 3D initial flow, the final solution after the transient period of the simulation always reaches an x-independent state, i.e., $\partial \mathbf{u}/\partial x = 0$ and $\partial p/\partial x = 0$. Different simulations with various values of L, either $L > 1$ or $L < 1$, confirm that the x-independent nonlinear solution is the only physically realizable flow for small and moderate Reynolds numbers. The time dependence of the 2D precessing flows resulting from the 3D nonlinear simulation is displayed in Figure 5.4(a) with $\Gamma = 1/\sqrt{3}$. Since the initial transient period of a nonlinear simulation depends upon an arbitrary initial condition and, hence, is of less significance, only the final state of the simulation is shown in the figure. A typical structure of the weakly precessing flow obtained from the 3D simulation is depicted in Figure 5.2(g,h,i), along with the asymptotic solution given by (5.25). The result of the 3D simulation shows a satisfactory agreement with the analytical expressions (5.25) and (5.28) in the approximate range $(ReE^{1/2}) < \mathrm{O}(1)$. This is consistent with the scaling provided by the asymptotic expression (5.25). The amplitude of the resonant precessing flow with $\Gamma = 1/\sqrt{3}$ is $|\mathbf{u}| \sim \epsilon/E^{1/2}$, giving rise to the nonlinear term $|\mathbf{u} \cdot \nabla \mathbf{u}| \sim \epsilon^2/E$ and the Coriolis force $|\hat{\mathbf{z}} \times \mathbf{u}| \sim \epsilon/E^{1/2}$. It follows that, when the rotational effect is dominant, $|\hat{\mathbf{z}} \times \mathbf{u}| > |\mathbf{u} \cdot \nabla \mathbf{u}|$ or $0 < (ReE^{1/2}) < \mathrm{O}(1)$, we would anticipate that the asymptotic solution (5.19) provides a reasonably good approximation and that the precessing flow remains two dimensional. In Figure 5.8, the isosurfaces of velocity components intuitively illustrate the 2D flow independent of x. It reinforces the view that the viscous effect, which is primarily linked with the viscous boundary layers, determines the key property of weakly precessing flows at exact resonance.

A large effort is then made to identify the critical value of Re at which the 2D precessing flow becomes fully three dimensional in a channel with $\Gamma = 1/\sqrt{3}$. By carrying out many 3D simulations at different values of Re, we found that the instabilities that introduce the $x-$dependence and lead to a fully 3D precessing flow take place at $\epsilon \approx 7.0 \times 10^{-3}$, or $ReE^{1/2} \approx 1$ for $\Gamma = 1/\sqrt{3}$ and $E = 5 \times 10^{-5}$. Figure 5.5(a) shows the time dependence of the 3D precessing flows for three different Re, where the transient behavior is not displayed. In the range $1.5 \times 10^2 \leq Re \leq 5 \times 10^2$, the nonlinear precessing flow is fully three dimensional but remains largely laminar. A long timescale temporal modulation can be clearly seen in Figure 5.5(a) while the spatial modulation in the $x-$direction is shown in Figure 5.6 and 5.9 for $\epsilon = 7.5 \times 10^{-3}$ or $Re = 1.5 \times 10^2$. When Re increases to about $Re = 10^3$, however, the laminar 3D flow breaks down, leading to the small-scale disordered turbulence shown in Figure 5.7 and 5.10. In short, three different regimes are identified with increasing Re: (i) 2D oscillatory and laminar flow that is in quantitative agreement with the

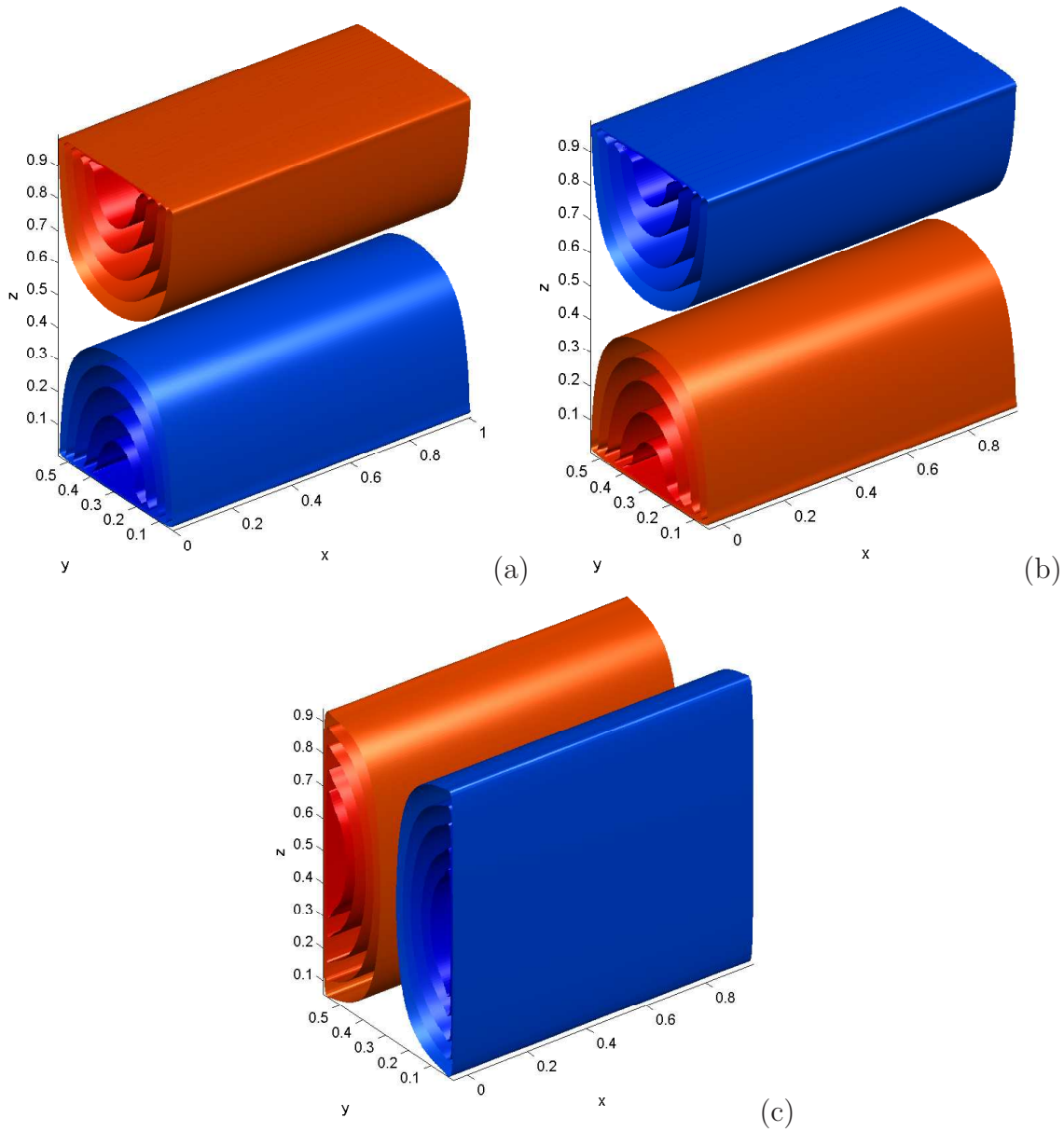

Figure 5.8: 3D illustration of two dimensional solutions in the channel of $\Gamma = 1/\sqrt{3}$: brown isosurfaces denote positive level values while blue ones represent negative values. The physical parameters in the calculations are $\epsilon = 5 \times 10^{-4}$ and $E = 5 \times 10^{-5}$. (a) u_x, (b) u_y and (c) u_z are all x independent.

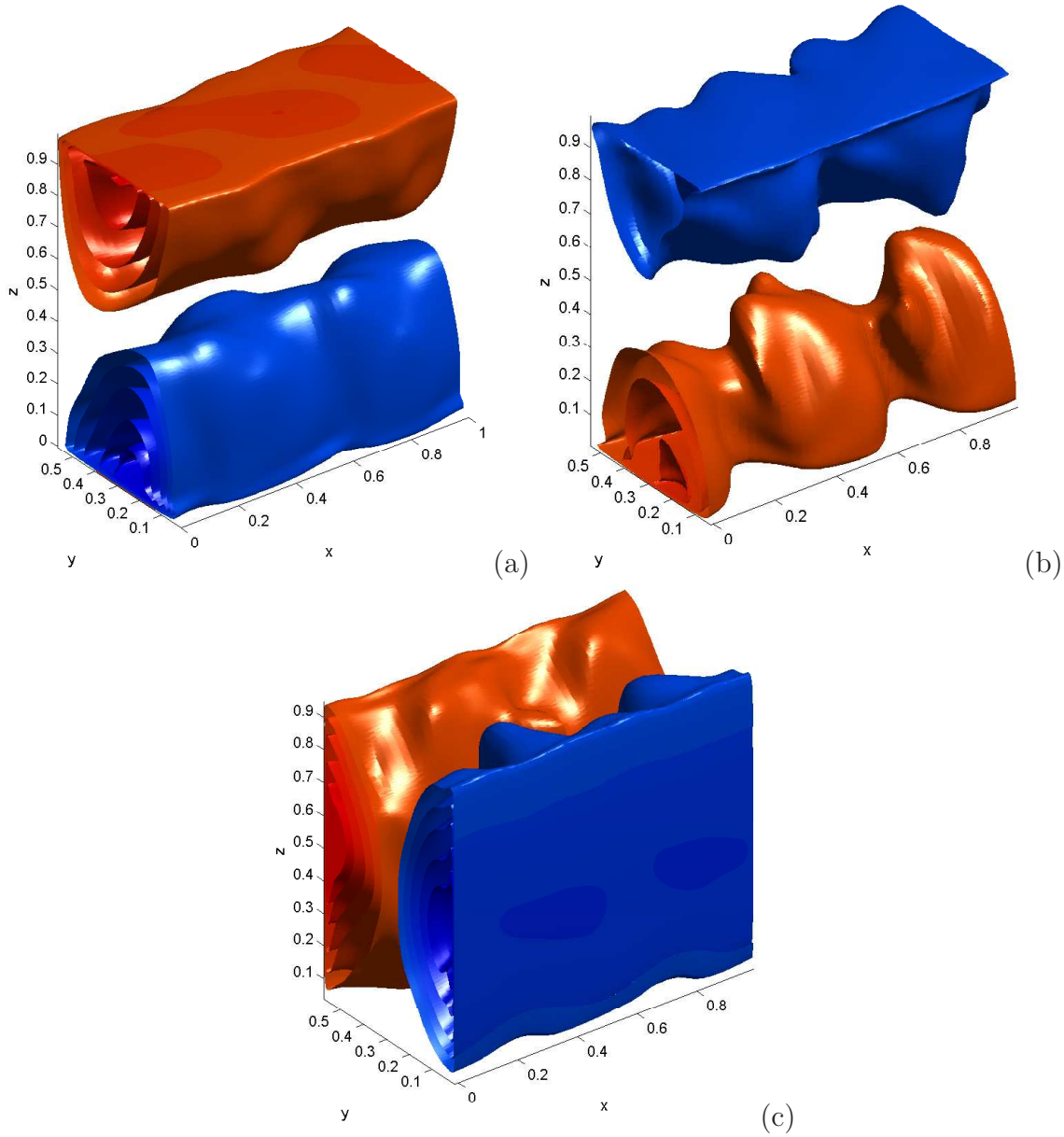

Figure 5.9: 3D illustration of three dimensional laminar solutions in the channel of $\Gamma = 1/\sqrt{3}$: brown isosurfaces denote positive level values while blue ones represent negative values. The parameters in the calculation are $\epsilon = 7.5 \times 10^{-3}$ and $E = 5 \times 10^{-5}$. (a) u_x, (b) u_y and (c) u_z are all x dependent but still smooth.

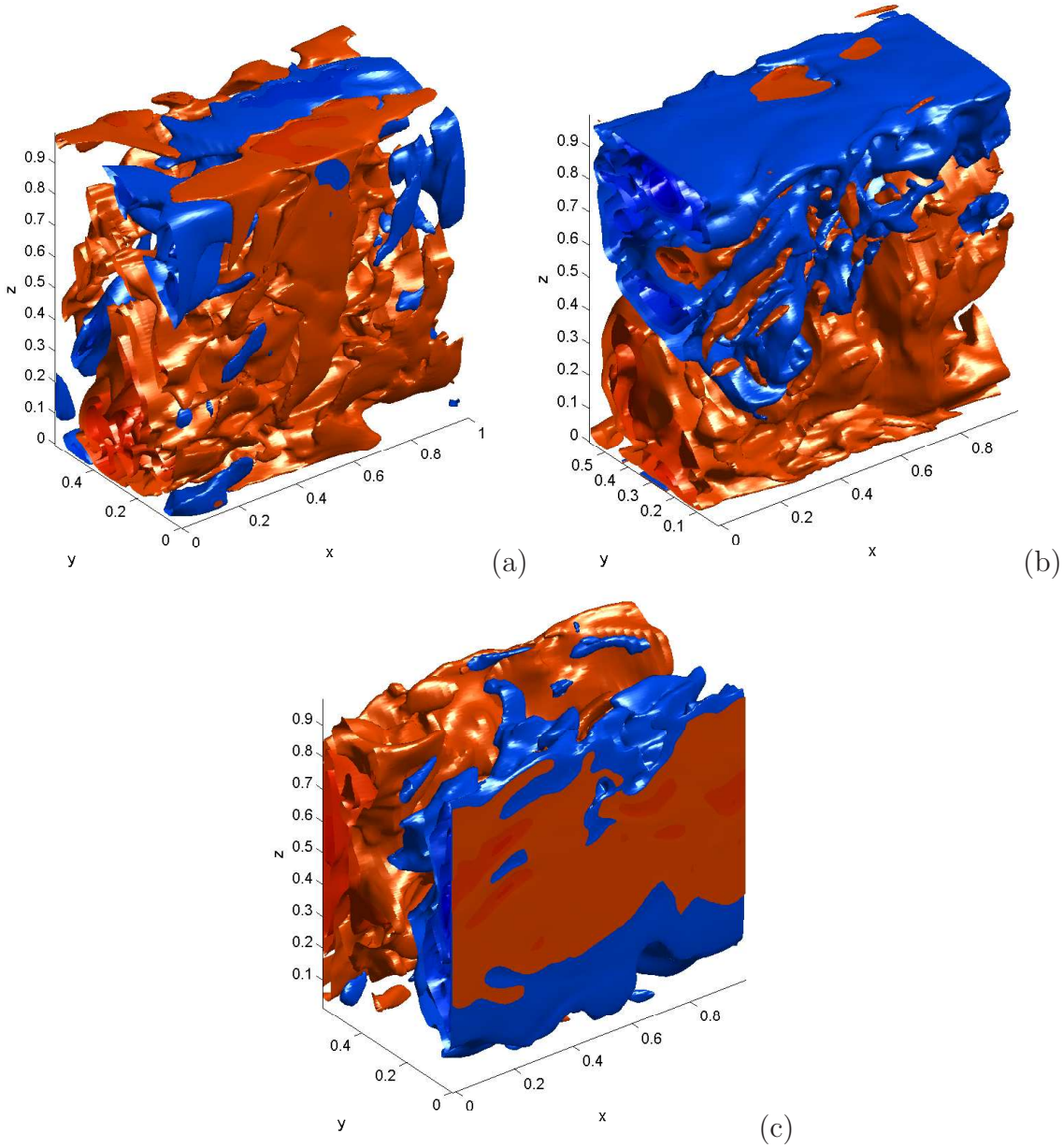

Figure 5.10: 3D illustration of three dimensional turbulent solutions in the channel of $\Gamma = 1/\sqrt{3}$: brown isosurfaces denote positive level values while blue ones represent negative values. The parameters in the calculation are $\epsilon = 5\times10^{-2}$ and $E = 5\times10^{-5}$. (a) u_x, (b) u_y and (c) u_z are all turbulent.

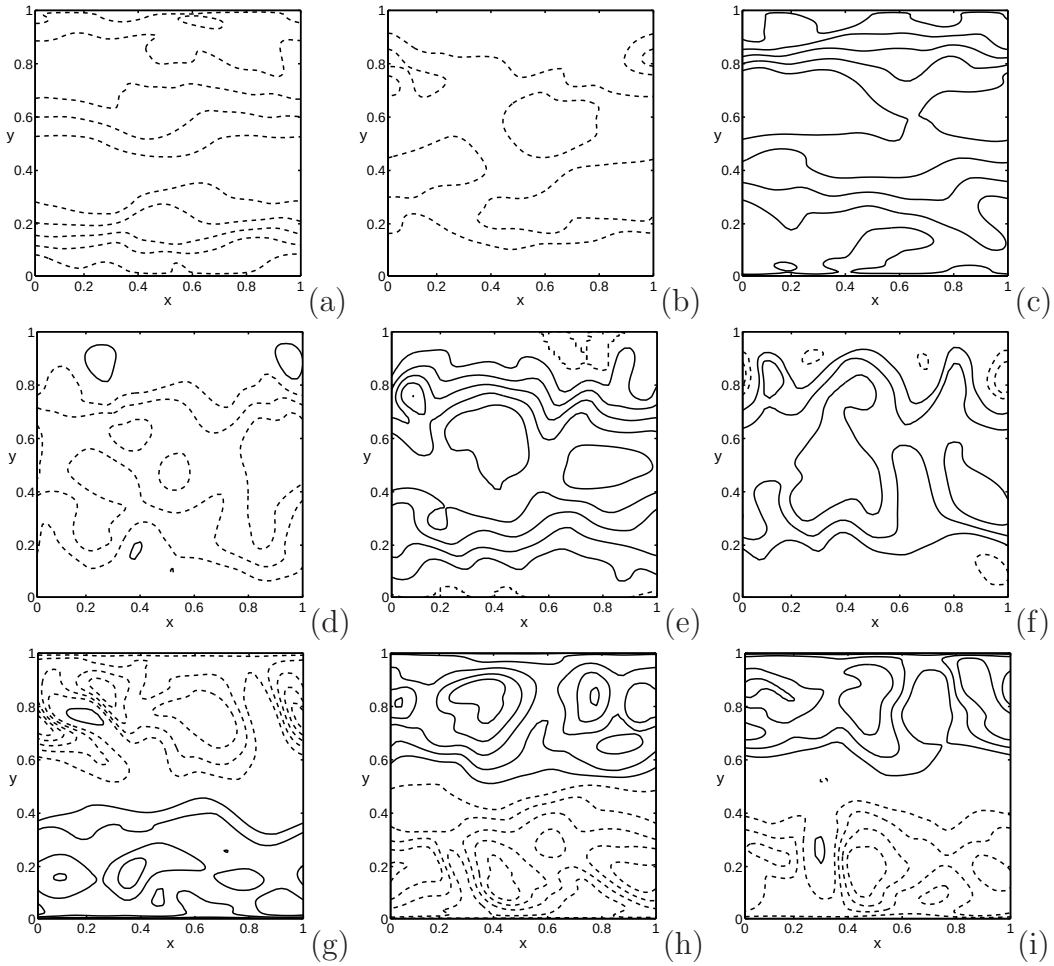

Figure 5.11: Snapshots of a 3D precessing flow at three different instants in a horizontal xy plane: contours of u_x at $z = 1/4$ are displayed in (a)-(c), contours of u_y at $z = 1/4$ are displayed in (d)-(f), and contours of u_z at $z = 1/2$ are displayed in (g)-(i). The parameters for this nonlinear solution are $\epsilon = 7.5 \times 10^{-2}$ and $\Gamma = 1$ at $E = 5 \times 10^{-5}$.

analytical expression (5.25), (ii) 3D spatial-temporally modulated 3D precessing flow and (iii) small-scaled disordered turbulence.

Finally, we consider a typical non-resonant case with $\Gamma = 1$ also at $E = 5 \times 10^{-5}$. In comparison with the resonant case $\Gamma = 1/\sqrt{3}$, our simulations starting with an arbitrary 3D flow show that the precessing flows remain two dimensional, i.e., $\partial \mathbf{u}/\partial x = 0; \partial p/\partial x = 0$, within a much larger range $0 < Re \leq 10^3$. A satisfactory quantitative agreement between the 3D simulation and the analytical expression (5.31) is achieved for $0 < Re \leq 10^3$, which is shown in Table 5.1, where the physically preferred flow is 2D, oscillatory and laminar. While the time-dependence of the 2D oscillatory flow resulting from the 3D simulation is shown in Figure 5.4(b) for $\Gamma = 1$ and $E = 5 \times 10^{-5}$, the typical spatial structure of the flow obtained from the 3D nonlinear simulation is displayed in Figure 5.3(g,h,i), along with the asymptotic solution. Figure 5.13 also confirms the 2D flow by isosurfaces plot. An extensive 3D simulation for different values of ϵ, which is shown in Figure 5.5(b), indicates that the 2D precessing flow becomes unstable to 3D instabilities at $Re \approx 1.5 \times 10^3$ ($\epsilon =$

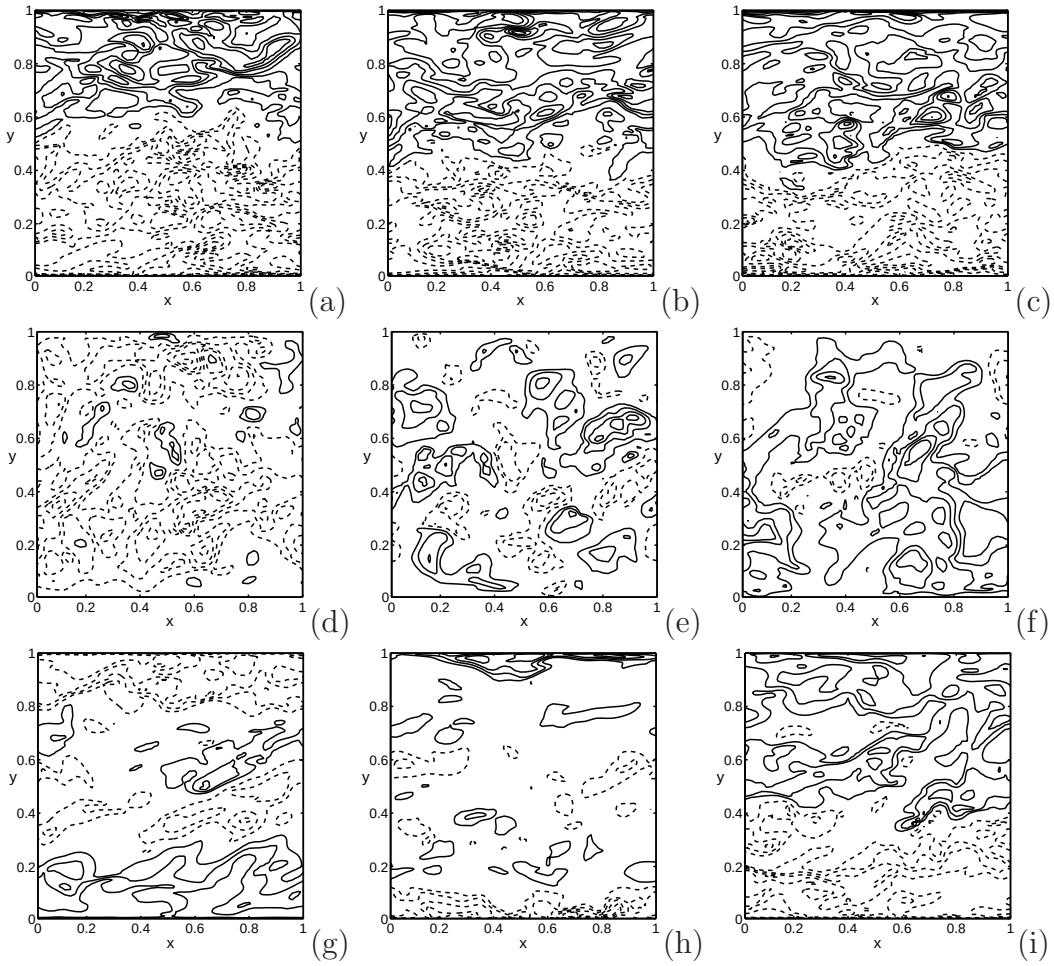

Figure 5.12: Snapshots of a 3D precessing flow at three different instants: contours of u_x in a horizontal xy plane at $z = 1/4$ are displayed in (a)-(c); contours of u_y at $z = 1/4$ are displayed in (d)-(f); contours of u_z at $z = 1/2$ are displayed in (g)-(i). The parameters for this nonlinear solution are $\epsilon = 5 \times 10^{-1}$ and $\Gamma = 1$ at $E = 5 \times 10^{-5}$.

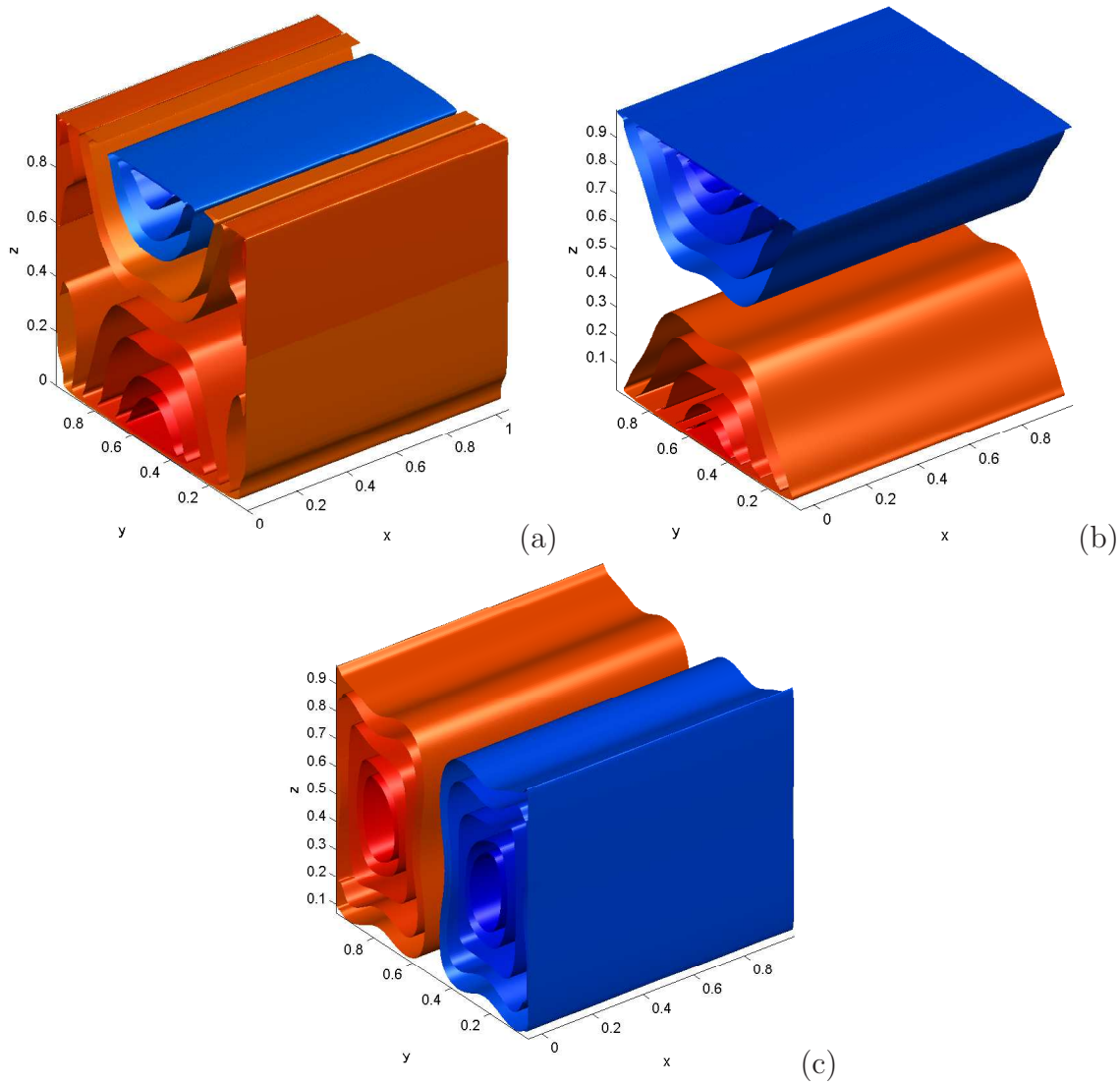

Figure 5.13: 3D illustration of two dimensional solutions in the channel of $\Gamma = 1$: brown isosurfaces denote positive level values while blue ones represent negative values. The parameters in the calculation are $\epsilon = 5 \times 10^{-4}$ and $E = 5 \times 10^{-5}$. (a) u_x, (b) u_y and (c) u_z are all x independent.

7.5×10^{-2}), in contrast to $Re \approx 1.5\times10^{2}$ in the resonant case $\Gamma = 1/\sqrt{3}$. The strongly precessing flow at $Re = 1.5\times10^{3}$ becomes fully three dimensional and is spatially and temporally modulated. Its temporal modulation is shown in Figure 5.5(b) while the spatial modulation in the $x-$direction is depicted in Figure 5.11 and 5.14. When ϵ increases further to 5×10^{-1}, i.e., $Re = 10^{4}$, the precessing flow breaks down, leading to the small-scale disordered flow which is shown in Figure 5.12 and 5.15.

There exist two major differences between the non-resonantly and resonantly precessing flows at exactly the same precessional rate. For resonantly precessing flows, the effect of viscosity, via both the Ekman boundary layers and interior viscous effects, plays a critical role while, for non-resonantly precessing flows, the effect of viscosity is of secondary importance. The amplitude of the precessing flow at resonance is $\mathrm{O}(\epsilon/E^{1/2})$ with $E \ll 1$ while the amplitude of a non-resonant precessing flow is $\mathrm{O}(\epsilon)$. It suggests the different underlying dynamics which is explicitly

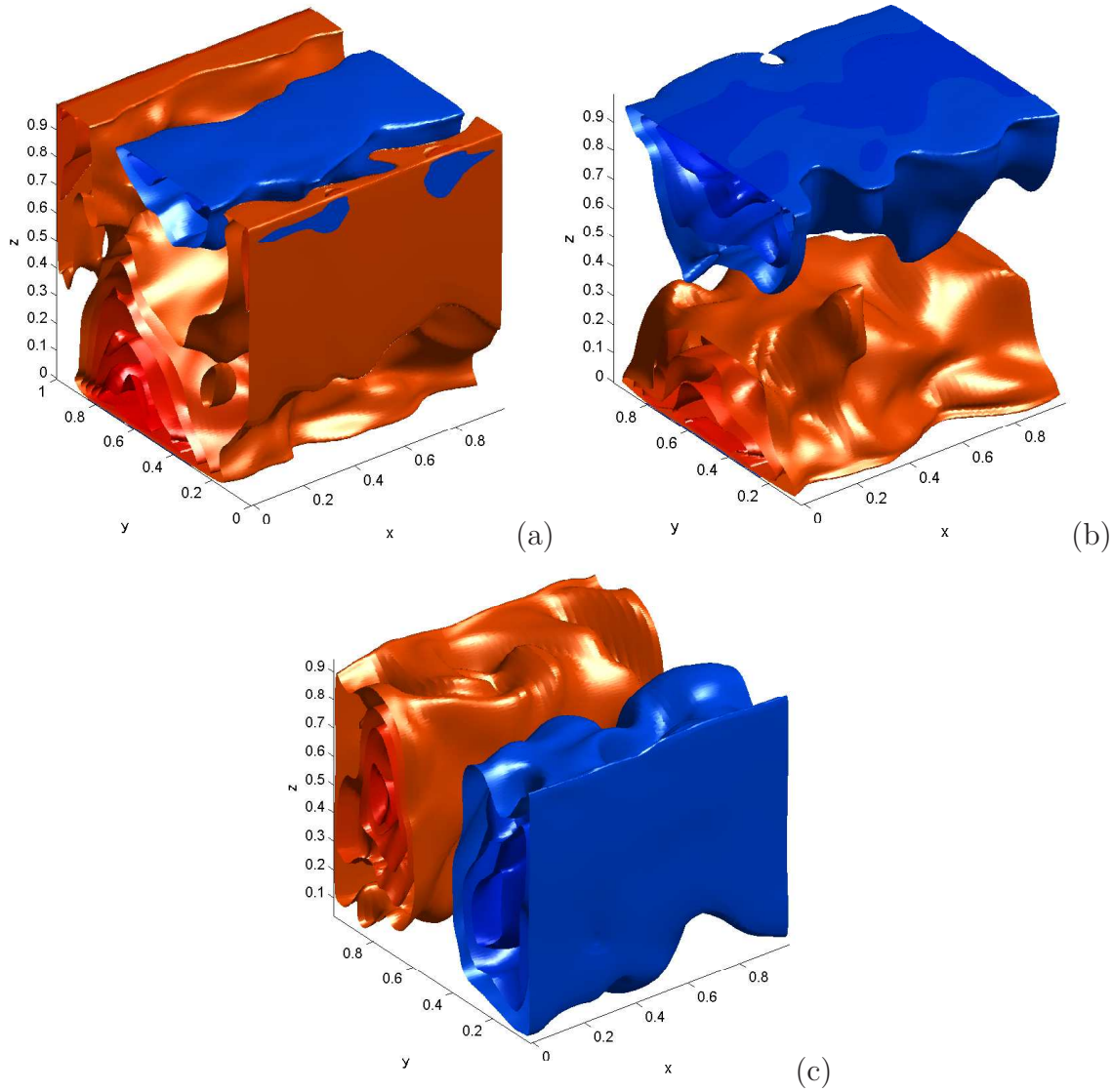

Figure 5.14: 3D illustration of three dimensional laminar solutions in the channel of $\Gamma = 1$: brown isosurfaces denote positive level values while blue ones represent negative values. The parameters in the calculation are $\epsilon = 7.5 \times 10^{-2}$ and $E = 5 \times 10^{-5}$. (a) u_x, (b) u_y and (c) u_z are all x dependent but still smooth.

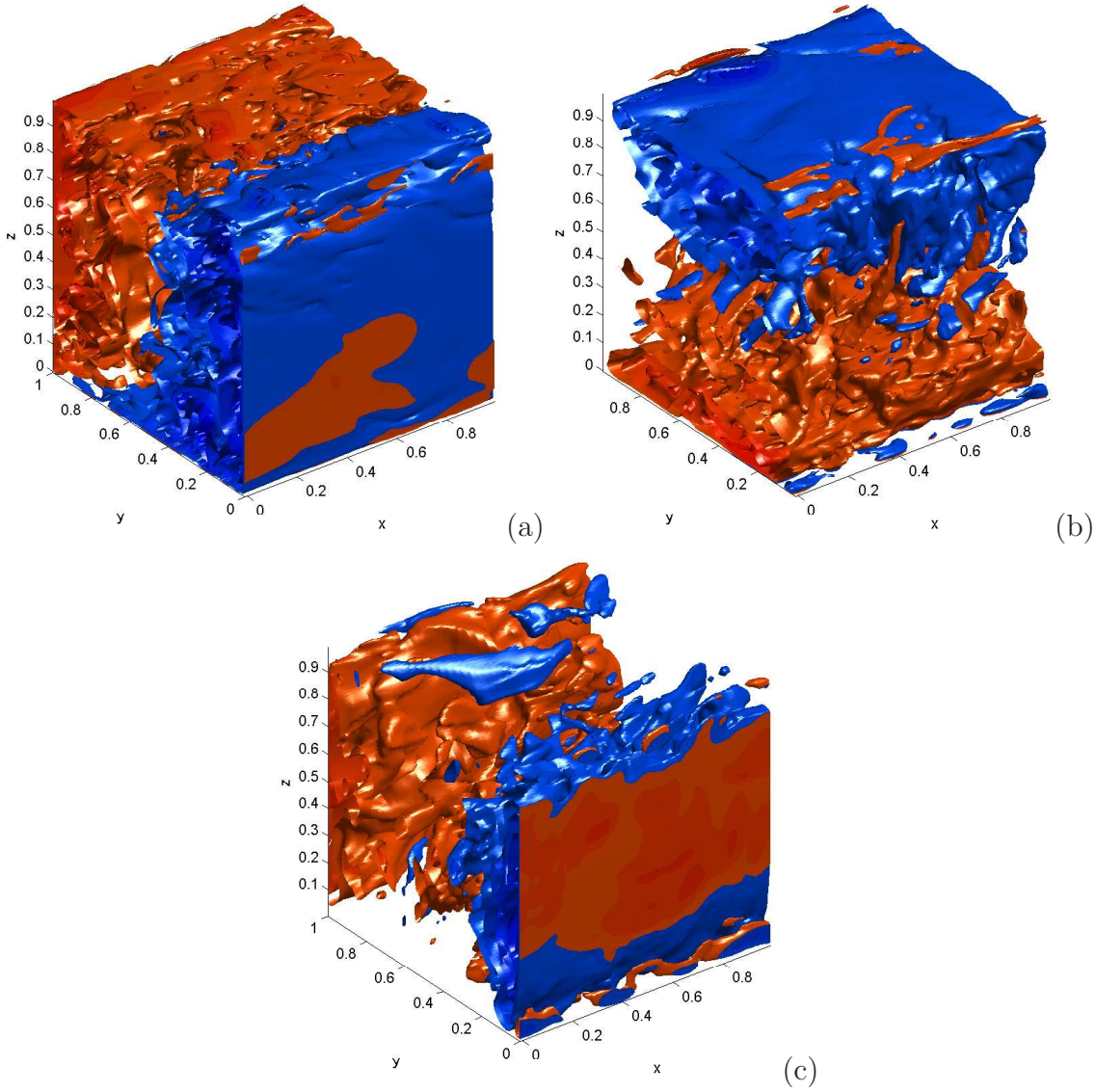

Figure 5.15: 3D illustration of three dimensional turbulent solutions in the channel of $\Gamma = 1$: brown isosurfaces denote positive level values while blue ones represent negative values. The parameters in the calculation are $\epsilon = 5\times10^{-1}$ and $E = 5\times10^{-5}$. (a) u_x, (b) u_y and (c) u_z are all turbulent.

exhibited by the asymptotic expressions (5.25) and (5.31). Since the amplitude of the flow is dramatically enhanced by resonance, the critical value of ϵ at which the three-dimensional turbulence sets in is hugely different between the non-resonantly and resonantly precessing flows.

5.5 Summary and remarks

We have studied, through both asymptotic analysis and numerical simulation, precessionally driven flows in a narrow annular channel that rotates rapidly about its axis of symmetry with angular velocity $\mathbf{\Omega}$ that itself precesses slowly about an axis fixed in an inertial frame. This precessional problem is not only experimentally realizable ([Davies-Jones and Gilman, 1971]) but also retains the mathematical simplicity and clarity of plane geometry. The essential asymptotic idea used for this study is in some ways similar to that developed for the convection problem in rotating fluid spheres ([Zhang and Liao, 2004]). Our asymptotic analysis reveals that, depending upon the aspect ratio Γ of a channel, there exist three different regimes of precessing flows for which we have derived the three asymptotic expressions. At the single-inertial-mode resonance with $\Gamma = \sqrt{3}$ for which the contribution from higher inertial modes is insignificant and the viscous effect in connection with the viscous boundary layer largely controls the precessing flow, a simple analytical solution satisfying the non-slip boundary condition is given by the expression (5.19). At the double-inertial-mode resonance with $\Gamma = 1/\sqrt{3}$ for which the viscous effect also plays an essential role in controlling the amplitude of the precessing flow, a slightly more complicated expression satisfying the non-slip boundary condition is given by (5.25). For other values of Γ, non-resonant precessing flows are described by the analytical expression (5.31) satisfying all the required non-slip boundary condition in which, however, the viscous effect no longer plays a critical role in determining the character and amplitude of the precessing flow. A satisfactory agreement between the three asymptotic solutions and the linear/nonlinear numerical simulation has been achieved for small and moderately large Reynolds numbers at an asymptotically small E.

An interesting nonlinear phenomenon found in the strongly resonant precessing flow in a precessing channel is a sudden breakdown of the large-scale 3D laminar flow to small-scale disordered turbulence. Our asymptotic and numerical analysis suggests the following transition scenario at exact resonance: the physically realizable flow in $0 < Re < \mathrm{O}(E^{-1/2})$ is 2D, oscillatory and laminar, which becomes unstable to three-dimensional instabilities at $Re = \mathrm{O}(E^{-1/2})$ leading a spatial-temporally modulated 3D flow; when Re increases slightly after the onset of the three-dimensional instability, the 3D modulated flow suddenly collapses towards small-scaled disordered turbulence. Similar sudden breakdowns of the precessing flows were observed

in various precessional experiments for spherical and cylindrical geometries ([Eloy et al., 2003; Gans, 1970; Malkus, 1989]).

Chapter 6

An Extensible Finite Element Code Built on PETSc Platform

6.1 Introduction

As a typical G2V main sequence star, the Sun is a very dynamic object mainly consisting of a radiative core and a convective envelope. Unveiled by both the direct multi-wavelength observations of its surface and indirect helioseismological investigations (See [Christensen-Dalsgaard, 2003; Gough and Toomre, 1991]) into its deep interior, complex flows, from turbulence at viscous dissipation scale (about 1cm for the Sun, see [Miesch, 2005]) up to giant granulation cells as large as $\sim$ 100Mm, exist in the convective region of the Sun. Solar convection combined with the rotational effects generates patterns of magnetic activities, for example, the 11-year cycle, through dynamo mechanisms. To understand the solar activities is so crucial for human beings because our Earth is largely subject to influences from the Sun. Even for pure scientific purposes, nowhere else can we observe the complex interactions between turbulent plasmas and magnetic fields with comparable details. As the governing equations of fluids flows and magnetic fields are mathematically difficult to solve, numerical methods are the only powerful means to look into solar convection and dynamo problems. However, modelling the flows and magnetic fields inside the convection envelope is so challenging because of the extreme parameter regimes. The molecular viscosity in the solar interior is estimated by $\nu \sim 1.2\times10^{-16}T^{5/2}\rho^{-1}\mathrm{cm}^2\mathrm{s}^{-1}$ ([Parker, 1985]). This yields $\nu \sim 1\mathrm{cm}^2\mathrm{s}^{-1}$ in the upper convection region. If we consider the giant granulation cells whose scale is 10^2Mm, the Reynolds number can be as large as 10^{14}, which implies a strongly nonlinear and hence extremely turbulent flows. Similarly, the thermal and magnetic dissipation scales are also well beyond the resolution a global numerical simulation can achieve. As pointed out in [Miesch, 2005], the dynamics over a wide range of scales, which can be 10 orders different, are not self-similar and are even coupled. This poses huge difficulties to any numerical schemes which try to resolve the full dynamics of solar convective motions. Mean-

while, the range of temporal scales is of the same situation as that of spatial scales, from a few minutes in the case of acoustic waves, up to centuries in such famous events as the Maunder minimum ([Usoskin and Mursula, 2003]). Therefore, it is also too ambitious to involve all the relevant processes in any single model. In other words, any feasible model must take into account proper approximations to capture flow structures at some scales and carefully parameterize or model the subgrid-scale (SGS) processes.

There are many high-resolution local simulations of solar convection focusing either on small scale surface layer phenomena or on dynamical processes taking place throughout the convection zone ([Hurlburt et al., 2002; Parchevsky and Kosovichev, 2007; Rincon et al., 2005; Robinson et al., 2003; Stein and Nordlund, 1998, 2000; Vögler et al., 2005; Weiss et al., 1996, 2002]). The commonly known numerical method in local simulations is the hybrid of spectral methods and finite-difference methods. Usually, fast Fourier transforms are efficient in the horizontal dimensions in the Cartesian coordinates and the vertical discretization is finite-difference schemes. Although local simulations can demonstrate characteristics of compressible convection such as granules and turbulent plumes, however, the large scale, global motions, such as giant granules, differential rotation, meridional flows and solar activity cycles, must be studied by global models. The difficulties with the vast range of spatial and temporal scales of the dynamics unavoidably enter the numerical regimes. For intermediate or even high resolution simulations, SGS turbulence can be reliably considered as effective diffusions (See [Ham et al., 2010; Miesch, 2005]). In other words, effective eddy viscosity, thermal diffusivity, and magnetic diffusivity are many orders of magnitude larger than the corresponding molecular values. There are also other more promising SGS models reviewed in [Foias et al., 2001; Lesieur and Métais, 1996]. Whatever SGS treatment adopted, currently, all the simulations fall into the class of so called large-eddy simulations (LES). Global solar convection simulations reported in the literatures were performed mainly by a few different codes. Because of the poor geometrical flexibility and difficult singularity problems, finite-difference schemes are not quite suitable for global simulations. One of well-known successful codes is the Anelastic Spherical Harmonic (ASH) code developed by [Clune et al., 1999]. Instead of fully compressible fluid equations or Boussinesq approximation, ASH code solves the equations of the anelastic approximation, which splits all variables into their horizontally mean values and fluctuations. The reference state of convection is then a 1D model ([Miesch, 2005]).Anelastic approximation filters out acoustic waves and linearize the relations between fluctuating thermal dynamical variables ([Latour et al., 1976]). ASH code is designed for spherical geometries and has been applied to such areas as global convection, tachocline and dynamo studies (see [Brown et al., 2010; Miesch, 2005] and references therein). A general-purpose hydrodynamical code mainly based on anelastic approximation as well is EULAG

(as reviewed in [Prusa et al., 2008]), whose applications to solar physics include [Elliott and Smolarkiewicz, 2002; Ghizaru et al., 2010]. More recently, a finite volume code called CharLES based on a fully compressible model was presented in [Ham et al., 2010]. CharLES solves convection-dominated fluid equations on 3D unstructured meshes. There are several beneficial features brought about by CharLES (see [Olshevsky et al., 2010]): unstructured grids offer the opportunity of resolving the thin tachocline and the sub-photospheric shear layers together with the whole convective zone in a single simulation domain; the fully compressible model can handle high specific-entropy gradient.

To tackle difficult fluid dynamics equations, such as the fully compressible convection model, a good numerical code should efficiently and intensively make use of the capability of massive parallel computing facilities. Efforts must be made to design a scheme of higher accuracy, stability, scalability, flexibility and extensibility. However, it is unlikely that all the good features are fulfilled simultaneously. We have to carefully study various numerical methods to make a suitable choice according to the specific demands of the interesting aspects of the full dynamical system.

Spectral methods, in the ASH code for example, generally don't have satisfying scalability, which limits its applications to high-resolution global simulations in which tens of thousands of CPUs may be involved. Secondly, the geometry flexibility is poor for spectral methods. The algorithm implemented in ASH code is only applicable in spherical geometries because all the variables are assumed to be expanded horizontally by spherical harmonics. Placing grids points at corresponding Gaussian abscissae further reduces the freedom of mesh generations (See [Clune et al., 1999] for more technical details). As already discussed in previous paragraphs, finite-difference methods are also not quite suitable for global simulations of solar convective motions mainly because of its difficulties in dealing with irregular boundaries and coordinates singularities ([Mohseni and Colonius, 2000]).

Finite-volume methods directly solve the integral equations of parabolic and hyperbolic conservation laws and hence are naturally adapt to fully compressible fluids equations. The spatial domain is divided into and filled with cells which can have generally irregular shapes (hexahedra, tetrahedra etc.). The accuracy order of a finite-volume scheme is determined partly by how many cells involved in the interface-value reconstructions ([Shu, 1997]). To deal with large advection terms, another big issue is the choice of stencils and numerical fluxes. Essentially Non-Oscillatory (ENO) and Weighted ENO (WENO) schemes are high order, TVD schemes which greatly ensure the numerical accuracy and stability for highly turbulent flow or even discontinuous shock waves (for example, [Liu et al., 1994; Shu, 1997; Shu and Osher, 1988; Shu et al., 1992]). The CharLES code introduced above has incorporated the WENO with an explicit Runge-Kutta time advancing scheme. The

explicit non-oscillatory schemes also have drawbacks. Both ENO and WENO will do harm to scalability. ENO adopt self-adaptive stencil choices in the regions where the solutions have large gradient while WENO allows several stencils to contribute, together, in a weighted manner, to the reconstructions. Therefore, compared with fixed-stencil schemes, ENO and WENO intensify the data exchanges among mesh blocks distributed to different CPUs. This implies that finite-volume schemes which benefit from the stability and accuracy resulting from advanced reconstruction techniques essentially cost their scalability under the circumstance of fine meshes and massive number of parallel processes.

Another class of well developed and widely applied numerical PDE solving methods are finite-element methods (hereafter FEM). Classical Galerkin FEM , based on the minimization of the energy norm, solve the variational form of PDEs by Galerkin approximation. General theories of FEM can be found in a huge number of references, in which [Brenner and Ridgway Scott, 2008] is strongly recommended and a detailed historical review of the evolution of FEM is in [Felippa, 2001]. Briefly speaking, as an illustration of FEM, we shall introduce the variational formulation of the elliptic boundary value problem

$$Lu = f \quad \text{in } \Omega, \ u = 0 \quad \text{on } \partial\Omega, \tag{6.1}$$

where Ω is a bounded open subset of $\mathbb{R}^d$ (hereafter $d = 3$) and $u : \Omega \to \mathbb{R}$ is the unknown function in some infinite dimensional function space V. Here $f : \Omega \to \mathbb{R}$ is a given function and L denotes the uniformly elliptic partial differential operator possibly of the form

$$Lu = -\partial_i(a_{ij}(x)\partial_j u) + b_i(x)\partial_i u + c(x)u.$$

. The related variational problem is

$$a(u, v) =< f, v >,$$

where

$$a(u, v) = \int_\Omega a_{ij}\partial_i v \partial_j u + v b_i \partial_i u + cvu \mathrm{d}x \tag{6.2}$$

is a bilinear form. v is a test function and the variational form is obtained by multiplying v to both sides of (6.1) and then doing integration by part in Ω. The Galerkin finite-element approximation of the variational problem is then to find $u_h \in V_h$, where V_h is a finite dimensional subspace of V, such that

$$a(u_h, v_h) =< f, v_h >, \ \forall v_h \in V_h.$$

Suppose that $\{\phi_1, \phi_2, \cdots, \phi_N\}$ is a basis for V_h. Usually, the basis functions can be

nodal interpolating polynomials and the order of local truncation error of a scheme is hence determined by the order of these piecewise polynomials. Then it is equivalent that

$$a(u_h, \phi_i) =< f, \phi_i >, \quad i = 1, 2, \cdots, N.$$

Writing u_h in the form

$$u_h = \sum_{i=1}^{N} z_i \phi_i,$$

we are led to the system of equations

$$a(\phi_j, \phi_i) z_j =< f, \phi_i >, \quad i = 1, 2, \cdots, N,$$

which we can write in the matrix-vector form as

$$Az = b. \tag{6.3}$$

A typical implementation of a finite-element scheme consists of four steps: first, a polyhedron mesh (e.g. tetrahedron triangulations) is generated to fill the whole simulation domain; second, element-wise matrices and right-hand-side (RHS) vectors are constructed; third, the global linear system is built by gathering element matrices and vectors; finally, the linear equations are solved globally, usually by Krylov subspace (KSP) iteration methods.

Classic FEM have proved successful and efficient in applications to symmetric, self-adjoint problems such as solid mechanics equations and diffusion type equations. However, the existence of convection terms prevents standard Galerkin FEM from being effectively applied to general convection-diffusion equations, especially the convection-dominated problems. This is because the non-symmetric convection operator leads to the loss of the best approximation property in energy norm of the Galerkin method. Various alternatives to standard FEM, e.g. the Streamline-Upwind Petrov-Glerkin (SUPG) method (see [Donea and Huerta, 2003]), have already been well studied to cope with convection-dominated problems. Generally, these FEM are called stabilized finite-element schemes, which make great breakthrough in modelling fluid dynamics problems. A finite-element scheme with a grad-div stabilization technique has been successfully applied to incompressible viscous flows and corresponding planetary dynamo problems ([Chan et al., 2001, 2007, 2010]).

There are many advantages in FEM. The first of all is the great flexibility. Geometrically, due to the general unstructured elements in the mesh, FEM are adapted to any arbitary physical domains with Lipschitz continuous boundaries. The refinement and non-uniform mesh grading are also simple to conduct. This property is extremely helpful in the presence of thin shear layers or viscous boundary layers, in which smaller mesh sizes are in need to resolve small-scale motions. Mathematically,

unlike finite-difference and finite-volume methods, which require local operations within wide stencils containing adjacent nodes or cells, the key implementations of FEM algorithms are localized into elements. Interpolations, integrations and local assembly are all done within elements. There is no explicit inter-element data exchanges at all. Then it is understandable why FEM have good *hp*-adaptivity – mesh refinement or elements merging are straightforward; changing the order of a scheme simply means adopting higher/lower order elements which contain more/less nodes; even changing element types only leads to small amount of code rewriting. By contrast, for instance, if the order of the scheme is changed, substantial global modifications must be done for finite-difference/finite-volume codes because the choice of stencils directly affects interior nodes/cells, boundary conditions implementations and communications among processes. The great flexibility is precious in any sense. In the code developing stage, we can always start from the simplest equation, such as Poisson equation, the simplest linear tetrahedral element and the simplest mesh partition, like Element-by-Element (EBE) technique. Such primitive code is quick to debug and validate. The ensuing extensions of the code can result in a lot of variants adapted for different dynamical problems, e.g. incompressible flows and compressible flows.

Another concern is the scalability. Generally speaking, the reason why we cannot simulate fluid dynamical processes on grids of very high resolution often is not because there are not enough CPUs available but there is no speedup at all if too many CPUs are used. Ideas of parallelization of fluid dynamics simulations are all mainly based on the decomposition of the global domain into subdomains. Smaller size local problems on subdomains are then distributed to a number of processes. These processes run simultaneously on different processors. If all the subdomain-problems were independent of one another, the parallelization would be fully scalable – the overall speed is doubled if the number of processes is doubled, which is called a "strong scalability". However, strong scalability is never achieved or even expected in fluid dynamics simulations because the physical interactions among fluid in different subdomains are inevitable. Numerically, data exchanges among processes, which pass the physical interactions, must happen and will limit the overall running speed if such communications are very intensive. Practically, high resolution grids or meshes mean vast number of grid nodes or degrees of freedom. If one employs more processors in the hope of reducing subdomain-problems, it must result in more subdomains and larger specific area of interfaces. Because information exchanges take place on interfaces, communications become more intensive. After some point, the slowdown owing to communications certainly will outweigh the speedup due to massive parallelization. Specifically speaking, for FEM, as schemes end up with a linear equations system like (6.3). During the parallel solving process, communications take place in such operations as matrix-vector products. The communications

are indirectly (but still essentially) related to underlying physical interactions among neighboring subdomains. The scalability of a parallel linear equations solver can be improved by elegant algebraic and geometric optimizations.

There are two major ideas to address the scalability dilemma. The first one is a hardware-level solution. If the bandwidth and clock-frequency of inter-processor communications could be comparable to the commands execution and data processing speed of CPUs, the communications would no longer become the bottle neck, which is unlikely in a near future. The other feasible option is better algorithms. Within the FEM framework, the development of numerical methods for large algebraic systems is central in the development of efficient codes. The domain-decomposition-methods (DDM) based on the matrix space decomposition has long been studied since 1980s (see [Chan and Mathew, 1994; Smith et al., 1996; Toselli and Widlund, 2005; Xu and Zou, 1998]). DDM are aimed to achieve so called "weak scalability" – the overall running time remains unchanged if the local workload on individual processors does not vary. Successful DDM schemes ensure that the convergence rate in solving the linear system resulting from FEM formulations is independent of the typical mesh size h. Abstract overlapping domain-decomposition methods such as the additive Schwarz method and its generalizations can be conveniently incorporated in various finite-element and implicit finite-difference/volume schemes (see [Aitbayev et al., 1999; Cai, 1990, 2005, 2009; Cai and Zou, 2002; Cai et al., 2002; Luo et al., 2011; Yang and Cai, 2011]). The other large class of DDM are the non-overlapping substructuring methods including dual methods, primal methods and hybrid dual-primal methods (see chapters in [Toselli and Widlund, 2005] and references therein). Generally speaking, according to [Kong, 2011], optimal implementations of substructuring methods are closely related to underlying properties of every particular equation and spatial domain. There has not been any standard/univeral implementation of such promising methods as FETI-DP. Nevertheless, there do exist quite a few applications, e.g. [Farhat et al., 2000; Klawonn and Rheinbach, 2010; Li, 2005]. DDM, theoretically, can guarantee the weak scalability of a finite-element scheme, which implies the potential of conducting unprecedentedly high resolution simulations.

Currently, a finite-element code for 3D fully compressible fluids convection is under development. This code finally will implement a SUPG finite element scheme with an abstract Additive Schwarz Preconditioner. Also, we will build the code on PETSc platform ([Balay et al., 2011]). PETSc is a parallel library assisting users by reducing their workload in managing communications. The carefully designed data structures and routines ensure the optimized quality of communications. Therefore, user defined codes can mainly focus on the delicate algorithm. PETSc provides interfaces to a number of optional external software packages and toolkits such as SuperLU, ParMetis and Parstix. It also supports various modes of parallelization

such as MPI, shared memory pthreads, and NVIDIA GPUs, as well as hybrid MPI-shared memory pthreads or MPI-GPU parallelism. The intensive error checking mechanism and friendly output format lead to very effective debugging. The code writing was launched in November 2011 and the code development is scheduled into four major phases.

- *Stage 1*: The code is solving second order general elliptic equations on a 3D tetrahedra mesh in the spherical/spheroidal domain. The objectives are to build the general data structures and to implement a standard finite-element scheme. All data abstraction and interfaces are ready for further extensions.
- *Stage 2*: The model will be extended to a general scalar convection-diffusion equation, which requires the SUPG finite element scheme to cope with the large convective term. At this stage, the code can model some transport processes with prescribed velocities.
- *Stage 3*: Fully compressible Navier-Stokes equations will be solved and intermediate resolution simulations of solar convection can be carried out.
- *Stage 4*: DDM will be incorporated in the code to challenge high-resolution simulations.

As a large project, it is impossible to complete the fully functional code in the short final stage of my PhD degree work. So far, the first stage has been completed. The code descriptions will be presented in this chapter. Meanwhile, we will also report the validation of the code and its application to a simple planetary mass distribution problem.

In the following sections, the declarations and public interfaces of important classes will be discussed in §6.2. A quick application will be found in §6.3. This chapter will be closed by concluding remarks in §6.4.

6.2 PETSc Finite Element Code for 3D Second Order Elliptic Equations

6.2.1 General Pictures

We are solving the second order elliptic equation in an oblate spheroidal domain whose equatorial radius is unity.

$$-\nabla^2 u + \lambda u = f, \quad u|_{\partial\Omega} = g, \tag{6.4}$$

Note that if $\lambda > 0$, the equation is the linearized Poisson-Boltzmann equation (LPBE) while if $\lambda < 0$, it is then the Helmholtz equation. The equation degenerates to a Poisson equation at $\lambda = 0$. If the 10-node tetrahedral elements are

adopted to form the mesh triangulations, the standard Galerkin FEM lead to the linear system (6.3). The degrees of freedom (Dof) can be split into two sets, interior Dof which are nodal values defined on interior nodes, and Dirichlet boundary Dof which are nodal values defined on Dirichlet boundary nodes. The matrix A and RHS b can also undertake such decomposition. Then the (6.3) can be fully written

$$\begin{pmatrix} A_{II} & A_{IB} \\ A_{BI} & A_{BB} \end{pmatrix} \begin{pmatrix} z_I \\ z_B \end{pmatrix} = \begin{pmatrix} b_I \\ b_B \end{pmatrix}, \tag{6.5}$$

where the subscripts I and B respectively denote the "interior" and "boundary" components. Because the Dirichlet boundary conditions impose the values on boundary Dof z_B, it can be shown that the linear system taking into account of Dirichlet boundary conditions is

$$A_{II} z_I = b_I - A_{IB} z_B \tag{6.6}$$

(See [Toselli and Widlund, 2005]). In other words, only the interior Dof are solved. We call the data "equation-mode data" if they are stored globally according to the indices of unknowns, which are directly linked to the global numbering of elements and mesh nodes; on the other hand, "element-mode data" are stored locally on elements and indexed according to the local numbering of nodes inside elements. FEM implementations require lots of gather/scatter processes between equation-mode data and element-mode data. Because of the parallelization, the indices mapping between two modes frequently take place among processes, which induces communications. In the coding, major efforts are done at three levels: the global parallel linear system, the local elementwise operations and data gather/scatter.

The code is written in C++, which is an Object-Oriented Programming (OOP) language. OOP has such modern features as data abstraction, encapsulation, polymorphism and inheritance. OOP became the dominant programming methodology since mid 1990s as the classical Process-Oriented Programming was no longer able to cope with and maintain codes of great complexity. The data abstraction of OOP indicates that objects containing data and corresponding actions are considered to be a new data type from an external point of view. For example, the element can be abstracted to be a type of data. Any object of the "element" type will self-contain its data and operations that represent properties a realistic element should hold. OOP mechanism also makes sure that users can manipulate and interact with an object only via its public interfaces. All the other data and operations are encapsulated and protected from any external access. The encapsulation not only is the means to realize the data abstraction but also is a guarantee of modularity. We shall still use the "element" type data as an example. An "element" object should be able to return a locally assembled matrix. However, how this object assembles its local matrix is encapsulated and invisible to its users. Users do not necessarily

know the matrix construction approach but only need to take away the matrix via some data-obtaining routine. It is apparent, if we switch from a tetrahedral element to a hexahedral one, for example, the local matrix construction part must be rewritten, but the users of the matrix do not have to make any little bit change because they are not affected and cannot see any difference, from an external point of view. A code with such good modularity would be extensible because improvements and updates are only localized into separate modules. Inheritance and polymorphism are also crucial in a good extensibility. Overloading and dynamic binding make it possible to determine at runtime the particular version of routines that should be activated or applied. In this sense, we are able to produce one unique user interface for different tasks under different conditions. This functionality will be well illustrated by the **Calc** class of this code. In what follows, the most important several classes will be introduced one by one.

6.2.2 ParallelEnv Class

The class **ParallelEnv** initializes the parallel environment. The declarations of members of this class are in **ParallelEnv.h** and function members are defined in **ParallelEnv.cpp**. **ParallelEnv** class encapsulates also a series of MPI toolkits. Although PETSc handles the majority of communications, we still have to explicitly call MPI functions to conduct some auxiliary communications. **ParallelEnv** class hence is also a supplementary module of parallelization. We will discuss a few important data and interfaces.

ParallelEnv::ParallelEnv(int *, char *, char *, char *)**:
The constructor initializes the global parallelization by **PetscInitialize(int *argc, char ***argv, char *file, char *help)**. The global communicator PETSC_COMM_WORLD is then established. The index of each process is assigned and the total number of processes within the communicator is recorded. The constructor of the **ParallelEnv** object is the first function called in the programme at runtime.

ParallelEnv::∼ParallelEnv():
The destructor finalizes the parallel environment at the end of the programme running. It is the last command in the execution.

void ParallelEnv::BCast(*varargin*):
This interface broadcasts data from a root process to others. Depending on different arguments passed to it, the function is overloaded for broadcasting integer/double variables/arrays. For example, "BCast(PetscReal *p);" will broadcast a double precision variable *p, while "BCast(PetscInt *Begin, PetscInt *End);" results in the broadcasting of an integer array from the address "Begin" to "End-1".

void ParallelEnv::Reduce(*varargin*):

Similar to **BCast()**, **Reduce()** is also multi-overloaded. It utilizes **MPI_Reduce()** and **MPI_Allreduce()** to apply such reducing operations as MPI_SUM, MPI_MAX, etc., to variables/arrays.

6.2.3 Element Class

Element class is one of the most central modules of the FEM code. In this version, **Element** class is an abstraction of a mixed 4-node linear/10-node quadratic isoparametric tetrahedral element, as depicted in the Figure 6.1(a). It contains not only geometrical data, such as nodes indices, nodes coordinates, boundary nodes, locations of Gaussian abscissae, etc., but also algebraic structures including local Dof, local Matrix, local RHS vector and so on. All relevant operations on these data are also contained within the scope of the class. The members declarations are in **Element.h** and corresponding definitions and implementations are in **Element.cpp**.

Important Private Data Members

GNum: **GNum** is an integer vector. The indices of **GNum** represent the local numbering of nodes within the element. Its components are the global numbering.
Coor: **Coor** stores the Cartesian coordinates of the ten nodes in the element. It is of a composite-vector type, namely, **vector**< **vector**<**PetscReal**> >.
DiriBdNode: This member contains the global indices of nodes located on the Dirichlet boundary. It can be an empty integer vector if the element does not intersect the boundary.
Neighbor: Because FEM implementations generally end up with a large sparse linear system, in PETSc, the knowledge of the non-zero pattern is required in the pre-allocation stage. Neighboring elements contribute to non-zeros in the global matrix. Therefore, we need such member holding a list of elements adjacent to this element.
LocMat: Elementwise Local matrix is computed by carrying out local integration of the bilinear form (6.2). It is worth mentioning that the dimension of **LocMat** is (NOD×NDOF)×(NOD×NDOF), where NOD and NDOF are two macros respectively denote the total number of nodes in an element and total number of Dof defined on each node. In the current code, NOD is ten as elements in the mesh are all quadratic ones; NDOF is one because we are solving a single scalar equation. To extend the code into multi-equation, vectorial-function mode, we simply change the macro NDOF.
LocRHS:**LocRHS** is the local RHS vector of the dimension NOD×NRHS. NRHS is another macro indicating the number of forcing components defined on each node. Usually, NRHS is equal to NDOF.

Key Private Implementation Functions

void Element::SetLocMat():

Let the elementwise matrix be A^e and an element domain be K. Its components are computed as

$$A_{ij}^{(e)} = \int_K \nabla\phi_i \cdot \nabla\phi_j + \lambda\phi_i\phi_j \mathrm{d}\tau. \tag{6.7}$$

Note the indices i, j here are all "element-mode" numbering.However, we always do the integration by Gaussian quadrature in a barycentric coordinate system (see [Coxeter, 1969]). In the tetrahedral element, we have four barycentric coordinates L_1, L_2, L_3 and L_4, three of which are independent. Due to the coordinates transformations inside the element.

$$x = \sum_{i=1}^{4} x_i L_i, \quad y = \sum_{i=1}^{4} y_i L_i, \quad z = \sum_{i=1}^{4} z_i L_i,$$

where x_i, y_i, z_i are the Cartesian coordinates of the four vertices of the tetrahedron, we can compute the Jacobian matrix

$$\mathbf{J} = \begin{bmatrix} \dfrac{\partial x}{\partial L_1} & \dfrac{\partial y}{\partial L_1} & \dfrac{\partial z}{\partial L_1} \\ \dfrac{\partial x}{\partial L_2} & \dfrac{\partial y}{\partial L_2} & \dfrac{\partial z}{\partial L_2} \\ \dfrac{\partial x}{\partial L_3} & \dfrac{\partial y}{\partial L_3} & \dfrac{\partial z}{\partial L_3} \end{bmatrix},$$

and its inverse $\mathbf{J}^{-1}$. The nodal interpolating basis functions can also be written in barycentric coordinates

$$\begin{aligned} &\phi_i = L_i(2L_i - 1), \quad i = 1, 2, 3, 4, \\ &\phi_5 = 4L_1L_2, \phi_6 = 4L_1L_3, \phi_7 = 4L_1L_4, . \\ &\phi_8 = 4L_2L_3, \phi_9 = 4L_2L_4, \phi_{10} = 4L_3L_4 \end{aligned}$$

In the implementation, we compute (6.7) by

$$A^{(e)} = \int_0^1 \int_0^1 \int_0^1 \left[(\mathbf{J}^{-1}\nabla_L \mathbf{N})^T (\mathbf{J}^{-1}\nabla_L \mathbf{N}) + \lambda \mathbf{N}\mathbf{N}^T\right] |\mathbf{J}| \mathrm{d}L_1 \mathrm{d}L_2 \mathrm{d}L_3,$$

where

$$\mathbf{N} = \{\phi_1, \phi_2, \cdots, \phi_{10}\}^T$$

and

$$\nabla_L \mathbf{N} = \begin{bmatrix} \frac{\partial \phi_1}{\partial L_1}, & \frac{\partial \phi_2}{\partial L_1}, & \cdots, & \frac{\partial \phi_{10}}{\partial L_1} \\ \frac{\partial \phi_1}{\partial L_2}, & \frac{\partial \phi_2}{\partial L_2}, & \cdots, & \frac{\partial \phi_{10}}{\partial L_2} \\ \frac{\partial \phi_1}{\partial L_3}, & \frac{\partial \phi_2}{\partial L_3}, & \cdots, & \frac{\partial \phi_{10}}{\partial L_3} \end{bmatrix}.$$

void Element::SetRHS():
Similar to setting local matrix, we compute a local integration to obtain the local RHS vector $b^{(e)}$. Using the notations introduced above, we have

$$b^{(e)} = \int_0^1 \int_0^1 \int_0^1 f(L_1, L_2, L_3)\mathbf{N}|\mathbf{J}|\mathrm{d}L_1\mathrm{d}L_2\mathrm{d}L_3.$$

void Element::SetDiriBC():
This function applies the boundary conditions according to (6.6). It extracts **LocMatII**,**LocMatIB** and modifies **LocRHS** into **LocRHSI**. After the execution of **SetDiriBC()**, the local matrix and RHS vector are ready to be gathered into their global locations.

Public User Interfaces

Majority of the public functions are data passing services and, hence, are declared with the **inline** directive due to their simplicity. Through these functions, constant references of private data members such as **GNum**, **LocMatII**, **LocRHSI**, etc., are fetched and passed to external users. The public interfaces also include a few other functional routines doing some elementwise quantities computations, which are useful in the post-processing. The data updating interfaces for future time-dependent problems are also placed without implementations in the current code.

6.2.4 Mesh Class

The **Mesh** class is global-level abstraction of the geometry and mesh grids. A **Mesh** object stores the mesh and partitioning data. The tetrahedral mesh is generated by NetGen ([Schöberl, 2004]) while a balanced partition is done by utilizing the parallel graph/mesh partitioning tool ParMetis ([Karypis and Schloegel, 2011]). The global mesh sketch in an oblate spheroidal domain is shown in the Figure 6.1(b). A proper partition is essential in minimizing the specific area of interfaces among substructures distributed onto different processes. As the convention, the declarations are all put in **Mesh.h** and corresponding definitions and implementations are placed in **Mesh.cpp**.

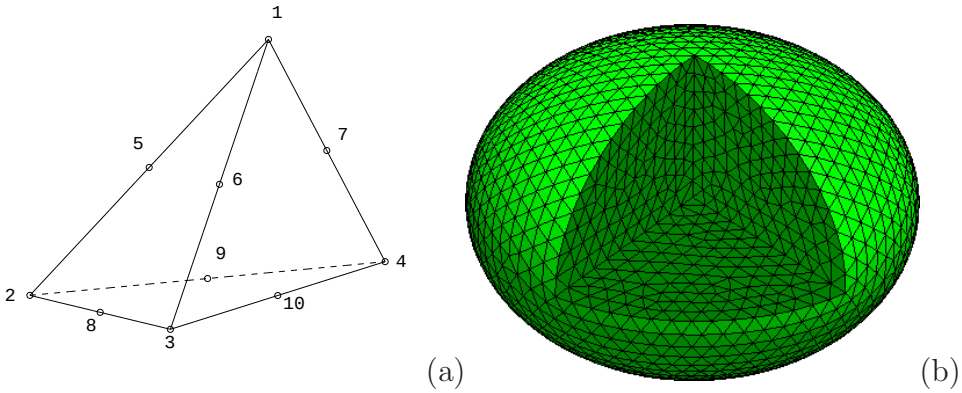

Figure 6.1: The sketch of a single ten-node tetrahedral element and the oblate spheroidal mesh, in the panel(a), the local numbering of nodes in the element is presented. A linear tetrahedral element only involves the four vertices while all the ten nodes will enable a quadratic element.

Important Public Data Members

Mat Coord: **Mat** is a PETSc matrix object. **Mat** type supports serial/parallel dense/sparse formats. **Coord** is a parallel dense matrix, namely **MATMPIDENSE** type. The Cartesian coordinates of all the mesh nodes are stored in this matrix. PETSc manages the storage of data over the communicator and all processes access the data via the routine **MatGetValues()**.

Mat ENod: Also as a parallel dense **Mat** object, **ENod** is a NEles×NOD matrix containing the global numbering of nodes in elements. NEles is the total number of elements in the mesh. Each row of **ENod** records an element by its ten nodes. Elementwise data **GNum** is the local portion of **ENod**.

Vec NdSurf: **Vec** is a PETSc vector object. Similar to the **Mat** object, **Vec** type also support both serial and parallel formats. **NdSurf** is a vector of boundary nodes indices. Element objects use the information to apply boundary conditions to the linear system.

AO Node2Unknown: Application Ordering (**AO**) is a very useful PETSc object. It is used to realize the mapping between "element-mode" indices and "equation-mode" ones. Only via the routines **AOApplicationToPetsc()** and **AOPetsc-ToApplication()** can the gather/scatter operations be done.

Usually, in OOP, data members should not be parts of the public interface. Here, in the **Mesh** class, however, we allow public access to the above four data members. It is safe because these PETSc objects can only be used via PETSc routines. Any access attempts in the manner of using objects of C++ built-in type fails at compiling time.

Key Private Implementation Functions

void Mesh::MeshGeneration():
This function generates the finite-element mesh at the pre-processing stage. Currently, the mesh is read in from mesh files exported by NetGen. It is also possible to generate the volume mesh through API of mesh generating libraries such as **nglib** and **tetgen**. In any case, the mesh generation is an independent module. Altering the means of mesh generation never causes modifications to the rest of the code.

void Mesh::MeshPartition():
Mesh partitioning divides the whole spatial domain into subdomains, which respectively are assigned to processes in the communicator. A subdomain is not necessarily an intact one piece. It is numerically feasible to form a subdomain by picking up elements randomly regardless of their spatial locations. Element-by-Element (EBE) schemes usually, either explicitly or implicitly, implement such irregular mesh partitioning. However, as we have discussed, irregular partitioning will result in much larger specific area of interfaces among subdomains, which leads to a very poor scalability. A non-trivial partition is to cut the whole domain into blocks consisting of similar number of elements and minimize the total contacting area among blocks. In other words, mesh partitioning balances the workload on processes and reduces communications. In this code, ParMetis is employed via PETSc **MatPartitioning** object. After the partitioning, the **vector<PetscInt>** type data member **EleIdx** will contain the indices of elements assigned to the current process and **ENod** will contain fill-reducing ordering of mesh nodes.

6.2.5 SubDomain Class

The **SubDomain** class is called sub-level abstraction. It acts as the bridge between global objects and local **Element** objects. A **SubDomain** object is the user of **Mesh** and **Element** objects. **SubDomain** objects are initialized by a **Mesh** object, from which relevant geometrical data are collected. A list of **Element** objects are then built. A few important public interfaces are provided, enabling the cross-process global linear system assembly in the **Calc** class.

Important Private Data Member

list<Element> EleList: The **list<T>** is a C++ standard sequence container. **Element** objects are pushed back into the list one by one. Because of the convenient components moving, insertion and removal in a double-linked list, the self-adaptive mesh with dynamic refinement and merging will be easier implemented in the future.

Mesh& MeshObj: The **SubDomain** class only includes a reference of a **Mesh** object instead of a copy of it.

Important Public Interfaces

void SubDomain::GatherGlobalMatrix(Mat &)
Consider a local matrix component $A_{ij}^{(e)}$. This function firstly determine its corresponding location in the global matrix (I, J) by virtual of the **AO** object contained in **MeshObj**. Then the value of $A_{ij}^{(e)}$ is sent to the global matrix by calling the PETSc routine **MatSetValues()**. After the loop over all elements, the global matrix will be properly assembled.

void SubDomain::GatherGlobalRHS(Vec &)
The procedures of gathering the global RHS vector b is quite similar to those in the matrix gathering. $b_i^{(e)}$ is gathered from each element and added to the global component b_I.

6.2.6 Calc Class and the Derived Classes

Calc class is the top application-level module. This class is expected to implement the PDE solving and post-processing. However, different types of PDEs always requires quite different schemes to solve. For the sake of extensibility, the code should tell the common features of numerical schemes from those problem-dependent ones. The inheritance mechanism of OOP plays an important role. **Calc** class, as the base class, only contains data and function members which are universally needed in any PDE solving scheme. For a particular PDE model, however, a corresponding derived class is defined. The derived class inherits the public and protected members from the base class and meanwhile defines more necessary members. It is also worth mentioning the concept "virtual function", which is one of features of polymorphism. In the base class, some functions are declared to be virtual functions such that they are allowed to have different implementations in the derived classes. We firstly make some explorations into the base class **Calc**.

Important Public and Protected Members of Calc Class

ParallelEnv *Par: Any parallel PDE solver must involve this parallel environment.
Mesh *MeshObj: A mesh object is also an essential component in any PDE solver. Together with ***Par**, ***MeshObj** initializes the **SubDomain** object.
SubDomain *SubObj: The **SubDomain** object is certainly one of the key data. The ***SubObj** use ***MeshObj** via its reference.
virtual void Calc::SolveIt() and
virtual void Calc::PostProcess(const PetscInt):
The two functions respectively carry out the PDE solving and the post-processing. However, as discussed above, these two functions are no more than virtual interfaces. The real implementations depend on specific derived classes. The significance

of virtual functions is the guarantee of unique user interfaces. Through dynamic binding between the base-class pointer and derived-class objects, users are able to employ different versions of functions by invoking common function names. This dynamic binding feature is illustrated in the function **main()**.

The Derived Class for Solving Helmholtz Equation

We will take an Helmholtz equation solver as an example of a typical class derived from the **Calc** class. The descriptions of a few important data and function members are as following.

Mat A: **A** is the global matrix, which is a PETSc parallel sparse matrix. It is assembled by calling **SubObj ->GatherGlobalMatrix(A)**
Vec x,b: The two PETSc parallel vectors have the identical storage pattern. **x** is the unknown vector which finally stores the solution. **b** is the global RHS vector built by **SubObj ->GatherGlobalRHS(b)**.
KSP ksp: **KSP** type is the PETSc implementations of Krylov-subspace-methods. It provides uniform and efficient access to all of the package's linear system solvers, including direct and iterative. A **KSP** object is initialized by **A**,**x** and **b** and more options of solvers can be specified at runtime.
HelmholtzCalc::HelmholtzCalc(int, char **, char *, char *):
When a **HelmholtzCalc** object is defined, the members of the base class are firstly initialized by the constructor of **Calc** class. Because **Calc** class does not have a default initialization, in the constructor of **Helmholtz** class, we then have to explicitly invoke **Calc(int, char **, char *,char *)** in the initialization list.
void HelmholtzCalc::SolveIt():
This is the **HelmholtzCalc**-class version of PDE solving routine. It can be called via a **Calc *** type pointer or a **Calc &** type reference. To solve the Helmholtz equation, **SolveIt()** calls several private functions successively. The calling sequence is
HelmholtzCalc::SetupGlbMat(); // Matrix A assembly
HelmholtzCalc::SetupGlbRhs(); // RHS b assembly
HelmholtzCalc::SetupPc(); // Preconditioner construction, N.A. currently
HelmholtzCalc::SetupKsp(); // Initializing KSP object
HelmholtzCalc::Solving(); // Invoking PETSc KSPSolve(ksp,b,x)

6.2.7 Function main()

By carefully designing the levels of data abstraction, the main function of the code is very compact. The dynamic binding takes place because we point a **Calc *** type pointer to a **HelmholtzCalc** object. At runtime, the **SolveIt()** and **PostProcess()** are then both the version in the derived class.

Main.cpp:

```
//Macros are passed to the compiler by –D options.
#include "Calc.h"
#include "HelmholtzCalc.h"
#ifdef PETSC
#include "PetscInclude.h"
#endif

using namespace std;

static char help[ ] = " This is a PETSc 3D Helmholtz equation solver.\n";

int main(int argc, char **argv) {
    Calc *CalcObj=new HelmholtzCalc(argc,argv,static_cast<char *>(0),help);
    CalcObj ->SolveIt();
    CalcObj ->PostProcess(POSTLEVEL);
    delete CalcObj;CalcObj=PETSC_NULL;
    return(0);
}
```

6.2.8 Code Validation

We validate the inhomogeneous Helmholtz equations solver by construction of an exact solution in the oblate spheroidal domain. Let the oblateness be denoted by the eccentricity of the boundary $\mathcal{E}$. We construct an exact solution, in oblate spheroidal coordinates (see Chapter 2,3), satisfying the zero boundary condition $u(\xi = \sqrt{1/\mathcal{E}^2 - 1}, \eta, \phi) = 0$,

$$u = -\frac{1}{12}(\tilde{r}^3 - 2\tilde{r}^2 + 1)(1 - \eta^2)\sin 2\phi, \tag{6.8}$$

where

$$\tilde{r} = c\sqrt{(1 + \xi^2)(1 - \eta^2) + \frac{\xi^2\eta^2}{1 - \mathcal{E}^2}}.$$

Substitution of (6.8) into (6.4), we can compute the artificial RHS forcing term. We then insert the artificial force to the code and solve the numerical solutions u_h on meshes of different element sizes. The correct implementation should observe the second order numerical accuracy, namely $||u - u_h||_2 \sim O(h^2)$, where h is the typical size of elements in the mesh. In the Table 6.1 and Figure 6.2, we list the numerical results of the validating simulations. The proper validated code is ready

for applications.

Table 6.1: The Helmholtz equations solver validation, the inhomogeneous Helmholtz equation is solved on four meshes of different typical mesh size h. The λ of (6.4) takes a general value -1.25. The relative error roughly follows the second order convergence rate. It is worth mentioning that because no DDM preconditioner is applied, the condition number of the global matrix is of $O(h^{-2})$. This is shown by the increase in number of iterations. More Dof and more iterations lower the efficiency of high-resolution simulations.

Mesh	h	Dof	KSP Iterations	KSP Time (s)	$\|\|u - u_h\|\|_2/\|\|u\|\|_2$
1	0.1	2169	49	0.039151	1.534525e-01
2	0.05	14705	100	0.120296	4.426556e-02
3	0.025	107745	199	2.005602	1.264994e-02
4	0.0125	823745	397	34.773177	3.610184e-03

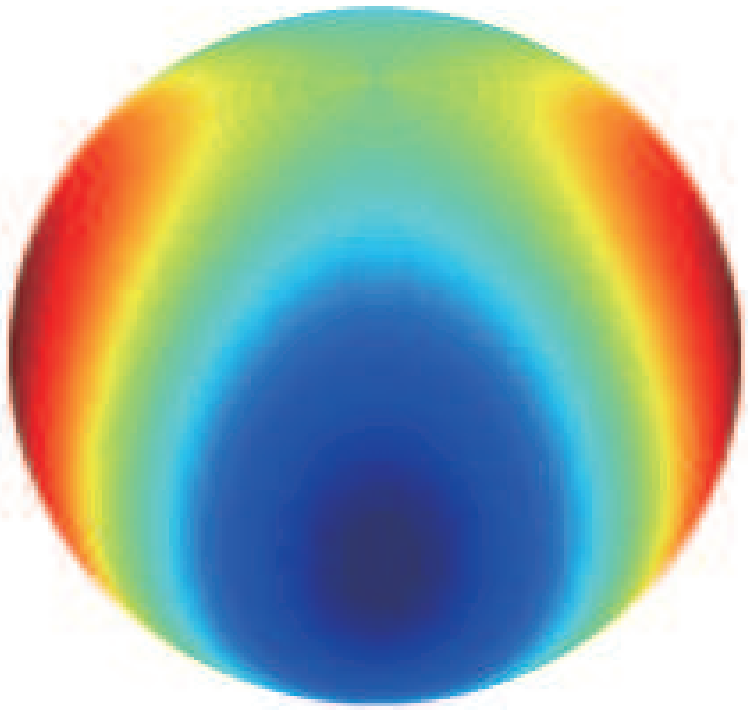

Figure 6.2: The illustration of the constructed analytic solution in an oblate spheroidal domain, the pattern on the spheroidal surface has nothing to do with any physics.

6.2.9 Comments

In this section, we have demonstrated the code by solving a second order elliptic PDE. We have picked up and discussed the most essential modules. Other supporting features and more detailed implementations can be found in the DVD-ROM attached to this thesis, in which, the complete source files are submitted as an appendix (Appendix B). The code licensing is included in all the files and may change in the future versions.

6.3 An Application to Rotating Gaseous Planets

The fluid in the envelope of stars and gaseous planets are closely related to the polytrope of index one (see [Anderson et al., 1974; Chandrasekhar, 1967; Hubbard and Horedt, 1983]). The equation of state (EOS) is

$$p = K\rho^2, \tag{6.9}$$

where p is the gas pressure and ρ is the density. The hydrostatic equilibrium state of a polytrope without rotation is established by well known Lane-Emden equation ([Lane, 1870], and also see[Chandrasekhar, 1939, 1967; Eddington, 1926; Horedt, 1986]). In one of a series of papers, [Chandrasekhar, 1933], firstly studied a polytrope in a rotational equilibrium state by an asymptotic analysis assuming the rotational parameter $\epsilon = \Omega^2/(2\pi G\rho)$ (see Chapter 2) is small. According to [Anderson, 2012], if we introduce the small parameter

$$q = \frac{\Omega^2 R^3}{GM},$$

where R is the radius of the planet and M is its total mass, to the first order, the coefficient K in (6.9) can be uniquely determined by

$$K = \frac{2GR^2}{\pi}\left(1 - \frac{4q}{\pi^2}\right). \tag{6.10}$$

If we adopt the physical parameters of Jupiter, we can compute that

$$K = 200570\text{Pam}^6\text{kg}^{-2}.$$

On the other hand, if we consider the momentum equation for gas in rotational hydrostatic equilibrium

$$-\frac{\nabla p}{\rho} - \nabla V_g - \nabla V_c = 0, \tag{6.11}$$

where V_g and V_c are respectively the gravitational potential and the centrifugal potential (see Chapter 2, 3). Making the substitution of (6.9) into (6.11) yields

$$-2K\nabla\rho - \nabla V_g - \nabla V_c = 0. \tag{6.12}$$

If we apply $\nabla\cdot$ to both sides of (6.12), taking into account of $\nabla^2 V_g = 4\pi G\rho$ and $V_c = -\frac{1}{2}\Omega^2 s^2$, the equation can be reduced to

$$K\nabla^2\rho + 2\pi G\rho = -\Omega^2. \tag{6.13}$$

Note the boundary condition of (6.13) is homogeneous, namely $\rho = 0$ on the surface

of the planet. We can further scale the dimensional equation by

$$\mathbf{r} \to \mathbf{r}R_J,$$
$$\rho \to \rho\frac{M_J}{R_J^3},$$

where $R_J = 69894$km is the mean radius of Jupiter at a one-bar level in its atmosphere, and $M_J = 1.8986 \times 10^{27}$kg is the Jovian total mass ([Williams, November 16, 2004]). Finally, the dimensionless equation is derived to be

$$\nabla^2\rho + \alpha\rho = \beta, \tag{6.14}$$

which is an inhomogeneous Helmholtz equation with two dimensionless parameters $\alpha = \frac{2\pi G R_J^2}{K}$ and $\beta = -\frac{\Omega^2 R_J^5}{M_J K}$. We then can solve (6.14) by virtual of our 3D Helmholtz solver in an oblate spheroidal domain. The eccentricity of the spheroidal mesh matches exactly the observed shape of Jupiter. The radial density and pressure distributions are shown in Figure 6.3(a) and (b), respectively. The illustration of the density in a meridional cross-section is in Figure 6.4. In [Chandrasekhar, 1933],

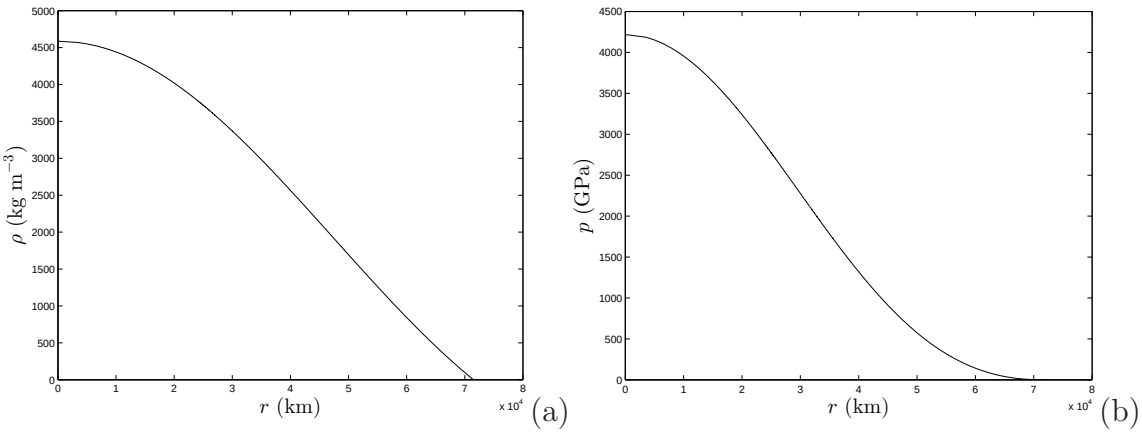

Figure 6.3: The density and pressure profiles of a Jupiter-like polytrope of index one

for a rotating polytrope of index one, the relation between the mean density and its central density, to the first order of the rotational parameter ϵ, is given by

$$\rho_c = \bar{\rho} \times 3.2899(1 + 0.710\epsilon), \tag{6.15}$$

where ρ_c is the density in the core and $\bar{\rho}$ is the mean density. For Jupiter, the mean density is $\bar{\rho} = 1326\text{kg/m}^3$ and $\epsilon = 0.0556$, we can compute the central density of Jupiter to be $\rho_c = 4535\text{kg/m}^3$ by (6.15). It can be seen, quantitatively, our direct 3D simulation reproduces and verifies the central density predicted by the approximation method. The two curves in Figure 6.3 are also consistent with the results given in [Anderson, 2012], which solves the density and pressure profiles analytically in a spherical geometry.

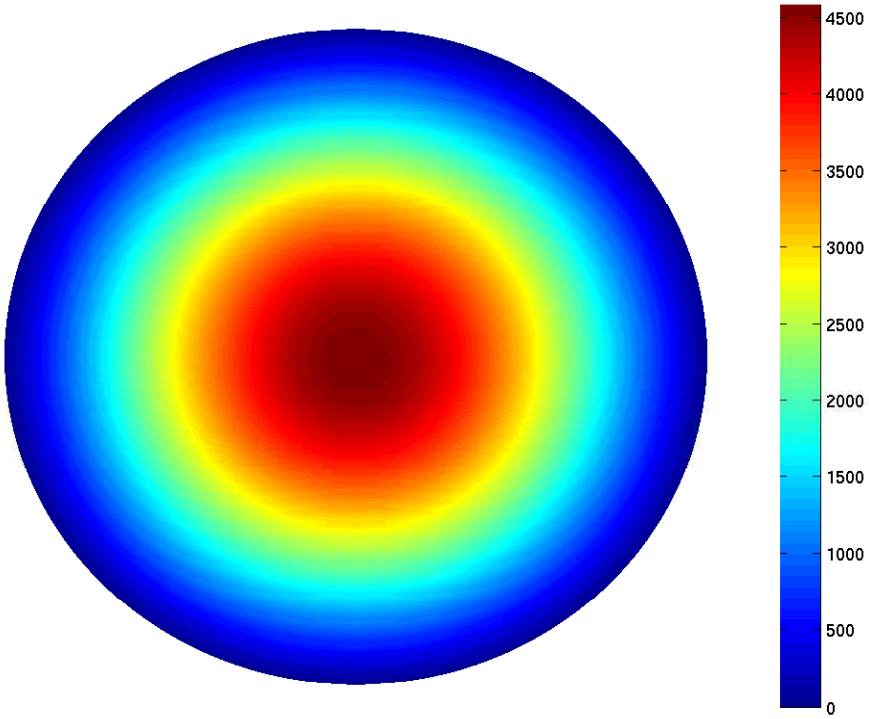

Figure 6.4: The density distribution of a Jupiter-like polytrope of index one in a meridional cross-section, the numbers by the side of the color bar are the density values in the unit kg/m^3.

It is important to point out that in our numerical analysis, the shape of the simulation domain is not part of the solution but an assumption. Just the same as [Anderson, 2012] where a spherical geometry is assumed, our density solution is also not a physical one. More precisely, we have studied a model of polytropic gas which is of an oblate shape as a result of the rotational hydrostatic equilibrium. Because we adopt such physical parameters of Jupiter, the shape of Jupiter enters our analysis as an empirical assumption. If the interior of Jupiter does not depart too much from the convective equilibrium, then our polytrope solution well represents the realistic Jupiter.

6.4 Summary and Remarks

We have demonstrated a parallel finite-element code in this chapter. Though it is in a very preliminary stage, it has already been applied to a planetary structure problem. As we have discussed a lot in the main text, the code must be extended and finally applied to compressible convection and solar dynamo problems. There are still plenty of efforts to be made, which may account for another one to two PhD degree projects. In this sense, the following work is no longer included into the thesis. On the other hand, we can continue exploring into the planetary structure problems. By means of the Helmholtz equation solver at hand, we are able to

generalize the two-layer problem discussed in Chapter 2 and the differential rotation problem presented in Chapter 3 to compressible gas configurations, which are better models for giant planets such as Jupiter, Saturn and most exsoplanets discovered so far.

Chapter 7

Conclusions

In this thesis, a few classical research areas of fluid mechanics are revisited. The figure of a self-gravitational system is one of such fundamental problems because it is closely related to the formation and evolution of celestial bodies. Stars, brown dwarves and planets are formed by collapse of interstellar gas clouds due to Jeans instability. As the result of the conservation of angular momentum, the formed celestial bodies generally are spinning. In the geological time scale, most of celestial bodies are "fluid-like", even for the terrestrial planets like our Earth. It is well known and simple to establish that an isolated static fluid under self-gravity must be in a perfect spherical shape. However, if rotation and some other internal flows are present, the fluid cannot withstand the shear stress as a consequence of the centrifugal force. Therefore, it must deform into some different geometry. As we have discussed in Chapter 2, 3 and 6, basically, the fluid body becomes an oblate spheroid. The spheroidal shapes of rotating stars and planets attracted so many notables such as Maclaurin, d'Alembert, Clairaut, Euler, Laplace, Legendre, Poisson, Gauss, and Chandrasekhar. The figure of a planet or a star is an important parameter controlling the interior flows and structures. On the other hand, in turn, the flows such as differential rotation and such structures as core-mantle-boundary (CMB) modify the equilibrium figure. In the corresponding chapters, we have looked into these complex fluid systems and made several breakthroughs. To summarize, we have mainly studied the feedback of interior structures and weak flows. The results will be generally useful in inversions of some non-observable properties of planets and stars. Currently, our figure models for two-layer spheroids and weak differential rotation are based on incompressible fluids. The involved mathematical analyses are relatively clear-cut and definite. In Chapter 6, however, we have attempted to study such more realistic compressible fluids models for gaseous planets and stellar bodies. We definitely will continue working on relevant theories and computations.

Another quite classical problem we tackle in this thesis is the Stokes flow theories. Unlike a lot of geophysical and astrophysical fluid systems in which flows are all with large Reynolds number, Stokes flow is a typical model for highly viscous cases. Flows driven by tiny and slow-moving bodies usually can be well approximated by Stokes

flow models. Such problems are commonly seen in many biological fluid systems, for example, the microswimming process of microorganism. An interesting frontier of the biomagnetism research is the magnetotaxis of a family of bacteria. The magnetotactic bacteria are closely related to the bio-mineralization of iron. It is also believed that the abilities of magnetotaxis seen in such advanced animals as pigeons and sea turtles actually have origins in the magnetotactic bacteria. As a result, lots of biologists are devoted to modelling the behaviors of magnetotactic bacteria under external magnetic fields. In all the models available nowadays, the bacteria are approximated by spherical shape such that the classical Stokes formulations of drag force and rotational torque can be applied. However, with more and more accurate and precise observations available, the spherical approximation is no longer satisfactory enough. In Chapter 4, we firstly consider the shape of bacteria to be elongated prolate spheroid, which perfectly matches most of Cocci and Bacilloses. The Stokes flow driven by such prolate spheroids are formulated fully analytically in prolate spheroidal coordinates, which enables the better modelling of dynamics of magnetotaxis. As the ensuing application of our theories, a manuscript on swimming magnetotactic bacteria has recently been submitted. We expect that our work will facilitate relevant research.

Computational fluid dynamics (CFD), without any doubt, is one of the most important means in analyses of flows and forces acting on them. Numerical work is also a major part of this thesis. In Chapter 5, we employ modern high performance parallel computers to help model the precession driven flows in channels. The astrophysical background is the fluid inside a precessing planet. Precession is a common phenomenon in the universe. Because of the interactions with other objects, any rotating celestial body is precessing. A good example is our own Earth, which is precessing slowly due to the torque imposed by the Sun and the Moon. Every about 25800 years, the rotational axis of the Earth completes a precessional cycle. Precession drives interior flows, which can be very strong in some occasions. The flows then may generate and maintain magnetic fields via dynamo processes. In our work, the flows inside precessing channels are found to be controlled by the strength of precession as well as the geometrical aspect ratio of the channel. For some particular aspect ratio, inertial modes can be resonant with the precessional forcing and hence produce strong and complex interior flows. The numerical analyses are done by a finite-difference scheme which is efficiently parallelized. The intensive numerical experiments have resulted in plenty of results, which confirm theoretical asymptotic analyses done by Prof. Keke Zhang. The channel precession problem does give an insight into the precession driven flows. However, further extensions of the studies into cylindrical and spherical geometries will be crucial for fully understanding the geomagnetic significance of precessions.

Projects discussed above all have ended up with publications in proper journals.

Chapter 6, however, only contains a mile stone in a large project. A finite-element code is under development for modelling fully compressible convection problems. The code is expected to be efficient, highly scalable and robust in solving 3D convection dominated Navier-Stokes equations. There is no straightforward approach to create such a big code. We have to gradually equip our code with more functionalities and finally build the complete code. At the current stage, the code is able to be applied to 3D general elliptic equations. The code has been designed to be flexible for extensions. We have studied the structure of rotating polytrope by virtue of this code and the results are shown and discussed in Chapter 6. This application has two significant aspects. First, the code is validated and hence is ready for further extensions. Second, it opens the studies of planetary structures in the regime of compressible fluids. Both the directions are promising scientifically.

To summarize, this thesis mainly reports the research work on several astrophysical fluid mechanical problems. The particular inter-discipline project linked to a biological fluid system is also of lots of importance. The thesis then is closed by this concluding remark.

Appendix A

The "Small Core" Case of a Two-layer Spheroid

Consider the more complicated case of the "small core" planet–when either the core is sufficiently small or the rotation rate Ω is fast enough that the foci of the free surface is located within the outer layer. We introduce a special level surface of the confocal hyperboloid given by

$$\eta_m = \sqrt{1 - \frac{c_1^2}{c_2^2}(1 + \xi_i^2)},$$

which is tangent to the equator of the interface $\mathcal{S}_1$; the hyperboloid is illustrated in Figure 2.5. Since the foci c_2 are located outside of the interface ξ_i and since the second coordinates are used as the working coordinates, the multiple integration over both the ξ and η directions must be broken up as a result of the discontinuous density across the interface. Compared to the "large core" case, this results in an even more complicated upper/lower limit of the multiple integration, although the general approach and method are similar to the "large core" case. Here we present the mathematical expressions for the condition on the outer free surface and the gravitational energy E_g that are needed in determining the shape of "small-core" planets.

After some manipulation using equation (2.29), the condition on the outer free

surface at $\xi = \xi_o$ for the "small core" case can be expressed as

$$
\begin{aligned}
C &= 2\pi G c_2^2 \Big\{ \Big[\rho_1 \int_{\eta_m}^{1} \int_{0}^{\xi_\jmath} f_1(\xi',\eta')\mathrm{d}\xi'\mathrm{d}\eta' \\
&+ \rho_1 \int_{-1}^{-\eta_m} \int_{0}^{\xi_\jmath} f_1(\xi',\eta')\mathrm{d}\xi'\mathrm{d}\eta' \\
&+ \rho_2 \int_{\eta_m}^{1} \int_{\xi_\jmath}^{\xi_o} f_1(\xi',\eta')\mathrm{d}\xi'\mathrm{d}\eta' \\
&+ \rho_2 \int_{-1}^{-\eta_m} \int_{\xi_\jmath}^{\xi_o} f_1(\xi',\eta')\mathrm{d}\xi'\mathrm{d}\eta' \\
&+ \rho_2 \int_{-\eta_m}^{\eta_m} \int_{0}^{\xi_o} f_1(\xi',\eta')\mathrm{d}\xi'\mathrm{d}\eta' \Big] \sin^{-1}\mathcal{E}_2 \\
&+ \Big[\rho_1 \int_{\eta_m}^{1} \int_{0}^{\xi_\jmath} f_2(\xi',\eta')\mathrm{d}\xi'\mathrm{d}\eta' \\
&+ \rho_1 \int_{-1}^{-\eta_m} \int_{0}^{\xi_\jmath} f_2(\xi',\eta')\mathrm{d}\xi'\mathrm{d}\eta' \\
&+ \rho_2 \int_{\eta_m}^{1} \int_{\xi_\jmath}^{\xi_o} f_2(\xi',\eta')\mathrm{d}\xi'\mathrm{d}\eta' \\
&+ \rho_2 \int_{-1}^{-\eta_m} \int_{\xi_\jmath}^{\xi_o} f_2(\xi',\eta')\mathrm{d}\xi'\mathrm{d}\eta' \\
&+ \rho_2 \int_{-\eta_m}^{\eta_m} \int_{0}^{\xi_o} f_2(\xi',\eta')\mathrm{d}\xi'\mathrm{d}\eta' \Big] \\
&\times \frac{5(3\eta^2-1)}{16\mathcal{E}_2^2} \Big[(3-2\mathcal{E}_2^2)\sin^{-1}\mathcal{E}_2 - 3\mathcal{E}_2\sqrt{1-\mathcal{E}_2^2} \Big] \Big\} \\
&- \frac{\Omega^2}{2}(1+\xi_o^2)(1-\eta^2)c_2^2. \qquad \text{(A.1)}
\end{aligned}
$$

Similarly, the total self-gravitational energy E_g can be written as a sum of several

quadruple integrals with the complicated upper/lower limits

$$
\begin{aligned}
&E_g(\mathcal{E}_1,\mathcal{E}_2) = -2\pi G c_2^5\Big\{\\
&\rho_1\int_{\eta_m}^{1}\int_{0}^{\xi_\jmath} f_3(\xi,\eta)\Big[\int_{\eta_m}^{1} g_1(\xi,\eta')\mathrm{d}\eta' + \int_{-1}^{-\eta_m} g_1(\xi,\eta')\mathrm{d}\eta' + \rho_2\int_{-\eta_m}^{\eta_m}\int_{0}^{\xi} f_1(\xi',\eta')\mathrm{d}\xi'\mathrm{d}\eta'\Big]\mathrm{d}\xi\mathrm{d}\eta\\
&\rho_1\int_{-1}^{-\eta_m}\int_{0}^{\xi_\jmath} f_3(\xi,\eta)\Big[\int_{\eta_m}^{1} g_1(\xi,\eta')\mathrm{d}\eta' + \int_{-1}^{-\eta_m} g_1(\xi,\eta')\mathrm{d}\eta' + \rho_2\int_{-\eta_m}^{\eta_m}\int_{0}^{\xi} f_1(\xi',\eta')\mathrm{d}\xi'\mathrm{d}\eta'\Big]\mathrm{d}\xi\mathrm{d}\eta\\
&\rho_2\int_{\eta_m}^{1}\int_{\xi_\jmath}^{\xi_o} f_3(\xi,\eta)\Big[\int_{\eta_m}^{1} g_1(\xi,\eta')\mathrm{d}\eta' + \int_{-1}^{-\eta_m} g_1(\xi,\eta')\mathrm{d}\eta' + \rho_2\int_{-\eta_m}^{\eta_m}\int_{0}^{\xi} f_1(\xi',\eta')\mathrm{d}\xi'\mathrm{d}\eta'\Big]\mathrm{d}\xi\mathrm{d}\eta\\
&\rho_2\int_{-1}^{-\eta_m}\int_{\xi_\jmath}^{\xi_o} f_3(\xi,\eta)\Big[\int_{\eta_m}^{1} g_1(\xi,\eta')\mathrm{d}\eta' + \int_{-1}^{-\eta_m} g_1(\xi,\eta')\mathrm{d}\eta' + \rho_2\int_{-\eta_m}^{\eta_m}\int_{0}^{\xi} f_1(\xi',\eta')\mathrm{d}\xi'\mathrm{d}\eta'\Big]\mathrm{d}\xi\mathrm{d}\eta\\
&\rho_2\int_{-\eta_m}^{\eta_m}\int_{0}^{\xi_o} f_3(\xi,\eta)\Big[\int_{\eta_m}^{1} g_1(\xi,\eta')\mathrm{d}\eta' + \int_{-1}^{-\eta_m} g_1(\xi,\eta')\mathrm{d}\eta' + \rho_2\int_{-\eta_m}^{\eta_m}\int_{0}^{\xi} f_1(\xi',\eta')\mathrm{d}\xi'\mathrm{d}\eta'\Big]\mathrm{d}\xi\mathrm{d}\eta\\
&\rho_1\int_{\eta_m}^{1}\int_{0}^{\xi_\jmath} f_1(\xi,\eta)\Big[\int_{\eta_m}^{1} g_2(\xi,\eta')\mathrm{d}\eta' + \int_{-1}^{-\eta_m} g_2(\xi,\eta')\mathrm{d}\eta' + \rho_2\int_{-\eta_m}^{\eta_m}\int_{\xi}^{\xi_o} f_3(\xi',\eta')\mathrm{d}\xi'\mathrm{d}\eta'\Big]\mathrm{d}\xi\mathrm{d}\eta\\
&\rho_1\int_{-1}^{\eta_m}\int_{0}^{\xi_\jmath} f_1(\xi,\eta)\Big[\int_{\eta_m}^{1} g_2(\xi,\eta')\mathrm{d}\eta' + \int_{-1}^{-\eta_m} g_2(\xi,\eta')\mathrm{d}\eta' + \rho_2\int_{-\eta_m}^{\eta_m}\int_{\xi}^{\xi_o} f_3(\xi',\eta')\mathrm{d}\xi'\mathrm{d}\eta'\Big]\mathrm{d}\xi\mathrm{d}\eta\\
&\rho_2\int_{\eta_m}^{1}\int_{\xi_\jmath}^{\xi_o} f_1(\xi,\eta)\Big[\int_{\eta_m}^{1} g_2(\xi,\eta')\mathrm{d}\eta' + \int_{-1}^{-\eta_m} g_2(\xi,\eta')\mathrm{d}\eta' + \rho_2\int_{-\eta_m}^{\eta_m}\int_{\xi}^{\xi_o} f_3(\xi',\eta')\mathrm{d}\xi'\mathrm{d}\eta'\Big]\mathrm{d}\xi\mathrm{d}\eta\\
&\rho_2\int_{-1}^{-\eta_m}\int_{\xi_\jmath}^{\xi_o} f_1(\xi,\eta)\Big[\int_{\eta_m}^{1} g_2(\xi,\eta')\mathrm{d}\eta' + \int_{-1}^{-\eta_m} g_2(\xi,\eta')\mathrm{d}\eta' + \rho_2\int_{-\eta_m}^{\eta_m}\int_{\xi}^{\xi_o} f_3(\xi',\eta')\mathrm{d}\xi'\mathrm{d}\eta'\Big]\mathrm{d}\xi\mathrm{d}\eta\\
&\rho_2\int_{-\eta_m}^{\eta_m}\int_{0}^{\xi_o} f_1(\xi,\eta)\Big[\int_{\eta_m}^{1} g_2(\xi,\eta')\mathrm{d}\eta' + \int_{-1}^{-\eta_m} g_2(\xi,\eta')\mathrm{d}\eta' + \rho_2\int_{-\eta_m}^{\eta_m}\int_{\xi}^{\xi_o} f_3(\xi',\eta')\mathrm{d}\xi'\mathrm{d}\eta'\Big]\mathrm{d}\xi\mathrm{d}\eta\\
&\frac{5\rho_1}{16}\int_{\eta_m}^{1}\int_{0}^{\xi_\jmath} f_4(\xi,\eta)\times\Big[\int_{\eta_m}^{1} g_3(\xi,\eta')\mathrm{d}\eta' + \int_{-1}^{-\eta_m} g_3(\xi,\eta')\mathrm{d}\eta' + \rho_2\int_{-\eta_m}^{\eta_m}\int_{0}^{\xi} f_2(\xi',\eta')\mathrm{d}\xi'\mathrm{d}\eta'\Big]\mathrm{d}\xi\mathrm{d}\eta\\
&\frac{5\rho_1}{16}\int_{-1}^{-\eta_m}\int_{0}^{\xi_\jmath} f_4(\xi,\eta)\times\Big[\int_{\eta_m}^{1} g_3(\xi,\eta')\mathrm{d}\eta' + \int_{-1}^{-\eta_m} g_3(\xi,\eta')\mathrm{d}\eta' + \rho_2\int_{-\eta_m}^{\eta_m}\int_{0}^{\xi} f_2(\xi',\eta')\mathrm{d}\xi'\mathrm{d}\eta'\Big]\mathrm{d}\xi\mathrm{d}\eta\\
&\frac{5\rho_2}{16}\int_{\eta_m}^{1}\int_{\xi_\jmath}^{\xi_o} f_4(\xi,\eta)\times\Big[\int_{\eta_m}^{1} g_3(\xi,\eta')\mathrm{d}\eta' + \int_{-1}^{-\eta_m} g_3(\xi,\eta')\mathrm{d}\eta' + \rho_2\int_{-\eta_m}^{\eta_m}\int_{0}^{\xi} f_2(\xi',\eta')\mathrm{d}\xi'\mathrm{d}\eta'\Big]\mathrm{d}\xi\mathrm{d}\eta\\
&\frac{5\rho_2}{16}\int_{-1}^{-\eta_m}\int_{\xi_\jmath}^{\xi_o} f_4(\xi,\eta)\times\Big[\int_{\eta_m}^{1} g_3(\xi,\eta')\mathrm{d}\eta' + \int_{-1}^{-\eta_m} g_3(\xi,\eta')\mathrm{d}\eta' + \rho_2\int_{-\eta_m}^{\eta_m}\int_{0}^{\xi} f_2(\xi',\eta')\mathrm{d}\xi'\mathrm{d}\eta'\Big]\mathrm{d}\xi\mathrm{d}\eta\\
&\frac{5\rho_2}{16}\int_{-\eta_m}^{\eta_m}\int_{0}^{\xi_o}\big[3\xi^2-1)\cot^{-1}\xi - 3\xi\big] f_2(\xi,\eta)\times\Big[\int_{\eta_m}^{1} g_3(\xi,\eta')\mathrm{d}\eta' + \int_{-1}^{-\eta_m} g_3(\xi,\eta')\mathrm{d}\eta'\\
&\qquad + \quad \rho_2\int_{-\eta_m}^{\eta_m}\int_{0}^{\xi} f_2(\xi',\eta')\mathrm{d}\xi'\mathrm{d}\eta'\Big]\mathrm{d}\xi\mathrm{d}\eta\\
&\frac{5\rho_1}{16}\int_{\eta_m}^{1}\int_{0}^{\xi_\jmath} f_2(\xi,\eta)\Big[\int_{\eta_m}^{1} g_4(\xi,\eta')\mathrm{d}\eta' + \int_{-1}^{-\eta_m} g_4(\xi,\eta')\mathrm{d}\eta' + \rho_2\int_{-\eta_m}^{\eta_m}\int_{\xi}^{\xi_o} f_4(\xi',\eta')\mathrm{d}\xi'\mathrm{d}\eta'\Big]\mathrm{d}\xi\mathrm{d}\eta\\
&\frac{5\rho_1}{16}\int_{-1}^{-\eta_m}\int_{0}^{\xi_\jmath} f_2(\xi,\eta)\Big[\int_{\eta_m}^{1} g_4(\xi,\eta')\mathrm{d}\eta' + int_{-1}^{-\eta_m} g_4(\xi,\eta')\mathrm{d}\eta' + \rho_2\int_{-\eta_m}^{\eta_m}\int_{\xi}^{\xi_o} f_4(\xi',\eta')\mathrm{d}\xi'\mathrm{d}\eta'\Big]\mathrm{d}\xi\mathrm{d}\eta\\
&\frac{5\rho_2}{16}\int_{\eta_m}^{1}\int_{\xi_\jmath}^{\xi_o} f_2(\xi,\eta)\Big[\int_{\eta_m}^{1} g_4(\xi,\eta')\mathrm{d}\eta' + \int_{-1}^{-\eta_m} g_4(\xi,\eta')\mathrm{d}\eta' + \rho_2\int_{-\eta_m}^{\eta_m}\int_{\xi}^{\xi_o} f_4(\xi',\eta')\mathrm{d}\xi'\mathrm{d}\eta'\Big]\mathrm{d}\xi\mathrm{d}\eta\\
&\frac{5\rho_2}{16}\int_{-1}^{-\eta_m}\int_{\xi_\jmath}^{\xi_o} f_2(\xi,\eta)\Big[\int_{\eta_m}^{1} g_4(\xi,\eta')\mathrm{d}\eta' + \int_{-1}^{-\eta_m} g_4(\xi,\eta')\mathrm{d}\eta' + \rho_2\int_{-\eta_m}^{\eta_m}\int_{\xi}^{\xi_o} f_4(\xi',\eta')\mathrm{d}\xi'\mathrm{d}\eta'\Big]\mathrm{d}\xi\mathrm{d}\eta\\
&\frac{5\rho_2}{16}\int_{-\eta_m}^{\eta_m}\int_{0}^{\xi_o} f_2(\xi,\eta)\Big[\int_{\eta_m}^{1} g_4(\xi,\eta')\mathrm{d}\eta' + \int_{-1}^{-\eta_m} g_4(\xi,\eta')\mathrm{d}\eta' + \rho_2\int_{-\eta_m}^{\eta_m}\int_{\xi}^{\xi_o} f_4(\xi',\eta')\mathrm{d}\xi'\mathrm{d}\eta'\Big]\mathrm{d}\xi\mathrm{d}\eta\Big\},
\end{aligned}
\tag{A.2}
$$

where the functions $g_n, n = 1, 2, 3, 4$ are the same as those for the "large core" case. The expression for the centrifugal energy V_c remains the same as in the "large core" case. Also, as in the case of the "large core", for a given set of the three parameters, we can solve (2.41) with the the gravitational energy E_g given by (A.2) and the

centrifugal energy given by (2.40), together with the following constraint

$$
\begin{aligned}
0 &= G(\mathcal{E}_1, \mathcal{E}_2) \\
&= -\Omega^2 + \frac{15\pi G}{4}\Big[\rho_1 \int_{\eta_m}^{1}\int_{0}^{\xi_\jmath} f_2(\xi',\eta')\mathrm{d}\xi'\mathrm{d}\eta' \\
&+ \rho_1 \int_{-1}^{-\eta_m}\int_{0}^{\xi_\jmath} f_2(\xi',\eta')\mathrm{d}\xi'\mathrm{d}\eta' \\
&+ \rho_2 \int_{\eta_m}^{1}\int_{\xi_\jmath}^{\xi_o} f_2(\xi',\eta')\mathrm{d}\xi'\mathrm{d}\eta' \\
&+ \rho_2 \int_{-1}^{-\eta_m}\int_{\xi_\jmath}^{\xi_o} f_2(\xi',\eta')\mathrm{d}\xi'\mathrm{d}\eta' \\
&+ \rho_2 \int_{-\eta_m}^{\eta_m}\int_{0}^{\xi_o} f_2(\xi',\eta')\mathrm{d}\xi'\mathrm{d}\eta'\Big] \\
&\times \Big[(3-2\mathcal{E}_2^2)\sin^{-1}\mathcal{E}_2 - 3\mathcal{E}_2\sqrt{1-\mathcal{E}_2^2}\Big],
\end{aligned}
\tag{A.3}
$$

which is derived from (A.1).

Appendix B

The 3D Helmholtz Equation Solver: Source Code

In the root directory of the DVD-ROM, the folder named **Helmholtz3D** can be found. There are four folders and one **Makefile** file inside it. To compile and link the code on a linux platform, one should firstly configure a stable version of PETSc with the following configuration options:

./configure
--PETSC_DIR= <dir>
--with-clanguage=C++
--with-c++-support=1 --with-c-support=1
--with-fortran=1 --with-fortran-interfaces=1
--with-large-file-io=1
--with-scalar-type=real --with-precision=double
--with-ar=ar --with-ranlib=ranlib
--with-mpi=1
--with-blas-lib= <dir> --with-lapack-lib= <dir>
--with-parmetis=1 --with-parmetis-dir= <dir>
--with-parmetis-include= <dir> --with-parmetis-lib= <dir>

The required packages such as ParMetis, MPICH2, BLAS&LAPACK also should be installed in prior. After successful compiling and linking the C++ source files in the **src** folder, the executable is put into the directory **bin**. By typing the command line **make run**, the **mpiexec** will be invoked to launch the parallel processes and all outputs are redirected to **jobs**. Note the **Makefile** is machine-dependent. One should properly modify the **Makefile** to enable the proper functionalities. Tetrahedral meshes for computations should be all put into **mesh** directory.

References

R. Aitbayev, X.-C. Cai, and M. Paraschivoiu. Parallel two-level methods for three-dimensional transonic compressible flow simulations on unstructured meshes. *Proceedings of Parallel CFD*, 1999. 131

J. D. Anderson. Polytropic interior for jupiter. *Private Email*, 2012. 144, 145, 146

J. D. Anderson, W. B. Hubbard, and W. L. Slattery. Structure of the jovian envelope from pioneer 10 gravity data. *Astrophys. J.*, 193:L149–L150, 1974. 144

M. Ansong, A. Kleinwächter, and M. Reinhard. Uniformly rotating axisymmetric fluid configurations bifurcating from highly flattened maclaurin spheroids. *Mon. Not. Roy. Astron. Soc.*, 339:515–523, 2003. 32

Satish Balay, Jed Brown, Kris Buschelman, William D. Gropp, Dinesh Kaushik, Matthew G. Knepley, Lois Curfman McInnes, Barry F. Smith, and Hong Zhang. Petsc web page, 2011. http://www.mcs.anl.gov/petsc. 20, 131

J. M. Bardeen. A reexamination of the post-newtonian maclaurin spheroids. *Astrophys. J.*, 167:425–446, 1971. 23

G. K. Batchelor. *An introduction to fluid dynamics*. Cambridge University Press, Cambridge, 1967. 66, 67

A. F. Bennett. *Lagrangian Fluid Dynamics*. Cambridge University Press, New York, 2006. 18

S. C. Brenner and L. Ridgway Scott. *The Mathematical Theory of Finite Element Methods*. Springer Science+Business Media, LLC, New York, 2008. 128

B. P. Brown, M. K. Browning, A. S. Brun, M. S. Miesch, and J. Toomre. Persistent magnetic wreaths in a rapidly rotating sun. *Astrophys. J.*, 711:424–438, 2010. 126

E. C. Bullard. The magnetic flux within the earth. *Pro. R. Soc. A*, 197:433–453, 1949. 22, 93

F. Busse. A simple model of convection in the jovian atmosphere. *Icarus*, 29:255–260, 1976. 47, 50, 51, 54, 63

F. H. Busse. Steady fluid flow in a precessing spheroidal shell. *J. Fluid Mech.*, 33: 739–751, 1968. 22

F. H. Busse. Convection driven zonal flows and vortices in the major planets. *CHAOS*, 4:123–134, 1994. 94

F. H. Busse. Convection in a narrow annular channel rotating about its axis of symmetry. *J. Fluid Mech.*, 537:145–154, 2005. 94, 95, 96

X.-C. Cai. Additive schwarz algorithms for parabolic convection-diffusion equations. *Numer. Math.*, 60:41–62, 1990. 131

X.-C. Cai. A parallel nonlinear additive schwarz preconditioned inexact newton algorithm for incompressible navier-stokes equations. *J. Comput. Phys.*, 204:666–691, 2005. 131

X.-C. Cai. Nonlinear overlapping domain decomposition methods. *Lecture Notes in Computational Science and Engineering, Springer*, 70:217–224, 2009. 131

X.-C. Cai and J. Zou. Some observations on the l^2 convergence of the additive schwarz preconditioned gmres method. *Numer. Lin. Alg. Applics.*, 9:379–397, 2002. 131

X.-C. Cai, D. E. Keyes, and L. Marcinkowski. Nonlinear additive schwarz preconditioners and applications in computational fluid dynamics. *International Journal for Numerical Methods in Fluids*, 40:1463–1470, 2002. 131

K. H. Chan, K. Zhang, J. Zou, and G. Schubert. A non-linear, 3-d spherical alpha(2) dynamo using a finite element method. *Physics of the Earth and Planetary Interiors*, 128:35–50, 2001. 129

K. H. Chan, K. Zhang, L. Li, and X. Liao. A new generation of convection-driven spherical dynamos using ebe finite element method. *Physics of the Earth and Planetary Interiors*, 163:251–265, 2007. 129

K. H. Chan, K. Zhang, and X. Liao. An ebe finite element method for simulating nonlinear flows in rotating spheroidal cavities. *Int. J. Numer. Meth. Fl.*, 63:395–414, 2010. 129

T. F. Chan and T. P. Mathew. Domain decomposition algorithms. *Acta Numerica*, pages 61–143, 1994. 131

S. Chandrasekhar. The equilibrium of distorted polytropes. i. the rotational problem. *Mon. Not. Roy. Astron. Soc.*, 93:390–406, 1933. 144, 145

S. Chandrasekhar. The internal constitution of the stars. *Proceedings of the American Philosophical Society*, 81:153–187, 1939. 144

S. Chandrasekhar. *An Introduction to the Study of Stellar Structure*. Courier Dover Publications, 1967. 144

S. Chandrasekhar. *Ellipsoidal Figures of Equilibrium*. The Silliman Foundation Lectures, Yale University Press, New Haven, CT., 1969. 20, 23

S. Chandrasekhar. *Hydrodynamic and hydromagnetic stability (Dover edition)*. Dover Publications, New York, 1981. 18

S. Chandrasekhar and N. R. Lebovitz. On the ellipsoidal figures of equilibrium of homogeneous masses. *ASTROPHYSICA NORVEGICA*, 9:323–332, 1964. 23

A. J. Chorin. Numerical solutions of navier-stokes equations. *Math. Comp.*, 22: 745–762, 1968. 109

J. Christensen-Dalsgaard. Lecture notes on stellar oscillations, 2003. http://users-phys.au.dk/jcd/oscilnotes/. 125

A. T. Chwang and T. Y. Wu. Hydromechanics of low-reynolds-number flow. part 2. singularity method for stokes flows. *J. Fluid Mech.*, 67:787–815, 1975. 68

T. C. Clune, J. R. Elliott, M. S. Miesch, J. Toomre, and G. A. Glatzmaier. Computational aspects of a code to study rotating turbulent convection in spherical shells. *Parallel Comput.*, 25:361–380, 1999. 126, 127

H. S. M. Coxeter. *Introduction to Geometry (Second Edition)*. Wiley, 1969. 136

Z. Cui, D. Kong, Y. Pan, and K. Zhang. On the swimming motion of spheroidal magnetotactic bacteria, (in progress). *Fluid Dynamics Research*. 91

G. Dassios and P. Vafeas. On the spheroidal semiseparation for stokes flow. *Research Letters in Physics*, 2008:135289, 2008. 68

R. P. Davies-Jones and P. A. Gilman. Convection in a rotating annulus uniformly heated from below. *J. Fluid Mech.*, 46:65–81, 1971. 94, 95, 123

J. Donea and A. Huerta. *Finite Element Methods for Flow Problems*. John Wiley & Sons Ltd., Chichester, England, 2003. 129

F. J. R. Eccles, P. L. Read, A. A. Castrejn-Pita, and T. W. N. Haine. Synchronization of modulated traveling baroclinic waves in a periodically forced, rotating fluid annulus. *Physical Review E*, 79:015202, 2009. 94

A. S. Eddington. *The internal constitution of the stars*. Cambridge University Press., Cambridge, 1926. 144

D. Edwardes. Steady motion of a viscous liquid in which an ellipsoid is constrained to rotate about a principal axis. *Quart. J. Math.*, 26:70–78, 1892. 68

A. B. Efimov, V. P. Zharkov, V. P. Trubitsyn, and Bobrov A. M. Figure parameters and gravitational moments of jupiter and saturn. *Sov. Astron.*, 21:635–640, 1977. 49

J. R. Elliott and P. K. Smolarkiewicz. Eddy resolving simulations of turbu-lent solar convection. *Int. J. Numer. Methods Fluids*, 39:855–864, 2002. 127

C. Eloy, P. Le Gal, and S. Le Dizs. Elliptic and triangular instabilities in rotating cylinders. *J. Fluid Mech.*, 476:357–388, 2003. 124

C. Farhat, M. Lesoinne, and K. Pierson. A scalable dualcprimal domain decomposition method. *Numer. Linear Algebra Appl.*, 7:687–714, 2000. 131

C. A. Felippa. A historical outline of matrix structural analysis: a play in three acts. *Comput. Struct.*, 79:1313–1324, 2001. 128

C. Foias, D. D. Holm, and E. S. Titi. The navier-stokes-alpha model of fluid turbulence. *Physica D*, 152:505–519, 2001. 126

R. F. Gans. On the precession of a resonant cylinder. *J. Fluid Mech.*, 476:865–872, 1970. 93, 124

M. Ghizaru, P. Charbonneau, and P. Smolarkiewicz. Magnetic cycles in global large-eddy simulations of solar convection. *Astrophys. J. Let.*, 715:L133–L137, 2010. 127

P. A. Gilman. Convection in a rotating annulus uniformly heated from below. part 2. nonlinear results. *J. Fluid Mech.*, 57:381–400, 1973. 94, 95, 96

D. O. Gough and J. Toomre. Seismic observations of the solar interior. *Ann. Rev. Astron. Astrophys.*, 29:627–684, 1991. 125

H. P. Greenspan. *The Theory of Rotating Fluids*. Cambridge University Press, Cambridge, UK, 1968. 96, 100

M. Griebel, T. Dornseifer, and T. Neunhoeffer. *Numerical Simulation in Fluid Dynamics, a Practical Introduction*. SIAM, Philadelphia, 1998. 109

T. Guillot and P. Morel. Cepam: a code for modeling the interiors of giant planets. *Astron. Astrophys. Suppl. Ser.*, 109:109–123, 1995. 49

C. R. Gwinn, T. A. Herring, and I. I. Shapiro. Geodesy by radio interferometry: Studies of the forced nutations of the earth. 2. interpretation. *J. Geophys. Res.*, 91:4755–4765, 1986. 43

O. Hall, C. P. Hills, and A. D. Gilbert. Nonaxisymmetric stokes flow between concentric cones. *Q. J. Mech. Appl. Math.*, 62:131–148, 2009. 69

F. Ham, Ch. Liang, and V. Terrapon. Hybrid central/weno method for com-pressible large eddy simulation on unstructured grids. *TFSA Conference 2010*, pages 375–382, 2010. 126, 127

J. Happel and H. Brenner. *Low Reynolds number hydrodynamics: with special applications to particulate media*. Springer, 1983. 68

M. Heimpel, J. Aurnou, and J. Wicht. Simulation of equatorial and high-latitude jets on jupiter in a deep convection model. *Nature*, 438:193–196, 2005. 47

R. Helled, G. Schubert, and J. D. Anderson. Jupiter and saturn rotation periods. *Planet. Space Sci.*, 57:1467–1473, 2009. 12, 44

J.S. Hesthaven and T. Warburton. *Nodal Discontinuous Galerkin Methods: Algorithms, Analysis and Applications*. Springer Science+Business Media, LLC, New York, 2008. 20

R. Hollerbach and R. R. Kerswell. Oscillatory internal shear layers in rotating and precessing flows. *J. Fluid Mech.*, 298:327–339, 1995. 93

G. P. Horedt. Seven-digit tables of lane-emden functions. *Astrophysics and Space Science*, page 357C408, 1986. 144

W. B. Hubbard. Gravitational field of a rotating planet with a polytropic index of one. *Astron. Zh.*, 51:1052–1059, 1974. 48

W. B. Hubbard. Effects of differential rotation on the gravitational figures of jupiter and saturn. *Icarus*, 52:509–515, 1982. 48, 50, 63

W. B. Hubbard. Gravitational signature of jupiter's deep zonal flows. *Icarus*, 137: 357–359, 1999. 48, 49, 63

W. B. Hubbard and G. P. Horedt. Computation of jupiter interior models from gravitational inversion theory. *ICARUS*, 54:456–465, 1983. 144

N. E. Hurlburt, D. Alexander, and A. M. Rucklidge. Complete models of axisym sunspots: Magnetoconvection with coronal heating. *Astrophys. J.*, 577:993–1005, 2002. 126

R. A. Jacobson, P. G. Antreasian, J. J. Bordi, K. E. Criddle, R. Ionasescu, J. B. Jones, M. C. Mackenzie, R. A. andMeek, D. Parcher, F. J. Pelletier, W. M. Owen Jr., D. C. Roth, I. M. Roundhill, and J. R. Stauch. The gravity field of the saturnian system from satellite observations and spacecraft tracking data. *Astron. J.*, 132:2520–2526, 2006. 12, 44

G. B. Jeffery. The motion of ellipsoidal particles immersed in a viscous fluid. *Proc. Roy. Soc. A*, 102:161–179, 1922. 68

C. A. Jones, J. Rotvig, and A. Abdulrahman. Multiple jests and zonal flow on jupiter. *Geophys. Res. Lett.*, 30:1–4, 2003. 94

G. Karypis and K. Schloegel. Parmetis web page, 2011. http://glaros.dtc.umn.edu /gkhome/metis/parmetis/overview. 137

Y. Kaspi, W. B. Hubbard, A. P. Showman, and G. R. Flierl. The gravity signature of jupiter's internal dynamics. *Geophys. Res. Lett.*, 37:L01204, 1999. 48, 63

R. R. Kerswell. The instability of precessing flow. *Geophys. Astrophys. Fluid Dyn.*, 72:107–144, 1993. 22, 93

R. R. Kerswell. Upper bounds on the energy dissipation in turbulent precession. *J. Fluid Mech.*, 321:335–370, 1996. 93

A. Klawonn and O. Rheinbach. Highly scalable parallel domain decomposition methods with an application to biomechanics. *Z. Angew. Math. Mech.*, 90:5–32, 2010. 131

J. J. Kobine. Inerital wave dynamics in a rotating and precessing cylinder. *J. Fluid Mech.*, 303:233–252, 1995. 93

J. Koiller, K. Ehlers, and R. Montgomery. Problems and progress in microswimming. *J. Nonlinear Sci.*, 6:507–541, 1996. 66

F.-D. Kong. Private discussions, 2011. 131

H. Lamb. *Hydrodynamics*. Cambridge University Press, Cambridge, UK, 1932. 18, 20, 23, 50, 52, 66, 68

J. H. Lane. On the theoretical temperature of the sun under the hypothesis of a gaseous mass maintaining its volume by its internal heat and depending on the laws of gases known to terrestrial experiment. *The American Journal of Science and Arts*, 50:57–74, 1870. 144

J. Latour, E. A. Spiegel, J. Toomre, and J.-P. Zahn. Stellar convection theory. i - the anelastic modal equations. *Astrophysical Journal*, 207:233–243, 1976. 126

Z. Lei. *Nonlinear Elastic Waves and Viscoelastic Fluids (unpublished lecture note of Fudan University)*. 2009. 17

Z. Lei, C. Liu, and Y. Zhou. Global solutions for incompressible viscoelastic fluids. *Arch. Ration. Mech. Anal.*, 188:371–398, 2008. 18

M. Lesieur and O. Métais. New trends in large-eddy simulations of turbulence. *Annu. Rev. Fluid Mech.*, 28:45–82, 1996. 126

J. Li. A dual-primal feti method for incompressible stokes equati. *Numer. Math.*, 102:257–275, 2005. 131

L. Li, X. Liao, K. H. Chan, and K. Zhang. Linear and nonlinear instabilities in rotating cylindrical rayleigh-bénard convection. *Phys. Rev. E*, 78:056303–1–056303–12, 2008. 94

X. Liao and K. Zhang. Inertial oscillation, inertial wave and initial value problem in rotating annular channels. *Geophys. Astrophys. Fluid Dyn.*, 103:199–222, 2009. 98

X. Liao and K. Zhang. A new legendre-type polynomial and its application to geostrophic flow in rotating fluid spheres. *Proc. R. Soc. A.*, 466:2203–2217, 2010. 54

X. Liao, K. Zhang, and Y. Chang. On boundary-layer convection in a rotating fluid layer. *J. Fluid Mech.*, 549:375–384, 2006. 94

G. F. Lindal, G. E. Wood, G. S. Levy, J. D. Anderson, D. N. Sweetnam, H. B. Hotz, B. J. Buckles, D. P. Holmes, P. E. Doms, V. R. Eshleman, G. L. Tyler, and T. A. Croft. The atmosphere of jupiter: An analysis of the voyager radio occultation measurements. *J. Geophys. Res.*, 86:8721–8727, 1981. 12, 44

G. F. Lindal, D. N. Sweetnam, and V. R. Eshleman. The atmosphere of saturn: An analysis of the voyager radio occultation measurements. *Astron. J.*, 90:1136–1146, 1985. 12, 44

X.-D. Liu, S. Osher, and T. Chan. Weighted essential nonoscillatory schemes. *J. Comput. Phys.*, 115:200–212, 1994. 127

S. Lorenzani and A. Tilgner. Fluid instabilities in precessing spheroidal cavities. *J. Fluid Mech.*, 447:111–128, 2001. 22

D. Lu. *University Physics (Second Edition)*. Higher Education Press, Beijing, 2004. 33

L. Luo, C. Yang, Y. Zhao, and X.-C. Cai. A scalable hybrid algorithm based on domain decomposition and algebraic multigrid for solving partial differential equations on a cluster of cpu/gpus. *Proceedings of 2nd International Workshop on GPUs and Scientific Applications*, 2011. 131

W. V. R. Malkus. Precession of the earth as the cause of geomagnetism. *Science*, 136:259–264, 1968. 22, 93

W. V. R. Malkus. An experimental study of global instabilities due to tidal (elliptical) distortion of a rotating elastic cylinder. *Geophys. Astrophys. Fluid Dyn.*, 48: 123–134, 1989. 93, 124

R. Manasseh. Breakdown regimes of inertia waves in a precessing cylinder. *J. Fluid Mech.*, 243:261–296, 1992. 93

R. M. Mason and R. R. Kerswell. Chaotic dynamics in a strained rotating flow: a precessing plane fluid layer. *J. Fluid Mech.*, 471:71–106, 2002. 93, 95, 96, 97, 109

P. M. Mathews, B. A. Buffett, T. A. Herring, and I. I. Shapiro. Forced nutations of the earth: Influence of inner core dynamics. 2. numerical results and comparisons. *J. Geophys. Res.*, 96:8243–8257, 1991. 43

P. Meunier, C. Eloy, R. Lagrange, and F. Nadal. A rotating fluid cylinder subject to weak precession. *J. Fluid Mech.*, 599:405–440, 2008. 93, 97

M. S. Miesch. Large-scale dynamics of the convection zone and tachocline. *Living Rev. Solar Phys.*, 2, 2005. 125, 126

K. Mohseni and T. Colonius. Numerical treatment of polar coordinate singularities. *J. Comput. Phys.*, 157:787–795, 2000. 127

A. Morelli and A. M. Dziewonski. Topography of the core–mantle boundary and lateral homogeneity of the liquid core. *Nature*, 325:678–683, 1987. 43

P.M. Morse and H. Feshbach. *Methods of Theoretical Physics*. McGraw Hill, New York, 1953. 27

NASA. Juno mission web page, 2012. http://www.nasa.gov/juno. 48

H. Neuber. Ein neuer absatz zur*ö*jsung r*ä*umlicher probleme der elastizi*ä*tstheorie. *Z. Anger. Math. Mech.*, 14:203–212, 1934. 69

J. Noir, D. Jault, and P. Cardin. Numerical study of the motions within a slowly precessing sphere at low ekman number. *J. Fluid Mech.*, 437:283–299, 2001. 93

J. Noir, P. Cardin, D. Jault, and Masson J. P. Experimental evidence of non-linear resonance effects between retrograde precession and the tilt-over mode within a spheroid. *Geophysical Journal International*, 154:407–416, 2003a. 93

J. D. J. Noir and P. Cardin. Numerical study of the motions within a slowly precessing sphere at low ekman number. *J. Fluid Mech.*, 437:283–299, 2001. 22

J. P. C. Noir, D. Jault, and J.-P. Masson. Experimental evidence of non-linear resonance effects between retrograde precession and the tilt-over mode within a spheroid. *Geophys. J. Int.*, 154:407–416, 2003b. 22

H. Oberbeck. *ü*ber station*ä*re fl*ü*ssigkeitsbewegungen mit ber*ü*cksichtigung der innere reibung. *J. Reine Angew. Math.*, 81:62–80, 1876. 68

J. G. Oldroyd. On the formulation of rheological equations of state. *Proc. R. Soc. Lond. A*, 200:523–541, 1950. 18

V. Olshevsky, Ch. Liang, F. Ham, Mansour A, and G. Kosovichev. Large-scale dynamics of the convection zone and tachocline. *Center for Turbulence Research Annual Research Briefs 2010*, pages 375–382, 2010. 127

P. F. Papkovich. The representation of the general integral of the fundamental equations of elasticity theory in terms of harmonic functions (in russian). *Izr. Akad. Nauk. SSSR Ser. Mat.*, 10:1425–1435, 1932. 69

K. V. Parchevsky and A. G. Kosovichev. Three-dimensional numerical simulations of the acoustic wave field in the upper convection zone of the sun. *Astrophys. J.*, 66:547–558, 2007. 126

E. N. Parker. Stellar fibril magnetic systems. iii. convective counterflow. *Astrophys. J.*, 294:57–65, 1985. 125

L. E. Payne and W. H. Pell. The stokes flow problem for a class of axially symmetric bodies. *J. Fluid Mech.*, 7:529–549, 1960. 68

C. C. Porco et. al. Cassini imaging of jupiter's atmosphere, satellites and rings. *Science*, 299:1541–1547, 2003. 8, 47, 55

W. H. Press, Teukolsky S. A., W. T. Vetterling, and P. B. Flannery. *NUMERICAL RECIPES: The Art of Scientific Computing (Third Edition)*. Cambridge University Press, New York, 2007. 38

J. M. Prusa, P. K. Smolarkiewicz, and A. A. Wyszogrodzki. Eulag, a computational model for multiscale flows. *Computers and Fluids*, 37:1193–1207, 2008. 127

E. M. Purcell. Life at low reynolds number. *AM J. Phys.*, 45:3–11, 1977. 66

F. Rincon, F. Lignières, and M. Rieutord. Mesoscale flows in large aspect ratio simulations of turbulent compressible convection. *Astron. Astrophys.*, 430:L57–L60, 2005. 126

P. H. Roberts and K. Stewartson. On the motion of a liquid in a spheroidal cavity of a precessing rigid body: Ii. *Mathematical Proceedings of the Cambridge Philosophical Society*, 61:279–288, 1965. 22, 95

F. J. Robinson, P. Demarque, L. H. Li, S. Sofia, Y.-C. Kim, and K. L. Chan. Three-dimensional convection simulations of the outer layers of the sun using realistic physics. *Mon. Not. R. Astron. Soc.*, 340:923–936, 2003. 126

J. Schöberl. Netgen web page, 2004. http://www.hpfem.jku.at/netgen/. 137

G. Schubert, J. Anderson, K. Zhang, D. Kong, and R. Helled. Shapes and gravitational fields of rotating two-layer maclaurin ellipsoids: Application to planets and satellites. *Physics of the Earth and Planetary Interiors*, 187:364–379, 2011. 45

R. K. Scott and L. M. Polvani. Equatorial superrotation in shallow atmospheres. *Geophys. Res. Lett.*, 35:L24202, 2008. 47

P. K. Seidelmann et. al. Report of the iau/iag working group on cartographic coordinates and rotational elements of the planets and satellites: 2006. *Celestial Mech. Dyn. Astr.*, 98:155–180, 2007. 61, 62

P. N. Shankar. *Slow Viscous Flows C Qualitative Features and Quantitative Analysis Using the Method of Complex Eigenfunction Expansions*. Imperial College Press, 2007. 66

P. N. Shankar. Exact solutions for stokes flow in and around a sphere and between concentric spheres. *J. Fluid Mech.*, 631:363–373, 2009. 69

C.-W. Shu. Essentially non-oscillatory and weighted essentially non-oscillatory schemes for hyperbolic conservation laws, 1997. NASA/CR-97-206253 ICASE Report No. 97-65. 127

C.-W. Shu and S. Osher. Efficient implementation of essentially non-oscillatory shork capturing schemes. *J. Comput. Phys.*, 77:439–471, 1988. 127

C.-W. Shu, T. A. Zang, G. Erlebacher, D. Whitaker, and S. Osher. High order eno schemes applied to two- and three-dimensional compressible flow. *Appl. Num. Math.*, 9:45–71, 1992. 127

B. F. Smith, F. E. Bjørstad, and W. Gropp. *Domain Decom,position: Parallel Multilevel Methods for Elliptic Partial Differential Equations*. Cambridge University Press, Cambridge, 1996. 131

W.R. Smythe. *Static and Dynamic Electricity(Second Edition)*. McGraw Hill, New York, 1950. 27, 31

R. F. Stein and Å. Nordlund. Simulations of solar granulation: I. general properties. *Astrophys. J.*, 499:914–933, 1998. 126

R. F. Stein and Å. Nordlund. Realistic solar convection simulations. *Solar Phys.*, 192:91–108, 2000. 126

H. Taseli and M. Demiralp. A new approach to the classical stokes flow problem: Part i methodology and first-order analytical results. *Journal of Computational and Applied Mathematics*, 78:213–232, 1997. 68

A. Tilgner. Magnetohydrodynamic flow in precessing spherical shells. *J. Fluid Mech.*, 136:303–318, 1999. 93

A. Tilgner. Precession driven dynamos. *Phys. Fluids*, 17:034104, 2005a. 22

A. Tilgner. Precession driven dynamos. *Physics of Fluids*, 17:034104–034106, 2005b. 93

A. Tilgner. *Rotational dynamics of the core, in Treatise on Geophysics*, pages 207–243. Elsevier B.V., Amsterdam, 2007a. 22

A. Tilgner. Kinematic dynamos with precession driven flow in a sphere. *Geophys. Astrophys. Fluid Dyn.*, 100:1–9, 2007b. 93

A. Tilgner and F. H. Busse. Fluid flows in precessing spherical shells. *J. Fluid Mech.*, 426:387–396, 2001. 93

A. Tornbergt. Multi-dimensional quadrature of singular and discontinuous functions. *BIT Numerical Mathematics*, 42:644–669, 2002. 38

A. Toselli and O. Widlund. *Domain Decomposition Methods – Algorithms and Theory*. Springer-Verlag, Berlin Heidelberg, 2005. 131, 133

T. Tran-Cong and J. Blake. General solution of the stokes' flow equations. *Journal of Mathematical Analysis and Applications*, 90:72–84, 1982. 69

V. P. Trubitsyn, P. P. Vasilev, and A. B. Efimov. Gravitational fields and figures of differentially rotating planets. *Sov. Astron.*, 20:724–729, 1976. 49

I. G. Usoskin and K. Mursula. Long-term solar cycle evolution: Review of recent developments. *Solar Phys.*, 218:319–343, 2003. 126

J. Vanyo, P. Wilde, P. Cardin, and P. Olson. Experiments on precessing flows in the earth's liquid core. *Geophys. J. Int.*, 121:136–142, 2007. 22

J. P. Vanyo. *Rotating Fluids in In Engineering and Science*. General Publishing Company, Toronto, 1993. 94

J. P. Vanyo, P. Wilde, P. Cardin, and P. Olson. Experiments on precessing flows in the earth's liquid core. *Geophysical Journal International*, 121:136–142, 1995. 93

P. P. Vasilev, A. B. Efimov, and V. P. Trubitsyn. Influence of the differential rotation of planets on their gravitational fields. *Sov. Astron.*, 22:83–87, 1978. 49

A. Vögler, S. Shelyag, M. Schüssler, F. Cattaneo, and T. Emonet. Simulations of magneto-convection in the solar photosphere. equations, methods, and results of the muram code. *Astron. Astrophys.*, 429:335–351, 2005. 126

N. O. Weiss, D. P. Brownjohn, P. C. Matthews, and M. R. E. Proctor. Photospheric convection in strong magnetic fields. *Mon. Not. R. Astron. Soc.*, 283:1153–1164, 1996. 126

N. O. Weiss, D. P. Brownjohn, P. C. Matthews, and M. R. E. Proctor. Magnetic flux separation in photospheric convection. *Mon. Not. R. Astron. Soc.*, 337:293–304, 2002. 126

D. R. Williams. Jupiter fact sheet, November 16, 2004. http://nssdc.gsfc.nasa.gov/planetary/factsheet/jupiterfact.html. 145

G. P. Williams. Planetary circulations: 1. barotropic representation of jovian and terrestial turbulence. *J. Atmos. Sci.*, 35:1399–1426, 1976. 47

J. Williams, D. Boggs, C. Yoder, J. Ratcliff, and J. Dickey. Lunar rotational dissipation in solid body and molten core. *J. Geophys. Res.*, 106:E11, 2001. 22

C. C. Wu and P. H. Roberts. A precesionally-driven dynamo in a plane layer. *Geophys. Astrophys. Fluid Dyn.*, 102:1–19, 2008. 22, 93, 94, 95, 96, 97, 109

C. C. Wu and P. H. Roberts. On a dynamo driven by topographic precession. *Geophys. Astrophys. Fluid Dyn.*, 103:467–501, 2009. 93

W. Wu. *Fluid Mechanics (in Chinese)*. Peking University Press, Beijing, 1982. 17

J. Xu and J. Zou. Some nonoverlapping domain decomposition methods. *SIAM Review*, 40:857–914, 1998. 131

H. Yang and X.-C. Cai. Parallel two-grid semismooth newton-krylov-schwarz method for nonlinear complementarity problems. *J. Sci. Comput.*, 47:258–280, 2011. 131

K. Zhang. Spiraling columnar convection in rapidly rotating spherical fluid shells. *J. Fluid Mech.*, 236:535–556, 1992. 51

K. Zhang and X. Liao. A new asymptotic method for the analysis of convection in a rotating sphere. *J. Fluid Mech.*, 518:319–346, 2004. 123

K. Zhang and G. Schubert. From penetrative convection to teleconvection. *Astrophys. J.*, 572:461–476, 2002. 51

K. Zhang, X. Liao, and P. Earnshaw. On inertial waves and oscillations in a rapidly rotating spheroid. *J. Fluid Mech.*, 504:1–40, 2004. 22

K. Zhang, D. Kong, and X. Liao. On fluid flows in precessing narrow annular channels: asymptotic analysis and numerical simulation. *J. Fluid Mech.*, 656: 116–146, 2010. 95, 98, 108

V. N. Zharkov and V. P. Trubitsyn. *Physics of Planetary Interiors, Edited by W. B. Hubbard*. Pachart Publishing House, Tucson, 1978. 49

V. N. Zharkov, V. V. Leontjev, and A. V. Kozenko. Models, figures, and gravitational moments of the galilean satellites of jupiter and icy satellites of saturn. *Icarus*, 61:92–100, 1985. 24, 45